Vortex Simulation of Separated Flows
in
Two and Three Dimensions

Thesis by

Kiat Chua

In Partial Fulfillment

of the Requirements for the Degree of

Doctor of Philosophy

California Institute of Technology

Pasadena, California

1990

(Submitted April 20th 1990)

to

my parents, Kia-Hong and Chi-Tai

Acknowledgments

Abstract

This thesis is concerned with the applications of vortex methods to the problem of unsteady, separated flows in two and three dimensions, and can be divided into three parts. In the first part, an improved method for satisfying the boundary conditions on a flat plate is developed and applied to the two-dimensional separated flow problem. In this method, boundary layers on both side of the plate are represented by stacks of multiple vortex panels, the strength of which are determined by enforcing both the no-through flow and no-slip boundary conditions at the plate. Vortex shedding at the sharp edge of the plate is represented as the separation of the boundary vortex elements. Both forced and unforced flows are studied and comparisons to experiments are carried out. For the case without forcing, large discrepancy between calculations and experiments, which is also reported by other workers using a different vortex method or Navier-Stokes calculations, is observed. In the case with forcing, the discrepancy is reduced with lateral forcing at low amplitude; and eliminated, regardless of amplitude, with streamwise forcing (acceleration). In the second part, an improved three-dimensional vortex particle method is developed. In this method, vortex elements of vorticity that move with the local velocity and are stretched and rotated according to the local strain field, are used. To mimic the effects of vorticity cancellations, close pairs of opposite sign vortex elements are replaced by high order dipoles. The method is designed to handle complex high Reynolds number vortical flows and a non-linear viscosity model is included to treat small-scale effects in such flows. Applications to two problems involving strong interactions of vortex tubes are carried out and core deformation with complex internal strucures and induced axial flow within vortex tubes are observed. Qualitative comparison to experiments are encouraging. In the third part, the two-dimensional method developed in the first part is modified and extended to three dimensions. Here, solenoidal condition for vorticity is considered and closed vortex loops are used to represent the boundary layer vorticity and the vorticity at shedding. For the evolution of the vortex wake, the vortex particle method developed in the second part is used. Applications to the flow past a normal square plate is carried out and the early stages of the flow are studied.

Table of Contents

List of Tables

List of Figures

CHAPTER 1

Introduction

Recently, there has been much interest in the classic fluid mechanic problem of high Reynolds number, unsteady, separated flows past a bluff body and much of this has been inspired by the possibilities of supermaneuverability and the related problem of dynamic stall. For such possibilities to be realized, we need a thorough understanding of the dynamics of vortices in the wake of the body, the interaction between these vortices, and the interaction between the vortices and the body. Several transient flows are particularly important for building a foundation for the understanding of these problems, and they include pitch-up, plunge-down, start-up and periodic oscillation of airfoils or airfoil-like bodies. The objective of this thesis is to study such flows through vortex simulations of flat plate flows at a high angle of attack in two and three dimensions. The flat plate is chosen because of its simple body geometry and fixed separation points. In spite of these simplifications, flat plate flows contain all the essential ingredients of high Reynolds number, separated flows such as asymmetric shedding of large vortical structures with fluctuating body forces, interactions between vortical structures in the wake, interactions between vortex wake and body, etc.

For a detailed representation of the wake evolution, vortex methods (Leonard 1980, 1985), which are designed to be most efficient in handling unsteady flows with massive separations, are used. Formulated in terms of a Lagrangian description, they continually track the motion of the regions of non-zero vorticity in the wake and concentrate the computing resources to provide a fine scale description within these regions. In regions where there is little or no vorticity, no computing resource is needed. From a computational point of view, this is an important advantage when compared to the more conventional Eulerian methods, where a grid is usually used and computing resources are needed everywhere.

In the literature, numerous applications of vortex methods to the problem of two-dimensional flow past flat plate are found (Kuwahara 1973, Sarpkaya 1975, Kiya and Arie 1977, 1980, Chein and Chung 1988 and Dutta 1988). In these calculations, a mapping technique is used to map the plate onto a circle, where the no-through flow boundary condition is enforced through the use of image vortices. However,

there are difficulties with this method:

(i) Because of the singularity in the mapping at the sharp edge, the flow in the physical plane is singular at the separation point.

(i) Because there is no boundary layer explicitly represented at the plate, it is difficult to specify the flux of vorticity at the separation point and to choose the location and strength of the newly shed vortex element without introducing some arbitrariness.

In Chapter 2, a new method for treating the boundary conditions and the shedding mechanism of the two-dimensional plate is developed. In this method, both the no-through flow and the no-slip boundary conditions at the plate are satisfied. This allows for a representation of the boundary layers at the plate. With such a representation, the actual shedding mechanism at the separation points, which is the separation of the boundary layers, can be accounted for without introducing any arbitrariness. Also, since both front and back boundary layers are allowed to separate, two signs of vorticity are included in the separated shear layer. Several flows, including both forced and unforced flows, are studied, and comparisons to experiments as well as other calculations are carried out.

Although the two-dimensional vortex methods are well developed and widely used in simulations of unsteady separated flows, their three-dimensional counterparts are still in an early stage of development. Numerical difficulties are encountered in applications of vortex methods to flows with strong interactions of vortex tubes in infinite domain (Leonard 1975, Shirayama and Kuwahara 1984, Anderson and Greengard 1984, Mosher 1985), and improvements of the method are needed before applications to separated flows are possible. In Chapter 3, a robust, three-dimensional, vortex-particle method capable of handling complex high Reynolds number flows with strong interactions of vortex tubes in infinite domain is developed. In this method, a non-linear eddy viscosity model is included to account for small-scale effects of the high Re flows. The method is tested on two vortex tubes interactions problems, and comparisons to experiments and other calculations are carried out.

For the problem of three-dimensional separated flows, several calculations could be found in the literature (Kandil et al. 1974, Katz 1984, Almosino 1985, Skomedal 1985) and typically, vortex-lattice methods are used. There is one calculation by Rehbach (1978) where a vortex-particle method is used. However, it is unclear how the vortex particles are shed into the fluid and whether the Kutta condition and the divergence condition of vorticity at separation are satisfied is questionable.

In Chapter 4, a three-dimensional vortex method for computing high Reynolds number, unsteady, separated flows, based on an extension of the two-dimensional method developed in Chapter 2, is proposed. In this method, the solenoidal condition of vorticity is properly enforced when representing the boundary layers and the shedding mechanism. At the plate, all three components of velocity are cancelled and two different type of loops are used for the no-through flow and no-slip boundary conditions. The evolution of the shed vorticity in the wake is computed using the vortex-particle method developed in Chapter 3. The method is applied to the problem of separated flow past normal square plate, and the early stage of the flow is studied.

CHAPTER 2
Two-dimensional Unsteady Separated Flow

This chapter presents the results of a study of two-dimensional high Reynolds number, unsteady, separated flow past a flat plate using vortex methods. The objective of this study is to develop a method that could properly account for the boundary conditions at the plate and the shedding mechanism at the separation points of the plate.

In Sec. (2.1), a survey of some of the related works in the literature is presented, and a discussion of the methods used is given. In Sec. (2.2) and (2.3), we present the mathematical foundation and numerical implementation of the proposed method of computation. Applications of the method to the problems of forced and unforced flow past a normal flat plate with an impulsive or ramp start are given in Sec. (2.4). In the present work, both lateral forcing and rotational forcing are considered. In lateral forcing, the plate is moved sinusoidally along its length in the crossflow direction. Several combinations of amplitude and period are used and the resulting flows are studied. Comparison to experiments is made. For the rotational forcing, the plate is pitched sinusoidally about the 90° position.

2.1 Previous Work

Following the pioneering work of Rosenhead (1931), vortex methods have been widely used as a means of computing complex two-dimensional, unsteady vortical flows and excellent reviews of the methods and its applications are given by Fink and Soh (1974), Clements and Maull (1975), Maull (1979), Saffman and Baker (1979), Leonard (1980a) and Sarpkaya (1989). However, despite their wide acceptance, there are still difficulties associated with their use, and one of the most forbidding difficulties is in the specification of the vorticity boundary conditions at the wall, especially for a smooth body. It is well known that vorticity is created as a result of viscous action in the boundary-layer and is shed into the outer flow when the boundary-layer separates. However, it is difficult to incorporate such an unsteady separation mechanism by coupling the classical unsteady boundary equation with a vortex method in the outer flow because the solution to the unsteady boundary-layer equations develops a singularity in finite time. This has been

shown analytically by Van Dommelen and Shen (1980) and confirmed numerically by Matsushita et al. (1984). Using an integral method to approximate the solution to the steady boundary-layer equations, Spalart (1982) and Spalart et al. (1983) estimated the locations of the separation points and allowed the vortices to depart from these points. However, it is unclear whether neglecting the unsteady effects in the boundary-layer equations is warranted.

For applications to flow past a body with sharp edges, such as the flat plate, the separation point is known a priori. However, other difficulties persist, and these include the following:

(i) mapping is usually used to map such body onto a circle where the no-through flow boundary condition is enforced through the use of image vortices, but because of the singularity in the mapping at the sharp edge, the flow in the physical plane is singular there.

(ii) it is difficult to specify the flux of vorticity at the separation point and to choose the location and strength of the newly shed vortex without introducing some arbitrariness.

One of the earliest applications of the vortex method to the problem of flow past sharp-edged bodies is by Ham (1968), wherein he studied the dynamic stall of an airfoil. Later, Clements (1973) and Clements and Maull (1975) computed the flow behind a square-based body by using a mapping technique. A new vortex is created at a fixed point downstream of the separation point (referred to as the Method of Fixed Position or MFP by Kiya and Arie 1977), and the Kutta condition at the separation point is satisfied by adjusting the circulation of the new vortex. Using a similar scheme with the point vortex method, Kuwahara (1973) computed the flow behind an inclined flat plate. In his results, large oscillations of the drag signal are apparent but no definite periodicity can be observed. The time-averaged drag coefficient is about 1.5-2.0 times that of the experiments (Fage and Johansen 1927, Roshko 1954 and Sarpkaya and Kline 1982). Later, Inoue and Kuwahara (1985) extended the calculation to include the effects of plate porosity.

Sarpkaya (1975) proposed a method where the circulation of the newly created vortex is given by,

$$
\begin{aligned}
\frac{d\Gamma}{dt} &= \frac{1}{2}(U_{e_2}^2 - U_{e_1}^2) \\
&\simeq \frac{1}{2}U_{e_2}^2 \\
&\simeq \frac{1}{2}U_{sh}^2 ,
\end{aligned}
\tag{2.1.1}
$$

where U_{e_1} and U_{e_2} are the velocities of the inner and outer edges of the shear layer leaving the separation point, and U_{sh} is the convection velocity of the shear layer and is estimated by taking the average of the velocities of the first four vortices in the shear layer. The position of the new vortex is chosen such that the Kutta condition is enforced at the separation point (referred to as the Method of Variable Position or MVP by Kiya and Arie 1977). He argued that the oscillation of the point of appearance of new vortex is essential in maintaining the periodicity of the drag signal and is coupled with the manner in which the shear layer rolls up, and he suggested that the violent oscillations of the drag signals observed in Kuwahara's calculations were due to the fact that he overlooked this point. In terms of drag coefficient, Sarpkaya's results compared favorably with experiments with a discrepancy of only 25%. Later, Kiya and Arie (1977) repeated Kuwahara's calculation, using smooth vortex blobs as suggested by Chorin (1973). They were able to obtain a drag signal with definite periodicity and suggested that the arguments of Sarpkaya were not justified. However, the Strouhal number estimated was about 30% lower than the experimental values. They also studied the effect of varying the creation point of a new vortex relative to the edge and found strong dependency of the drag coefficient on such an effect. Over the range of creation points studied, they found that the drag coefficient is always overestimated with a maximum of about 70% compared to experiments. Using a similar technique but with the no-slip boundary condition satisfied at a point near separation, Dutta (1988) computed the normal flat plate flow and found a time-averaged C_d of about twice the experimental value with violent oscillations in the signal. No definite periodicity was observed (see Table 2.1).

For flow past a bluff body with finite thickness, Spalart (1982) and Spalart et al. (1983) avoided the use of the conventional mapping technique and image vortices, and proposed a scheme where a layer of vortex blobs is created around the body with the strength of the vortices adjusted by requiring that the streamfunction be a constant on the body. He was able to show that both the no-through flow and no-slip boundary conditions are satisfied on the wall boundary. The method was

applied to various body geometries, including a circular cylinder, a square cylinder, pitching and non-pitching airfoil (Spalart and Leonard 1981, Spalart 1982, Spalart et al. 1983); a tandem array of two square cylinders (Couet and Spalart 1982); backward and forward facing triangular cylinder (Spalart 1984, unpublished); a cascade of airfoils with periodic boundary conditions (Spalart 1984, 1985, Speziale et al. 1986) and airfoil with flap (McCroskey et al. 1985). Comparison of the computed drag coefficient to experimental values showed reasonable agreement for the case of a circular cylinder and a pitching airfoil, although in most cases, it is usually overestimated; i.e. for the airfoil inclined at 90° to the freestream, the computed drag is about twice the experimental value. For the case of the cascade of airfoils, only qualitative comparison to flow visualization experiments was attempted. Using Spalart's vortex method, with minor modification, Park(1989) studied several body geometries, including a rectangular cylinder with/without a splitter plate, a triangular cylinder, a semi-elliptical cylinder, an elliptical concave cylinder and a circular arc, etc., over a wide range of L/W, where L and W are the length and width of the body. He found that the drag is always overestimated as L/W is reduced. For the normal flat plate, he reported an error of 40% compared to experiments. He also included the effects of viscous diffusion, using a variation of Leonard's corespreading scheme (1980a) and found no significant change in the computed drag. Similar studies were also carried out by McCroskey et al. (1985), where they modelled viscous diffusion using Chorin's random walk method (1973). They reported that "only by simulating low values of Reynolds number, on the order of 100, was the drag reduced to approximately the experimental values" and suggested that "the vorticity in the wake becomes highly three-dimensional.....reducing its effective induced-velocity field in the plane of the mean flow". Using the method of pseudo-compressibility, Rogers and Kwak (1988) obtained a Navier-Stokes solution to the problem of flow past a 90° airfoil at a Reynolds number of 200. The computed drag coefficient compared very well with experiments but the comparison of pressure distributions on the airfoil showed discrepancies, especially on the backside of the airfoil. More recently, Raghavan et al. (1990) computed the problem of flow past a slender ellipse, also at $\alpha = 90°$, using Navier-Stokes simulations at $Re = 200$ and reported a C_d of 2.8. No calculation at a higher Reynolds number was attempted.

Kiya et al. (1979, 1982) and Kiya and Arie (1980) suggested that some form of circulation decay with time can be introduced to include the 3D effects in a 2D calculation. They argued that such reduction is a result of the vorticity transfer from large-scale fluctuations to small-scale turbulence. However, one drawback of such a circulation reduction scheme is that it involves an arbitrary decay constant, which is usually determined empirically. Inamuro et al. (1983) and Inamuro (1988)

computed several different body geometries, including a square cylinder, a circular cylinder and two different bridge sections. They used vortex panels for the inviscid boundary condition and applied the circulation reduction scheme of Kiya and co-workers to the wake vortices. They were able to obtain good agreement of $\overline{C}_d$, $\overline{C}_l$ and St with experiments for some decay constant but observed that a chosen decay constant that gave good agreement for a particular body geometry at a given angle of attack might not be the best choice for a different body geometry or even the same body at a different angle of attack. Chein and Chung (1988) computed the problem of the inclined flat plate using a mapping technique with the circulation reduction scheme of Kiya and co-workers. They determined the decay constant using a fit with the experimental velocity profiles, turbulent intensities and Reynolds stresses. They studied the cases with the plate inclined at 60° and 90° and found strong dependence of the decay constant on the angle of inclination. The computed drag coefficient for $\alpha = 60°$ compared very well with experiments with only 10% error but at $\alpha = 90°$, the experimental value was overestimated by about 50%.

2.2   Mathematical Formulation

The motion of an incompressible viscous fluid in two dimensions is described by the Navier-Stokes equations,

$$\frac{\partial \underline{u}}{\partial t} + \underline{u} \cdot \nabla \underline{u} = -\nabla P + \nu \nabla^2 \underline{u} \ , \tag{2.2.1}$$

and the incompressibility condition,

$$\nabla \cdot \underline{u} = 0 \ , \tag{2.2.2}$$

where $\underline{u} = (u, v)$ and $\underline{x} = (x, y)$. Together, Eqn. (2.2.1) and (2.2.2) constitute a system of 3 equations with 3 unknowns, namely u, v and P. The boundary conditions for this set of equations are:

$$\underline{u} = \underline{u}_s \ \text{at solid wall} \ , \tag{2.2.3a}$$

$$\underline{u} = \underline{U}_\infty \ \text{at} \ \infty \ , \tag{2.2.3b}$$

where $\underline{u}_s$ and $\underline{U}_\infty$ are the velocity of the solid body and the freestream velocity, respectively.

In some applications, it is usually more convenient to cast the above set of equations in vorticity formulation form. This is done by taking the curl of Eqn. (2.2.1) to eliminate the pressure term and applying the incompressibility condition to eliminate the term involving the divergence of velocity. We are then left with the following vorticity conservation equation with only one unknown ω,

$$\frac{\partial \omega}{\partial t} + \underline{u} \cdot \nabla \omega = \nu \nabla^2 \omega \ , \tag{2.2.4}$$

where the left-hand side of the equation treats the convection of vorticity and the right-hand side diffusion of vorticity by viscous effects. Here, ω is the scalar vorticity. The vector vorticity is the curl of the velocity field,

$$\omega \hat{e}_z = \nabla \times \underline{u} \ . \tag{2.2.5}$$

For an inviscid fluid, Eqn. (2.2.4) reduces to

$$\frac{\partial \omega}{\partial t} + \underline{u} \cdot \nabla \omega = 0 \ . \tag{2.2.6}$$

Eqn. (2.2.6) is the foundation for the Kelvin and Helmholtz Theorems, which state that infinitesimal packets of vorticity convect at the local velocity like material elements (see Batchelor 1967). To express the velocity field in terms of the vorticity field, we take the curl of Eqn. (2.2.5), resulting in the Poisson's equation

$$\nabla^2 \underline{u} = -\nabla \times \omega \hat{e}_z \ . \tag{2.2.7}$$

If the flow field has no interior boundary and the fluid is at rest at infinity, the solution to Eqn. (2.2.7) is given by the Biot-Savart formula,

$$\underline{u}(\underline{x}, t) = -\frac{1}{2\pi} \int \frac{(\underline{x} - \underline{x}') \times \omega \hat{e}_z}{\mid \underline{x} - \underline{x}' \mid^2} d\underline{x}' \ . \tag{2.2.8}$$

2.2.1 Vortex Method

In the vortex method, the vorticity field is represented by a collection of discrete vortex particles

$$\omega(\underline{x}, t) = \sum_{i=1}^{N_v} \Gamma_i \gamma_i(\mid \underline{x} - \underline{x}_i(t) \mid) \ , \tag{2.2.9}$$

where Γ_i and $\underline{x}_i$ are the circulation and location, respectively, of the ith vortex particle and γ_i is the core function describing the vorticity distribution within the vortex. Substituting Eqn. (2.2.9) in Eqn. (2.2.8) results in the following discretized Biot-Savart formula,

$$\underline{u}(\underline{x}, t) = -\frac{1}{2\pi} \sum_{i=1}^{N_v} (\underline{x} - \underline{x}_i) \times \Gamma_i \hat{e}_z f_i(\mid \underline{x} - \underline{x}_i \mid) \ , \tag{2.2.10}$$

where

$$f(\mid \underline{x} - \underline{x}_i \mid) = \frac{1}{\mid \underline{x} - \underline{x}_i \mid^2} g(\mid \underline{x} - \underline{x}_i \mid) \ , \tag{2.2.11}$$

and

$$g(r) = \int_0^{2\pi} \int_0^r \gamma(r') r' dr' d\theta \ . \tag{2.2.12}$$

For a system with N_v vortex particles, and assuming that each particle moves at the velocity evaluated at its center, we have a system of N_v simultaneous equations,

$$\frac{d\underline{x}_i}{dt} = \underline{u}(\underline{x}_i, \ t), \quad i = 1, \ N_v \ . \tag{2.2.13}$$

Leonard (1980a) suggested a more elaborate assumption concerning convection, where the velocity is not evaluated at the center of the particle but computed as

$$\frac{d\underline{x}_i}{dt} = \int \gamma(\underline{x}_i - \underline{x}') \underline{u}(\underline{x}', \ t) d\underline{x}' \ . \tag{2.2.14}$$

This method has the advantage that energy is conserved. However, the integral is costly to evaluate and the model is not usually used in practice.

2.2.1.1 Point Vortex Method

In most earlier calculations, the point vortex method was used because of its simplicity and the fact that its dynamics give a weak solution to the inviscid Euler's equations (Saffman and Meiron 1986). In this method, the Dirac delta function $\delta(\underline{x})$ is used as the core function $\gamma(\underline{x})$, resulting in the following set of N_v simultaneous equations,

$$\frac{d\underline{x}_i}{dt} = -\frac{1}{2\pi} \sum_{\substack{j=1 \\ j \neq i}}^{N_v} \frac{(\underline{x}_i - \underline{x}_j) \times \Gamma_j \hat{e}_z}{|\,\underline{x}_i - \underline{x}_j\,|^2} \ . \tag{2.2.15}$$

Here, the vorticity field is represented as a collection of spikes in a field that is otherwise identically zero. The velocity field is correspondingly non-smooth with singularities at the locations of the vortices.

One of the first attempts to compute a fluid flow problem using the point vortex method was by Rosenhead (1931). Using just a few point vortices, he computed the roll-up of a singular vortex sheet by hand. Later, with the advent of digital computers, calculations of the same problem using more and more vortices of reduced strength and accurate time integration (Birkhoff 1962, Takami 1964, Moore 1971, 1974) did not show convergence of the method. Moore (1971) used 16 digit arithmetic and a fourth-order Runge-Kutta integration scheme and found that chaotic motion of the vortices always occurs regardless of the size of the time step used. He concluded that the integration method was accurate and suggested that the exact solution of the discrete system does not converge to the solution of the equation governing the continuous sheet, as the number of point vortices tends to infinity. More recent work by Krasny (1986) has suggested that round-off error produces catastrophic effects and that the vortex sheet problem is ill-posed in the sense that singularity develops in finite time even if the initial condition is smooth.

Despite its simplicity and exactness (in the sense of a weak solution to Euler's equations), most workers have preferred the less singular vortex blob methods and one of the reasons for such preference is that the earlier convergence proof of vortex methods found in the literature (Hald and Del Prete (1978), Hald 1979, Beale and Majda 1982) were for vortex blobs with sufficient overlap. Recently, Goodman et al. (1989a) was able to prove the convergence of the point vortex method to the Euler's equations.

2.2.1.2 Vortex Blob Method

In 1973, Chorin employed vortex particles with the following core function,

$$\gamma(|\,\underline{x}\,|) = \begin{cases} \frac{1}{2\pi\sigma|\underline{x}|} \ , & \text{if } |\,\underline{x}\,| < \sigma, \\ 0 \ , & \text{otherwise,} \end{cases} \qquad (2.2.16)$$

to get a bounded induced velocity. Here, the induced velocity is cut off to a constant within the core.

The advantage of using such blobs over point vortices is obvious because of the smoother induced velocity field and, of course, a smooth vorticity field is more realistically represented. Here, the function γ must satisfy the following constraints,

$$\int \gamma(\underline{x}, \sigma)d\underline{x} = 1 \ , \qquad (2.2.17a)$$

$$\gamma(\underline{x}, \sigma) \rightarrow \delta(\underline{x}) \ \ as \ \ \sigma \rightarrow 0 \ . \qquad (2.2.17b)$$

Some example of core functions frequently encountered in the literature include the Gaussian,

$$\gamma(|\,\underline{x}\,|) = \frac{1}{\pi\sigma^2}e^{(\frac{|\underline{x}|}{\sigma})^2} \ , \qquad (2.2.18)$$

and the algebraic function

$$\gamma(|\,\underline{x}\,|) = \frac{\sigma^2}{\pi}\frac{1}{(\sigma^2 + |\,\underline{x}\,|^2)^2} \ . \qquad (2.2.19)$$

The Gaussian is second-order accurate in space and offers the advantage of satisfying the diffusion term in Eqn. (2.2.4) exactly (Leonard 1980a), if σ is allowed to increase according to the following equation,

$$\frac{d\sigma^2}{dt} = 4\nu \ . \qquad (2.2.20)$$

However, because of its costly evaluation, it is not usually used in practice. The algebraic core function, in contrast, is very simple to evaluate but offers only first-order accuracy in space. Recently, Winckelmans (1989) suggested a second-order algebraic function that is as accurate in space as the Gaussian but much simpler to evaluate,

$$\gamma(|\underline{x}|) = \frac{2\sigma^4}{\pi} \frac{1}{(\sigma^2 + |\underline{x}|^2)^3} \; . \tag{2.2.21}$$

The convergence of the solution given by such vortex methods to the solution of Euler's equations as $N_v \to \infty$ and $\sigma \to 0$ was first considered by Dushane (1973) and Hald and Del Prete (1978). They were able to show convergence only for a short time. Later, Hald (1979) was able to show $O(h^2)$ convergence of the scheme for an arbitrary long-time interval, provided that the blobs have compact support and $\sigma = h^{1/2}$. Here, h is the spacing between vortices and σ is the core size. Building on this work, Beale and Majda (1982) showed that with proper choice of γ, the vortex method could be designed to converge with higher order accuracy. Here, the order of accuracy m is indicated by the following moment conditions of γ,

$$\int x^\alpha y^\beta \gamma(\underline{x}) d\underline{x} = 0 \text{ for } 0 < \alpha + \beta \leq m - 1 \; . \tag{2.2.22}$$

In their analysis, they split the error in the velocity field into three different terms, i.e. the smoothing error, the discretization error and the stability estimate, and showed that the smoothing error is $O(\sigma^m)$, the discretization error is bounded by $Ch(h/\sigma)^M$ for M large, and the stability estimate is bounded in a discrete L^p-norm by $\|\underline{x}_i' - \underline{x}_i\|$ in L^p, provided that $\sigma \geq C_o h$. Here, $\underline{x}_i'$ is the computed vortex location, while $\underline{x}_i$ is the exact vortex location. However, one drawback of these papers is that they all showed convergence when $N_v \to \infty$, $h \to 0$, $\sigma \to 0$ but $\sigma/h \to \infty$. More recently, Goodman et al. (1989b) was able to relax this constraint and show convergence for the vortex blob method with σ/h finite, which is usually the case in practice.

2.2.2 Treatment of a Solid Wall

In this section, we show that if surface singularities are used, both no-through flow and no-slip boundary conditions may be satisfied on the flat plate. Consider a solid body S' of thickness L immersed in a fluid F' (Fig. 2.2.1a). The boundary between S' and F' is $\partial S'$ and the union of the two is the $x' - y'$ plane D'. Let $\psi'(x', y')$ be the streamfunction defined over D',

$$\nabla \times \psi' \hat{e}_z = \underline{u}' \quad \text{in } D' \ , \tag{2.2.23}$$

and $\psi'_s(x', y')$ be the streamfunction defined over S',

$$\nabla \times \psi'_s \hat{e}_z = \underline{u}'_s \quad \text{in } S' \ . \tag{2.2.24}$$

Here, $\underline{u}'_s$ is the velocity field for points on the solid body and the vorticity ω', which is defined over D', satisfies Eqn. (2.2.4) in F' and the following solid body rotation formula in S',

$$\omega' = 2\Omega_s \ , \tag{2.2.25}$$

where Ω_s is the angular velocity of the solid S'. Since there is no singularity in S',

$$\nabla^2 \psi' = \omega' \quad \text{in } S' \ , \tag{2.2.26}$$

and

$$\nabla^2 \psi'_s = 2\Omega_s \quad \text{in } S' \ . \tag{2.2.27}$$

Applying Eqn. (2.2.25) to the above, we get

$$\nabla^2(\psi' - \psi'_s) = 0 \quad \text{in } S' \ . \tag{2.2.28}$$

On $\partial S'$, we enforce the Dirichlet condition,

$$\frac{\partial \psi'}{\partial s} = \frac{\partial \psi'_s}{\partial s} \ , \tag{2.2.29}$$

or

$$\frac{\partial(\psi' - \psi'_s)}{\partial s} = 0 \ . \tag{2.2.30}$$

The solution to Eqns. (2.2.28) and (2.2.30) can be determined up to a constant,

$$\psi' - \psi'_s = \text{const.} \quad \text{in } S' \ , \tag{2.2.31}$$

and

$$\frac{\partial(\psi' - \psi'_s)}{\partial n} = 0 \ \text{ on } \ \partial S' \ . \tag{2.2.32}$$

Therefore, by enforcing Eqn. (2.2.29), we find that both no-through flow and no-slip boundary conditions are satisfied on the boundary,

$$\underline{u}' = \underline{u}'_s \ \text{ on } \ \partial S' \ , \tag{2.2.33}$$

provided there is no singularity within S'.

To get the wall boundary conditions for a line (thin plate), we map the solid S' in D' onto a line S in the physical plane D (Fig. 2.2.1b). Because of Eqn. (2.2.33), the following is also true in the mapped plane,

$$\underline{u} = \underline{u}_s \ \text{ on } \ \partial S \ . \tag{2.2.34}$$

Note that there is no velocity singularity at the edges of the line S and that the velocity field is smooth. Also, since there is a vortex sheet around S' just outside of $\partial S'$, correspondingly, there is also a vortex sheet on each side of the line S. This completes the theoretical consideration of having vortex sheets on both sides of the line S to yield both no-through flow and no-slip boundary conditions on S.

In practice, it is more convenient to enforce the boundary conditions directly on the thin plate. This has the advantage of avoiding the use of a mapping, thus simplifying the calculation and making the extension to three dimensions possible. The numerical implementation of such a scheme will be discussed in Sec. (2.3).

2.2.3   On the Kutta Condition

In many inviscid calculations of unsteady flow past an airfoil or airfoil-like body (e.g. Basu and Hancock 1978, Stansby and Dixon 1982), auxiliary conditions, known as the Kutta conditions, are invoked. These conditions, like conformal mappings and image vortices, serve as tools for the flow calculations. They are related to the assumptions of the flow characteristics in the neighbourhood of a sharp edge (or more generally, separation point) and are needed because in the absence of an inner viscous solution, no interaction between the outer solution and a solid boundary is considered and the former is non-unique. The imposition of a Kutta condition removes the primary singularity at an edge and enforces the uniqueness of the solution.

For a full viscous method or a method where an inviscid outer solution is allowed to interact with a viscous inner solution, the imposition of a Kutta condition is not needed. This is the case with the present method. Here, the outer inviscid wake region, where the solution is given by the inviscid vortex method, is coupled with an inner viscous region, of length scale δ_{bl}, where the no-slip boundary condition of a solid wall is enforced. The interaction between the inner and outer regions is allowed through the shedding of vorticity, created in the inner region, into the outer flow.

To consider the consistency of such a method, where no Kutta condition is explicitly imposed, we cite the works of Orszag and Crow (1970), who studied the coupling effect between spatial instabilities on a vortex-sheet and the edge of a semi-infinite splitter plate from which it emanates, and Daniels (1978), who examined the consistent matching of these eigensolutions to a viscous inner flow structure. In their studies, Orszag and Crow found three admissible eigensolutions for the vortex sheet: (i) "no-Kutta-condition" solution, (ii) "rectified-Kutta-condition" solution and (iii) "full-Kutta-condition" solution. In the first solution, the pressure decays upstream but has an edge singularity. The second solution involves a vortex sheet that sharply deflects into the moving stream. Singularities remain at the edge point but it is argued that these are artifacts of the linearization. The authors argued, based on physical grounds, in favor of this second solution but the argument is valid only if the flow on one side is stagnant. The third solution has no singularity at the edge but with the pressure growing upstream like $|x|^{1/2}$ and is regarded as "indefensible" by the authors. The absence of a satisfactory "full-Kutta-condition" eigensolution indicates that either all spontaneous oscillations of the shear layer are in fact forced oscillations, with the forcing being associated with some downstream obstacle, or that the "no-Kutta-condition" eigensolution is acceptable.

The matching of these inviscid eigensolutions to a consistent viscous flow structure at the trailing edge is examined by Daniels. He found that the "full-Kutta-condition" solution leads to a consistent viscous inner flow. For the "no-Kutta-condition" solution, consistency with inner solution appears plausible for small amplitude oscillations. A pressure jump of $O(Re^{-1/2})$ is smoothed in an innermost $Re^{-3/4} \times Re^{-3/4}$ region where the full Navier-Stokes equations apply. The consistency of the "full-Kutta-condition" solution and the plausible consistency of the "no-Kutta-condition" solution with inner viscous solution suggests that a coupling method with no Kutta condition enforced in the outer solution is consistent. In this case, the type of "Kutta-condition" associated with the outer solution, whether of the "full-Kutta-condition" type, the "no-Kutta-condition" type, or a combination of both, is presumably selected through a consistent coupling with the inner viscous solution.

2.2.4 Condition of Conservation of Circulation

For a system D consisting of a thin plate S immersed in a fluid F (Fig. 2.2.1b), the total circulation (including that within the plate S) is given by

$$\Gamma = \int_D \omega(\underline{x}) d\underline{x} \ , \tag{2.2.35}$$

and the time rate of change of the circulation is given by

$$\frac{d\Gamma}{dt} = \frac{d}{dt} \int_D \omega(\underline{x}) d\underline{x} \ . \tag{2.2.36}$$

Let us write the above integral as two separate integrals,

$$\int_D \omega(\underline{x}) d\underline{x} = \int_S \omega(\underline{x}) d\underline{x} + \int_F \omega(\underline{x}) d\underline{x} \ , \tag{2.2.37}$$

where the first integral is over the infinitesimally thin line S and can be written as

$$\int_S \omega(\underline{x}) d\underline{x} = \int_S \nabla \times \underline{u} \cdot \hat{e}_z dA$$
$$= \oint_{\partial S} \underline{u} \cdot \hat{e}_s ds \ . \tag{2.2.38}$$

The above closed contour ∂S consists of two straight path ∂S^+ and ∂S^-, which are in the opposite direction and lie infinitesimally close to one another. Provided there is no singularity within the plate, $\underline{u} = \underline{u}_s$ on ∂S and is single-valued; i.e., $\underline{u}\,|_{\partial S+} = \underline{u}\,|_{\partial S-}$. Therefore, the above equation is identically zero and Eqn. (2.2.36) is given by

$$\frac{d\Gamma}{dt} = \frac{d}{dt} \int_F \omega(\underline{x}) d\underline{x} \ . \tag{2.2.39}$$

To evaluate Eqn. (2.2.39), it is more convenient to work in the Lagrangian coordinates $\underline{x}_L$ since here the boundary between the solid and fluid domains, F and S, does not change with time, and the time derivative in Eqn. (2.2.39) can be taken into the integral,

$$\frac{d\Gamma}{dt} = \int_F \frac{D\omega}{Dt} d\underline{x}_L \ . \tag{2.2.40}$$

Now since the flow is incompressible, the Jacobian of transformation between Eulerian coordinates and Lagrangian coordinates is unity, and we can transform back to the Eulerian coordinate to evaluate Eqn. (2.2.40),

$$\begin{aligned}
\frac{d\Gamma}{dt} &= \int \frac{D\omega}{Dt} d\underline{x} \\
&= \nu \int \nabla^2 \omega d\underline{x} \\
&= \nu \oint \frac{\partial \omega}{\partial n} ds \ ,
\end{aligned} \tag{2.2.41}$$

where $\hat{e}_n$ points into the fluid domain and the integral is evaluated in the clockwise sense. To evaluate the above equation, we write the momentum equation, Eqn. (2.2.1), at ∂S, take the dot product with the unit tangent and integrate along ∂S to find

$$\oint \frac{\partial P}{\partial s} ds = \nu \oint \frac{\partial \omega}{\partial n} ds \ . \tag{2.2.42}$$

Here, the pressure is single-valued and the closed contour integrates to zero. Therefore, Eqn. (2.2.36) becomes,

$$\frac{d\Gamma}{dt} = 0 \ . \tag{2.2.43}$$

Eqn. (2.2.43) implies that for a flat plate, if the total circulation of the system is zero at $t = 0$, then it is also zero at all later time, regardless of whether the plate is undergoing rotational motion. This is not the case for a finite body where the angular acceleration of the body contributes the term $2A_s d\Omega_s/dt$ to the right-hand side of Eqn. (2.2.43). Here, A_s is the area of the solid body and Ω_s is the angular velocity.

2.2.5   Pressure and Force Calculation

In calculations of flow past a body, the pressure distribution and the forces exerted on the body are usually the quantities of interest. To compute the pressure distribution, we write the momentum equation, Eqn. (2.2.1), at the wall,

$$\nabla P = \nu \nabla^2 \underline{u}$$
$$= -\nu \nabla \times \omega \hat{e}_z \ . \tag{2.2.44}$$

Taking the dot product of the above with the tangential direction $\hat{e}_s$ gives

$$\frac{\partial P}{\partial s} = -\nu \frac{\partial \omega}{\partial n} \ . \tag{2.2.45}$$

This is the formula used by Chorin (1973) in his calculation of flow past a circular cylinder. However, because it depends on the detail of the viscous profile near the wall, it is highly sensitive to small fluctuations there. Recently, Spalart (1982) and Spalart et al. (1983) suggested rewriting the term $-\nu \partial \omega/\partial n$ as a circulation flux at the wall,

$$\frac{\partial P}{\partial s} = \frac{\partial^2 \Gamma}{\partial s \partial t}\bigg|_{\text{wall}} \ . \tag{2.2.46}$$

This formula is particularly suited for vortex calculations because the term on the right-hand side, $\partial^2 \Gamma/\partial s \partial t \,|_{\text{wall}}$, is the rate of creation of circulation per unit length at the wall to cancel exactly the velocity there and is known.

To extract the net pressure force acting on the body, we integrate the pressure around the body to get

$$\underline{F} = \oint P(s)\hat{e}_z \times \hat{e}_s \ ds \ . \tag{2.2.47}$$

Integrating the above by parts and using Eqn. (2.2.46), we get

$$\underline{F} = \oint \hat{e}_z \times \underline{x} \frac{\partial^2 \Gamma}{\partial t \partial s}\bigg|_{\text{wall}} ds \ . \tag{2.2.48}$$

Although $\partial^2 \Gamma / \partial t \partial t \ |_{\text{wall}}$ doesn't depend on the detail of the viscous profile at the wall, it is still sensitive to small local disturbances; i.e., if a vortex approaches the wall, a circulation comparable in magnitude to that of the vortex must be created in the boundary-layer to satisfy the boundary conditions, resulting in large instantaneous $\partial^2 \Gamma / \partial t \partial s|_{\text{wall}}$. Another formula for computing the forces acting on a body is

$$\underline{F} = -\frac{d}{dt} \int_F \underline{u} \ d\underline{x} \ , \tag{2.2.49}$$

which, for the case of a zero thickness plate, is equal to

$$\underline{F} = -\frac{d}{dt} \int_F \underline{x} \times \omega \hat{e}_z \ d\underline{x} \ , \tag{2.2.50}$$

by integration by parts. When compared with Eqn. (2.2.48), Eqn. (2.2.50) is more global in nature and is less sensitive to local disturbances. Also, Eqn. (2.2.50) contains viscous forces on the boundary. Care must be taken when treating a body with finite thickness because if the body is undergoing acceleration, boundary terms that appear in the integration by parts may not be zero.

2.3   Numerical Implementation

Having developed the mathematical background of the current method of computation in the last section, we proceed to describe the numerical implementation of the method.

2.3.1 Solid Wall Boundary

As discussed in Sec. (2.2.2), the boundary conditions are enforced directly on the flat plate to avoid using a mapping technique. This is done by laying vorticity layers on both sides of the plate and adjusting the circulation distribution of the two layers such that the appropriate boundary conditions are satisfied. Both boundary conditions of no-through flow and no-slip have to be enforced explicitly. This is different from the case of a finite-thickness body, where enforcing one boundary condition on the wall automatically ensures that both boundary conditions are satisfied. To illustrate this difference, consider Fig. (2.3.1a), where the vorticity layer around the body S' is discretized into $2N'$ boundary vortex elements, and there are $2N'$ control points on the wall boundary $\partial S'$. If we map the body S' onto a line S (see Fig. 2.3.1b), the upper and lower boundaries of the body both map onto the same line, with the control points from the two boundaries sitting on top of one another on the line and effectively, we are left with only half the number of control points. However, the number of boundary vortex elements representing the vorticity layers remained unchanged through the mapping. Therefore, to solve for the unknown strength of all the boundary vortex elements, we need two boundary conditions for each control point on the flat plate. Another way of looking at this is to enforce the mixed boundary condition, at the wall $\partial S'$ of the finite thickness body. Here, no-through flow is satisfied on the top boundary $\partial S'^{+}$ and no-slip is satisfied on the bottom boundary $\partial S'^{-}$, or vice versa. When we map the finite body S' onto the line S, both the top and bottom boundary of S' get mapped onto the same line S, and both boundary conditions are enforced at the same control points on the line S.

We proceed to discretize the two vorticity layers into N boundary vortex elements each, giving a total of $2N$ unknown circulations. N control points are specified on the plate, and the no-slip boundary condition is specified at all these points. The no-through flow boundary condition is specified at $N-1$ of these points, giving a total of $2N-1$ equations. The choice of choosing $N-1$ points for the normal condition is not arbitrary and will be clarified later. The last condition is given by Eqn. (2.2.43). Since at $t = 0$, the flow is irrotational and the circulation in the flow is zero, it remained zero at all later times and Eqn. (2.2.43) is implemented as

$$\sum_{i=1}^{2N} \Gamma_{p_i} = -\sum_{i=1}^{N_v} \Gamma_{v_i} \; , \qquad (2.3.1)$$

where Γ_p is the strength of boundary vortex elements, and N_v and Γ_v are the total number and strength of the wake vortices, respectively. This gives a total of $2N$ simultaneous equations and $2N$ unknowns. If we proceed to solve this system of equations, we find that the matrix of influence coefficients is ill-conditioned and cannot be solved. This is the same difficulty encountered by Spalart (1982) and Spalart et al. (1983), when they applied their method to a body with thickness on the order of the vortex spacing in the vorticity layer.

2.3.1.1   A Scheme for Enforcing Boundary Conditions

To treat the boundary conditions correctly and to avoid any numerical problem of the matrix, we note that for the flat plate, the normal and tangential velocity boundary conditions are completely decoupled. Therefore, we can treat each condition separately. For the normal boundary condition, we use pairs of boundary vortex elements with equal strength and sign to represent the two vorticity layers. Such a pair will not induce any tangential velocity at the center line between the two layers where the plate is. However, since each pair has non-zero net circulation, they contribute to Eqn. (2.3.1), and the circulation conservation condition has to be included in the simultaneous system. For the tangential boundary condition, we use pairs of vortex elements with equal strength and opposite sign. Such a pair does not induce any normal velocity at the center line between the two layers where the plate is. Also, since each pair has zero net circulation, this system does not contribute to Eqn. (2.3.1), and the conservation condition need not be considered. Three different schemes for solving the above systems have been tested and are described below.

Scheme (a) involves specifying two different sets of control points. For the normal boundary condition, since Eqn. (2.3.1) has to be included, we can specify only $N - 1$ control points for N pairs of vortex elements. The control points are placed at locations midway between the centers of neighboring pairs (see Fig. 2.3.2a)†, and the unknown strength of each pair is adjusted such that the normal velocity is set to zero at the control points. For the tangential boundary condition, we specify N control points for N pairs of boundary vortex elements. The control points are placed at the centers of the pairs (see Fig. 2.3.2b), to ensure diagonal dominance of matrix of influence coefficients. The unknown strength of the elements is then adjusted such that the tangential velocity is canceled at each of the control points.

---

† In Fig. (2.3.2), multiple vortex elements are placed in the η-direction on each side of the plate, this will be discussed in the next section. Also, for a definition of parameters, see Fig. (2.4.1).

Using this scheme, we computed the problem of an impulsively started normal flat plate. Here, each vorticity layer is discretized into a row of circular vortex blobs and the boundary conditions are enforced as described. Shedding is modeled as the convection of the edge vortex blob into the outer flow domain.

Using the data at $t = 10$, we computed the velocity at the plate. Figs. (2.3.3a) and (2.3.3b) show the normal and tangential velocities, respectively. Here, each velocity component is computed at points between control points and at control points. Note that except at the edges and near $\zeta \simeq -0.1$ and -0.35, the velocity boundary conditions of no-slip and no-through flow are very well satisfied, with the rms of each component at approximately 2×10^{-4}. Near $\zeta \simeq -0.1$ and -0.35, the disturbances are due to the presence of wake vortices near the downstream vorticity layer there (see Fig. 2.3.3c). These disturbances will be dealt with in more detail in the next section.

In Scheme (b), we use control strips, instead of control points, and specify that the average normal velocity and average tangential velocity over the strips be zero,

$$\int_{s_1}^{s_2} u_{\mathrm{n}}(x(s), y(s)) ds = 0 \ , \tag{2.3.1a}$$

$$\int_{s_1}^{s_2} u_{\mathrm{t}}(x(s), y(s)) ds = 0 \ , \tag{2.3.2b}$$

where s_1 and s_2 are the two end points of the control strip. Here, the velocity components are integrated analytically at the strip. Using the data at $t = 10$, we enforced the boundary conditions of Eqns. (2.3.1a) and (2.3.2b) and checked the velocity at the plate. The normal and tangential velocities are given in Figs. (2.3.4a) and (2.3.4b). Here, the velocity tends to be highly oscillatory, especially near the edges, and the boundary conditions of no-slip and no-through flow are not well satisfied. The rms normal and tangential velocities at the plate are 5×10^{-3} and 2×10^{-3}, respectively, about 10 times greater than that obtained using Scheme (a).

In Scheme (c), we enforce both boundary conditions at the same control points and solve an overdetermined system. This appeared to be an attractive alternative to Scheme (a) because the total velocity is zero at the same control points. Here, the control points are specified at points in the center of the vortex pairs as well as between the vortex pairs (see Fig. 2.3.6)†. For N pairs of vortex elements, this

---

† For a definition of parameters, see Fig. (2.4.1).

gives $2N + 1$ control points. For the no-slip boundary condition, we have $2N + 1$ equations for N unknowns, and for the no-through flow boundary conditions, we have $2N + 2$ equations, including Eqn. (2.3.1), for N unknowns. The two over-determined systems are solved by multiplying each of the matrix equations by the transpose of the matrix,

$$\underline{\underline{M}}^T \underline{\underline{M}} \ \underline{a} = \underline{\underline{M}}^T \ \underline{b} \ , \tag{2.3.3}$$

where $\underline{\underline{M}}$ is the matrix of influence coefficients and $\underline{\underline{M}}^T$ is its transpose. Note that this would satisfy the boundary conditions only approximately at all control points. Figs. (2.3.5a) and (2.3.5b) show the normal and tangential velocities at the plate with boundary conditions satisfied using this scheme. Note the oscillatory behavior of both components near the edges. Here, the mean of the normal velocity is 2×10^{-3} and that of the tangential velocity is 4×10^{-3}. Comparing Figs. (2.3.4a) and (2.3.4b) of scheme (b) and Figs. (2.3.5a) and (2.3.5b) of scheme (c) to Figs. (2.3.3a) and (2.3.3b) of scheme (a), we find that scheme (a) gave the best results, in terms of satisfying the boundary conditions given by Eqn. (2.2.33), and will be used in all later calculations.

2.3.1.2 Vortex Panel Model for Vorticity Layer

In previous work (Spalart and Leonard 1981, Spalart 1982, Spalart et al. 1983, Park 1989), a single layer of circular vortex blobs is used to represent the vorticity layer around the body. However, because of the circular symmetry of the blobs, they do not conform to the geometry of the vorticity layer which they represent; i.e., the vorticity layer has steep variations in the η direction, normal to the plate, but only slow variations in the ζ direction, along the plate. Also, to obtain a smooth vorticity distribution along the layer, a large number of vortex blobs with sufficient overlap must be used. However, if there is too much overlap, the resulting matrix of influence coefficients is ill-conditioned and numerical difficulties associated with the inversion of the matrix tend to contaminate the results, giving an oscillatory circulation distribution of the boundary vortex blobs, especially in regions with a steep gradient, i.e. near a sharp edge. This is a serious problem since the shedding of vorticity takes place at such locations, thus leading to shed particles containing large oscillatory components. To deal with this problem, workers usually choose core size σ, which is smaller than the vortex spacing h. Spalart and co-workers recommended using $\sigma = h/2$, while Park (1989) used $\sigma = \pi h/2$. Unfortunately, this yields a vorticity field in the vorticity layer which is not smooth with the corresponding non-smooth velocity field.

To deal with this difficulty, we propose the use of a constant strength vortex panel to represent the vorticity layer. Each panel represents a continuous distribution of vortex blobs of constant strength and is obtained by a uniform distribution of blobs along the panel length. Therefore, it has only a small vorticity gradient along its length and a steep vorticity gradient in the lateral direction, similar to the corresponding gradients in the vorticity layers which they model. Using these panels, we can obtain a smooth and continuous representation of the vorticity layer, provided the core size σ of the panel is small compared to its length δs. Typically, $\sigma = 0.25\delta s$ is used. If σ is comparable to δs, there is too much overlap between panels, and oscillatory behavior of the circulation distribution results.

The vorticity distribution of a panel extending from s_1 to s_2 is given as

$$\omega(\underline{x}) = \frac{d\Gamma}{ds} \int_{s_1}^{s_2} \gamma(\underline{x} - \underline{x}'(s))ds \ , \tag{2.3.4}$$

and the induced velocity is given as

$$\underline{u}(\underline{x},t) = -\frac{1}{2\pi}\frac{d\Gamma}{ds} \int_{s_1}^{s_2} \frac{(\underline{x} - \underline{x}'(s)) \times \hat{e}_z g(\mid \underline{x} - \underline{x}'(s) \mid)}{\mid \underline{x} - \underline{x}'(s) \mid^2}ds \ , \tag{2.3.5}$$

where the function $g(r)$ is given by Eqn. (2.2.12). In the current calculations, the second-order core function suggested by Winckelmans (1989) is used. With such smoothing, a panel that extends from (x_1', y') to (x_2', y') gives a vorticity field of,

$$\omega(x,y) = -\frac{1}{2\pi}\frac{d\Gamma}{ds}\frac{\sigma^4}{((y-y')^2 + \sigma^2)}$$

$$\times \left\{ \frac{(x-x')}{((x-x')^2 + (y-y')^2 + \sigma^2)}\left[\frac{3}{2(\sigma^2 + (y-y')^2)} + \frac{1}{((x-x')^2 + (y-y')^2 + \sigma^2)}\right]\right.$$

$$\left.+\frac{3}{2(\sigma^2 + (y-y')^2)^{\frac{3}{2}}}\tan^{-1}\left[\frac{(x-x')}{\sqrt{(y-y')^2 + \sigma^2}}\right]\right\}_{x_1'}^{x_2'}$$

$$\tag{2.3.6}$$

and an induced velocity field of

$$
u(x,y) = \frac{1}{2\pi}\frac{d\Gamma}{ds}(y-y')\left\{ \frac{\sigma^2(x-x')}{2\big((y-y')^2+\sigma^2\big)\big((x-x')^2+(y-y')^2+\sigma^2\big)} \right.
$$
$$
\left. +\frac{1}{\sqrt{(y-y')^2+\sigma^2}}\Big[1+\frac{\sigma^2}{2\big((y-y')^2+\sigma^2\big)}\Big]\tan^{-1}\Big[\frac{(x-x')}{\sqrt{(y-y')^2+\sigma^2}}\Big]\right\}_{x_1'}^{x_2'}
$$

$$(2.3.7a)$$

$$
v(x,y) = \frac{1}{2\pi}\frac{d\Gamma}{ds}(y-y')\left\{ \frac{\sigma^2}{2\big((x-x')^2+(y-y')^2+\sigma^2\big)} \right.
$$
$$
\left. -\frac{1}{2}\log\big[(x-x')^2+(y-y')^2+\sigma^2\big]\right\}_{x_1'}^{x_2'} .
$$

$$(2.3.7b)$$

The above expressions for the induced velocity involve arc-tangent and logarithmic terms and are costly to evaluate compared to the circular blobs used by Spalart and co-workers. However, it is important to have a smooth and continuous vorticity distribution in the inner flow region (the vorticity layers) since this is where vorticity is created and shed into the flow.

A first approximation of the vorticity layer can be obtained by representing it with a single layer of vortex panels, placed at a small distance $\delta\eta_{bl}$ above or below the plate. $\delta\eta_{bl}$ is usually chosen to be $\sigma/2$, such that there is enough overlap to ensure smooth vorticity distribution in the η direction. Here, the thickness of the vorticity layer depends on the core size and is given by $\delta_{bl} \simeq 1.5\sigma$. However, we feel that δ_{bl} is a length scale of the problem and should not depend on the smoothing parameter σ. Also, with a single layer of vortex panels, the maxima of the vorticity profile occur at $\delta\eta_{bl}$. At shedding, all the vorticity concentrated in the panel next to the edge is convected at the local velocity, $\underline{u}(\zeta_{edge},\ \delta\eta_{bl})$ into the outer flow. However, it is known that the maxima of the vorticity profile in the physical boundary-layer occurs at the plate, and at the edge where separation takes place, an infinitesimal portion of vorticity is convected at the local velocity into the outer flow. Therefore, a single layer of vortex panels may be too crude a model for representing the details of the vorticity layer and the mechanism of shedding.

A better model is to represent the vorticity layer by a layer of vortex stack. Each stack consists of N_η vortex panels stacked on top of one another (see Fig. 2.3.2). The individual circulation of the panels within each stack cannot be determined directly, and a circulation profile with a length scale δ_{bl} must be specified. The profile relates the strength of the panels within each stack, and this results in only one unknown per stack. Any profile that approximates the boundary-layer profile can be used and in our calculations, we choose the Gaussian for its simplicity.

One of the improvements of the multilayer scheme over the single-layer model is the elimination of the σ-dependence of δ_{bl}. Here, σ is a numerical smoothing parameter, while δ_{bl} is the thickness of the vorticity layer, which at the separation point, defines the Reynolds number. To show that with the present model, the dominant length scale of the problem is given by δ_{bl} only, we compute the start-up flow problem with $N_\eta = 2, 4$, and 5. σ is varied accordingly such that δ_{bl} is held constant. Figs. (2.3.7a) and (2.3.7b) show plots of C_d and $d\Gamma/dt$. Note that with δ_{bl} held fixed, the results obtained using different σ are indistinguishable even at a very early time when small scales in the vorticity layer at separation point are important. Apparently, the small-scale effects of σ have been eliminated. We also studied the effects of varying δ_{bl}. Here, δ_{bl} is varied by varying σ at fixed N_η. Figs. (2.3.8a) and (2.3.8b) show plots of C_d and $d\Gamma/dt$ from the calculations. Here, the signals are found to be different at an early time, indicating the small-scale effects of δ_{bl}.

Another improvement of the present multilayer model is that the maxima of the discretized vorticity profile can be made close to the plate compared to δ_{bl} by increasing the resolution within the stack, i.e., increasing the number of panels per stack. This gives a better representation of the actual vorticity profile in a boundary-layer because there, the maximum vorticity occurs at the plate and decays away from the plate, with a length scale δ_{bl}, beyond which it drops rapidly to zero. At the edge where shedding occurs, this vorticity profile "sees" a wake-type velocity profile and each infinitesimal portion of vorticity within the profile is shed at the local velocity into the outer flow domain. With the multiple layer scheme, the described shedding process can be closely modelled because the vorticity profile is now discretized by N_η panels, each of which carries the correct amount of vorticity and is shed at the local velocity. Note that with the single layer model, the vorticity is concentrated at $\eta \simeq \delta_{bl}/2$ and is shed at the velocity there, which is about half the velocity at the outer edge of the vorticity layer.

To compare the current vortex panel model with the usual vortex blob model, we examine the data for the impulsively started normal flat plate, obtained in the previous section. Using the wake data at $t = 25$, we enforced the boundary

conditions at the plate using a single layer of vortex blobs on each side of the plate. The circulation distributions of the upstream and downstream vorticity layers are shown in Figs. (2.3.9a) and (2.3.9b), respectively. Note that both distributions are smooth, except near $\zeta = 0.1$, where they are highly oscillatory. This is due to the presence of a wake vortex very close to the back face of the plate near $\zeta = 0.1$. However, its location is away from the edges of the plate, and to the vortex, the plate "appeared" to be an infinite plate. Therefore, its effects should be local and be confined to the downstream vorticity layer only. However, because of the crudeness of the model, the disturbance is "felt" even in the upstream vorticity layer, as indicated by the oscillation in the circulation distribution there. There are also oscillations near the edges of both layers, and these numerical oscillations may cause serious errors in the computed circulation flux at shedding, as discussed earlier.

In Figs. (2.3.10a) and (2.3.10b), we show the circulation distribution of the upstream and downstream vorticity layers, modeled using 5 layers of vortex panels each. Here, the disturbance near $\zeta = 0.1$ is manifested as a smooth dip in the circulation distribution of the downstream layer. Also, as expected, the disturbance is local, and its effects on the upstream vorticity layer are very small. At the edges, the oscillations previously encountered in the vortex blob model are eliminated and shedding is more accurately portrayed. To illustrate this, we compute the impulsively started normal plate from $t = 0$ to $t = 1.2$ using the two models: (i) a single layer of vortex blobs; (ii) 5 layers of vortex panels. Figs. (2.3.11a) and (2.3.11b) show the plots of C_d and $d\Gamma/dt$. We see that the signals computed using the single-layer vortex blob model are highly oscillatory, especially at an early time, compared to that computed using the multilayer vortex panel model.

In Figs. (2.3.12a) and (2.3.12b), we show the distribution of residual tangential and normal velocity error at the plate, computed using several different numbers of layers N_η. The velocity components are computed at and between control points on the plate†. The wake data at $t = 50$, computed in the last section, is used. The rms velocity error of each component is also computed and plotted against N_η in Fig. (2.3.13). Note that the error decreases with N_η, indicating that the boundary conditions are better satisfied as N_η is increased, presumably because the vorticity profile at the plate becomes fuller and the boundary-layer is better represented; i.e., with a single layer of vortex panels placed at $\eta = \sigma/2$ above the plate, maximum vorticity occurs at the location of the layer, whereas in the actual boundary-layer, maximum vorticity occurs at the plate ($\eta = 0$). With more and more layers, the

---

† The velocity components computed at control points are exactly zero, represented by points on the x-axis in Figs. (2.3.12a) and (2.3.12b)

location of maximum vorticity could be made to approach the plate.

2.3.2 Vorticity Shedding Model

To model the vorticity shedding process at the edges of the plate, the tangential velocity is computed at the center of all vortex panels within the stack at the edge. If the velocity vector is found to be outwardly pointing, i.e. into the outer flow domain, then the panel is shed at the tangential velocity. The normal velocity is assumed to be small and is ignored. For time integration of the shedding process, the first-order Euler scheme is used and the time step Δt is chosen such that the panel with the highest outward velocity will move at most one panel length δs. A maximum allowable time step $\Delta t_{\max}$ is prescribed to minimize numerical errors in the time integration. After the Euler step, the portion of the panel that is in the outer flow domain, i.e. beyond the ζ-coordinate of the plate edge, is considered shed and is replaced by a smooth, circular vortex blob, placed at the center of the shed portion. If the shed portion of the panel has length δs_{shed}, then the circulation of the new vortex is given by

$$\Gamma = \delta s_{\text{shed}} \frac{\partial \Gamma}{\partial s} \ , \tag{2.3.8}$$

where $\partial \Gamma / \partial s$ is the strength of the panel. The core size σ of the vortex is taken to be the same as the smoothing parameter of the panel. Fig. (2.3.14) illustrates the steps involved in the shedding process.

2.3.3 Wake Vorticity Modeling

As discussed in Sec. (2.2.1), the concentrated vorticity patches or eddies in the wake are represented as a collection of smooth vortex blobs, and the evolution of these eddies is tracked by following the motion of the vortices. In standard vortex calculations, the computation of such motion accounts for a major portion of the work load. Here, each vortex is convected at the local velocity induced by all other vortices in the wake, and all vortex panels representing the vorticity layers at the plate plus the freestream. If there are a total of N_v wake vortices and N_p boundary vortex panels, the velocity calculation is $O(N_v N_p + N_v^2)$; i.e., the amount of CPU time required increases quadratically with the number of vortices, and this limits the number of vortices to $O(10^3)$ in a typical calculation. To minimize the CPU time required, cheap algebraic smoothing functions are usually chosen over other more elaborate functions so as to make the velocity evaluations as simple as possible. The first-order algebraic smoothing function, given by Eqn. (2.2.19), is frequently used. For this choice, the function f_i in Eqn. (2.2.10) is given by

$$f(r) = \frac{1}{r^2 + \sigma^2} \ , \tag{2.3.9}$$

and is inexpensive to evaluate. However, this choice yields a method that is first-order accurate only in space and has very poor convergence properties. In the current calculations, the higher-order algebraic smoothing function given by Eqn. (2.2.21) is used. This function is second-order accurate in space and has much better convergence properties (Winckelmans 1989). The corresponding function in the velocity expression is given by

$$f(r) = \frac{(r^2 + 2\sigma^2)}{(r^2 + \sigma^2)^2} \ . \tag{2.3.10}$$

Note that this expression is only slightly more complicated than that of Eqn. (2.3.9).

2.3.3.1   Time Integration

To compute the motion of a vortex blob, Eqn. (2.2.13) is integrated in time and the position of the vortex is updated according to the following,

$$\underline{x}_i(t + \Delta t) = \underline{x}_i(t) + \int_t^{t+\Delta t} \underline{u}(\underline{x}_i(t'), \ t')dt' \ , \qquad (2.3.11)$$

where subscript i represents the ith vortex. To evaluate Eqn. (2.3.11), the integral on the right-hand side is replaced by a discrete integration scheme. We choose the fourth-order Runge-Kutta scheme with four substeps,

$$
\begin{aligned}
\underline{x}_i(t + \Delta t) &= \underline{x}_i(t) + \frac{1}{6}(k_1 + k_2 + k_3 + k_4) \ , \\
k_1 &= \Delta t \ \underline{u}(\underline{x}_i(t), \ t) \ , \\
k_2 &= \Delta t \ \underline{u}(\underline{x}_i(t) + \frac{1}{2}k_1, \ t + \frac{1}{2}\Delta t) \ , \qquad (2.3.12) \\
k_3 &= \Delta t \ \underline{u}(\underline{x}_i(t) + \frac{1}{2}k_2, \ t + \frac{1}{2}\Delta t) \ , \\
k_4 &= \Delta t \ \underline{u}(\underline{x}_i(t) + k_3, \ t + \Delta t) \ .
\end{aligned}
$$

In each substep, the boundary conditions at the plate are enforced to solve for the strength of each panel in the vorticity layers. For a non-deformable body, this involves only $2N^2$ multiplications, where N is the number of control points, because the two matrices of influence coefficients, one for no-through flow and one for no-slip, remain constant for all time and are inverted only once at the beginning of the calculation. The velocity is then computed at the location of all the wake vortices and the vortices advanced a fraction of a step according to Eqn. (2.3.12). This is an expensive integration scheme as four velocity evaluations are required for each time step. However, the error in time is $O(\Delta t^4)$, and large time steps can be taken without compromising on accuracy. Also, in unsteady separated flow calculations, the calculation is usually carried out to large time, and integration errors introduced at each time step may accumulate and become significant at large time. It is therefore felt that a high-order scheme should be used to minimize such an error. A note of caution is that the first-order Euler scheme has been used for the shedding process at the edge of the plate; therefore, the overall accuracy is only $O(\Delta t)$. A high-order multistep integration scheme is not used for shedding because at every shedding step, the vortex panel next to the edge is convected, at the velocity evaluated at its mid-length, into the outer flow domain, and at the end of the step,

the portion that is in the outer flow is transformed into a circular vortex blob, while the portion that remains in the inner flow domain, i.e., the vorticity layer, is deleted. Because such transformations and deletions of elements take place over a time step, the step cannot be divided into multiple substeps for use in a high-order scheme.

2.3.3.2 Vortex Merging Scheme

In separated flow calculations, the continuous shedding of vorticity at the separation point is represented as the creation of vortex blobs at every discrete time step. Once created, the vortices remain in the flow until they are deleted upon entering a vorticity layer near the wall or are merged with other vortices. Merging acts as a balancing mechanism to offset the constant insertion of new vortices at the separation points. This is essential because with an $O(N_v^2)$ operation, a maximum number of vortices must be imposed to keep the CPU time within reasonable bound. Merging of vortices is usually done where fine scale resolution is not required, i.e., in the far wake. As described below, pairs or even groups of vortices are tested to see if certain conditions are satisfied and if so, the vortices are merged to form a single vortex. The process is similar to using a coarser grid in the far wake.

Spalart (1982) and Spalart et al. (1983) suggested the following scheme. Circulation is conserved by setting the circulation of the new vortex to be the sum of the circulation of the old vortices,

$$\Gamma_n = \Gamma_1 + \Gamma_2 \ , \qquad (2.3.13)$$

and linear impulse is conserved by choosing the new position to be the centroid of circulation,

$$\underline{x}_n = \frac{\Gamma_1 \underline{x}_1 + \Gamma_2 \underline{x}_2}{\Gamma_n} \ . \qquad (2.3.14)$$

The dimensionless error in the velocity field at the observation point $\underline{x}_o$, that is due to the merging, is found to be

$$\epsilon = \frac{\mid \Gamma_1 \Gamma_2 \mid}{U_\infty \mid \Gamma_1 + \Gamma_2 \mid} \frac{\mid \underline{x}_1 - \underline{x}_2 \mid^2}{\mid \underline{x}_o - \underline{x}_1 \mid^{\frac{3}{2}} \mid \underline{x}_o - \underline{x}_2 \mid^{\frac{3}{2}}} \ , \qquad (2.3.15)$$

and merging is carried out if the error ϵ is less than a tolerance ϵ_0. Spalart and co-workers chose $\epsilon_0 \simeq O(10^{-4})$. Dutta (1988) applied Eqns. (2.3.13) and (2.3.14) to merge a large group of vortices. The angular impulse of the system is also conserved by choosing the core size of the new vortex according to

$$\sigma_{\mathrm{n}}^2 = -2x_{\mathrm{n}}^2 + 2 \sum_{i=1}^{k} \frac{\Gamma_i(x_i^2 + \frac{1}{2}\sigma_i^2)}{\Gamma_{\mathrm{n}}} \; . \tag{2.3.16}$$

However, no merging criteria were specified.

In the present calculations, we use the merging scheme of Eqns. (2.3.13), (2.3.14) and (2.3.15), as proposed by Spalart and co-workers. From Eqn. (2.3.14), we note that when two vortices of equal sign are merged, the centroid lies between the two old vortices on the line connecting them. However, if two opposite sign vortices are merged, Eqn. (2.3.14) requires that the new vortex be placed at a position possibly far away from the old vortices; e.g., if the two vortices are of exactly opposite strength, the new vortex would be placed at infinity. Mathematically, this is correct. However, in practice, when opposite sign vortices are merged, the scheme may create a numerical problem; i.e., a new vortex may be placed upstream of the body, within the body or even in the vorticity layer near the wall of the body, causing serious numerical oscillations in the circulation distribution within the layer. On the basis of these observations, we choose not to merge opposite sign vortices. In addition, the error ϵ in Eqn. (2.3.15) is computed for all possible pairs of vortices, and only those pairs giving the smallest error are merged. The tolerance ϵ_0 is allowed to adjust itself according to the number of vortices in the wake; i.e., if there are too many vortices, a less stringent tolerance is used such that more vortices would be merged to reduce the number. For the selection of the tolerance ϵ_0, the upper and lower bounds $\epsilon_{0_{\max}}$ and $\epsilon_{0_{\min}}$ are prescribed, together with the maximum allowable number of wake vortices $N_{v_{\max}}$. At $t = 0$, ϵ_0 is set equal to $\epsilon_{0_{\min}}$ and is updated at every time step according to

$$\epsilon_0^{t+\Delta t} = \epsilon_0^t \frac{N_v}{N_{v_{\max}}} \; . \tag{2.3.17}$$

If ϵ_0 computed from Eqn. (2.3.17) is found to lie outside the range between $\epsilon_{0_{\min}}$ and $\epsilon_{0_{\max}}$, then it is set to equal the appropriate limit.

In an attempt to conserve angular impulse, the use of Eqn. (2.3.16) was tested. Figs. (2.3.15a) and (2.3.15b) show the drag histories of the normal plate problem, computed without and with the conservation of angular impulse. We found that the use of Eqn. (2.3.16) is very diffusive, and the calculation presented in Fig. (2.3.15b) is contaminated by the excessive artificial diffusion. Therefore, we decided not to use Eqn. (2.3.16) in all later calculations, and a constant core size σ is used for all vortices, including the new vortex created from merging.

2.3.4   Implementation of Pressure and Force Formulas

To compute the pressure distribution on the plate, we use Eqn. (2.2.46). The term on the right-hand side of the equation, $\partial^2\Gamma/\partial s\partial t|_{\text{wall}}$, represents the creation of circulation per unit time per unit length at the wall and is given by the change in panel strength, i.e., creation minus absorption, at each time step. To compute this quantity, the plate is divided into N strips, similar to the discretization of the vorticity layer along its length. At $t = t'$, the boundary conditions at the wall are enforced and the strength $\partial\Gamma/\partial s$ of each panel is determined. This represents the new circulation created at the corresponding strip on the appropriate side of the plate. The tangential velocity of each vortex panel is then computed at the center of the panel, and the position of the panel at $t = t' + \Delta t$ is updated using a first-order Euler integration step. For the panels next to an edge, the portion of the panel that lies in the outer flow after the convection step is considered shed, while the portion that remains in the inner flow region is absorbed back into the wall and deleted. If the portion of the panel that is deleted has length δs_{abs}, then it contributes $-(1/\Delta t)(\delta s_{\text{abs}}/\delta s)\partial\Gamma/\partial s$ to the pressure gradient $\partial P/\partial s|_{t=t'+\Delta t}$ at the control strip near the edge of the plate. For all inner panels that are not shed, they are deleted at the new updated positions, and the absorbed circulation is assigned to the appropriate control strip; i.e., if the updated position of the kth panel is such that a fraction f of the panel is within the ith control strip while $1-f$ of the panel is within the $(i+1)^{th}$ control strip, then $-(f/\Delta t)\partial\Gamma/\partial s$ is allocated to $\partial P/\partial s|_{t=t'+\Delta t}$ at the ith control strip and $-\{(1-f)/\Delta t\}\partial\Gamma/\partial s$ to that at the $(i+1)^{th}$ control strip. Also, if any wake vortex blob crashes into the vorticity layer during the time between $t = t'$ and $t = t' + \Delta t$, it is also deleted and its circulation absorbed, contributing to $\partial P/\partial s|_{t=t'+\Delta t}$ at the appropriate control strip. After the deletion, new panels are created as the boundary conditions are enforced at $t = t' + \Delta t$. The circulation of the new panels adds the positive term $(1/\Delta t)\partial\Gamma/\partial s$ to $\partial P/\partial s|_{t=t'+\Delta t}$ and the pressure gradient at $t = t' + \Delta t$ is determined. The pressure is then integrated using the central difference,

$$P_{i+\frac{1}{2}} = P_{i-\frac{1}{2}} + \delta s \ \frac{\partial P_i}{\partial s} \ . \tag{2.3.18}$$

Integration is carried out along a closed contour from a fixed point on the upstream side of the plate. At the edges of the plate, the pressure on both sides of the plate are taken to be the same. This gives the pressure distributions on the plate to within a constant. To determine the constant, we note that the maximum pressure occurs at the stagnation point on the upstream side of the plate where the flow is irrotational and the pressure is given by Bernoulli's equation,

$$P_0 = P_\infty + \frac{1}{2}\rho U_\infty^2 \ , \tag{2.3.19}$$

where P_0 is the stagnation pressure. We therefore set the maximum pressure on the upstream side of the plate to be the stagnation pressure, eliminating the arbitrary constant. A time-averaged pressure distribution is then determined using,

$$\overline{P} = \frac{1}{T} \int_t^{t+T} P dt' \ , \tag{2.3.20}$$

where averaging is usually taken over one or more Strouhal cycles.

To determine the forces using the instantaneous pressure distribution, we discretize Eqn. (2.2.48),

$$\underline{F} = \sum_{i=1}^{2N} \hat{e}_z \times \underline{x}_i \frac{\partial^2 \Gamma_i}{\partial t \partial s} \delta s \ , \tag{2.3.21}$$

where the summation is over the control strips on both sides of the plate. As discussed in Sec. (2.2.4), this formulation may be sensitive to local disturbances. A better force formulation is given by Eqn. (2.2.50). Here, the time derivative is computed using the central difference†,

---

† For normal flat plate flow, this formula includes a viscous contribution to C_l.

$$\underline{F}(t) = -\frac{1}{2\Delta t} \left\{ \sum_{i=1}^{N_v(t+\Delta t)} \underline{x}_i(t+\Delta t) \times \hat{e}_z \Gamma_i - \sum_{i=1}^{N_v(t-\Delta t)} \underline{x}_i(t-\Delta t) \times \hat{e}_z \Gamma_i \right.$$
$$\left. + \sum_{i=1}^{N_p} \underline{x}_{p_i} \times \hat{e}_z \left[\frac{\partial \Gamma}{\partial s}_i (t+\Delta t) - \frac{\partial \Gamma}{\partial s}_i (t-\Delta t) \right] \delta s \right\} .$$

$$(2.3.22)$$

To compare Eqns. (2.3.21) and (2.3.22), we use the test data from Sec. (2.3.1.1) and compute the drag force using both formulas. Figs. (2.3.16a) and (2.3.16b) show the drag histories computed using Eqns. (2.3.22) and (2.3.21), respectively. As expected, the signal computed using Eqn. (2.3.21) is noisier because of disturbances in the flow.

2.4 Parameter Study

A common problem encountered in vortex methods, as well as in other numerical methods, is the selection of numerical parameters. In the current method, the parameters involved are the vortex core size σ, the panel length δs, the spacing between vortex panels within each stack h, the displacement of the first vortex panel within each stack above/below the plate $\delta \eta_{bl}$, the number of vortex stacks per vorticity layer N, the number of vortex panels per stack N_η, the maximum number of vortices $n_{v_{max}}$ and the error in the velocity field at the plate that is due to vortex-merging ϵ.

In Sec. (2.3.1.2), we found that with the current multilayer scheme, the calculation does not depend on σ as long as $\sigma << \delta s$ (typically, $\sigma \simeq 0.25 \delta s$ is used). This constraint is to ensure that the matrices of influence coefficients are well-conditioned. For a smooth representation of the vorticity field, we choose $\delta s = L/N$, $h = \sigma$ and $\delta \eta_{bl} = \sigma/2$. From Fig. (2.4.1), $\delta_{bl} = (N_\eta - 1)h + \sigma + \delta \eta_{bl}$ and this fixes σ, given δ_{bl}. For the wake vortices, $n_{v_{max}}$ is specified and ϵ is allowed to vary within a range of 10^{-4} to 10^{-6} to keep n_v within $n_{v_{max}}$. In preliminary calculations, it was found that for $n_{v_{max}} = 1250$, the dimensionless error ϵ remained fairly constant at 2×10^{-6} throughout the long-time calculations. This gives an error per merger of $O(10^{-6})$ in the induced velocity field at the plate, which we feel is acceptable[†]. Therefore, $n_{v_{max}} = 1250$ is used in all later calculations.

In the following, we study the variation of N and N_η.

---

† The total error per time step is $O(10^{-5})$ for an average of 10 mergers per time step.

2.4.1 Convergence Study of the t=0 Solution

In this section, the convergence of the solution of flow past a normal flat plate at $t = 0$ with N and N_η is studied. Potential flow solution, discussed by Batchelor (1967), Lamb (1945) and Milne-Thomson (1938), is used as a guide.

Fig. (2.4.2a) shows the velocity distribution on the outer edge of the vorticity layer computed using different N with $N_\eta = 5$. Note that in the inner region of the plate, the solution given by the calculations agreed very well with the theory, regardless of N. However, near the edge where the potential flow solution becomes singular, slight discrepancies could be observed, especially for the course grid calculations. Fig. (2.4.2b) shows a "magnified version" of Fig. (2.4.2a) near the edge. It can be observed that as N is increased, the computed results approach that of the potential flow solution. For the fine grid of $N = 150$, the computed curve lies on top of the potential flow solution except for the grid point next to the edge.

Fig. (2.4.3a) shows the same velocity distribution computed using different N_η with $N = 150$. A "magnified version" of this near the edge is given in Fig. (2.4.3b). Except for the case with $N_\eta = 1$, all calculations seem to agree very well with the potential theory, with the agreement improving as N_η is increased. This occurs because with potential flow, vorticity is concentrated as a zero-thickness, singular sheet at the plate. However, the effect of viscosity is such that vorticity is diffused out in the direction normal to the plate. This produces a vorticity profile that has its maximum at the plate and decays rapidly away from the plate. However, since almost all vorticity remains concentrated within the thickness δ_{bl} of the layer, the net circulation within the layer and the velocity at the outer edge of the layer remains very close to that of the potential flow solution. With several layers of vortex panels representing the vorticity layer on each side of the plate, such vorticity distribution could be represented as closely as possible with more and more layers. However, if only one layer is used, then maximum vorticity cannot be made to occur at the plate, and the resulting vorticity profile is different with a corresponding error in the velocity distribution. Fig. (2.4.4) shows the distribution of $d\Gamma/d\zeta$ on the vorticity layer near the edge of the plate. Note that the solution converges very rapidly for $N_\eta \geq 2$.

2.4.2 Variation of Numerical Results with N

In this section, we study the effects of varying N on the long-time behavior of the flow. Here, two test flows are used. The first involves an impulsively started normal flat plate, and the second involves a ramp-started, laterally oscillating, normal flat plate. For each test flow, four different cases with $N = 60$, 90, 120 and 150 are computed and compared. To keep the computational cost low, $N_\eta = 1$ is used in all cases and calculation is carried out to $t = 50$ only.

Fig. (2.4.5) shows the comparison of the drag computed using three different N for the first test flow. In general, C_d decreases from the large value at impulsive start to a value of about 1. At this time, the flow behind the plate forms a symmetric recirculating bubble, and when the bubble becomes unstable and breaks, the drag increases dramatically. This process will be discussed in more detail later. Here we are interested in the comparison of different N. Note that in the early stages of the flow with $t < 10$, the computed drag is the same regardless of the grid used. It appears that because the flow is very regular for early time, a course grid of $N = 90$ is sufficient. However, the time of breaking of the symmetric bubble is very sensitive to the grid resolution and decreases with increasing N. The most likely reason is as follows: with a fine mesh for the vorticity layer, the sharp circulation gradient near the edge is better resolved, resulting in a strong induced velocity field. Correspondingly, smaller time steps are used for the fine-grid calculation and more vortices are shed for a given length of time, resulting in a higher degree of freedom for the system and a free shear layer with a faster growth rate for instabilities. With the bubble breaking at different times, convergence of results with increasing N could not be observed even at $t = 50$. The basic flow is chaotic, i.e., very sensitive to the initial conditions or changes in parameter.

A better test case for studying the effects of N is one where the breaking time could be controlled and a good way of doing this is to apply some external forcing to the flow. In the second test, the flow is forced by oscillating the plate in the lateral direction. Fig. (2.4.6) shows the drag computed using three different grids. In this case, the time of breaking does not change with the grid. However, the peak drag that is due to the breaking of the bubble is higher with the finer grid. We expect that this is so because of the better resolution of the steep circulation gradient near an edge as explained earlier. Note that for $t > 30$, the signals computed with $N = 120$ and $N = 150$ are very close to one another, indicating near convergence of results with $N = 150$.

2.4.3 Variation of Numerical Results with N_η

In this section, we study the effects of varying N_η on the long-time behavior of the flow. The test problem of a ramp-started, laterally oscillating, normal flat plate is computed using three different N_η ($N_\eta = 1, 2$ and 3). Fig. (2.4.7) shows the comparison of drag history. Note that in the early stages of the flow at $t < 15$, the drag computed using $N_\eta = 2$ and 3 showed very little difference, while that using $N_\eta = 1$ is slightly higher. This indicates that a good representation of the vorticity profile and the shedding process is obtained with $N_\eta = 2$, and this is used in all later calculations.

2.5 Numerical Results

In this section, we present the results of several calculations of forced and unforced flow past a normal flat plate. In the forced cases, both lateral and pitching motions are employed. In all calculations, unless otherwise stated, the parameters used are $N = 150$, $N_\eta = 2$, $\sigma = 1.67 \times 10^{-3}$, $\delta_{bl} = 4.175 \times 10^{-3}$, $N_{v_{max}} = 1250$ and $\epsilon \simeq O(10^{-6})$.

2.5.1 Non-oscillating Normal Flat Plate

In this test case, an impulsively started non-oscillating flat plate† is placed normal to a constant on-coming freestream. Three different stages of the flow can be identified:

(i) As the flow is started from rest, the boundary-layer simply cannot negotiate the sharp turning angle and a starting vortex is formed at each of the two edges of the plate. Fig. (2.5.1a) shows a streamline plot, with superimposed velocity vectors and vortex particles, typical of this stage of the flow. Similar experimental "flow-vis" pictures of this flow are given by Taneda and Honji (1971) and Pullin and Perry (1980).

(ii) Later, the pair of vortices grow to form a closed recirculating bubble behind the plate and a plot of the flow is given in Fig. (2.5.1b). Similar experimental "flow-vis" pictures of this flow could be found in Taneda and Honji (1971) and Lisoski and Roshko (1989).

---

† Ramp-started flat plate flows are also considered in Secs. (2.5.1.1) and (2.5.1.2).

(iii) The symmetric flow configuration in (ii) is unstable to infinitesimal disturbance and eventually breaks down, causing the flow to go into an asymmetric shedding mode, as shown in Fig. (2.5.1c). The experimental "flow-vis" pictures of the flow in this mode may be found in Fage and Johansen (1927).

2.5.1.1 Time Law for Circulation Flux at Early Time

The problem of a starting-flow behind an infinite wedge of angle $\pi\beta$, $0 < \beta < 1$, has been studied by Pullin (1978). In the inviscid limit, the separated flow forms a growing vortex sheet, and well-known similarity solutions may be used to transform the unsteady problem into an integro-differential equation. Pullin showed that for an attached flow with the complex velocity potential,

$$W(z, t) = U_\infty t^m F(z) \ , \tag{2.5.1}$$

where $F(z)$ satisfies the appropriate boundary conditions, the circulation of the sheet is given by

$$\Gamma(t) = C^n U_\infty^{\left(\frac{2}{2-n}\right)} t^{2\left(\frac{1+m}{2-n}\right)-1} J \ ,$$

$$C = \left\{ \frac{(2-n)(1-n)}{(1+m)} \right\}^{\left(\frac{1}{2-n}\right)} \ , \tag{2.5.2}$$

where $n = 1/2 - \beta$ and J is a constant. Eqn. (2.5.2) is the similarity solution discovered by Rott (1956) and for different values of m, Pullin computed J through a numerical solution.

This problem is also studied by Cortelezzi and Leonard (1990). They map the flow domain in the semi-infinite plate problem into the upper half plane and studied the motion of a single vortex of variable circulation as a system of two coupled differential equations. The Kutta condition at the edge of the plate is enforced. They found the same time law for the circulation but with a slightly different constant J.

We computed the impulsively started finite normal flat plate, corresponding to $m = 0$ and $\beta = 0$, and a comparison of $d\Gamma/dt$ to those predicted by Pullin (1978) and Cortelezzi and Leonard (1990) is given in Fig. (2.5.2a). At very small time, $t \simeq O(10^{-3})$, which is due to discretization in the calculations, the singularity at the edge of the plate is not well represented and a smaller $d\Gamma/dt$ is obtained. At slightly larger time around $t \simeq O(10^{-1})$, the computed flux approaches the analytical results and the agreement is fairly good. Later, the calculations deviate from the analytical results as the size of the vortex becomes comparable to the half-length of the finite plate, and the solution could no longer be approximated by that given by the theory for flow past a semi-infinite plate.

As a second example, we computed the ramp-started, normal flat plate, corresponding to $m = 1$ and $\beta = 0$. Six different discretizations with $N = 50$, 75, 100, 125, 150 and 200 are used. Fig. (2.5.2b) shows the comparison of $d\Gamma/dt$ to the analytical results. Again, the calculations underestimate $d\Gamma/dt$ at very small times. However, the agreement is improved as the resolution is refined. This is because with a finer resolution, the singularity at the edge is better approximated. Later on, at about $t \simeq 0.1$, the computed $d\Gamma/dt$ approaches the analytical curves. Note that there is slight disagreement between the analytical results of Pullin (1978) and those of Cortelezzi and Leonard (1990) with the current calculations between the two. Because of the ramp start in this example, the vortex does not grow as fast as in the previous example. Therefore, at $t \simeq O(1)$, the dimension of the vortex remains insignificant compared to the length of the plate, with better agreement between calculations and theory.

2.5.1.2 Short-time Drag History

In this section, we compare the drag history of the normal flat plate in a flow started from rest at three different accelerations: (i) $a = \infty$, i.e., an impulsive start; (ii) $a = 0.5$ and (iii) $a = 0.1$. The flow is accelerated from rest to $U_\infty = 1.0$, after which the acceleration is turned off. Fig. (2.5.3) shows the drag history of the plate for the three cases. For the case of an impulsive start, the drag at $t = 0$ has two infinite components:

(i) Apparent mass effect — during the infinitesimally small acceleration time δt, the drag that is due to apparent mass effect is infinite because of the infinite acceleration. However, as soon as the acceleration is reduced to zero, so too is this component, which is given by $C_{d_{\mathrm{app}}} \sim \delta(t)$, where $\delta(t)$ is the Dirac delta function, and has no significance for $t > 0$.

(ii) Infinite circulation flux — for an impulsively started normal plate, the circulation flux, given by $d\Gamma/dt \sim t^{-2/3}$ for small time (Rott 1956), is infinite at $t = 0$. Correspondingly, the drag, given in terms of the circulation flux by the Blasius formula, is also infinite.

In the calculations, the infinite drag that is due to (i) cannot be represented, and its effect is eliminated by setting the flow speed to U_∞ at $t = 0$. This is equivalent to having the impulsive start at $t = 0^-$ and reducing the acceleration, and therefore the apparent mass effect, to zero at $t = 0$. For the drag component that is due to (ii), the singularity at $t = 0^+$† is manifested in the pressure singularities at the edges of the plate. Fig. (2.5.4) shows the pressure distributions on the two sides of the plate at very small time, $t = 0.008$, and the singularities at the edges, which give the large drag, could be observed.

For finite acceleration, the drag force that is due to apparent mass effect can be computed. For a flat plate, the apparent mass is given by the mass of fluid in a circle inscribing the plate, which is $\pi L^2 \rho/4$. This gives a drag coefficient that is due to apparent mass effect of

$$C_{d_{\text{app}}} = \frac{\frac{1}{4}\pi L^2 a}{\frac{1}{2}U_\infty^2} \ .$$

(2.5.3)

For $a = 0.5$ and $a = 0.1$, with $L = 1$, $U_\infty = 1$, Eqn. (2.5.3) gives $C_{d_{\text{app}}}$ of 0.7854 and 0.1571, respectively, while vortex calculations give $C_{d_{\text{app}}}$ of 0.7885 and 0.1577. As the flow is accelerated from rest, the drag is observed to increase steadily until the acceleration is shut off, at which point it starts to decrease (Fig. 2.5.3). Because the acceleration is reduced to zero instantaneously, there is a discontinuity in the drag signal. At $t = 20$, C_d for all three cases decreases to approximately the same value of 0.88, which is the C_d predicted by the freestreamline theory. Figs (2.5.5a), (2.5.5b) and (2.5.5c) show "flow-vis" pictures of the flow at $t = 20$ from the three cases. The features of the flow in the three different cases are surprisingly similar despite differing start-up processes and probably account for the fact that the drag curves are at about the same level.

Fig. (2.5.6) shows comparison of computed results to experimental measurements of Lisoski and Roshko (1989) for the two cases of $a = 0.5$ and 0.1. The experiments are conducted in a water tank at $Re = 5 \times 10^3$, and the flat plate is accelerated from rest at the same acceleration. During the accelerating phase, and

---

† At $t = 0$, the flow is potential and there is zero drag.

for a short time after, the agreement between calculations and experiments is very good. However, after the acceleration is turned off, the computed drag begins to deviate from the experimental measurements.

Similar reasonable agreement with experiments in terms of drag is also observed by Mostafa (1987), Munz (1987), Mostafa et al. (1989) and Sarpkaya et al. (1990) in their calculations of decelerating flow about cambered plates. They used a different vortex method and computed a flow that is impulsively started and subsequently decelerated to rest. The agreement of computed results with experiments in an accelerating or decelerating flow where the laboratory flow is expected to be more two-dimensional because of the imposed external forcing, indicates that the observed discrepancy at later stages of the unforced (non-accelerating) flow may be due to three-dimensionality in the experiments.

2.5.1.3 Growth of a Recirculating Bubble

The problem of the spatial growth of a recirculating bubble behind an impulsively started normal flat plate has been studied experimentally by Taneda and Honji (1971). They found that regardless of the Reynolds number, a symmetric recirculating bubble, similar to that shown in Fig. (2.5.1b), is always formed behind the plate at early times. The growth of the bubble is found to obey the following similarity law,

$$\frac{L_v}{L} = 0.89 \left[\frac{U_\infty t}{L} \right]^{\frac{2}{3}} , \qquad (2.5.4)$$

where, L_v is the length of the bubble, L is the length of the plate, U_∞ is the freestream velocity and t is time.

From streamline plots similar to Fig. (2.5.1b), the length of the vortex pair is estimated by measuring the streamwise distance from the plate to the farthest point on the zero-streamline, i.e. the streamline separating off the edges of the plate. The length is plotted, in dimensionless form, together with the experimental data of Taneda and Honji† in Fig. (2.5.7). For $0.5 < t < 5.0$, when the bubble is

---

† The experimental measurements of Taneda and Honji were made at different Reynolds number in the range $10^1 - 10^3$. They reported that the bubble become asymmetric at an earlier time with increasing Reynolds number and presented data up to the time when asymmetry sets in.

fully developed, the computed bubble length agrees very well with the experimental measurements and its growth obeys the $t^{2/3}$ law. For $t > 5$, the calculation begins to deviate from the experimental data. This is because the recirculating bubble in the calculation has become asymmetric†. Fig. (2.5.8) shows a streamline plot of the flow at $t \simeq 10$. The asymmetry of the flow is clear. Fig. (2.5.9a) shows the time histories of the circulation fluxes at the edges of the plate. At very early time, the fluxes at the two edges of the plate are smooth and exactly equal to one another. At $t \simeq 3$, slight oscillations of the fluxes are observed as perturbations of the flow set in. These perturbations grow as time progresses and at $t \simeq 7$, they become quite significant, as indicated by the violent oscillations of the fluxes. Integrating the fluxes gives the net circulation of each of the two vortices and they are plotted in Fig. (2.5.9b). From the figures, it is observed that as the fluxes become unsmooth, due to internal perturbations, the circulation of one of the two vortices become higher, by some random selection process, compared to the other vortex. The stronger vortex grows at a faster rate, resulting in the asymmetry of the flow and the subsequent deviation of the bubble growth from the $t^{2/3}$ law.

2.5.1.4   Onset of Asymmetric Shedding

After the onset of asymmetry of the attached vortex-pair, as described in the last section, the difference in the circulations of the two vortices increases with time (Fig. 2.5.9b). A positive feed-back system is created because the stronger vortex (lower) induces a higher shedding velocity, and a corresponding higher circulation flux, at its edge which feeds its shear layer, increasing its strength further. Also, as it grows, it displaces the weaker vortex (upper) away from the plate, thus reducing the shedding velocity and circulation flux at its edge. Fig. (2.5.10a) shows a streamline plot of the flow at $t = 25.0$. The displacement and compression of the upper vortex by the lower vortex is clear. Also, the zero-streamline separating the two vortices, which is at the symmetry plane when the flow is symmetric (Fig. 2.5.1b), has moved considerably upward. Slightly later at $t = 25.4$ (Fig. 2.5.10c), the zero-streamline emanating from the upper edge has moved downward, very close to the zero-streamline which separates the two vortices. A close-up plot of streamlines in this region (Fig. 2.5.11), with the values of the streamfunction multiplied by 10, shows that the two zero-streamlines have actually 'pinched-off' and reconnected to form a small recirculating bubble near the upper edge and a saddle point between the bubble and the detached upper vortex. The fluid in the neighborhood of the

---

† For the experimental data, the bubble remains symmetric even for $t > 5$, presumably because of the low Reynolds number.

saddle point is such that the shear layer is pulled downward, eventually rolling up into a vortex structure at $t = 25.6$ (Fig. 2.5.10d). The rolled-up vortex structure induces large shedding velocities at the upper edge and sharp increases in the upper circulation flux (Fig. 2.5.9a), the upper net circulation (Fig. 2.5.9b) and the drag coefficient (Fig. 2.5.9c) are observed. This is because large circulation flux has to be created at the wall to cancel the high slip velocity and according to Eqn. (2.2.48), this results in a higher pressure force. As the upper rolled-up structure grows to form a tight vortex behind the upper edge (Fig. 2.5.10g), the flow state is changed, irreversibly, to an asymmetric shedding mode.

2.5.1.5 Long-time Behavior of Flow

In the asymmetric shedding mode, a vortical structure is being shed at alternating edges every half Strouhal cycle. Figs. (2.5.12a), (2.5.12b) and (2.5.12c) show the time histories of drag coefficient C_d, lower circulation flux $d\Gamma/dt|_{lower}$ and upper circulation flux $d\Gamma/dt|_{upper}$, respectively. The periodicity of a half Strouhal cycle is observed in the drag signal. However, superimposed on the Strouhal variation is a longer-time constant fluctuation, which decays out to near-steady-state at $t \simeq 80$. Figs. (2.5.13a) and (2.5.13b) show the shedding period T_{sh} and the peak circulation flux $|d\Gamma/dt|_{max}$ at the edges. The fluctuations of the quantities at early stages of the asymmetric shedding flow, especially for $t < 60$, are apparent. From Fig. (2.5.13a), we estimate the steady state T_{sh} by averaging over the period for $t > 60$. A mean value of $T_{sh} = 9.4$ is obtained. This gives $St \simeq 0.11$.

2.5.1.6 Asymmetric Shedding Mechanism

In this section, the mechanism behind the asymmetric shedding mode of the flow is studied. Fig. (2.5.14) shows a sequence of streamline plots of the flow over half a Strouhal cycle. At $t = 54$ (Fig. 2.5.14a), there is a vortical structure, in the early stage of its growth, close to the lower edge and a smooth shear layer extends from the upper edge. As the flow evolves, the lower vortex grows in size and displaces the upper vortex away from the plate. The stagnation point on the back of plate is observed to move upward toward the upper edge (Fig. 2.5.14b). Both the streamwise displacement of the upper vortex and the growth of the lower vortex result in the reduction of shedding velocities, especially that on the downstream side, at the upper separation point and this can be observed from the time history of the velocities at the outer edges of the boundary-layers at the upper separation

point, given in Fig. (2.5.15a). The zero-streamline emanating from the lower edge, which ends at a stagnation point on the back of the plate at $t = 55$, no longer does so at $t = 56$, but joins with the zero-streamline which forms the outer edge of the upper vortex. The remaining portion of the upper zero-streamline which emanates from the upper edge is observed to turn sharply downward, suggesting that the flow behind the upper edge has reversed direction which Fig. (2.5.15a) confirms†. The large upper vortex is now completely detached from the plate (i.e. the zero-streamline which forms its outer edge no longer connects to the upper edge) and a saddle point is formed between the small bubble at the upper edge of the plate and the large vortex. The flow in the neighborhood of the saddle point is such that the shear layer leaving the upper edge is pulled inward. This perturbs the shear layer, causing it to subsequently roll up ($t = 57$) and starts off another half Strouhal cycle. As the vortex rolls up tightly behind the upper edge, it induces large shedding velocity and circulation flux; this creates a feed-back system where the increased circulation flux fuels and strengthens the rolled-up vortex which further increases the flux, leading to the observed sharp increase (Fig. 2.5.15b). According to Eqn. (2.2.48), the pressure forces and drag also increase (Fig. 2.5.15c).

To understand the process that occurs during the critical time $56 < t < 57$, close-up plots of the streamlines during this time are studied. They are given in Fig. (2.5.16). For purpose of illustration, the values of the streamfunction, which are very close to zero, have been multiplied by 100. At $t = 55.75$ (Fig. 2.5.16a), the zero-streamline emanating from the upper edge of the plate, at coordinates of (0, 0.5), is close to the zero-streamline which forms the outer edge of the lower vortex. The singularity in the streamline deflection (slope) is associated with viscous and nonlinear effects (Crighton 1985) and is observed by Daniels (1978) in his studies of local-interaction theory. In Daniels' work, the flow configuration involves a uniform stream above a splitter plate and stagnant fluid below. The zero-streamline is observed to deflect into the moving stream with a "full-Kutta-condition" enforced on an outer flow solution. In the present case, the zero-streamline deflects into a region which is almost stagnant presumably because of a freestream flow which is in that direction. Slightly after this at $t = 55.8$ (Fig. 2.5.16b), the two streamlines "pinch-off" and reconnect in a fashion similar to that described in Sec. (2.5.1.4) for the breaking of the attached vortex-pair, with some observable differences: Here, the "pinching" occurs in a small neighborhood of the edge of the plate, i.e. the stagnation point moves all the way to the edge of the plate, at which point, the lower zero-streamline joins with the upper zero-streamline, thus separating the upper vortex from the plate in the sense that the upper vortex is completely enclosed

---

† A direct implication of this is that it is incorrect, at least for a short time, to estimate the circulation flux using Eqn. (2.1.1), as is done in some previous investigations.

by a zero-streamline in the fluid. Note that it is necessary for the stagnation point to move pass the edge for the shedding velocity there to be zero and subsequently negative, as observed in Fig. (2.5.15a). Recall that in the previous case in Sec. (2.5.1.4), the stagnation point remains slightly away from the edge at all time. The difference can be attributed to the shape of the vortical structures: In the asymmetric shedding flow, the vortical structures are elongated in the lateral direction. In contrast, the structures of the attached asymmetric vortex-pair, as described in Sec. (2.5.1.4), are elongated in the streamwise direction and the lateral extent of each vortical structure is much less. Also, the sizes and strengths of the attached vortex-pair are more comparable, and this is presumably why the stagnation point is not "pushed" all the way to the edge.

After the "pinching" and reconnection process, the zero-streamline emanating from the upper edge turns around sharply very close to the plate†. At $t = 56.0$ (Fig. 2.5.16c), due to the induction of the rolled-up shear layer, a closed recirculating region forms slightly behind the plate. This region is completely detached from the plate, as indicated by the closed zero-streamline. As the rolled-up vortex structure grows, the size of the recirculating region increases, eventually joining up with the plate as the zero-streamline which forms the outer edge of the recirculation region comes into contact, and subsequently connects, with the edge of the plate (Fig. 2.5.16d).

2.5.1.7 Comparison to Experiments and Other Calculations

Fig. (2.5.17) shows the streamlines of the time-averaged flow. The time-averaged wake width L_w is estimated by measuring the maximum separation between the two streamlines that emanate from the edges of the plate. The normalized width, L_w/L, estimated at 2.6, is about 50% wider than that measured by Roshko (1954), and we expect that the computed drag would be correspondingly higher.

In Fig. (2.5.18), we compare the streamline pattern of the current high Reynolds number calculation ($Re \simeq 10,000$) to that of the Navier-Stokes calculations ($Re = 200$) of Rogers and Kwak (1988) at the same phase in the shedding cycle. In the current calculations, Re is computed based on an estimate of the momentum thickness Θ on the front side of the separation point. Here, Θ is approximated

---

† It should be noted that the absolute-zero-streamline may not be well-resolved at this fine scale. A well-resolved calculation would require resolving scales much smaller than the core size of the boundary-layer vortex elements. Also, the grid of 20 × 20, with grid size of 0.01, used in computing the streamfunction-contours may be too coarse.

using the Blasius shape factor of $\Theta/\delta_{\rm bl} \simeq 1/8$. The time-averaged C_p distribution is then used to compute Θ^2/ν by integrating Thwaites' equation (see White 1974). Eliminating Θ from the two expressions gives ν, which is used to compute the Reynolds number. Despite the difference in Re, the shed vortex at the upper edge of both calculations compares very well in terms of dimension and location. This is because in bluff-body flow, the momentum thickness Θ at separation is very thin and depends only weakly on ν through $\Theta \simeq \sqrt{\nu}$. For the downstream vortical structures, the streamwise locations of the structures, which depend on the inviscid dynamics of the flow, compare very well. However, the vortical structures in the current calculation are stronger and displaced farther in the lateral direction compared to the Navier-Stokes solution. This must be due to the strong viscous effect in the low Reynolds number Navier-Stokes calculations, which tends to diffuse out the vorticity in the eddies, resulting in a weaker induced velocity field upstream, and a narrower wake. A similar comparison to experiments is also attempted where the streamwise locations of the eddies in Fig. (2.5.18a) are compared to Fig. 1 of Fage and Johansen (1927). It is found that except for the first vortex at the upper edge, the streamwise locations of all downstream vortices compared very well. In the current calculations, the vortex near an edge seems to roll up closer to the plate than in the experiments. Such discrepancy in the observed roll-up of the vortex near a sharp edge is not restricted to the current calculation but is quite common in two-dimensional separated flow calculations, including vortex calculations by Basuki and Graham (1987) as well as Navier-Stokes calculations by Osswald et al. (1985) and Rogers and Kwak (1988). The most likely explanation is that in the laboratory flow, vortex shedding is not well correlated in the spanwise direction, resulting in a weaker spanwise component of shed vorticity and a corresponding weaker roll-up. Such imperfect spanwise correlation of vorticity is well known to investigators of flow-induced vibration (Toebes 1969). The close vortex roll-up near the edge leads to a large suction peak in the pressure distribution on the back face very close to the edge, and the drag is expected to be overestimated. Fig. (2.5.19) shows the computed time-averaged C_p distribution on the plate, together with the measurements of Fage and Johansen (1927). On the front face of the plate, the two distributions compare very well. However, on the back face, they are very different. The experimental distribution is very flat with $C_{p_{\rm base}} = -1.3$. The computed distribution, however, has strong suction dips near the two edges, as expected from the strong roll-up. Such low pressure dip near a sharp edge is also observed in the vortex calculations of Basuki and Graham (1987) and the Navier-Stokes calculations of Rogers and Kwak (1988).

From Fig. (2.5.12a), $\overline{C}_d$ is estimated to be 3.6. In the literature, the experimental $\overline{C}_d$ ranges between 1.8 and 2.2; i.e., Fage and Johansen (1927) reported $\overline{C}_d$ of

1.96, Roshko (1954) quoted $\overline{C}_d$ of 1.8, Sarpkaya and Kline (1982) gave a value of 2.2. and more recently, Lisoski and Roshko (1989) measured $\overline{C}_d$ to be 2.0 (Table 2.1). Such large discrepancy in $\overline{C}_d$ is expected from the previous analysis of the wake width, the close roll-up at the sharp edge and the high suction peak, and are observed in other vortex calculations; i.e., Kuwahara (1973), Spalart et al. (1983) and Dutta (1988) all reported $\overline{C}_d$ of about twice the experimental value. Chein and Chung (1988) and Park (1989) quoted discrepancies of about 50%, while Kiya and Arie (1977) reported a maximum discrepancy of 70%. Recently, Raghavan et al. (1990) quoted $\overline{C}_d$ of 2.8 from their Navier-Stokes calculations at $Re = 200$. From his high Reynolds number Navier-Stokes calculations, Kuwahara (1989) noted that $\overline{C}_d$ tends to increase with the refinement of grids but did not offer any quantitative information. The computed St of 0.11, however, compares more favorably with the experimental value which ranges between 0.13 and 0.15 (Table 2.1).

2.5.2 Plunging Normal Flat Plate at "Natural Frequency"

In the last section, we computed the problem of flow past normal flat plate and found that for an accelerating flow, the computed drag agreed very well with experiments. However, for the non-accelerating flow at large time with asymmetric shedding, we found that the calculations overestimated the experimental drag by about 100%. Comparison to other calculations showed a similar trend. This indicates that the laboratory flow may be very three-dimensional with a lower drag than that of the two-dimensional calculation. To determine if three-dimensionality in the experiments is indeed the major contributor to the observed discrepancies, we computed the same normal flat plate problem with forcing. It was hoped that with external forcing, the flow in the experiments would be more two-dimensional, and a comparison of a two-dimensional calculation to such experiments would be more reasonable in determining the correctness of the model used in the calculations. Also, both the calculations and experiments are likely to be less sensitive to small-scale random perturbations, and comparison of temporal distribution of various quantities of interest is more meaningful.

In this section, we present calculations of the problem of separated flow past a periodically plunging normal flat plate. The plate is moved sinusoidally in the cross flow direction along its length. Since this involves translational motion only, a change of the frame of reference does not affect the forces and we can work in the body frame where the plate is stationary, and the velocity of the oncoming stream is given by

$$u(t) = U_\infty \qquad\qquad\qquad (2.5.5a)$$

$$v(t) = V_\mathrm{f}\,\sin(\frac{2\pi t}{T_\mathrm{f}})\ , \qquad\qquad\qquad (2.5.5b)$$

where V_f and T_f are the amplitude and period of forcing imposed on the plate. Here, forcing at approximately the "natural frequency" of $T_\mathrm{f} = 9$ with low amplitude of $V_\mathrm{f} = 0.2U_\infty$, is used. With such forcing, the resulting flow is expected to remain fairly close to that of the unforced case, and a study of this controlled flow could reveal useful information about the natural flow.

2.5.2.1 Early Development of Flow

Fig. (2.5.20) shows a sequence of the forced flow in the early stages of the recirculating bubble regime, and C_d, $|d\Gamma/dt|$, Ue_lower and Ue_upper for this flow are given in Figs. (2.5.21a), (2.5.21b), (2.5.21c) and (2.5.21d). Ue is the outer edge boundary-layer velocity, in the frame of the plate, computed at the edges. As a result of the lateral oscillation of the plate, the two vortices that are formed at the edges are no longer symmetric at early times. For $0 < t < 4.5$, during the downstroke of the plate, the upper vortex is pulled outward with the shear layer extending at a large radius of curvature from the edge, the flow there is smooth and the circulation flux is low, compared to that at the lower edge, where the shear layer is pushed inward behind the plate, with reduced radius of curvature. The difference in the curvature of the shear layers at the edges is most notable at the quarter period ($t = 2.25$), when the downward speed of the plate is maximum and the fluid that leaves the front boundary layer at the lower edge has to make a sharp turn as it enters into the shear layer. The circulation flux there is correspondingly higher. This can be observed from Fig. (2.5.21b)†. Because of the large $|d\Gamma/dt|$ at the lower edge, the lower vortex is much stronger, and as it moves upward, it flattens out the weaker upper vortex. At $t = 4.5$, the plate has completed its downstroke motion, and its lateral speed has decreased to zero. Here, the curvature of both shear layers at the edges is almost symmetrical, giving a similar velocity field at both edges. With this flow configuration, the circulation fluxes at both edges are the same, as shown in Fig. (2.5.21b), indicating a one-to-one correspondence between curvature and circulation flux. During the upstroke of the plate ($4.5 < t < 9.0$), the situation is reversed, with a tighter shear layer curvature, higher flow speed and higher circulation flux at the upper edge. The upper vortex is now the dominant one and as it moves downward, it compresses the weaker lower vortex.

---

† Note that the discontinuous slope in the signals at $t = 2$ is due to the instantaneous shutoff of the acceleration in the ramp start.

With the lateral forcing, the recirculating bubble behind the plate is no longer symmetric and is expected to become unstable at an earlier time compared to the symmetric bubble in the unforced case. From Fig. (2.5.21d), the boundary-layer velocity on the back face of the plate is observed to lag slightly behind the plate velocity, and during the downstroke of the plate starting at $t > 9$, the boundary-layer velocity changes direction at $t \simeq 10$. This is because of the strong downward velocity induced by the lower vortex. Following such velocity reversal, the flow on the front side has to speed up to negotiate the sharp turn, resulting in a large circulation flux created at the wall and a corresponding high C_d, as shown in Fig. (2.5.21a)†.

Fig. (2.5.22) shows a comparison of C_d to the experiments of Lisoski and Roshko (1989); the agreement between calculations and experiments is very good up to $t \simeq 4$, and the agreement for $t \geq 18$ is significantly improved over the unforced case (Fig. 2.5.28). Thus, we expect that three-dimensional effects in the laboratory flow have been reduced by the forcing. For $t > 4$, the experimental drag remains fairly flat before increasing very slightly at $t \simeq 10$. In the calculations, the drag continues to decrease until the vortex roll-up at $t \simeq 10$ where it increases sharply. Fig. (2.5.23a) shows a comparison of the flow at $t = 5$. In terms of the size and configuration of the recirculating region, qualitative agreement between the two is good, with the upper vortex being flattened to the same extent. The lower vortex, however, is somewhat more distorted in the experiments.

2.5.2.2 Long-time Behavior of Flow

Once the recirculating bubble becomes unstable and a vortex is formed at the upper edge, the asymmetric shedding mode of the flow sets in. Here, a vortex is shed at alternating edges similar to that observed in the unforced flow. Figs. (2.5.24a), (2.5.24b) and (2.5.24c) show the long-time history of C_d, $d\Gamma/dt|_{\mathrm{lower}}$ and $d\Gamma/dt|_{\mathrm{upper}}$, respectively. Definite periodicity corresponding to the asymmetric shedding, with superimposed long-wave fluctuation, is observed. Compared to the unforced case, the long-wave fluctuation is more significant in this case. In Figs. (2.5.25a), (2.5.25b) and (2.5.25c), we plot the period of shedding T_{sh}, the peak circulation flux $|d\Gamma/dt|_{\mathrm{max}}$, and the phase of shedding θ_{lag}. θ_{lag} is defined to be the relative temporal location of the peak flux within each stroke. For the lower edge,

---

† Note that although such velocity reversal also occur at $t \simeq 3$, the reversal is smooth (due to the plate motion) and no sharp increase in C_d occur. This is because the flow is at an early stage and the attached vortex is not strong enough (have not accumulated enough vorticity) to cause a breaking of the shear layer at the other edge.

it is relative to the beginning of the upstroke of the plate, while for the upper edge, it is relative to the beginning of the downstroke. At large time ($t \simeq 100$), all three quantities approach steady-state values with $T_{\text{sh}}|_{t\to\infty} = 9$ and $\theta_{\text{lag}}|_{t\to\infty} \simeq 40\%$. This implies that even though we are not forcing the flow at its "natural" shedding period of 9.4, as estimated previously, and the shedding at the beginning of the asymmetric mode was out of phase with the forcing (recall that velocity reversal on the back boundary-layer, which signifies the beginning of vortex roll-up, lags behind the downstroke motion of the plate), as $t \to \infty$, the flow locks in with the phase and frequency of the forcing. Comparing T_{sh} and $|d\Gamma/dt|_{\text{max}}$ of Figs. (2.5.25a) and (2.5.25b) to that of the unforced case in Figs. (2.5.12a) and (2.5.12b) shows that at steady state, the fluctuations of T_{sh} and $|d\Gamma/dt|_{\text{max}}$ in the forced case is much reduced, as expected.

2.5.2.3   Asymmetric Shedding Mechanism

Figs. (2.5.26a), (2.5.26b), (2.5.26c) and (2.5.26d) show C_d, $|d\Gamma/dt|$ at the lower and upper edges, and U_e at the upper edge, over one forcing cycle at large time. A corresponding sequence of plots of the vortex elements is given in Fig. (2.5.27). Because of the external forcing, the flow is more regular, and the signals are less noisy compared to those of Fig. (2.5.15) for the unforced case. From Fig. (2.5.26d), it is observed that the peak of the reversed velocity on the backside of the plate coincides with the maximum speed of the downstroke of the plate, indicating that the flow is in-phase with the forcing at that point. Following the velocity reversal on the back boundary-layer and the sharp rise in $|d\Gamma/dt|$ at $t \simeq 7$, a tight vortex roll-up is observed with a sharp rise in drag force.

2.5.2.4   Comparison to Experiments

Fig. (2.5.28) shows a comparison of the computed drag for $0 < t < 60$ to that measured by Lisoski and Roshko (1989). The qualitative agreement in terms of transient behavior is very good although the first sharp rise in drag at $t \simeq 10$ is not observed in the experiments. For large time of $40 < t < 60$, $\overline{C_d}$ in the calculation is estimated at 2.9, while that in the experiments is estimated at 2.2. This gives a discrepancy of only 30%, which is an improvement from the discrepancy of 100% in the unforced case. A qualitative comparison of the flow at $t = 19$ shows good agreement in terms of the phases of the motions (see Fig. 2.5.23b). Again, in the calculations, the vortex seems to roll up more tightly and closer to the plate than was observed in the experiments. This is probably why the computed drag is slightly higher than the experimental value. Also, as a result of the tighter roll-up of the lower vortex, the upper vortex is pushed farther upward, compared to that observed in the experiments.

2.5.3   Plunging Normal Flat Plate at 'Off-natural Frequency'

In this test case, the flow is forced with the same forcing function as the last case with $T_f = 11$ and $V_f = 0.2U_\infty$. Fig. (2.5.29a), (2.5.29b) and (2.5.29c) show C_d, $d\Gamma/dt|_{lower}$ and $d\Gamma/dt|_{upper}$. After the sharp increase in drag at $t \simeq 10$, indicating the breakup of the recirculating region, definite periodicity with superimposed long-wave fluctuations similar to those of Fig. (2.5.24), can be observed. However, in this case, the amplitude of the long fluctuation remained significant even at $t = 100$. To understand this, the time histories of T_{sh}, $|d\Gamma/dt|_{max}$ and θ_{lag}, given in Figs. (2.5.30a), (2.5.30b) and (2.5.30c), respectively, are examined. For $t > 20$, T_{sh} varied between 8.3 and 9.7 with a mean of about 9.3, indicating that the flow is shedding at the "natural" frequency, despite the external forcing at $T_f = 11$. This is probably because of the low amplitude of the forcing. From Fig. (2.5.30b), a definite trend with a period of about 60 could be observed in the variation of $|d\Gamma/dt|_{max}$, indicating that the circulation shed at the "natural" frequency is modulated by the long-wave variation. Examining Fig. (2.5.30c) shows that this variation comes about because the shedding is out of phase with the forcing, and it takes about 60 time units for the shedding cycle to get back to its initial lag state, i.e., the same θ_{lag}. This behavior is a strong indication that the long-wave oscillations will persist.

2.5.4 Pitching Normal Flat Plate

In this section, we study the flow behind a flat plate pivoted at mid-chord and pitched sinusoidally about the normal position, i.e., 90° angle of attack. Here, the angle of attack is given, as a function of time, by the following,

$$\alpha(t) = \alpha_o + \alpha_f \sin(\frac{2\pi t}{T_f}) \ . \tag{2.5.6}$$

The parameters used are $\alpha_o = 90°$, $\alpha_f = 36.5°$ and $T_f = L/U_\infty$. This is a large amplitude forcing with maximum speed of $2U_\infty$ of the tip of the plate.

Fig. (2.5.31) shows a complete cycle of the flow at steady state. At $t = 15.0$, the plate is going through its clockwise rotation at a maximum rotation rate, and a positive sign vortex is being deposited into the flow from each of the edges. At the upper edge, because of the angular velocity of the plate, the shed vortex is forming upstream. The shear layer connecting the vortex to the negative vortex shed in the previously half cycle is still intact, although vortices along the shear layer have rolled up into small eddies because of Kelvin-Helmholtz instability. At the lower edge, the negative vortex shed in the last half cycle has merged with the positive vortex shed in the last cycle, and the shear layer that connects it to the newer vortex is no longer visible, probably because of the high stretching. At $t = 15.25$, the upper positive vortex has collided with the negative vortex shed in the earlier half cycle. Note that the shear layer that connects the new vortex to the plate, being between the two vortices, is compressed into an almost straight line. This feature is also observed by Freymuth (1988) in his flow visualization experiments of a pitching airfoil with $\alpha_o = 5°$ and $\alpha_f = 20$. Later, at $t = 15.5$, the two vortices are observed to merge and move downstream. At this point, the flow has completed half a cycle and in the next half cycle, because of the top-bottom antisymmetry of the problem, that which had been observed for the top half portion of the flow would be repeated at the lower half portion and vice-versa.

Figs. (2.5.32a), (2.5.32b), (2.5.32c) and (2.5.32d) show the time histories of C_d, C_l, $d\Gamma/dt|_{lower}$ and $d\Gamma/dt|_{upper}$. Because of the strong forcing, steady state is achieved very rapidly, after only about $7L/U_\infty$ (Fig. 2.5.32a), whereas in the previous case with weak forcing, the flow took a very long time to settle down to steady state. At steady state, $\overline{C}_d$ is estimated to be 2.3, although the instantaneous C_d could be as high as 4. This is because the pitching motion of the plate results in opposite sign vortex structures being shed from the same edge over one complete cycle. These pairs of opposite sign vortices self-propel away from the plate (Fig.

2.5.31), and the formation of a large vortical region with low pressure behind the plate such as that observed in the unforced normal plate flow is avoided with corresponding lower drag. Also, the circulation of each vortex structure shed could be high, but the net circulation of the pair of opposite sign vortices is low. This can be observed in the variation of $d\Gamma/dt|_{\text{lower}}$ and $d\Gamma/dt|_{\text{upper}}$ (Figs. 2.5.32b and 2.5.32c), where the circulation flux changes sign every half cycle, resulting in low net circulation shed per cycle.

CHAPTER 3

Three-dimensional Vortex-tube Interactions

This chapter presents the results of a study of three-dimensional high Reynolds number flows using vortex methods. The objective of this study is to develop a robust vortex stick method that is capable of handling complex interactions of vortex tubes. In Sec. (3.1), a survey of related work in the literature is presented. The mathematical foundations are presented in Sec. (3.2) and in Sec. (3.3), a modified vortex method is developed. Applications of the method to problems involving the interactions of vortex tubes are presented in Sec. (3.4).

3.1 Previous Work

Recently, there have been numerous applications of vortex methods, including both vortex filament methods and vortex stick methods, to three-dimensional unsteady flow problems, and comprehensive reviews of these works are given by Leonard (1980a, 1985) and Sarpkaya (1989). In contrast to its two-dimensional counterpart, which is used extensively in calculations of unsteady separated flows, three-dimensional vortex methods are still in an early stage of development in the sense that most applications are limited to calculations of flows in an infinite domain with no solid boundaries. Examples of these calculations include vortex-tube interactions (Leonard 1975, Shirayama and Kuwahara 1984, Mosher 1985, Anderson and Greengard 1984, Ashurst and Meiron 1987, Winckelmans and Leonard 1988a, Winckelmans 1989), growth of turbulent spot in a laminar boundary layer (Leonard 1980b), bifurcating jet (Parekh et al. 1983), a temporally growing shear layer (Ashurst and Meiburg 1985), spatially growing shear layer (Inoue 1989), etc.

The study of interacting vortex tubes is particularly interesting and has been undertaken by many researchers. One example is the collision of two ring vortices, studied experimentally by Kambe and Takao (1971), Fohl and Turner (1975), Oshima and Asaka (1977), Izutsu et al. (1987) and Schatzle (1987). In this problem, cancellation, because of viscous effects, of opposite sign vorticity at the collision region is observed with subsequent cross-linking of the two collided rings into one single vortex loop. Because of self-induced motion, the contorted loop latter fissions into two ring vortices travelling in a plane orthogonal to the initial motions.

In spite of its simplicity in problem definition, this class of problems contains some of the fundamental ingredients of complex turbulent flows such as vortex stretching, vortex reconnection, vortex breakdown, complex evolution of the space curve of the vortex tube and the development of internal structure and axial flow within the vortex core. Because of the complexity of these processes, in particular the vortex reconnection process present in many such flows, this problem also represents a challenging test case for vortex method researchers. Comparison to flow visualization experiments is frequently used as validation.

One of the earliest calculations of collision problem for vortex rings is that by Leonard (1975). Using an inviscid vortex filament method, he computed the problem up to the time of collision, at which point the geometry of the vortex filaments in the collision region is redefined to mimic viscous effects there. Such redefinition process is necessary because in the inviscid vortex filament method, each filament is constrained to be in a close loop, and reconnection with other filaments is not allowed. A similar procedure is used in the calculations of Yamashita and Oshima (1988). In the calculations of Ashurst and Meiron (1987), the vortex filament method is also used to compute the collision problem up to the collision time. At that time, a grid is placed in the collision region and the Navier-Stokes equations is solved with fixed boundary conditions obtained from the outer vortex filament solution. They were able to observe cancellation of vorticity within the region and reported that the process occurred at the convective time scale, σ_R^2/Γ_R, which is much faster compared to the viscous time scale, σ_R^2/ν, where σ_R and Γ_R are the core thickness and circulation, respectively, of the vortex tube. Similar behavior is observed in the analytical work of Takaki and Hussain (1986). These results (Ashurst and Meiron 1987, Takaki and Hussain 1986) are used as a foundation for developing a vorticity cancellation model in Sec. (3.3.2).

Calculations using the more versatile vortex stick methods have been attempted by several investigators. Mosher (1985) computed the collision problem without any modeling of viscous effects and encountered a numerical blowup of the solution after the two rings have collided, presumably because in the absence of viscosity, intense stretching of vorticity occurs. Shirayama and Kuwahara (1984) includes viscous effects using the core expansion scheme suggested by Leonard (1980a) and were able to observe reasonable reconnection process of the rings. Anderson and Greengard (1984) applied the random walk scheme of Chorin (1973) to the problem but were unable to reproduce the reconnection phenomena. In their calculations, the vortex vectors have been misaligned because of the random process used to represent viscous effects. Using the circulation exchange scheme of Degond and Mas-Gallic (1988) for viscous effects, Winckelmans and Leonard (1988a) and Winckelmans (1989) computed the collision problem at low Reynolds number, and the reconnec-

tion process (fussion), as well as the subsequent splitting of the single reconnected vortex loop into two vortex rings (fission), are well represented in their calculations. More recently, Zawadzki and Aref (1989) used the method of vortex-in-cell to compute the same problem, and in their calculations both the processes of fusion and fission of vortex rings are observed.

3.2   Mathematical Formulation

The vorticity equation for an incompressible viscous fluid in three dimensions is given by

$$\frac{\partial \underline{\omega}}{\partial t} + \underline{u} \cdot \nabla \underline{\omega} = \underline{\omega} \cdot \nabla \underline{u} + \nu \nabla^2 \underline{\omega} \ , \qquad (3.2.1)$$

where ν is the viscosity and $\underline{\omega}$ is the vorticity vector field, defined as the curl of the velocity field,

$$\underline{\omega} = \nabla \times \underline{u} \ . \qquad (3.2.2)$$

Thus, $\underline{\omega}$ satisfies the divergence-free condition,

$$\nabla \cdot \underline{\omega} = 0 \ . \qquad (3.2.3)$$

Some differences between the above set of equations and the corresponding two-dimensional equations discussed in Chapter 2 are to be noted :

(i) Eqn. (3.2.1) is the same as the two-dimensional vorticity equation, Eqn. (2.2.4), except for the vorticity stretching term $\underline{\omega} \cdot \nabla \underline{u}$, which is not present in two-dimensional flows because the vortex lines are orthogonal to the flow gradients in two-dimensional flows.

(ii) In two-dimensional flows, Eqn. (3.2.3) is automatically satisfied by vortex methods and need no longer be considered. This is not the case in three-dimensional flows and Eqn. (3.2.3) must be enforced, for example, when specifying initial conditions or enforcing boundary conditions on a solid wall using vortex elements.

For an inviscid fluid, Eqn. (3.2.1) reduces to

$$\frac{\partial \underline{\omega}}{\partial t} + \underline{u} \cdot \nabla \underline{\omega} = \underline{\omega} \cdot \nabla \underline{u} \ . \tag{3.2.4}$$

This can also be written as

$$\frac{D\underline{\omega}}{Dt} = \underline{\omega} \cdot \nabla \underline{u} \ . \tag{3.2.5}$$

Eqn. (3.2.5) gives the inviscid motion of vorticity in three-dimensional flow, and together with the Kelvin and Helmholtz Theorems, forms the foundation for the three-dimensional vortex stick methods. To express the velocity field in terms of the vorticity field, we take the curl of Eqn. (3.2.2) and apply the incompressibility condition,

$$\nabla \cdot \underline{u} = 0 \tag{3.2.6}$$

to obtain a Poisson's equation for $\underline{u}$,

$$\nabla^2 \underline{u} = -\nabla \times \underline{\omega} \ . \tag{3.2.7}$$

The solution to Eqn. (3.2.7) for an infinite domain is given by the Biot-Savart formula,

$$\underline{u}(\underline{x}, t) = -\frac{1}{4\pi} \int \frac{(\underline{x} - \underline{x}') \times \underline{\omega}}{\mid \underline{x} - \underline{x}' \mid^3} \ d\underline{x}' \ + \nabla \phi \ . \tag{3.2.8}$$

This completes the vorticity formulation in three-dimensional flows.

3.3 Vortex Particle Method

In the three-dimensional vortex particle method, the vorticity field is represented by a collection of discrete vortex vector particles, commonly referred to as vortex sticks or vortons, as follows:

$$\underline{\omega}(\underline{x}, t) = \sum_{i=1}^{N_v} \underline{\alpha}_i \gamma_i(\mid \underline{x} - \underline{x}_i(t) \mid) \ . \qquad (3.3.1)$$

Each vector particle is defined by a location $\underline{x}_i$ and a vector strength $\underline{\alpha}_i$. The vector strength $\underline{\alpha}_i$ has units of circulation times length (vorticity times volume) and is smeared out over a volume according to the spherically symmetric distribution function γ_i, defined by

$$\gamma_i(\underline{x}) = \frac{1}{\sigma_i^3} P(\frac{|\underline{x}|}{\sigma_i}) \ , \qquad (3.3.2)$$

where σ_i is the core size of the particle and gives a measure of the spread of vorticity within each particle. Substituting Eqn. (3.3.1) in Eqn. (3.2.8) results in the following discretized Biot-Savart formula,

$$\underline{u}(\underline{x}, t) = -\frac{1}{4\pi} \sum_{i=1}^{N_v} \frac{(\underline{x} - \underline{x}_i) \times \underline{\alpha}_i}{\mid \underline{x} - \underline{x}_i \mid^3} g_i(\mid \underline{x} - \underline{x}_i \mid) \ , \qquad (3.3.3)$$

where

$$g(r) = 4\pi \int_0^r P(r')r'^2 dr' \ . \qquad (3.3.4)$$

In accordance with the inviscid vorticity equation, Eqn. (3.2.5), and the Kelvin and Helmholtz Theorems, we used the approximation that each particle moves at the local velocity,

$$\frac{d\underline{x}_i}{dt} = \underline{u}(\underline{x}_i) \ , \qquad (3.3.5)$$

and that the inviscid rotation and amplification of the vector particle is computed by

$$\frac{d\underline{\alpha}_i}{dt} = \underline{\alpha}_i \cdot \nabla \underline{u}(\underline{x}_i) \ . \tag{3.3.6}$$

Convergence of the above scheme to the inviscid vorticity equation in the limit $N_v \to \infty$, $h \to 0$, $\sigma \to 0$ but $\sigma/h \to \infty$ has been shown by Beale and Majda (1982a, 1982b), Cottet (1982, 1988), Anderson and Greengard (1985), Beale (1986a, 1986b) and Choquin and Cottet (1988). However, Saffman and Meiron (1986) have shown that the formulation given by Eqns. (3.3.5) and (3.3.6) does not constitute a weak solution of the three-dimensional vorticity equation. Although Eqn. (3.3.6) seems a natural representation of Eqn. (3.2.5), as discussed by Rehbach (1978), Choquin and Cottet (1988), Winckelmans and Leonard (1988a and 1988b) and Winckelmans (1989), the vorticity equation, Eqn. (3.2.5), could be rewritten as

$$\frac{\partial \underline{\omega}}{\partial t} + \underline{u} \cdot \nabla \underline{\omega} = \underline{\omega} \cdot \nabla^{\mathrm{T}} \underline{u} \ , \tag{3.3.7}$$

or

$$\frac{\partial \underline{\omega}}{\partial t} + \underline{u} \cdot \nabla \underline{\omega} = \frac{1}{2}\Big[\underline{\omega} \cdot (\nabla^{\mathrm{T}} + \nabla)\Big]\underline{u} \ . \tag{3.3.8}$$

The corresponding evolution equations for $\underline{\alpha}_i$ are

$$\frac{d\underline{\alpha}_i}{dt} = \underline{\alpha}_i \cdot \nabla^{\mathrm{T}} \underline{u}(\underline{x}_i) \ , \tag{3.3.9}$$

or

$$\frac{d\underline{\alpha}_i}{dt} = \underline{\alpha}_i \cdot \Big[\frac{1}{2}(\nabla + \nabla^{\mathrm{T}})\Big]\underline{u}(\underline{x}_i) \ , \tag{3.3.10}$$

both of which lead to schemes that converge to the vorticity equation, Eqn. (3.2.5). In addition, Eqn. (3.3.9) conserves total vorticity (Choquin and Cottet 1988) and leads to a weak solution of the vorticity equation (Winckelmans and Leonard 1988b). In the current work, only Eqn. (3.3.6) is used.

For conservation of volume of vorticity, the change in core radius, σ_R, of a continuous vortex tube subjected to inviscid stretching is computed according to

$$\frac{d\sigma_R^2}{dt} = -\sigma_R^2 \frac{1}{\omega}\frac{d\omega}{dt} \quad , \tag{3.3.11}$$

which satisfies the conservation equation

$$\frac{dv_R}{dt} = 0 \quad , \tag{3.3.12}$$

where v_R is the volume of vorticity, given by $\pi\sigma_R^2 l$ and l is the length of the tube. Since the discretized vortex tube is represented by a collection of vortex vector particles along its length, Eqn. (3.3.11) is approximated by the following:

$$\frac{d\sigma_i^2}{dt} = -\sigma_i^2 \frac{1}{\alpha_i}\frac{d\alpha_i}{dt} \quad , \tag{3.3.13}$$

where α_i is the modulus of the vector strength $\underline{\alpha}_i$.

3.3.1 Viscosity Model

As discussed in Sec. (3.1), calculations of vortex-tube interactions using inviscid vortex methods usually lead to a blowup of the numerical solutions that mimics the intense vortex stretching and possible singularity present in the exact inviscid solution. Several methods have been developed to incorporate viscous effects into vortex methods. They are random walk (Chorin 1973), core spreading (Leonard 1980a) and circulation redistribution (Degond and Mas-Gallic 1988). In the present work, the core spreading scheme of Leonard is modified to include subgrid-scale viscous effects of high Reynolds number flows.

In full Navier-Stokes simulations, the smallest viscous or Kolmogorov scale that can be resolved is determined by the grid spacing, and this limits the Reynolds numbers that can be treated to relatively low value, of the order of several hundred. To treat high Reynolds number flows, large eddy simulation, where the effect of the subgrid scales on the larger scales are modeled, is usually used. One example of such modeling for finite difference calculations is the use of Smagorinsky's (1963) eddy viscosity model given by,

$$\nu_{\mathrm{e}} = \mathrm{C}\Delta^2 \left(\frac{\partial \overline{u}_i}{\partial x_k} \frac{\partial \overline{u}_k}{\partial x_i} \right)^{\frac{1}{2}} , \qquad (3.3.14)$$

where ν_{e} is the turbulent eddy viscosity, Δ is the grid size, $(\partial \overline{u}_i/\partial x_k)(\partial \overline{u}_k/\partial x_i)$ is the squared deformation tensor computed on the large eddy grid, and C is a constant of order unity. For further discussions of the model and its applications, the interested reader is referred to Smagorinsky (1963), Smagorinsky et al. (1965) and Lilly (1962, 1966).

In vortex methods, a deterministic treatment of the viscous term in the Navier-Stokes equation also limits the Reynolds number to a relatively low value, usually of the order of several hundred (Winckelmans and Leonard 1988, Winckelmans 1989). For calculations of high Reynolds number flows, a non-linear core expansion scheme with an eddy viscosity analogous to Smagorinsky's model is proposed. In the present model, the core size of each vector particle evolves according to the following equation,

$$\frac{d\sigma^2}{dt} = 4\nu_{\mathrm{e}} - \sigma^2 \frac{1}{\omega}\frac{d\omega}{dt} , \qquad (3.3.15)$$

where the first term on the right-hand side is the viscous term similar to that used by Leonard (1980a) and the second term is the inviscid stretching of Eqn. (3.3.13). The eddy viscosity ν_{e} in the viscous term is used for subgrid modeling and depends on the local vorticity stretching rate,

$$\nu_{\mathrm{e}} = \mathrm{C}' \sigma^2 \frac{1}{\omega}\frac{d\omega}{dt} , \qquad (3.3.16)$$

where C' is a constant of order unity. To prevent antidiffusion, the viscosity term is turned off when the local stretching is negative, i.e., during compression.

3.3.2 Vorticity Cancellation Model : Vortex Dipole

In the calculations of a collision of two vortex rings, Ashurst and Meiron (1987) solved the Navier-Stokes equations in the region of the collision. Cancellation of opposite sign vorticity because of viscous effects was observed. In vortex methods, with circulation exchange used to represent viscous effects (Degond and Mas-Gallic 1988), cancellation of vorticity is explicit, and such process can be accurately described (Winckelmans and Leonard 1988, Winckelmans 1989). However, with other viscous schemes such as random walk or core spreading, there is no actual cancellation of vorticity, and such process cannot be properly accounted for.

According to the works of Takaki and Hussain (1986) and Ashurst and Meiron (1987), vorticity cancellation occurs at the inviscid convective time scale, and the effect of viscosity is necessary only for the cancellation to take place. Following these guidelines, a new computational element will be used to represent the cancellation process. In particular, pairs of opposite sign vortex vectors with equal strength α and separation distance ε less than a prescribed value ε_m, are replaced by high-order vortex dipoles. For a pair of vortex vectors $\underline{\alpha}_i$ and $\underline{\alpha}_j$, at $\underline{x}_i$ and $\underline{x}_j$ respectively, which satisfies the conditions $\varepsilon < \varepsilon_m$ and $\underline{\alpha}_i \cdot \underline{\alpha}_j < 0$, but with $\underline{\alpha}_i \neq -\underline{\alpha}_j$, the two unit vectors $\hat{e}_{\text{sum}} = (\underline{\alpha}_i + \underline{\alpha}_j)/|\underline{\alpha}_i + \underline{\alpha}_j|$ and $\hat{e}_{\text{diff}} = (\underline{\alpha}_i - \underline{\alpha}_j)/|\underline{\alpha}_i - \underline{\alpha}_j|$ are computed. Each vortex vector is then resolved into two components, $\underline{\alpha} \cdot \hat{e}_{\text{sum}}$ and $\underline{\alpha} \cdot \hat{e}_{\text{diff}}$. The vectors $\underline{\alpha}_i \cdot \hat{e}_{\text{diff}}$ and $\underline{\alpha}_j \cdot \hat{e}_{\text{diff}}$ are merged to form a dipole at $(\underline{x}_i + \underline{x}_j)/2$, while the vectors $\underline{\alpha}_i \cdot \hat{e}_{\text{sum}}$ and $\underline{\alpha}_j \cdot \hat{e}_{\text{sum}}$ are placed at their original locations at $\underline{x}_i$ and $\underline{x}_j$, respectively. The resultant dipole is defined by two vectors $\underline{\alpha}$ and $\underline{\varepsilon}$, where $\underline{\alpha}$ is the vorticity vector of one of the vortex particles and $\underline{\varepsilon}$ is the separation vector between the particles. The effective strength μ is given by the product $\alpha\varepsilon$, (see Fig. 3.3.1). Being derivatives of vortex particles, the dipoles also move at the local velocity,

$$\frac{d\underline{x}_k^d}{dt} = \underline{u}(\underline{x}_k^d) \ , \qquad (3.3.17)$$

where $\underline{x}_k^d$ is the position of the kth vortex dipole. The rotation and amplification (or decay) of each dipole is computed by following the time evolution of the two vectors $\underline{\alpha}_k$ and $\underline{\varepsilon}_k$, which are vorticity and material vector elements, respectively, and obey the inviscid vorticity equation, Eqn. (3.2.5),

$$\frac{d\underline{\alpha}_k}{dt} = \underline{\alpha}_k \cdot \nabla\underline{u} \ , \qquad (3.3.18)$$

$$\frac{d\underline{\varepsilon}_k}{dt} = \underline{\varepsilon}_k \cdot \nabla \underline{u} \; . \tag{3.3.19}$$

The induced velocity that is due to a dipole μ_k at $\underline{x}_k$, formed from the merging of the vortex pair $\underline{\alpha}_i$ and $\underline{\alpha}_j$ at $\underline{x}_i$ and $\underline{x}_j$, respectively, is derived as expansions of the induced velocities, $\underline{u}_i$ and $\underline{u}_j$, of $\underline{\alpha}_i$ and $\underline{\alpha}_j$, respectively, about the point $\underline{x}_k$,

$$\begin{aligned}
\underline{u}(\underline{x},t) &= \underline{u}_i(\underline{x}_i,t) + \underline{u}_j(\underline{x}_j,t) \\
&\simeq \underline{u}_i(\underline{x}_k,t) + \frac{1}{1!}\frac{1}{2}\varepsilon\frac{\partial \underline{u}_i}{\partial \underline{x}_\varepsilon} + \frac{1}{2!}\frac{1}{2}\varepsilon^2\frac{\partial^2 \underline{u}_i}{\partial \underline{x}_\varepsilon^2} + \frac{1}{3!}\frac{1}{2}\varepsilon^3\frac{\partial^3 \underline{u}_i}{\partial \underline{x}_\varepsilon^3} + \cdots \\
&\quad + \underline{u}_j(\underline{x}_k,t) - \frac{1}{1!}\frac{1}{2}\varepsilon\frac{\partial \underline{u}_j}{\partial \underline{x}_\varepsilon} + \frac{1}{2!}\frac{1}{2}\varepsilon^2\frac{\partial^2 \underline{u}_j}{\partial \underline{x}_\varepsilon^2} - \frac{1}{3!}\frac{1}{2}\varepsilon^3\frac{\partial^3 \underline{u}_j}{\partial \underline{x}_\varepsilon^3} + \cdots \; ,
\end{aligned} \tag{3.3.20}$$

where $\underline{x}_k = (\underline{x}_i + \underline{x}_j)/2$, $\underline{\varepsilon} = \underline{x}_i - \underline{x}_j$, $\varepsilon = |\underline{\varepsilon}|$ and $\partial/\partial \underline{x}_\varepsilon$ denotes gradient in the direction of $\underline{\varepsilon}$. Because the vortex pair have equal and opposite strength, all terms with even power of ε cancel out, and the leading term in the induced velocity is $O(\varepsilon)$,

$$\underline{u}(\underline{x},t) = \varepsilon\frac{\partial \underline{u}_i}{\partial \underline{x}_\varepsilon} + O(\varepsilon^3) \; , \tag{3.3.21}$$

and decay according to the inviscid equation, Eqn. (3.3.19). Effectively, this represents cancellation of vorticity at the inviscid time scale. The above is non-zero at $\underline{x}_k$, and the dipole has self-induced velocity.

3.3.3   Remeshing of Vortex Particles

In specifying the initial conditions of a vortex calculation, each vortex filament is discretized into a collection of vortex particles placed along its length. The strength $\underline{\alpha}$ of each particle is given by $\Gamma\delta\underline{l}$, where Γ is the circulation and $\delta\underline{l}$ is the segment of the filament assigned to the particle. With such a discretization, the condition Eqn. (3.2.3) is not satisfied but approximated. Because of the stretching term $\underline{\omega}\cdot\nabla\underline{u}$ in Eqn. (3.2.5), a vortex filament may become highly stretched and neighboring particles representing the filament may move away from each other. This results in non-smooth vorticity and velocity fields with the condition Eqn. (3.2.3) badly approximated. Numerical instability may then occur. To avoid such problems, a remeshing scheme is proposed. In this scheme, if a vortex particle is stretched such that its length segment $|\delta\underline{l}|$ is too large compared to its initial length, it is split into two or more particles with the appropriate length (i.e. if it is split into two particles, then half the previous length is used). The circulation and the core size of the particles are kept constant and the new particles are equally spaced along the direction of the vorticity vector (see Fig. 3.3.2).

3.4   Numerical Results

In this section, the proposed vortex method is tested on two problems involving the interaction of two vortex tubes: (i) The collision problem for ring vortices and (ii) The vortex knot problem. The problem definition of (i) and (ii) is shown in Figs. (3.4.1a) and (3.4.1b), respectively. In both test cases, each vortex ring has a circulation of $\Gamma_R = 1$, a core thickness of $\sigma_R = 0.2$ and a radius of $r_R = 1$. Unless otherwise specified, each ring is discretized into 5 filaments per cross section and 54 particles along the length of each filament, giving a total of 270 particles per vortex ring. Each vortex particle has a core size of $\sigma = 0.117$ and a circulation of $\Gamma = \Gamma_R/5$. Merging of vortex pairs into dipoles takes place when the separation distance ε of the pair is less than 0.05, and splitting of a vortex vector into two shorter vectors takes place when the length is twice the original length. A fourth-order Runge-Kutta time-integration scheme is used.

3.4.1   Case (i) : Collision of Two Ring Vortices

In this test case, two vortex rings with the same clockwise circulation are separated by a distance of $s = 3$ and tilted at a slight angle of $\theta_t = 7.5°$ toward each other (see Fig 3.4.1a). In this initial configuration, the neighboring sections of the vortices lag behind, producing an induced flow toward each other. This leads to the collision of the rings at a later time. During the collision, the rings reconnect to form one single contorted ring. In the early stages of the calculation ($t < 6$, where t has units of r_R^2/Γ), when the two rings are still relatively far apart, large time steps of $\Delta t = 0.1$ are used. For $t > 6$, Δt is reduced to 0.01.

3.4.1.1   Viscosity Modeling

In the following, several different core size evolution models are tested and compared.

(i) Linear viscosity modeling

In this case, the linear core spreading model of Leonard (1980a) is tested. Conservation of the volume of vorticity according to Eqn. (3.3.13) is imposed,

$$\frac{d\sigma^2}{dt} = 4\nu - \sigma^2 \frac{1}{\omega}\frac{d\omega}{dt} \quad . \tag{3.4.1}$$

Fig. (3.4.2) shows the front view of the time sequence of vortex rings collision computed, using $\nu = 4.5 \times 10^{-4}$. At $t \simeq 6$, the two rings collide and start a complex vorticity cancellation process in the region of collision. The cancellation is completed by $t \simeq 7.25$, as shown by the disappearance of the y-vorticity, and the two rings have joined to form a single contorted ring. In the region of reconnection, one observes the sharp turning and large stretching of the vortex tubes with steep gradients. These lead eventually to numerical blowup at $t = 11.75$.

Variation of linear viscosity - In this section, calculations at four values of ν ($\nu = 4.5 \times 10^{-4}$, 5.0×10^{-4}, 6.25×10^{-4} and 12.5×10^{-4}) are carried out. Figs. (3.4.3a), (3.4.3b), (3.4.3c) and (3.4.3d) show the vortex ring at $t = 8.0$ for the four cases. In terms of large-scale features, there is very little difference between the cases. However, slight differences in small scales could be observed in the reconnection region, indicating the importance of small-scale effects, presumably because of the intense deformations $(\partial \overline{u}_i / \partial x_k)(\partial \overline{u}_k / \partial x_i)$ in this region. Figs. (3.4.4a), (3.4.4b), (3.4.4c) and (3.4.4d) show the computed ring at the time step just before numerical divergence. Perhaps contrary to intuition, note that the solution computed using a larger ν becomes unstable earlier. It is suspected that the cause is due to the larger discretization error because of the larger core size σ.

Variation of grid size - Figs. (3.4.5a) and (3.4.5b) show the contorted vortex ring at $t = 11.75$, computed using two different grids with 5 and 9 filaments per cross section, respectively. $\nu = 4.5 \times 10^{-4}$ is used. With the finer grid, the solution is slightly better behaved and numerical blowup is delayed, but not prevented, and occurs at $t = 12.50$.

Variation of merging criteria - In selecting a parameter value for the merging criterion ε_{m}, two points must be considered: If ε_{m} is too large, then the error in the velocity field, which is $O(\varepsilon^3)$ from Eqn. (3.3.21), may be large. However, if ε_{m} is too small, then the stretching of the opposite sign vortex particles may lead to a numerical instability. In this section, the variation of the numerical results with the merging parameter ε_{m} is studied. Two cases with $\varepsilon_{\mathrm{m}} = 0.01$ and 0.05 are computed. Figs. (3.4.6a) and (3.4.6b) show the collided vortex rings at $t = 10.75$. Qualitatively, there is very little difference, except in the region of reconnection, where the case with $\varepsilon_{\mathrm{m}} = 0.01$ is less regular and becomes unstable sooner. This is because the close pairs of opposite sign vortices in the collision region, which would be effectively cancelled in the presence of viscosity, are not merged because of an overly stringent criterion. These highly stretched vortex vectors would become unstable and lead to numerical blowup of the solution. Therefore, it is decided that the slightly larger value of $\varepsilon_{\mathrm{m}} = 0.05$ will be used in all future calculations.

(ii) No change of core size with stretching

In this case, the change of core size that is due to stretching is turned off. This violates the conservation of volume of vorticity but it is hoped that by not allowing such reduction in core size, the singular behavior of very thin vortex filaments could be avoided. Fig. (3.4.7a) shows the contorted ring at $t = 10.50$, computed

without any viscosity model. Slightly after this time, the calculation becomes singular. Turning on the linear viscosity to $\nu = 4.5 \times 10^{-4}$ modified the configuration slightly (Fig. 3.4.7b), but did not prevent the numerical instability. Apparently, the numerical difficulties are not just because of the shrinking of vortex core due to large stretching.

(iii) Non-linear viscosity modeling

In these cases, the non-linear core spreading model given by Eqns. (3.3.15) and (3.3.16) is used. Figs. (3.4.8a) and (3.4.8b) show a sequence of front views of the vortex rings undergoing a collision, computed using $\nu_e = 1.25$ and 1.05, respectively. The top and side views are given in Figs. (3.4.9) and (3.4.10), respectively. In both cases, the collision and subsequent reconnection process proceed to completion with no numerical instability. Presumably, small-scale effects that are below the resolution of the vortex calculation but appear to be important in the region of reconnection are being represented by the subgrid viscosity model. Note the similarity between the two calculations in spite of the different ν_e used. For the case $\nu_e = 1.25$, the calculation is carried beyond the reconnection stage (to $t = 24$) and the results are discussed in the next section.

3.4.1.2 Qualitative Comparison To Experiments

Fig. (3.4.11) compares the calculations, using non-linear viscosity model, to the experiments of Schatzle (1987) in terms of flow visualization. In the experiments, $Re \simeq 1800$, $r_R = 1$, $\sigma_R \simeq 0.3$, $s = 2.7$ and $\theta_t = 13°$. For the calculations, recall that $r_R = 1$, $\sigma_R = 0.2$, $s = 3.0$ and $\theta_t = 7.5°$. Despite the difference in the parameters defining the problem, a comparison of global features as the flow evolves is very good. After the rings have collided and reconnected to form one single contorted ring, the two outer arms of the ring (a and a' in the top view) continued to move downward and inward, while the two reconnected portions (b and b' in the side view) moved outward. Later, the arms a and a' come together and pinch off to form two rings moving off on a plane orthogonal to that of the initial motion. The vortex tubes in the calculations appear to be in an "agitated" state, especially near the reconnected region where significant twisting of vortex filaments (helical modes) could be observed. These disturbances propagate outward along the tubes into the undisturbed region. These features are not observed in the experiments because the dye gives only an indication of the spatial configuration of the fluid containing vorticity and not the vector directions.

3.4.1.3   Collision Process

In the following, contour plots of vorticity and out-of-plane stretching are computed on three planes (P_I, P_{II} and P_{III} in Fig. 3.4.12) intersecting the vortex tube. Fig. (3.4.13a) shows a contour plot of ω_y in the $x - z$ symmetry plane of the collision, P_I, at $t = 6.0$ (the beginning of the collision process). The deformations of the pair of opposite sign vortex cores, that are due to the in-plane compression and out-of-plane stretching, is clear. A contour plot of the out-of-plane stretching, $\partial v/\partial y$, in this region is given in Fig. (3.4.13b). Its intensity, when compared to the corresponding out-of-plane stretching in the $x - z$ plane P_{II} (see Fig. 3.4.13c), is relatively high. The corresponding contour plot of ω_x in the $y - z$ plane P_{III}, given in Fig. (3.4.13d), shows the state of the component, ω_x, that is reconnecting. Note the slightly lower intensity when compared with ω_y of Fig. (3.4.13a). Fig. (3.4.14) shows the same set of plots at the later time, $t = 7.5$. The intensity of ω_y is now reduced significantly (Fig. 3.4.14a) compared to that at $t = 6.0$. The corresponding out-of-plane stretching rate is also reduced. Fig. (3.4.14d) shows the corresponding plot of ω_x on the $y - z$ plane. At this time, the core is well developed with a higher intensity of ω_x. The rings have essentially reconnected in the x-direction.

3.4.1.4   Internal Core Structure and Axial Flow

After the collision process, as observed in Figs. (3.4.8), (3.4.9) and (3.4.10), helical disturbances appear to propagate outward from the region of reconnection. With helical twisting of vortex lines, axial flow within the vortex core is expected from kinematics. Fig. (3.4.15a) shows the front view of a portion of the contorted ring at $t = 10.5$. The velocity field and vorticity field in a plane normal to the vortex tube and centered at the vortex core near the region of reconnection were computed using Eqns. (3.2.8) and (3.3.1), respectively. The plane is at the center of the indicated box. Figs. (3.4.15b), (3.4.15c), (3.4.15d) and (3.4.15e) show contour plots of the magnitudes of the swirling velocity, axial velocity, out-of-plane vorticity and in-plane (helical-component) vorticity, respectively, and Fig. (3.4.15f) shows the vector plot of the in-plane vorticity vector. Significant axial flow with a magnitude comparable to the swirling component, and maxima coinciding with the center of the helical component of vorticity, can be observed. The minima of the modulus of in-plane velocity, however, does not coincide with the vortex core because of the mean convective velocity of the vortex tube. Fig. (3.4.16) shows the corresponding set of plots at $t = 12.0$. Compared to the plots at $t = 10.5$, the magnitude of the out-of-plane vorticity has increased, indicating continued stretching along the vortex tube; the magnitude of axial flow has also increased, indicating an amplification of the helical modes on the tube.

3.4.2 Case (ii) : Vortex Knots Problem

In this case, the evolution of two vortex rings that are initially interlocked as shown in Fig. (3.4.1b) is computed using the non-linear viscosity scheme. This problem was first suggested to the author's advisor Professor Leonard by Dr. Stanley Corrsin in 1975 and has since been computed by several researchers. Kuwahara (1986) computed the problem using singular vortex particles. He used a very coarse mesh with only 32 particles per vortex ring and added particles as the vortex tubes are stretched. Winckelmans (1989) used smooth vortex particles with the circulation exchange scheme for treating viscous effects. Two additional features, remeshing and relaxation of the divergence of vorticity, were used. In the latter, the strengths of the vortex particles are adjusted periodically such that the vorticity field is almost divergence-free. He computed the flow problem for a relatively short time, stopping the calculation after the rings had come together.

In the present calculation, the following set of parameters are used: $\Gamma_R = 1.0$, $r_R = 1.0$, $\nu_e = 1.25$ and $\Delta t = 0.05$. Figs. (3.4.17a) and (3.4.17b) show two views of the time evolution of the rings. The initial motion consists of uniform translation by self-induction of each vortex tube (putting them on a collision course) plus non-uniform stretching and in-plane deformations (evident by $t = 1$) that are due to the induced velocity of the other tube. The non-uniformity of the stretch is most pronounced where the loops pass through the center of the other loop and the result is a variable core thickness. As a consequence, the thinner sections rotate about the center of the core at a higher angular velocity than that of the thicker sections. This effect produces helical vortex lines and hence, axial flow, as is evident at $t = 2$. The axial flow is such that it tends to reduce the non-uniformity in thickness.

Out-of-plane deformations are quite apparent by $t = 3$. These deformations occur where the tubes are in close proximity, which in turn is a result of their earlier translation. Roughly speaking, the deformations are analogous to the deformation of a straight line lying in the plane normal to a two-dimensional line vortex. Three-dimensional deformations of the space curves of the vortex tubes, as well as the non-uniform axial flows, continue in time. By $t = 5$, a significant section of each tube has been attracted to the corresponding section of the other tube, a situation that persists for all later times. Thus, for most practical purposes, the original pair of vortex rings is effectively reduced to a single tube of vorticity plus an antiparallel double-tube structure. However, as opposed to the first test case, the tubes do not actually pinch off and reconnect, nor is there any significant cancellation of vorticity in the double-tube structure. The double-tube structure appears to evolve in a very complicated fashion, similar to that described in a model for vortex-tube interactions by Siggia (1985) and Pumir and Siggia (1987). The results of these

complicated, self-induced motions are the formation of a convoluted entanglement of filamentary structures and twisted hairpins, similar to that observed by Kida and Takaoka (1987) in their pseudospectral calculation of the problem of a closed, knotted vortex tube, and to that by Melander (1987) in his spectral calculation of two initially orthogonal vortex tubes that attract each other in a fashion similar to that observed here.

CHAPTER 4

Three-Dimensional Unsteady Separated Flow

In this chapter, the three-dimensional, unsteady separated flow past a square plate is studied using a vortex method. Boundary conditions on the plate are enforced using a scheme analogous to that used in Chapter 2 and developed in Sec. (4.1). In Sec. (4.2), a vorticity-shedding scheme that satisfies the solenoidal condition for vorticity is proposed. In Sec. (4.3), the modified vortex particle method developed in Chapter 3, coupled with the boundary-condition scheme and vorticity-shedding scheme, is used to compute the flow past a square plate. The early stage of the flow is studied.

4.1 Wall Boundary Conditions

In this section, the two-dimensional scheme used in Chapter 2 to treat boundary conditions on a flat plate is modified and extended for use in three dimensions. The no-through flow boundary condition is enforced using a pair of equal-sign, finite-area vortex sheets, while no-slip boundary conditions ($u = 0$, $v = 0$) are enforced using a pair of opposite sign vortex sheets. Each vortex sheet is placed at a small distance $\delta\eta_{bl}$ above/below the plate (Fig. 4.1.1) and is represented by discrete vortex elements. The solenoidal condition for vorticity given by Eqn. (3.2.3), which must be satisfied at least approximately, implies using closed vortex loops for such discretizations.

In the current method, rectangular vortex loops, with each straight segment of the loop represented by discrete vortex element, are used. To give a smooth representation of the vorticity field, the vector strength of each vortex element, given by $\underline{\alpha}_{i,j} = \Gamma\delta\underline{l}$, where i and j are the indices of the grid location of the element, Γ is the circulation of the loop and $\delta\underline{l}$ is the vector length of the segment, is distributed over an area of 4×4 grid points. These grid points represent a 2D set of $N_p \times N_p$ equally spaced points on the plate of dimension $L \times L$, with a separation $\delta l_p = L/(N_p - 1)$. The following pyramidal distribution function is used,

$$\frac{\partial^2 \underline{\alpha}(x,y)}{\partial x \partial y} = \frac{\underline{\alpha}_{i,j}}{A} f_x(x, x_i) f_y(y, y_j) \ , \qquad (4.1.1)$$

where $\partial^2 \underline{\alpha}(x, y)/\partial x \partial y$ is the local strength distribution at (x, y), $\underline{\alpha}_{i,j}$ is the net strength of the vortex element at the grid point (i, j), A is the normalization constant,

$$A = \int_{y_{j-2}}^{y_j+2} \int_{x_{i-2}}^{x_i+2} f_x(x', x_i) f_y(y', y_j) dx' dy' \ , \qquad (4.1.2)$$

and the functions f_x and f_y are given by

$$f_x(x, x_i) = \begin{cases} \left(1 + a_x(x - x_i)\right) & \text{if} \quad x_{i-2} < x < x_{i+2} \ ; \\ 0, & \text{otherwise} \ , \end{cases} \qquad (4.1.3a)$$

$$f_y(y, y_i) = \begin{cases} \left(1 + a_y(y - y_i)\right) & \text{if} \quad y_{j-2} < y < y_{j+2} \ ; \\ 0, & \text{otherwise} \ , \end{cases} \qquad (4.1.3b)$$

with

$$a_x = \begin{cases} 1/(x_i - x_{i-2}), & \text{if} \quad x < x_i \ ; \\ 1/(x_i - x_{i+2}), & \text{otherwise} \ , \end{cases} \qquad (4.1.4a)$$

$$a_y = \begin{cases} 1/(y_i - y_{i-2}), & \text{if} \quad y < y_i \ ; \\ 1/(y_i - y_{i+2}), & \text{otherwise} \ . \end{cases} \qquad (4.1.4b)$$

Schematics of the pyramidal distribution given by Eqn. (4.1.1) and the corresponding functions f_x and f_y are given in Fig. (4.1.2). For elements close to the edge where the end points $i \pm 2$ or $j \pm 2$ may be beyond the edge, the step functions,

$$H(x) = \begin{cases} 1 & \text{if } x \in S(x, y); \\ 0, & \text{otherwise}, \end{cases} \qquad (4.1.5a)$$

$$H(y) = \begin{cases} 1 & \text{if } y \in S(x, y); \\ 0, & \text{otherwise}, \end{cases} \qquad (4.1.5b)$$

are imposed on the functions f_x and f_y, respectively (see Fig. 4.1.2c). In the above, $S(x, y)$ indicates the plate domain.

4.1.1 No-through Flow Boundary Condition

For the normal velocity boundary condition, the square loop as shown in Fig. (4.1.3) is used. Each segment of the loop has a length $\delta l = 2\delta l_{\mathrm{p}}$ and is represented by a smooth vortex element with pyramidally distributed strength as described above. To ensure that the matrix of influence coefficients is diagonally dominant, the control point is placed at the center (x_i, y_j) of the loop. With such an arrangement, the boundary condition can be enforced only at interior points but not at points along the edges, giving a total of $N_{\mathrm{c_n}} \times N_{\mathrm{c_n}}$ control points with $N_{\mathrm{c_n}}^2$ simultaneous equations, where $N_{\mathrm{c_n}} = (N_{\mathrm{p}} - 1)/2$.

This arrangement is similar to the dipole panels used in the Boeing LEV Method (Johnson et al. 1975, Johnson 1980) or the NLR VORSEP Method (Hoeijmakers et al. 1982), with the difference that in the previous schemes, the plate is modeled as a singular vortex sheet represented by dipole panels (singular vortex loops), whereas in the current method, smooth vortex elements are placed at a small distance $\delta\eta_{\mathrm{bl}}$ above/below the plate to represent the boundary layers of the plate.

Solution of a square plate normal to flow at $t = 0$ (no wake)

In the following, the scheme is tested on a square plate of dimensions $L \times L$ placed normal to a constant on-coming freestream of $\underline{u} = U_\infty \hat{e}_z$. Both L and U_∞ are taken to be unity. Four calculations with grids of $N_{\mathrm{p}} = 15$, 19, 23 and 27, corresponding to a total number of control points of $N_{\mathrm{c_n}}^2 = 7 \times 7$, 9×9, 11×11 and 13×13, are compared. A smoothing parameter of $\sigma = 0.4\delta l_{\mathrm{p}}$ and vortex sheets displacement of $\delta\eta_{\mathrm{bl}} = \sigma$ are prescribed.

Fig. (4.1.4) shows the $x-$distribution of the velocity component w at different sections between $-0.5 < y < 0$ on the $x - y$ plane, computed using the above-mentioned grids (the plate domain $S(x, y)$ is given by $-0.5 < y < 0.5$ and $-0.5 < x < 0.5$ on the $x - y$ plane). Velocity on sections that go through control points, as well as sections that are halfway between control points, where velocity error is expected to be maximum, are computed. For the potential flow problem, the velocity becomes singular at the edges; in the discretized and smoothed problem, this is manifested as a sharp increase in w at the edge (given by the distribution at $y = -0.5$, indicated by the solid line; and at $x = \pm 0.5$ for other distributions). The magnitude of w at the edge increases with grid resolution and in the limit $N_{\mathrm{p}} \to \infty$ and $\sigma \to 0$, it should become singular (potential flow solution). Fig. (4.1.5) shows the vector field $\underline{\alpha}$ on the boundary layer resulting from the flow. The high intensity

of $\underline{\alpha}$ near the edges is a direct result of the singular behavior of the velocity at the edges.

Using such potential flow calculations, the apparent mass of a square plate can be calculated. This is done by accelerating the plate from rest at constant acceleration and computing the time rate of change of impulse of the vortex sheets to give the body force. At small time, the freestream velocity is small and the impulse that is due to the shed vorticity is negligible and can be ignored. In this case, however, the computations have been carried out with full shedding at the edges, the shedding process of which is described in later sections, and the drag force at $t = 0^+$ is extracted to give the apparent mass effect. This is compared to the analytical results of Meyerhoff (1970) (see Sarpkaya and Isaacson 1981). Fig. (4.1.6) shows a plot of the computed C_d that is due to apparent mass effect for various grid resolutions, together with the analytical value. With increasing resolution, the computed value is observed to approach the analytical results.

4.1.2 No-slip Boundary Conditions

Consider now the tangential velocity boundary conditions. To ensure that the matrix of the influence coefficients is well conditioned and diagonally dominant, a computational segment (referred hereon as the major segment M) is placed directly above/below the control point where the component of tangential velocity, orthogonal to the vortex lines of the segment, is enforced. To satisfy the solenoidal condition of vorticity, six segments of vortex lines, L_1, L_2, L_3, R_1, R_2 and R_3, each with half the circulation of the major segment, are added with three on each side of M, as shown in Fig. (4.1.7). M, L_1, L_2, L_3, R_1, R_2 and R_3 form two complete vortex loops, thus satisfying the solenoidal condition. Each vortex segment is replaced by a smooth vortex element of strength $\underline{\alpha} = \Gamma \delta \underline{l}$, where $\delta \underline{l}$ is the vector length of each individual segment. Therefore, α of M is four times that of L_1, L_3, R_1 and R_3 and twice that of L_2 and R_2. This fact, in essence, leads to a diagonally dominant influence matrix. For major segments near the edges, odd numbered (i.e., 1 or 3) L and R elements sitting directly on the edge are not employed. The vortex lines are assumed to wrap around the plate and connect to the other side. This is a valid assumption, since for every vortex loop on one side of the plate, there is a corresponding opposite sign vortex loop on the other side. (Recall that a pair of opposite sign vortex sheets are used for enforcing the tangential velocity conditions.) With this assumption, the boundary conditions are satisfied at edge points also, giving a total of $N_{c_t} \times N_{c_t}$ control points where $N_{c_t} = (N_p + 1)/2$. In enforcing the no-slip condition for the other tangential component, pairs of vortex loops similar to those

just described, but rotated 90°, are used. Since each loop consists of vortex elements in both x and y directions, the two tangential velocity boundary conditions are coupled and given $N_{c_t}^2$ control points, there are $2N_{c_t}^2$ simultaneous equations.

Solution of a square plate tangential to flow at $t = 0$ (no wake)

In the following, the scheme described above is tested on a square plate placed tangential to the constant, on-coming freestream, $\underline{u} = U_\infty \hat{e}_y$ (zero angle of attack). U_∞ is taken to be unity. With the freestream velocity having only a component that is parallel to the plate surface, the vorticity field on the plate boundary layer is expected to be constant with only a non-zero component perpendicular to the velocity field. However, in satisfying the solenoidal condition, non-zero vorticity in line with the velocity may be generated as an error.

Fig. (4.1.8) shows the $x-$distribution of the velocity component v at various sections between $-0.5 < y < 0$ in the $x - y$ plane, computed using the above-mentioned grids. At large $|x|$, the velocity magnitude approaches the freestream value. As $|x| \rightarrow 0.5$ (the edge), the velocity drops to zero rapidly. This behavior is different from that observed for the normal flow problem because here the tangential velocity field in the potential flow solution is given by a step function, which becomes zero at the edge. This is manifested in the discretized solution as slight oscillations near the edge. As the resolution increases, the locations of these oscillations decrease in wavelength and approach the edge, but the magnitude remains unchanged. At the other interior points, the velocity boundary conditions are very well satisfied.

Fig. (4.1.9) shows the vector field $\underline{\alpha}$ of the boundary layer resulting from the freestream flow, computed using four grids of $N_p = 15, 19, 23$ and 27, corresponding to a total number of control points of $N_{c_t}^2 = 8 \times 8, 10 \times 10, 12 \times 12$ and 14×14. As expected, the almost constant $\underline{\alpha}$ field has a component in the x direction only, with slight perturbations near the corners.

4.2 Shedding Model

To compute flows with vortex shedding, shedding points P_{shv} are defined at all even numbered points along the edges (eg. $i = 2, 4, 6,...$ or $j = 2, 4, 6,...$) and a shedding area, $A_{\mathrm{shv}} = 2\delta l_{\mathrm{p}}^2$, is assigned to each shedding point (see Fig. 4.2.1a). For the shedding point next to a corner, the area is smaller at $1.5\delta l_{\mathrm{p}}^2$, see Fig. (4.2.1b). At each shedding point, the tangential velocity is computed and the component orthogonal to the edge is checked to see if it points into the fluid domain. If so, shedding is considered to have occurred and the area A_{shv} is convected at the local tangential velocity into the flow, using a first-order Euler scheme. At the end of the step, the portion of A_{shv}, which has moved into the fluid domain, referred from here on as a_{shv}, is considered shed and the vector strength $\underline{\alpha}_{\mathrm{shv}}$ within a_{shv} is assigned evenly to N_{par} particles (see Fig. 4.2.2). N_{par} is a prescribed number chosen such that the shed vorticity field is smooth; i.e., there is enough overlap between shed particles. Typically, $N_{\mathrm{par}} > 1$ is used because the core size σ of the vortex elements in the boundary layers are chosen to be less than δl_{p} (such that the matrices of influence coefficients from the boundary conditions is well conditioned), while the separation distance between neighboring shedding points is $2\delta l_{\mathrm{p}}$. Figs. (4.2.3a) and (4.2.3b) show the distributions of v along a shedding edge parallel to the x-axis, computed using $N_{\mathrm{par}} = 3$ and 5, respectively. The flow is that of an impulsively started normal plate at $t = 0.02$. In both cases, $\sigma = \delta l_{\mathrm{p}}/3$. For the first case where there is insufficient overlap of the particle cores, the outward tangential velocity has a "saw-tooth" behavior. Since vortex particles are shed at this velocity, "numerical waves" on shed vortex lines may result. With sufficient overlap, the outward tangential velocity distribution is smooth.

The net shed vector strength $\underline{\alpha}_{\mathrm{shv}}$ is given by the contribution that is due to the portion of the (i, j) vortex element within the area a_{shv}, where (i, j) is the grid location of the shedding point P_{shv}, plus all other contributions from 14 neighboring elements. (Recall that the vector strength of each pyramidal element has its maximum at the center and drops linearly to zero over a distance of 2 grid points in both directions. Also see Fig. 4.2.1.) Equation (3.3.6) is used to account for vorticity stretching within the shedding step. For the shedding point next to a corner, there are only 11 neighboring elements that contribute.

To determine the locations of the N_{par} shed particles, a vector with length $2\delta l_{\mathrm{p}}$ and direction $\underline{\alpha}_{\mathrm{shv}}$ is placed at the location $\underline{x} = \underline{P}_{\mathrm{shv}} + \Delta t\, \underline{u}_t$, where $\underline{P}_{\mathrm{shv}}$ is the shedding point and $\underline{u}_t$ is the tangential velocity computed at $\underline{P}_{\mathrm{shv}}$. The particles are then placed equally spaced on this vector (see Fig. 4.2.4a). This scheme, referred from here on as shedding scheme a, works well when there is little gradient between neighboring $\underline{\alpha}_{\mathrm{shv}}$. However, if there is a steep gradient, e.g., near a corner,

then particles from neighboring shedding points may not be well aligned. Fig. (4.2.5a) shows the vortex particles behind a square plate at $t = 0.15$ (15 steps with $\Delta t = 0.01$). Near the corners the vector particles are not "well connected" because of the steep gradients in $\underline{\alpha}_{\text{shv}}$. To correct for this problem, shedding scheme b is proposed. In this scheme, N_{par} equally spaced points, referred from here on as P_{par}, are assigned along the edge of the shedding area A_{shv} and the tangential velocity is computed at each of these points. Given the tangential velocity at $\underline{P}_{\text{shv}}$, which is outwardly pointing, the corresponding tangential velocity at each P_{par} may or may not be outwardly pointing. If it is found to be outwardly pointing, then the particle associated with that point is shed at the computed tangential velocity and its new location computed using Euler integration (see Fig. 4.2.4b). The stretching of vorticity of each individual particle is computed using the local velocity gradient at each P_{par}. Fig. (4.2.5b) shows the results computed using shedding scheme b. With this improved scheme, the particles are "well connected" even in the neighbourhood of the corners where the gradient of $\underline{\alpha}_{\text{shv}}$ is steep.

After the shedding step, the solenoidal condition of the shed vorticity must be enforced. To do this, attached elements are placed at grid points along the edge. These attached elements are basically of the same type as the elements used for enforcing boundary conditions, with the difference that they are not deleted at the end of each time step. For the vector strength $\underline{\alpha}_{\text{shv}}$ shed from the (i, j) shedding point, the corresponding strength of $-\underline{\alpha}_{\text{shv}}$ is assigned to the attached element at the same grid point. To complete the loop, components orthogonal to $\underline{\alpha}_{\text{shv}}$ but with their magnitude reduced by $\delta l_{\text{shv}}/(2\delta l_{\text{p}})$, where δl_{shv} is the outward displacement of the shedding area A_{shv}, are assigned to the attached elements at $(i - 1, j)$ and $(i + 1, j)$ (see Fig. 4.2.6).

At each time step, the portion of $\underline{\alpha}_{\text{att}}$ (vector strength of attached element) that is within the area a_{shv} is lumped, together with those of the regular edge element, into the shed vector strength $\underline{\alpha}_{\text{shv}}$. The portion that is not shed is retained (recall that for the regular edge element, the portion that is not shed is effectively deleted and the new strength is computed at the next time step by enforcing the appropriate boundary conditions). However, these attached elements are, in some sense, already connected to particles in the wake and satisfy the solenoidal condition; therefore, no additional negative or orthogonal vector strength need be added at the attached element because of this portion of the shed vector strength.

4.3 Numerical Results

In this section, the modified vortex particle method of Chapter 3, coupled with the schemes described in Sec. (4.1) and (4.2), is used to compute the problem of separated flow past a square plate.

The plate with dimensions $L \times L$ is placed centered at the origin and normal to the z axis. A freestream with $\underline{u} = U_\infty \hat{e}_z$ is impulsively started at $t = 0$. The parameters used are $N_p = 25$, $N_{par} = 5$, $\sigma = 0.016$, $\delta\eta_{bl} = \sigma$ and $\Delta t = 0.01$. Time integration is computed using the second-order Adams-Bashforth integration scheme. To reduce computational time, the symmetry of the flow is exploited and velocity integration is carried out for $1/8$ of the total number of vortices only. Calculation is carried out to $t = 0.4L/U_\infty$.

Fig. (4.3.1) shows three different views of the time sequence of the shed vortex sheet behind the plate. At an early time of $t = 0.1$, the vortex lines remain almost parallel to the edge, even away from the plate, with little or no apparent roll-up. Later in time, vortex lines away from the corners are observed to roll up into tight rollers ($t = 0.2$) which become stronger (thicker) as more vortex particles are shed into the flow ($t = 0.4$). At the corner, because of the plate configuration, the vortex line has to turn sharply, resulting in steep vorticity and velocity gradients. This leads to strong stretching of vorticity with little or no vortex roll-up. For an alternative visualization, streakline plots (represented by vortex particles shed from the same shedding point) are used. Fig. (4.3.2) shows the streaklines at different shedding points along the edge of the plate at $t = 0.2$. In these plots, the half length of the edge is divided into 6 sections, and the vortex particles shed from points within each section are plotted in Figs. (4.3.4a) - (4.3.4f)†. For the section next to the symmetry plane (Fig. 4.3.4a), roll-up of the vortex sheet is apparent with the streaklines remaining almost parallel to the $y - z$ plane. Thus at this time, the flow in this region has little or no lateral component. Away from the symmetry plane, the streaklines are observed to roll toward the symmetry plane, forming a tilted spiral. At the corner, because of the interference between the two shear layers shed from the two orthogonal edges, a streakline leaves the edge at an angle of $45°$ to the vertical. Fig. (4.3.3) shows the same set of plots at $t = 0.4$. At this later time, the portion of shear layer near the symmetry plane has rolled up into a tight vortex. However, slight lateral displacement of the streaklines can be observed. For sections away from the symmetry plane, strong lateral displacement, especially in the vortex core, can be observed, indicating strong axial flow within the core of the

---

† There are 6 shedding points within each section; thus 6 streaklines are shown in each plot.

vortex. The flow is highly three-dimensional and indicates the importance of the corner or end effect of the plate even at a very early time.

Fig. (4.3.5) shows the in-plane velocity vector field at $t = 0.2$, computed at six different sections at $x = 0.0, 0.1, 0.2, 0.3, 0.4$ and 0.45, all of which are orthogonal to the plate (Fig. 4.3.4). For sections near the symmetry plane (i.e., sections at $x = 0, 0.1$ and 0.2), the in-plane velocity fields are almost identical, indicating that the flow away from the corner is quite two-dimensional. The shear layer at these sections roll up in a similar fashion to that of the two-dimensional case discussed in Chapter 2. Away from the symmetry plane ($x = 0.4, 0.45$), no vortex roll-up is apparent, but thinning of the vortex sheet, indicated by the reduced vortex particle density, can be observed. Fig. (4.3.6) shows the corresponding plots at $t = 0.4$. For sections near the symmetry plane, the rolled-up vortex behind the plate has grown larger as more vorticity is shed into the fluid. For the section at $t = 0.3$, thickening of the shear layer can be observed. This is because of the strong stretching effect at the corner, which tends to pull the vortex sheet away from the corner. A major portion of the stretched vortex sheet is deposited in a region slightly away from the corner (i.e., $x = 0.3$) where the stretching effect is insignificant. In Fig. (4.3.7), the symmetry plane velocity vector plots at $t = 0.2$ and 0.4 are compared to the corresponding plots from a two-dimensional calculation. At both times, the 2D vortex pair is stronger and larger, because of the higher flow speed at the edges of the plate, in turn because of larger blockage of the two-dimensional plate.

CHAPTER 5
Summary and Conclusions

In this thesis, the problems of unsteady and separated flows in two and three dimensions are investigated through vortex simulations and the work presented in previous chapters are summarized as follows:

- Contributions to the problem of two-dimensional separated flow past a normal flat plate are made. Although this problem has been studied previously by many researchers, several difficulties remain and are dealt with in the present work. They are:

  - Singularities are present at the edges of the plate.

  - With only the inviscid boundary condition enforced and no boundary layers at the plate, shedding of vorticity (separation of boundary layers) cannot be represented correctly.

  - Boundary layer separation sometimes occurs on both sides of a sharp edge while at other times, it only occurs on the upstream side (i.e. at early stage of potential start-up flow or beginning of each new Strouhal cycle, as described in Sec. 2.5.1.6). The two situations cannot be differentiated with previous methods since there are no boundary layers at the plate.

  - With some previous methods, after vorticity is shed into the flow, it is difficult to choose the location and strength of a new vortex without introducing some form of ad-hoc assumptions.

  - Only one sign of vorticity is represented in the shear layer.

In the current work, a new method designed to deal specifically with the above difficulties is developed and the following are some of the improved features:

  - Both no-through flow and no-slip boundary conditions are enforced, allowing the representation of boundary layers on both sides of the plate.

- In the absence of a mapping and with no-slip boundary condition enforced, singularities at the edges of the plate are eliminated and the Kutta condition is implicitly satisfied.

- With boundary layers at the plate, representation of the shedding of vorticity follows naturally as the convection of the boundary layer vorticity into the fluid.

- Two separation points, one on each side of an edge, are specified and shedding from one or both points are allowed.

- Both signs of vorticity are included in the separated shear layer.

• Contributions to the understanding of the process leading to the onset of the asymmetric shedding mode of the two-dimensional flat plate flows are made. Due to small perturbations in the flows, the attached symmetric vortex-pair, which is formed at the early stage of the flow, become asymmetric. As the stronger vortex of the pair grows, it displaces and compresses the weaker vortex; as the "compression" progresses, the zero streamline which separates the two vortices approaches that which forms the outer edge of the weaker vortex, and as the two comes into contact, a saddle point is formed which eventually leads to the roll-up of the shear layer and the onset of asymmetric shedding.

• Contributions to the understanding of the asymmetric shedding mechanism in flow past a two-dimensional flat plate are made. In the asymmetric shedding flow, as a vortex structure grows, it displaces the stagnation point on the back face of the plate. As the stagnation point passes through a separation point, it induces reversed flow and suppresses separation from the back side of the edge; also, a saddle point is formed as the two zero streamlines come into contact and this causes the shear layer to roll up. The rolled-up vortex sets up a feed-back system which increases the circulation flux sharply and starts off a new Strouhal cycle.

• Comparison of computed drag on a two-dimensional normal flat plate to experiments showed significant discrepancy. Such discrepancies are not restricted to the present study but are observed in other vortex calculations and Navier-Stokes calculations. Imposing lateral forcing with small amplitude reduces the discrepancy significantly while streamwise forcing (acceleration) eliminates it. Since external forcing is expected to reduce three-dimensional effects in the laboratory flows, it is concluded that such effects played important roles in contributing to the observed discrepancies.

- An improved three-dimensional vortex particle method is developed. The method is designed specifically for high Reynolds number flows with strong interactions of vortex tubes. In this method, a non-linear viscosity model is used to account for small scale effects and dipole elements are used to represent close pairs of opposite-sign vortex particles. Remeshing of particles is implemented where excessive stretching of vorticity takes place. The method is tested successfully on two flows involving the interactions of vortex rings. In these simulations, phenomena typically observed in complex high Reynolds number flows, such as core deformations, internal core structures, axial flows, helical twisting of vortex filaments, complex evolution of vortex filaments, formation of hairpin structures and vortex merging, are observed. Qualitative comparison to flow visualization experiments is encouraging and it is concluded that the proposed method is robust and suitable for complex high Reynolds number flow simulations.

- Extension of the two-dimensional method for enforcing boundary conditions on a flat plate to three dimensions is made. In this method, vortex elements are placed on both sides of the plate and all three components of velocity are set to zero at the plate. In addition, the solenoidal condition of vorticity is satisfied through the use of closed loop elements. For shed vortex elements, additional attached elements are added to explicitly enforce the solenoidal condition. The method is tested on the start up flows of a square plate placed normal or tangential to the flow direction and the solutions are shown to be well behaved. Applications to the flow past a normal square plate is carried out and the early stage of the flow is studied.

For future work, several suggestions are in order:

- In the present work, the boundary layers at the plate are represented by vortex panels. These elements give smooth vorticity distribution but are computationally intensive. For more efficient use of computational resources, it is suggested that the inner region of boundary layer by represented by 'cheap' vortex blobs while at the edge where shedding occur, stack with large number of panels could be used to give a high resolution vorticity (and velocity) profile in this region (i.e. fine resolution where it is needed and coarse where it is not). Also, some form of time dependence of the boundary layer thickness can be incorporated into the method. This can be done, for instance, by first enforcing the inviscid boundary condition on the plate using singular vortex panels. The resulting velocity distribution on the plate is then used as input to Thwaite's equation, which is integrated from a stagnation point to give the distribution of boundary layer thickness on the plate. The boundary layers, with the computed thickness

distribution, are then discretized into layers of smooth vortex panels and the velocity boundary conditions enforced as described in Chapter 2.

- Separated flows with external forcing are a class of flows which are particularly interesting because they can be controlled in such a manner that certain features of the flows can be isolated and studied. In the present study, several forced flows have been examined but this is just 'a tip off the iceberg' and many other form of forcing remain to be studied. One flow which is particularly interesting is that which involves both lateral and streamwise forcing. At large time, this would give an accelerating flow with asymmetric shedding, which is particularly interesting especially as a comparison tool.

- The question of how important is three-dimensionality in the wake of a two-dimensional flat plate can be answered by doing a full three-dimensional calculation of the supposedly 'two-dimensional' problem. This can be done by computing the flow past a rectangular plate with periodic boundary conditions similar to those used by Inoue (1989) in his calculations of three-dimensional, spatially developing shear layer.

- For large-time three-dimensional separated flow calculations, it is recommended that simple vortex elements such as spherical vortex particles or smooth vortex lines be used to represent the vortex sheets at the plate. The elements used in the present work give smooth vorticity field but involve complicated functions and are costly to evaluate.

References

Abernathy, F. H. 1962. *Flow over an inclined flat plate.* J. Basic Eng., Trans. ASME D **84**, 380.

Almosnino, D. 1985. *High angle of attack calculations of the subsonic vortex flow on slender bodies.* AIAA Journal **23**, No. 8, 1150.

Anderson, C. and Greengard, C. 1984. *On vortex methods.* SIAM J. Numer. Analysis **22**, 413.

Ashurst, W. T. and Meiburg, E. 1985. *Three-dimensional shear layers via vortex dynamics.* Sandia Nat. Lab., Livermore, SAND85-8777.

Ashurst, W. T. and Meiron, D. I. 1987. *Numerical study of vortex reconnection.* Phys. Rev. Letters **58**, No. 16, 1632.

Basu, B. C. and Hancock, G. J. 1978. *The unsteady motion of a two-dimensional aerofoil in incompressible inviscid flow.* J. Fluid Mech. **87**, Part 1, 159.

Basuki, J. and Graham, J. M. R. 1987. *Discrete vortex computation of separated airfoil flow.* AIAA Journal **255**, No. 11, 1409.

Batchelor, A. K. 1967. *Introduction to Fluid Dynamics.* Cambridge University Press, London.

Beale, J. T. and Majda, A. 1982a. *Vortex methods. I: Convergence in accuracy in two and three dimensions.* Math. Comp. **39**, 1.

Beale, J. T. and Majda, A. 1982b. *Vortex methods. II: Higher-order accuracy in two and three dimensions.* Math. Comp. **39**, 29.

Beale, J. T. 1986a. *On the accuracy of vortex methods at large times.* Proceedings of the Workshop on Computational Fluid Dynamics and Reacting Flows, IMA, University of Minnesota.

Beale, J. T. 1986b. *A convergent 3D vortex method with grid-free stretching.* Math. Comp. **46**, 401.

Birkhoff, G. 1962. *Helmholtz and Taylor instability.* Proc. Symp. Appl. Math., Amer. Math. Soc. **XIII**, 55.

Chein, R. and Chung, J. N. 1988. *Discrete-vortex simulation of flow over inclined and normal plates.* Computers and Fluids **16**, No. 4, 405.

Choquin, J. P. and Cottet, G. H. 1988. *Sur l'analyse d'une classe de méthodes de vortex tridimensionnelles.* C. R. Acad. Sci. Paris **306**, Série I, 739.

Chorin, A. J. 1973. *Numerical study of slightly viscous flow.* J. Fluid Mech. **57**, 785.

Clements, R. R. 1973. *An inviscid model of two-dimensional vortex shedding.* J. Fluid Mech. **57**, 321.

Clements, R. R. and Maull, D. J. 1975. *The representation of sheets of vorticity by discrete vortices.* Prog. Aerospace Sci. **16**, 129.

Cortelezzi, L. and Leonard, A. 1990. *Private communication.* California Institute of Technology.

Cottet, G. H. 1982. *Méthode particulaire pour l'équation d'Euler dans le plan.* Thèse de 3ème cycle. Université Paris IV.

Cottet, G. H. 1988. *A new approach for the analysis of vortex methods in two and three dimensions.* Ann. Inst. Henri Poincaré **5**, 227.

Couet. B. and Spalart, P. R. 1982. *Simulation of the vortex emission behind a pair of bluff bodies by a vortex tracing algorithm.* Proceedings of the International ASME Conference on Modeling and Simulation, Paris-Sud 81.

Crighton, D. G. 1985. *The Kutta condition in unsteady flow.* Ann. Rev. Fluid Mech. **17**, 411.

Daniels, P. G. 1978. *On the unsteady Kutta condition.* Q. J. Mech. Appl. Math. **31**, 49.

Degond, P. and Mas-Gallic, S. 1988. *The weighted particle method for convection-diffusion equations - part I: the case of an isotropic viscosity.* To appear in *Math. Comp.*

Dushane, T. E. 1973. *Convergence for a vortex method for solving Euler's equation.* Math. Comp. **27**, 719.

Dutta, P.K. 1988. *Discrete vortex method for separated and free shear flows.* Ph.D. Thesis, Indian Institute of Science, Bangalore, India.

Fage, A. and Johansen, F.C. 1927. *On the flow of air behind an inclined flat plate of infinite span.* Proc. Roy. Soc. A **116**, 170.

Fink, P. T. and Soh, W. K. 1974. *Calculation of vortex sheets in unsteady flow and applications in ship hydrodynamics.* Proceedings of The 10th Symp. Nav. Hydrodyn., Cambridge, Mass. 463.

Flachsbart, O. 1932. *Messungen an ebenen und gewölbten platten.* Ergben. Aerodyn. Versuchsanstalt Göttingen **4**, 96.

Fohl, T. and Turner, J. S. 1975. *Colliding vortex rings.* Phys. of Fluids **18**, No. 4, 433.

Freymuth, P. 1988. *Propulsive vortical signature of plunging and pitching airfoils.* AIAA Journal **26**, No. 7, 881.

Goodman, J., Hou, T. Y. and Lowengrub, J. 1989a. *Convergence of the point vortex method for the 2D Euler equations.* To appear in *CPAM*.

Goodman, J., Hou, T. Y. and Lowengrub, J. 1989b. *Convergence of vortex blob methods with small blobs for the Euler equations.* In preparation.

Hald, O. H. and Del Prete, V. M. 1978. *Convergence of vortex methods for Euler's equations.* Math. Comp. **32**, 791.

Hald, O. H. 1979. *Convergence of vortex methods for Euler's equations.* SIAM J. Num. Analysis **16**, 726.

Ham, N. D. 1968. *Aerodynamic loading on a two-dimensional airfoil during dynamic stall.* AIAA Journal **6**, No. 10, 1927.

Hoeijmakers, H. W. M., Vaatstra, W. and Verhagen, N. G. 1982. *On the vortex flow over delta and double delta wings.* AIAA-82-0949.

Inamuro, T. 1988. *Numerical simulation of separated flow by discrete vortex method.* In Japanese, translation as: Flow **7**, 104.

Inamuro, T., Adashi, T. and Sakata, H. 1983. *A numerical analysis of unsteady separated flow by vortex shedding model.* Bulletin of JSME **26**, No. 222, 2106.

Inoue, O. and Kuwahara, K. 1985. *A new approach to flow problems past a screen.* AIAA-85-1645.

Inoue, O. 1989. *Vortex simulation of spatially growing three-dimensional mixing layers*. AIAA Journal **27**, No. 11, 1517.

Izutsu, N., Oshima, K. and Oshima, Y. 1987. *Experimental study of interacting vortex rings*. Inst. Space and Astron. Sci. SP **5**, 3.

Johnson, F. T., Lu, P., Brune, G. W., Weber, J. A. and Rubbert, P. E. 1975. *Three-dimensional solution of flows over wings with leading-edge vortex separation*. AIAA-75-866.

Johnson, F. T. 1980. *A general panel method for the analysis and design of arbitrary configurations in incompressible flows*. NASA Contractor Report 3079.

Kambe, T. and Takao, T. 1971. *Motion of distorted vortex rings*. J. Phys. Soc. Japan **31**, No. 2, 591.

Kandil, O. A., Chu, L. C. Tureaud, T. 1984. *A nonlinear hybrid vortex method for wings at large angle of attack*. AIAA Journal **22**, No. 3, 329.

Katz, J. 1984. *Lateral aerodynamics of delta wings with leading-edge separation*. AIAA Journal **22**, No. 3, 323.

Kida, S. and Takaoka, M. 1987. *Bridging in vortex reconnection*. Phys. Fluid **30**, No. 10, 2911.

Kiya, M. and Arie, M. 1977. *A contribution to an inviscid vortex-shedding model for an inclined flat plate in uniform flow*. J. Fluid Mech. **82**, Part 2, 223.

Kiya, M., Arie, M. and Harigane, K. 1979. *Unsteady separated flow behind a normal plate calculated by a discrete-vortex model*. Memoirs of the Faculty of Engineering, Hokkaido University **15**, Part 2, 211.

Kiya, M. and Arie, M. 1980. *Discrete-vortex simulation of unsteady separated flow behind a nearly normal plate*. Bull. JSME **23**, 1451.

Kiya, M., Sasaki, K. and Arie, M. 1982. *Discrete-vortex simulation of a turbulent separation bubble*. J. Fluid Mech. **120**, 210.

Koochesfahani, M. M. 1987. *Vortical pattern in the wake of an oscillating airfoil*. AIAA-87-0111.

Krasny, R. 1986. *A study of singularity formation in a vortex sheet by the point-vortex approximation*. J. Fluid Mech. **167**, 65.

Kuwahara, K. 1973. *Numerical study of flow past an inclined flat plate by an inviscid model.* J. Phys. Soc. Japan **35**, 1545.

Kuwahara, K. 1986. *Studies on vortex motion based on the dividing vorton model.* Inst. Space and Astron. Sci. Rep. SP **4**, 11.

Kuwahara, K. 1989. *Private communication.* Inst. Space and Aero. Science, Tokyo, Japan.

Lamb, H. 1945. *Hydrodynamics.* Dover Publications, New York.

Leonard, A. 1975. *Numerical simulations of interacting, three-dimensional vortex filaments.* Proceedings of the 4th International Conference on Numerical Methods in Fluid Dynamics, Colo., Heidelberg.

Leonard, A. 1980a. *Vortex methods for flow simulation.* J. Comput. Phys. **37**, 289.

Leonard, A. 1980b. *Vortex simulation of three-dimensional spotlike disturbances in a laminar boundary layer.* Turbulent Shear Flows II, Springer-Verlag, Berlin/Heidelberg. p.67.

Leonard, A. 1985. *Computing three-dimensional incompressible flows with vortex elements.* Ann. Rev. Fluid Mech. **17**, 523.

Lilly, D. K. 1962. *On the numerical simulation of buoyant convection.* Tellus **14**, 148.

Lilly, D. K. 1966. *On the application of the eddy viscosity concept in the inertia sub-range of turbulence.* NCAR Manuscript No. 123.

Lisoski, D. and Roshko, A. 1989. *Private communication.* California Institute of Technology.

Matsushita, M., Murata, S. and Akamatsu, T. 1984. *Studies on boundary layer separation in unsteady flows using an integral method.* J. Fluid Mech. **149**, 477.

Maull, D.J. 1979. *An Introduction to Discrete Vortex Method.* IUTAM/IAHR, Karlsruhe.

McCroskey, W. J., Spalart, P. R., Laub, G. H., Maisel, M. D. and Maskew, B. 1985. *Airloads on bluff bodies with application to rotor-induced downloads on tilt-rotor aircraft.* Vertica **9**, No. 1, 1.

Melander, M. V. 1987. *Fundamental processes in 2D and 3D incompressible vortex dynamics*. Bull. Am. Phys. Soc. **32**, No. 10, 2123.

Meyerhoff, W. K. 1970. *Added masses of thin rectangular plates calculated from potential theory*. J. Ship Res. **14**, 100.

Milne-Thomson, L. M. 1938. *Theoretical Hydrodynamics*. MacMillan and Co., London.

Moore D. W. 1971. *The discrete approximation of a vortex sheet*. California Inst. of Tech. Rep. AFOSR-1084-69.

Moore, D. W. 1974. *A numerical study of the roll-up of a finite vortex sheet*. J. Fluid Mech. **63**, 225.

Mosher, M. C. 1985. *A method for computing three-dimensional vortex flows*. Z. Flugwiss. Weltraumforsch **9**, Heft 3, 125.

Mostafa, S. M. 1987. *Numerical simulation of unsteady separated flows*. Ph. D. thesis, Naval Postgraduate School.

Mostafa, S. M., Munz, P., Sarpkaya, T. and Strickland, J. H. 1989. *Numerical simulation of unsteady flows about cambered plates*. AIAA-89-0290.

Munz, P. 1987. *Unsteady flow about cambered plates*. M.S. thesis, Naval Postgraduate School.

Oshima, Y. and Asaka, S. 1977. *Interactions of two vortex rings along parallel axes in air*. J. Phys. Soc. Japan **42**, No. 2, 708.

Orszag, S. A. and Crow, S. C. 1970. *Instability of a vortex sheet leaving a semi-infinite plate*. Stud. Appl. Math. **49**, 167.

Osswald, G. A., Ghia, K. N. and Ghia, U. 1985. *An implicit time-marching method for studying unsteady flow with massive separation*. AIAA-85-1489.

Parekh, D. E., Leonard, A. and Reynolds, W. C. 1983. *A vortex filament simulation of a bifurcating jet*. Bull. Am. Phys. Soc. **28**, 1353.

Park, W. C. 1989. *Computation of Flow past Single and Multiple Bluff Bodies by a Vortex Tracing Method*. Ph. D. thesis, University of Minnesota.

Pullin, D. I. 1978. *The large-scale structure of unsteady self-similar rolled-up vortex sheets.* J. Fluid Mech. **88**, Part 3, 401.

Pullin, D. I. and Perry, A. E. 1980. *Some flow visualization experiments on the starting vortex.* J. Fluid Mech. **97**, Part 2, 239.

Pumir, A. and Siggia, E. D. 1987. *Vortex dynamics and the existence of solutions to the Navier-Stokes equations.* Phys. Fluid **30**, 1606.

Raghavan, V., McCroskey, W. J., Van Dalsem, W. R. and Baeder, J. D. 1990. *Calculations of the flow past bluff bodies, including tilt-rotor wing sections at $\alpha = -90°$.* AIAA-90-0032.

Rehbach, C. 1978. *Numerical calculation of three-dimensional unsteady flows with vortex sheets.* AIAA-78-111 (also La Recherche Aérospatiale, Sep.-Oct., 1977, 289).

Rogers, S. E. and Kwak, D. 1988. *An upwind differencing scheme for the time-accurate incompressible Navier-Stokes equations.* AIAA-88-2583.

Rosenhead, L. 1931. *The formation of vortices from a surface of discontinuity.* Proc. Roy. Soc., Ser. A **134**, 170.

Roshko, A. 1954. *On the drag and shedding frequency of two-dimensional bluff bodies.* NACA-TN-3169.

Rott, N. 1956. *Diffraction of a weak shock with vortex generation.* J. Fluid Mech. **1**, 111.

Saffman, P. G. and Baker, G. R. 1979. *Vortex interactions.* Ann. Rev. Fluid Mech. **11**, 95.

Saffman, P. G. and Meiron, D. I. 1986. *Difficulties with three-dimensional weak solutions for inviscid incompressible flows.* Phys. Fluid **29**, No. 8, 2373.

Sarpkaya, T. 1975. *An inviscid model of two-dimensional vortex shedding for transient and asymptotically steady separated flow over an inclined plate.* J. Fluid Mech. **68**, Part 1, 109.

Sarpkaya, T. and Isaacson, M. 1981. *Mechanics of wave forces on offshore structures.* Van Nostrand Reinhold Co., New York. pp. 49..

Sarpkaya, T. and Kline, H.K. 1982. *Impulsively started flow about four types of bluff bodies.* J. Fluids Eng. **104**, 207.

Sarpkaya, T. 1989. *Computational methods with vortices - The 1988 Freeman Scholar lecture.* J. Fluid Eng. **111**, Part 1, 5.

Sarpkaya, T., Mostafa, S. M. and Munz, P. D. 1990. *Numerical simulation of unsteady flow about cambered plates.* J. Aircraft **27**, No. 1, 51.

Schatzle, P. R. 1987. *An experimental study of fusion of vortex rings.* Ph. D. thesis, California Institute of Technology.

Shirayama, S. and Kuwahara, K. 1984. *Vortex method in three-dimensional flows.* Proceedings of the Ninth International Conference on Numerical Methods in Fluid Dynamics, Saclay, France.

Siggia, E. D. 1985. *Collapse and amplification of a vortex filament.* Phys. Fluid **28**, No. 3, 794.

Skomedal, N. G. 1985. *Application of a vortex tracking method to three-dimensional flow past lifting surfaces and blunt bodies.* Ph.D. thesis, The University of Trondheim, Trondheim, Norway.

Smagorinski, J. 1963. *General circulation experiments with the primitive equations:I. The basic experiment.* Monthly Weather Rev. **91**, 99.

Smagorinski, J., Manabe, S. and Holloway, J. L. 1965. *Numerical results from a nine-level general circulation model of the atmosphere.* Monthly Weather Rev. **93**, 727.

Spalart, P. R. and Leonard, A. 1981. *Computation of separated flows by a vortex-tracing algorithm.* AIAA-81-1246.

Spalart, P. R. 1982. *Numerical simulation of separated flows.* Ph. D. thesis, Stanford University.

Spalart, P. R., Leonard, A. and Baganoff, D. 1983. *Numerical simulation of separated flows.* NASA-TM-84328.

Spalart, P. R. 1984. *Two recent extensions of the vortex method.* AIAA-84-0343.

Spalart, P. R. 1985. *Simulation of rotating stall by the vortex method.* J. Propulsion **1**, 3, 235.

Speziale, C. G., Sisto, F. and Jonnavithula, S. 1986. *Vortex simulation of propagating stall in a linear cascade of airfoils.* J. Fluids Eng. **108**, 304.

Stansby, P. K. and Dixon, A. G. 1982. *The importance of secondary shedding in two-dimensional wake formation at very high Reynolds number.* Aero. Quart. **33**, Part 2, 105.

Takaki, R. and Hussain, A. 1986. *Theoretical study of strong interaction of vortex filaments.* Inst. Space and Astron. Sci. Rep. SP **4**, 3.

Takami, H. 1964. *A numerical experiment with discrete vortex approximation with reference to the rolling up of a vortex sheet.* Stanford Univ. Rep. SUDAFR 202.

Taneda, S. and Honji, H. 1971. *Unsteady flow past a flat plate normal to the direction of motion.* J. Phys. Soc. Japan **30**, 262.

Toebes, G. H. 1969. *The unsteady flow and wakes near an oscillating cylinder.* J. Basic Engr. **91**, 493.

Tokumaru, P. and Dimotakis, P. E. 1988. *Private communication.* California Institute of Technology.

Van Dommelen, L. L. and Shen, S. F. 1980. *The spontaneous generation of the singularity in a separating laminar boundary layer.* J. Comp. Phys. **38**, 125.

White, F. M. 1974. *Viscous fluid flow.* McGraw Hill, Inc., New York.

Winckelmans, G. and Leonard, A. 1988a. *Improved vortex methods for three-dimensional flows.* Proceedings of the SIAM Workshop on Vortex Dynamics, Leesburg, Virginia.

Winckelmans, G. and Leonard, A. 1988b. *Weak solutions of the three-dimensional vorticity equation with vortex singularities.* Phys. Fluid **31**, No. 7, 1838.

Winckelmans, G. 1989. *Topics in vortex methods for the computation of three- and two-dimensional incompressible unsteady flows.* Ph. D. thesis, California Institute of Technology.

Yamashita, A. and Oshima, Y. 1988. *Vortex filament simulation for the crosslinking rings.* Inst. Space and Astron. Sci. SP **6**, 13.

Zawadzki, I. and Aref, H. 1989. *Simulation of vortex ring reconnection using a vortex-in-cell method.* Bull. Am. Phys. Soc. **34**, No. 10, 2295.

Method	Reference	Cd	St	Re
vortex calc.	present	3.6	0.11	$10^{4\,(1)}$
"	Kuwahara (1973)	3.0-4.0	N.A.	N.A.
"	Sarpkaya (1975)	$2.4^{(2)}$	0.154	N.A.
"	Kiya and Arie (1980)	2.4-2.8	0.14-0.16	N.A.
"	Spalart et. al. (1983) $^{(3)}$	3.5	N.A.	10^7
"	Chein & Chung (1988)	2.8	0.14	N.A.
"	Dutta (1988)	3.39	0.154	N.A.
"	Park (1989) $^{(3)}$	2.53	0.165	$2.5 \times 10^4 - 1.0 \times 10^6$
Navier-Stokes calc.	Roger and Kwak (1988) $^{(3)}$	1.58	N.A.	200
"	Raghavan et. al. (1990) $^{(3)}$	2.8	0.15	200
wind tunnel expr.	Fage & Johansen (1927)	1.84	0.146	1.5×10^5
"	Flaschbart (1932)	1.96	0.146	$6.0 \times 10^3 - 6.0 \times 10^5$
"	Roshko (1954)	1.74	0.135	$4.0 \times 10^3 - 1.0 \times 10^4$
"	Abernathy (1962)	N.A.	0.150	N.A.
water tunnel expr.	Sarpkaya and Kline (1982)	2.2	N.A.	2.1×10^4
tow tank expr.	Lisoski and Roshko (1989)	2.0-2.1	0.133	5×10^3

(1) Based on estimate of boundary layer thickness at separation.
(2) Computed flat plate at $\alpha = 80$.
(3) Flat plate modelled as finite thickness body normal to flow.

Table (2.1) Comparison of calc. and expt. of an impulsively started normal flat plate.
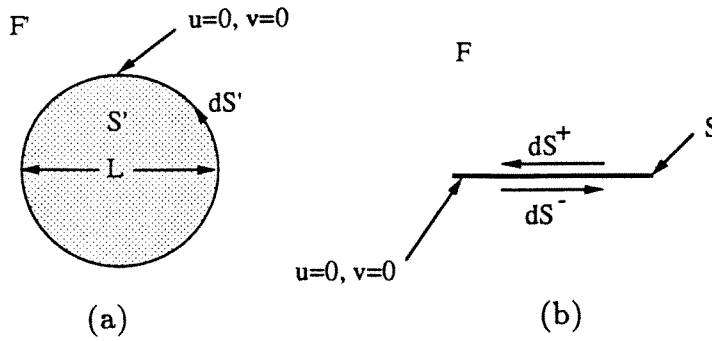
FIGURE (2.2.1) Schematic showing (a) the finite-thickness body S' in a fluid F'; (b) the zero-thickness flat plate S in a fluid F.
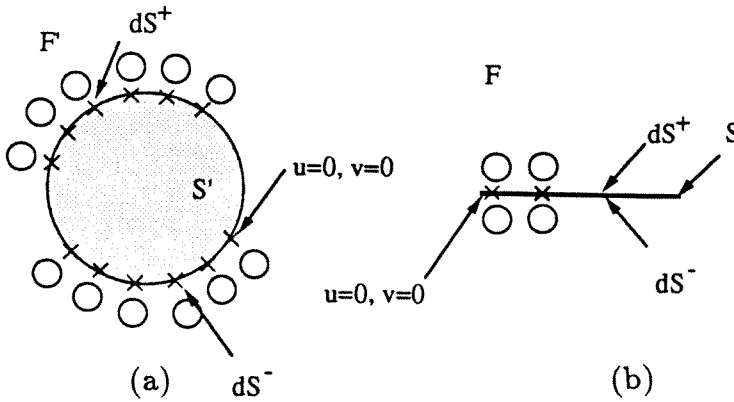
FIGURE (2.3.1) Schematic showing the boundary vortex elements and control points on the wall of (a) the finite-thickness body S' ; (b) the zero-thickness flat plate S.
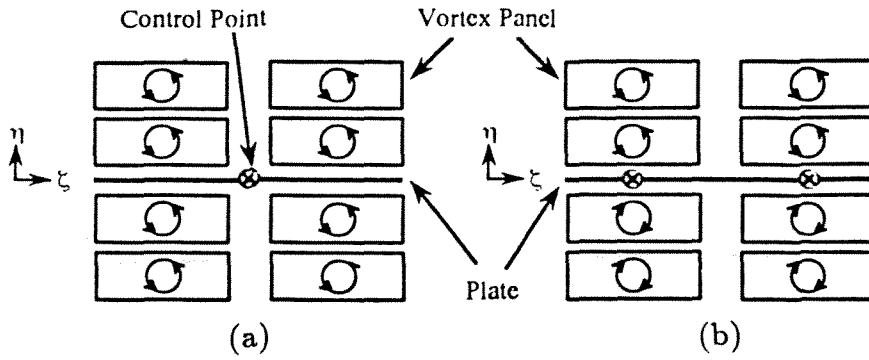
FIGURE (2.3.2) Schematic showing the arrangement of boundary vortex elements and control points for (a) the no-through flow boundary condition; (b)the no-slip boundary condition.

(a)
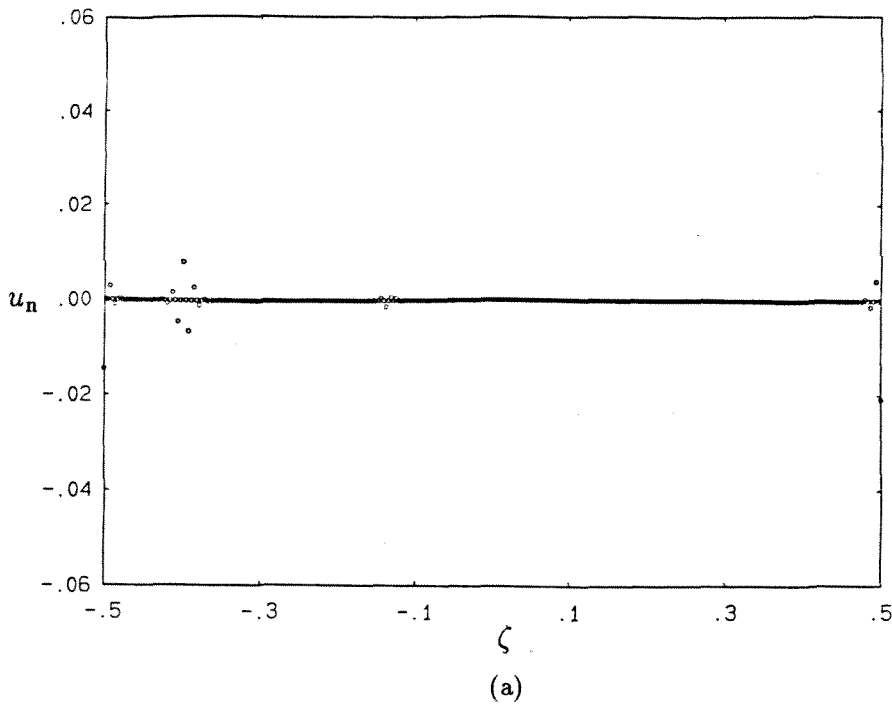
FIGURE (2.3.3) Velocity distribution on an impulsively started normal flat plate at $t = 10$, boundary conditions enforced using scheme a of Sec. (2.3.1.1). (a) u_n; (b) u_t; (c) visualization of vortex particles.

(b)

(c)
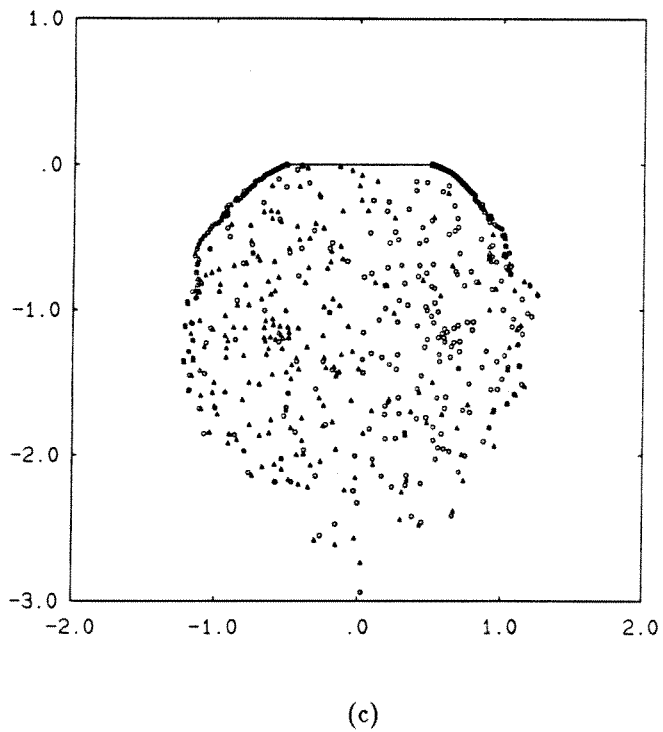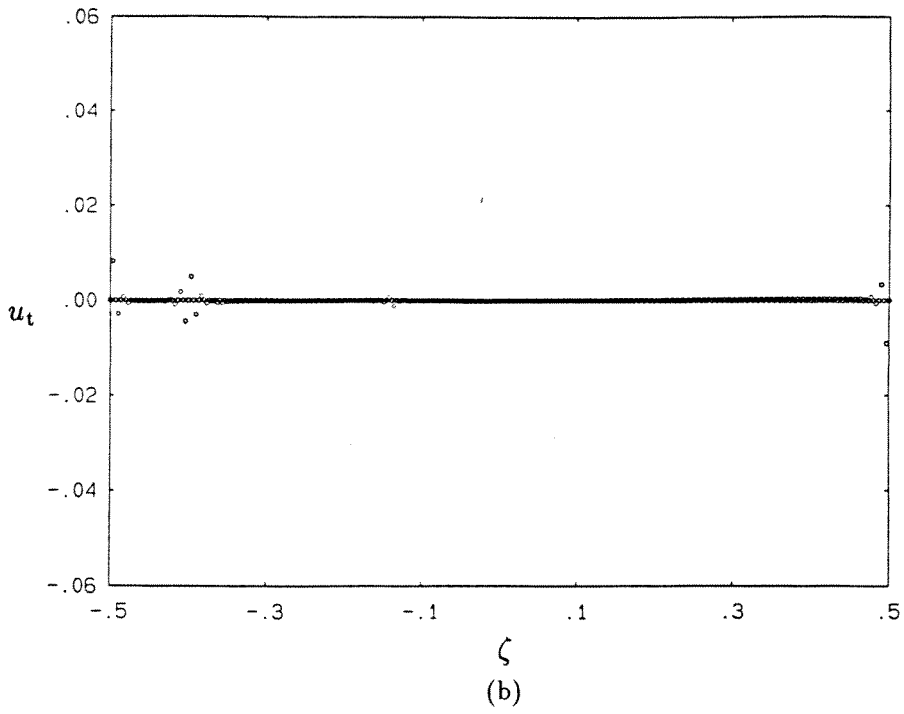
FIGURE (2.3.3) Cont.
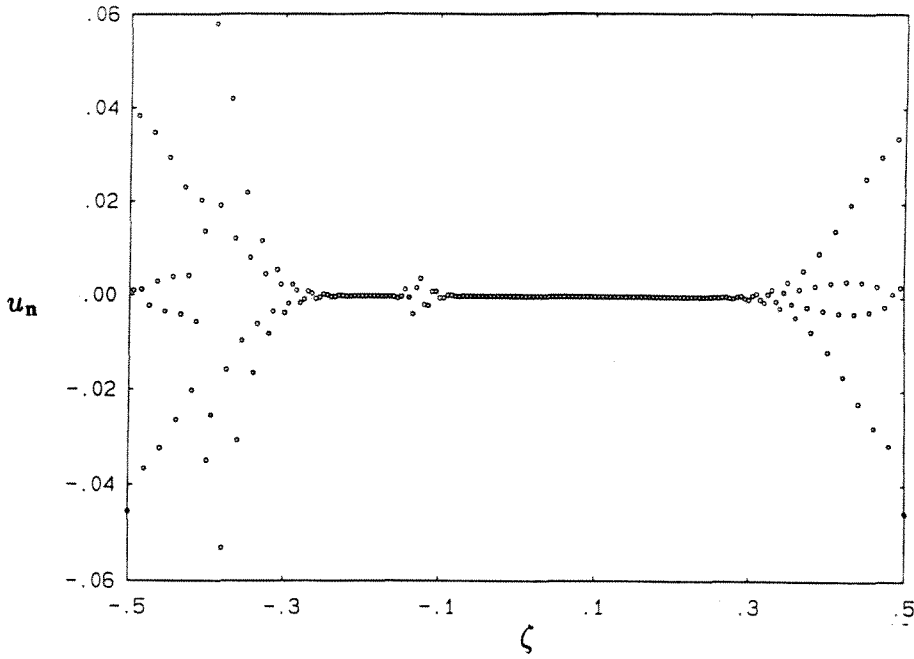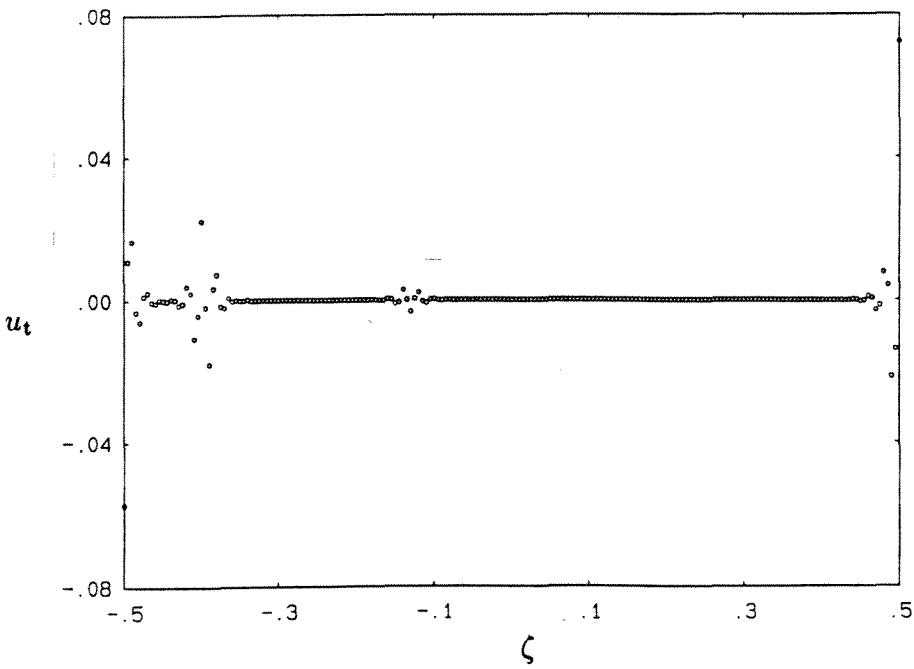
FIGURE (2.3.4) Velocity distribution on a flat plate with boundary conditions enforced using scheme b of Sec. (2.3.1.1); data the same as Fig. (2.3.3). (a) u_n; (b) u_t.
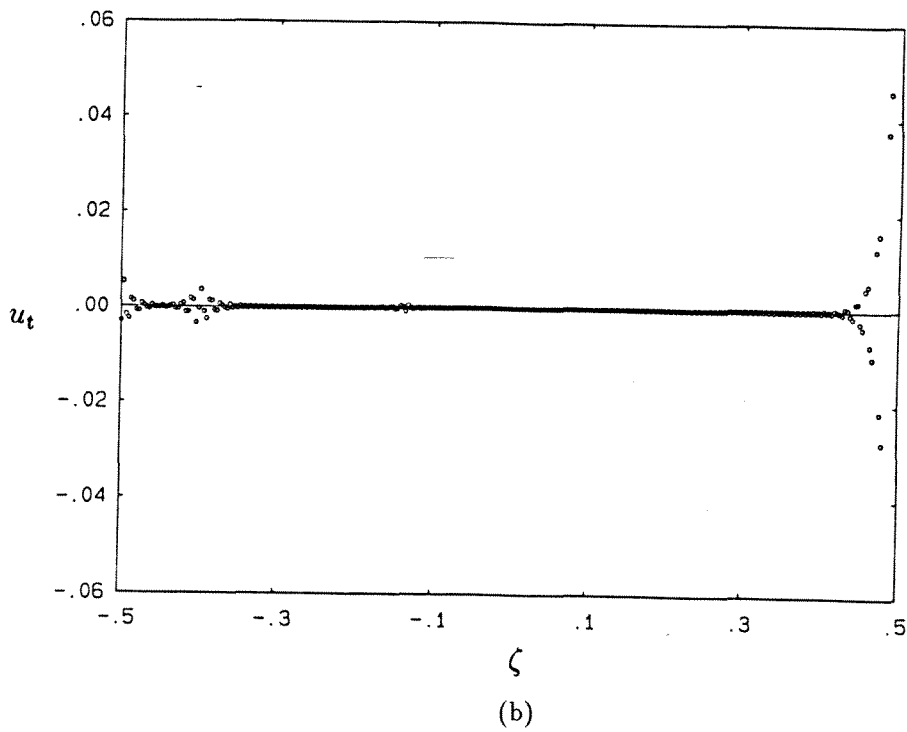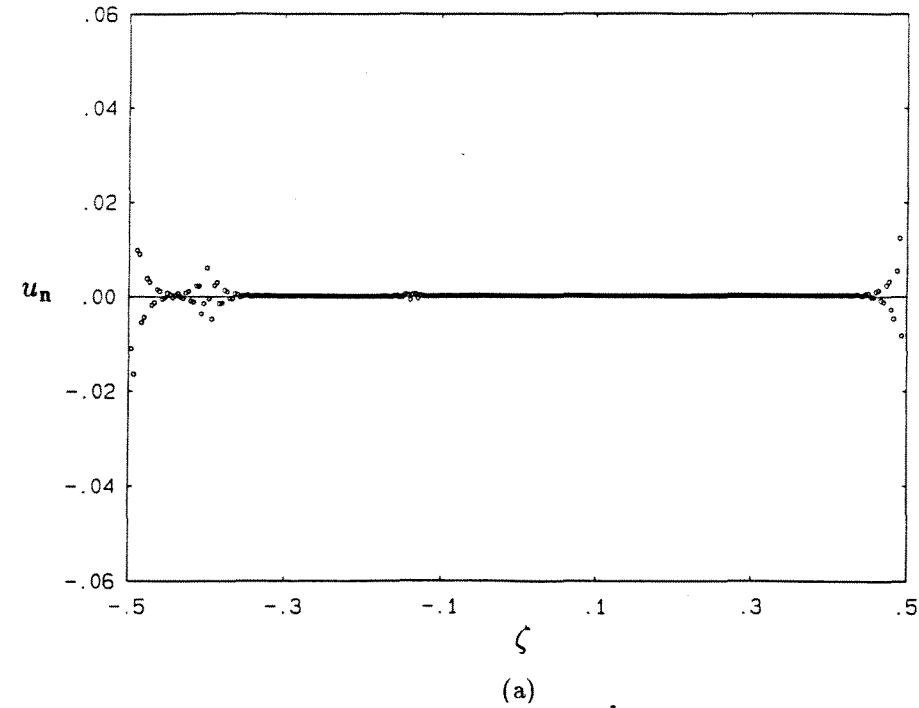
FIGURE (2.3.5) Velocity distribution on a flat plate with boundary conditions enforced using scheme c of Sec. (2.3.1.1); data the same as Fig. (2.3.3). (a) u_n; (b) u_t.
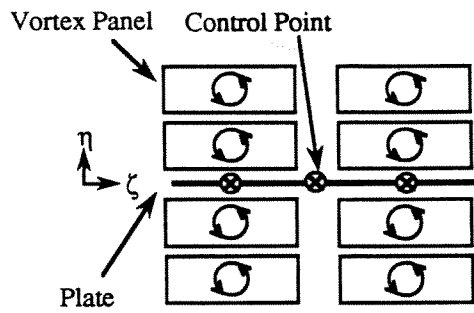
FIGURE (2.3.6) Schematic showing the arrangement of control points on a flat plate for scheme c of Sec. (2.3.1.1).

(a)

(b)
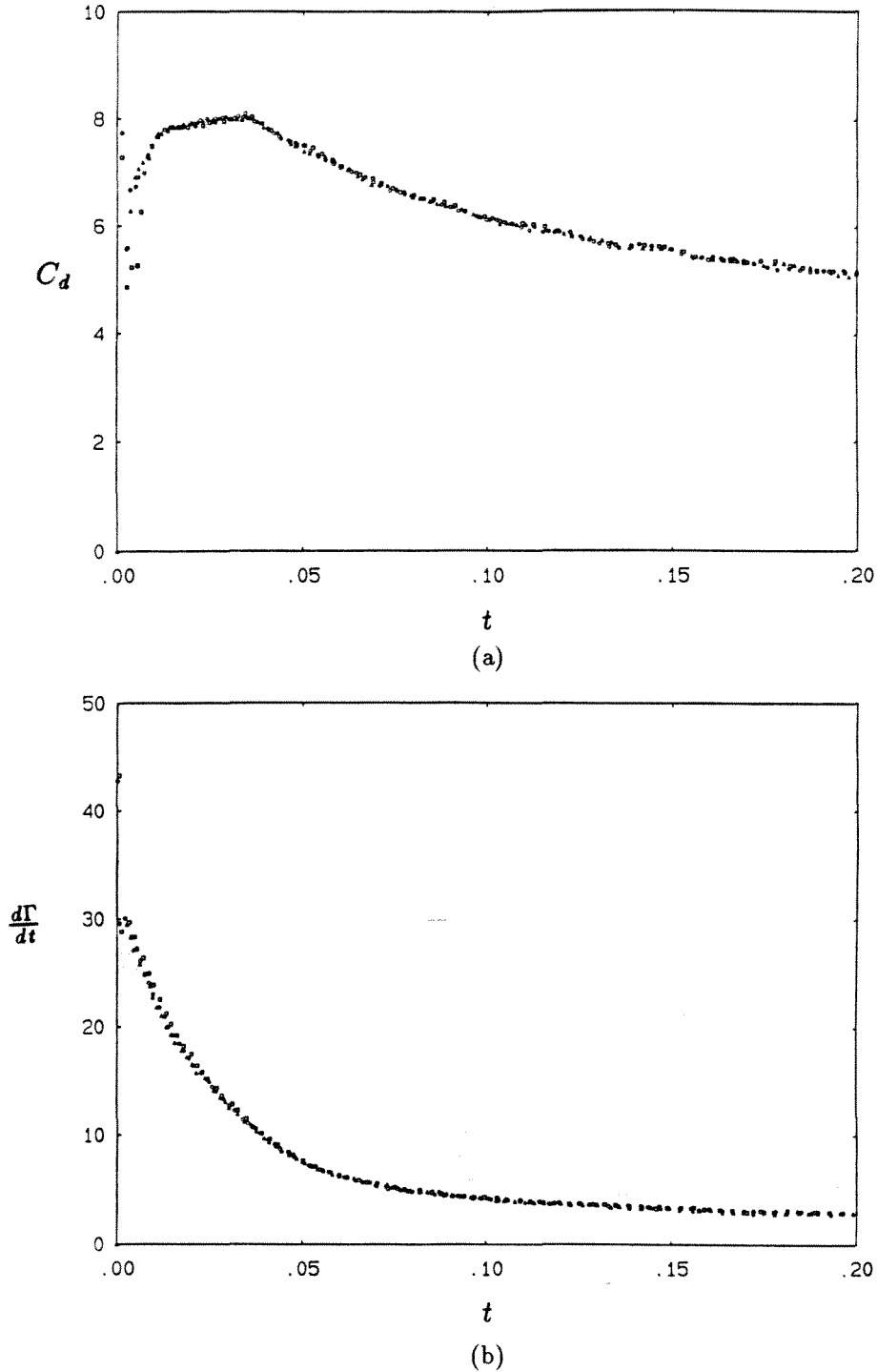
FIGURE (2.3.7) Time histories of (a) C_d and (b) $d\Gamma/dt$ of an impulsively started normal flat plate. $\delta_{bl} = 4.175 \times 10^{-3}$; □ $N_\eta = 2$, $\sigma = 1.67 \times 10^{-3}$; o $N_\eta = 4$, $\sigma = 9.28 \times 10^{-4}$; △ $N_\eta = 5$, $\sigma = 7.59 \times 10^{-4}$.

(a)

(b)
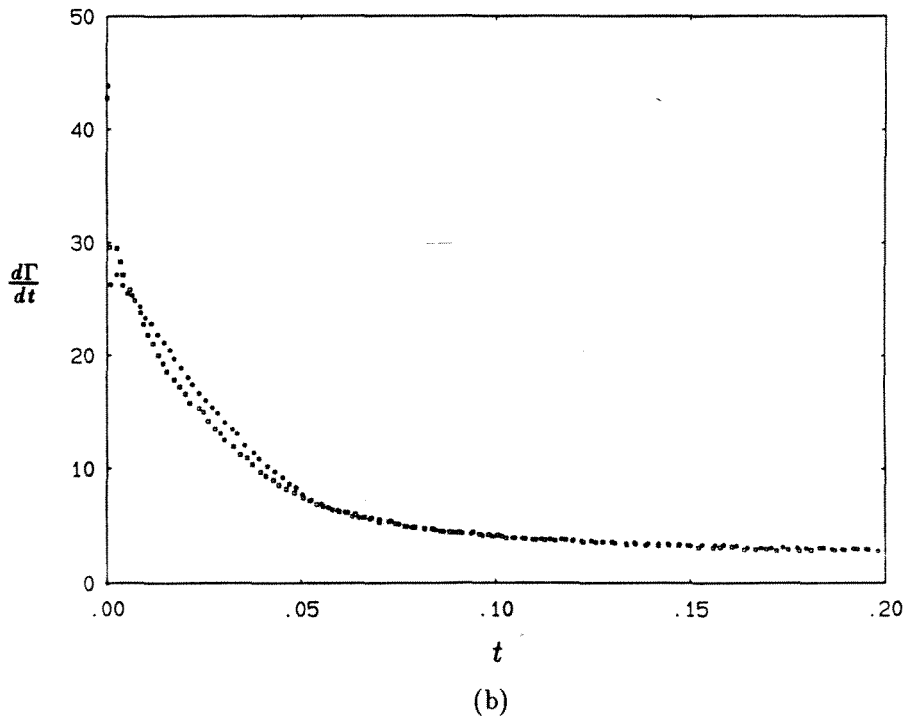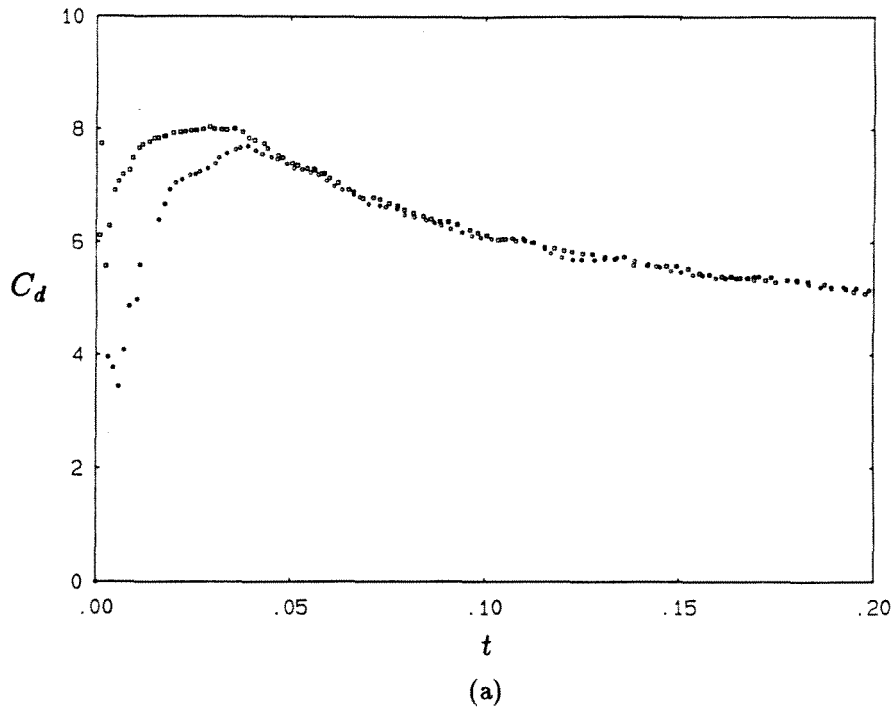
FIGURE (2.3.8) Time histories of (a) C_d and (b) $d\Gamma/dt$ of an impulsively started normal flat plate. $N_\eta = 5$; □ $\delta_{bl} = 4.175 \times 10^{-3}$, $\sigma = 7.59 \times 10^{-4}$; ○ $\delta_{bl} = 9.185 \times 10^{-3}$, $\sigma = 1.67 \times 10^{-3}$.
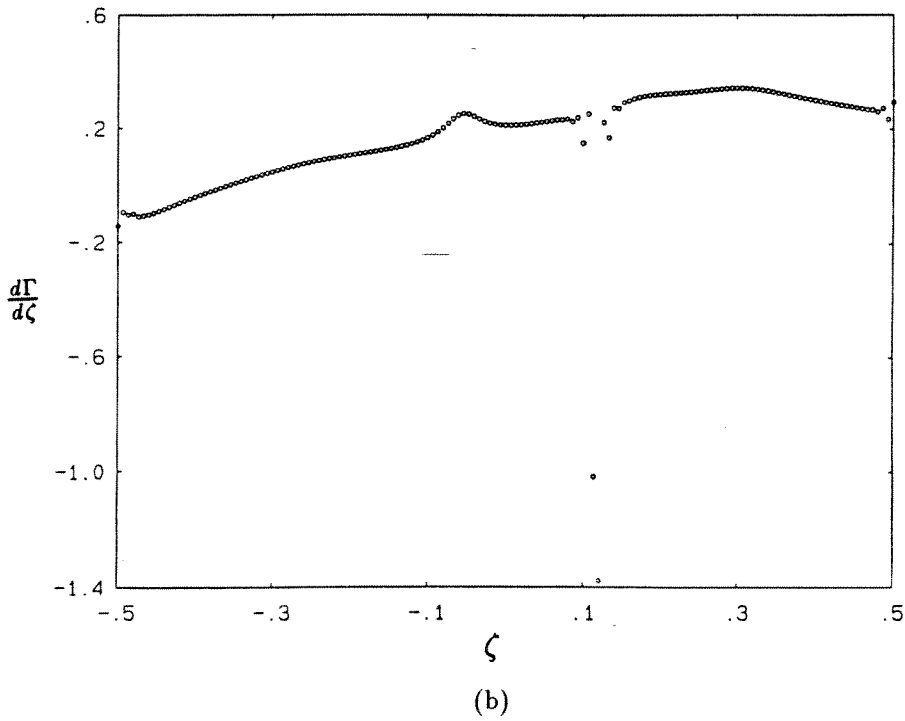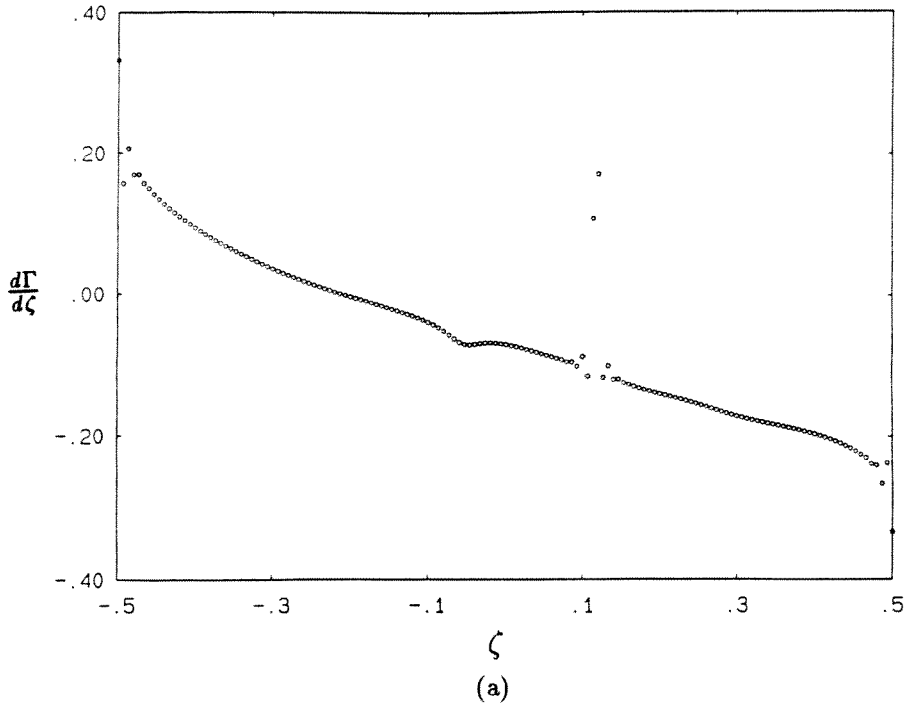
FIGURE (2.3.9) Distribution of $d\Gamma/d\zeta$ on an impulsively started normal flat plate. The vorticity layer is modeled as a single layer of vortex blobs. (a) front side; (a) backside.
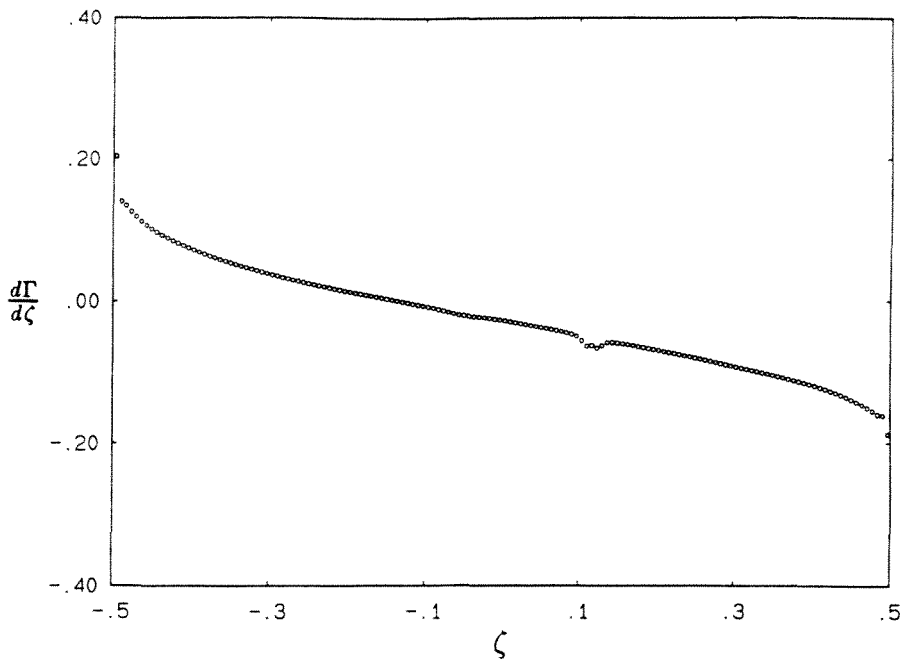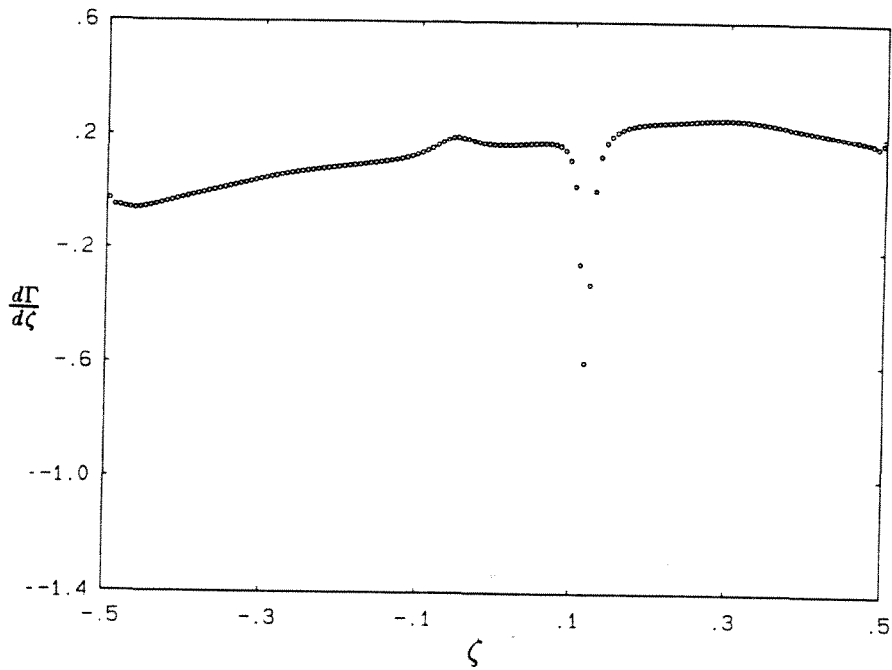
FIGURE (2.3.10) Distribution of $d\Gamma/d\zeta$ on an impulsively started normal flat plate. The vorticity layer is modeled as 5 layers of vortex panels. (a) front side; (a) backside.
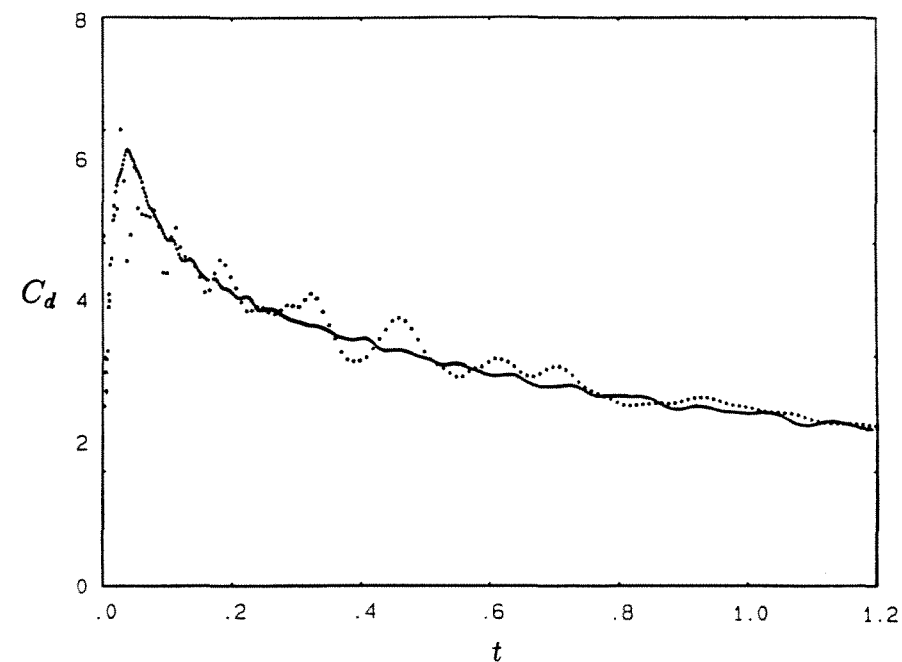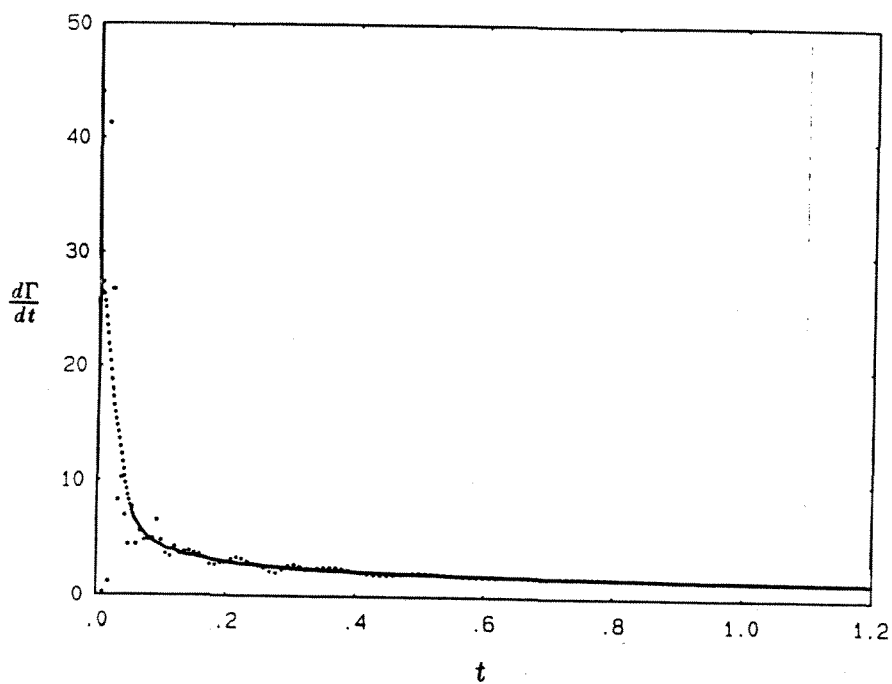
FIGURE (2.3.11) Time histories of (a) C_d and (b) $d\Gamma/dt$ for an impulsively started normal flat plate; plate boundary layer represented as o a single layer of vortex blobs; • 5 layers of vortex panels.
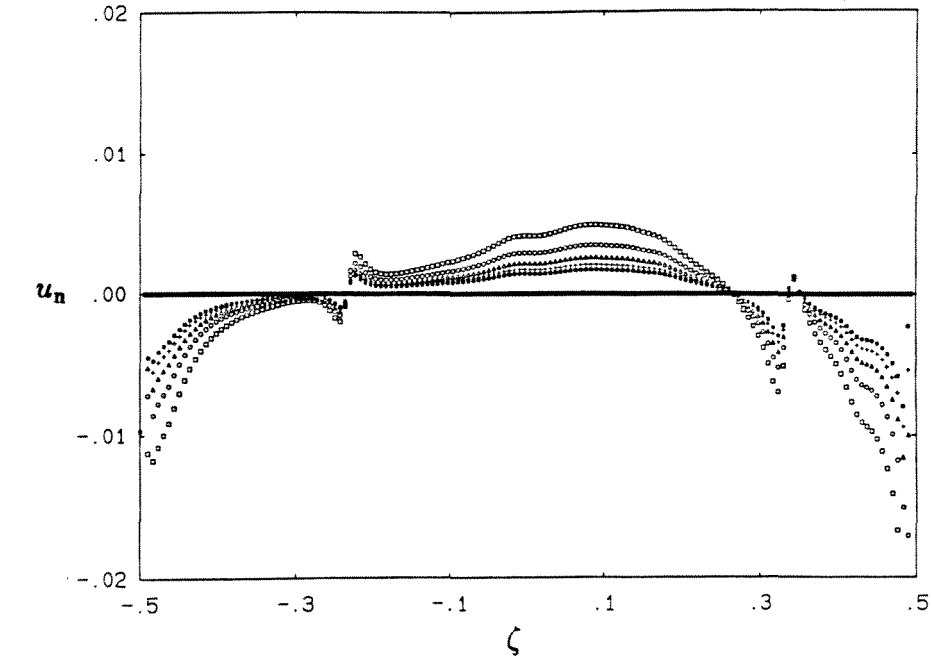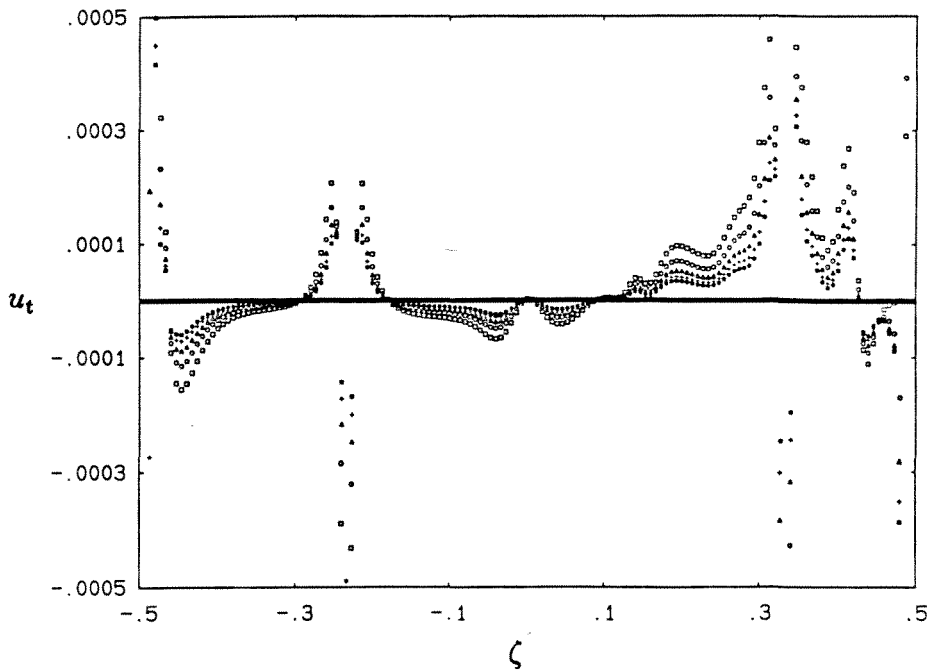
FIGURE (2.3.12) Comparison of (a) u_n and (b) u_t on a normal flat plate computed using $*$ $N_\eta = 1$; $+$ $N_\eta = 2$; $\triangle$ $N_\eta = 3$; $\circ$ $N_\eta = 4$; $\square$ $N_\eta = 5$.
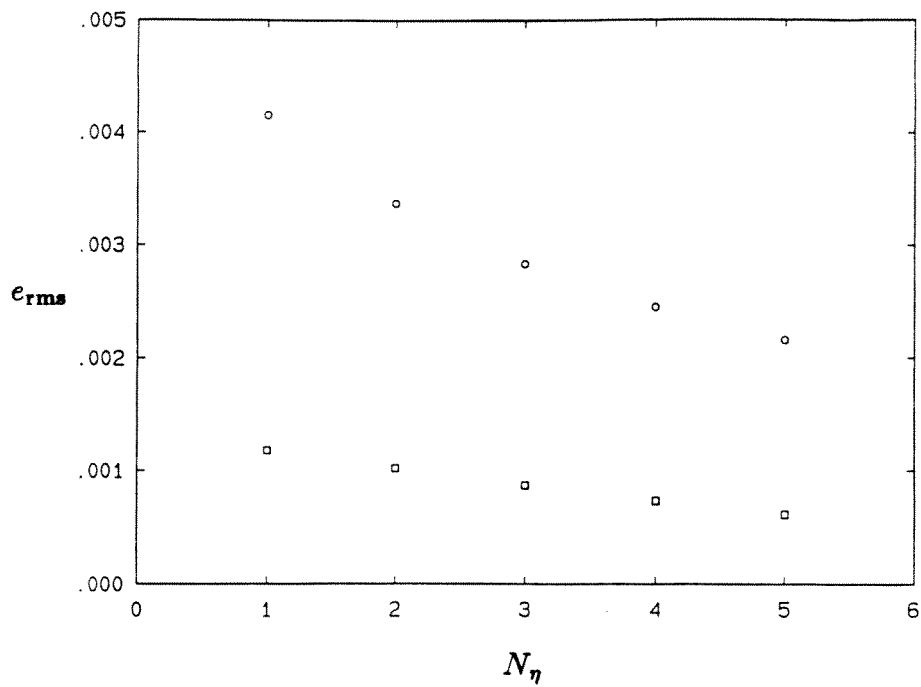
FIGURE (2.3.13) Plot of the rms velocity error e_{rms} versus N_η; $\circ$ u_{n}; $\square$ u_{t}.
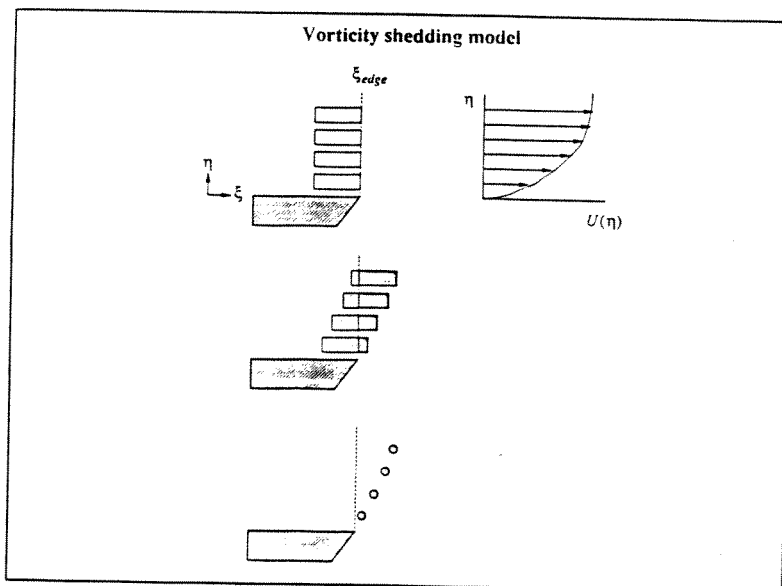
FIGURE (2.3.14) Schematic showing the vorticity shedding model.
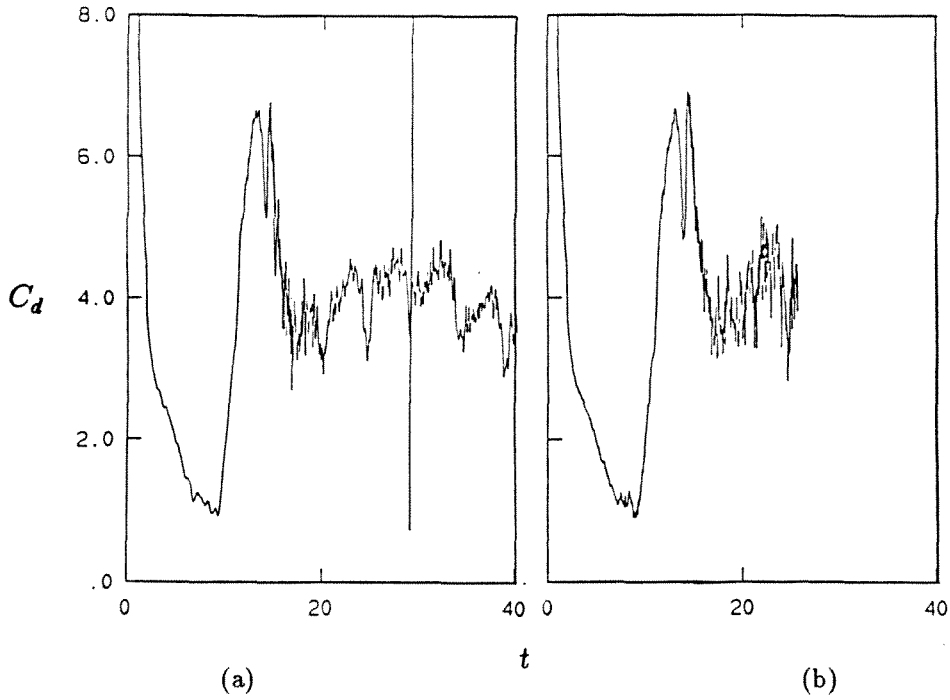
FIGURE (2.3.15) Comparison of C_d of an impulsively started normal flat plate, computed (a) without and (b) with conservation of angular momentum in the vortex-merging scheme.
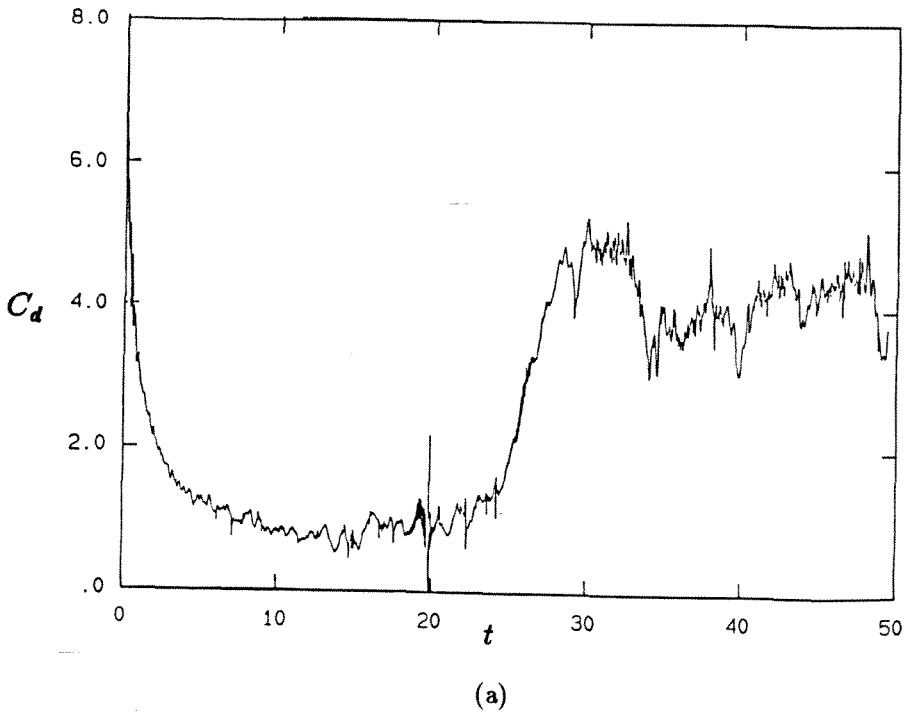
FIGURE (2.3.16) Comparison of C_d of an impulsively started normal flat plate, computed using (a) Eqn. (2.3.22) and (b) Eqn. (2.3.21).
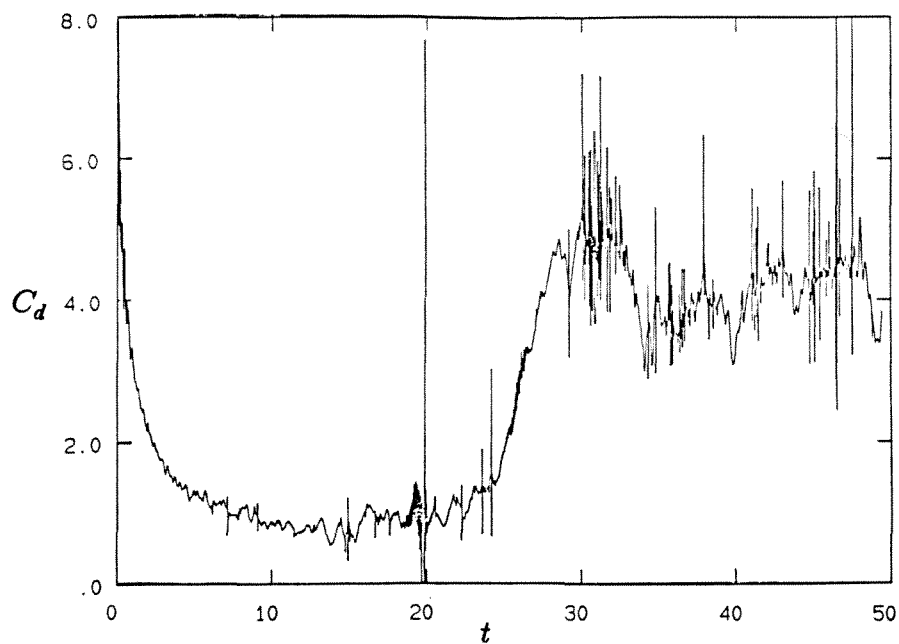
(b)

FIGURE (2.3.16) Cont.
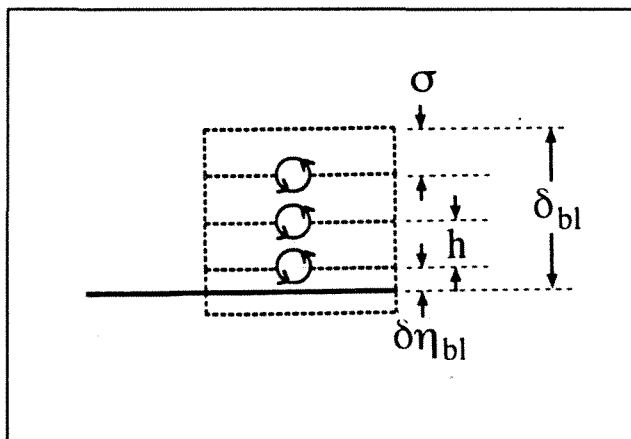
FIGURE (2.4.1) Schematic showing the definition of parameters.
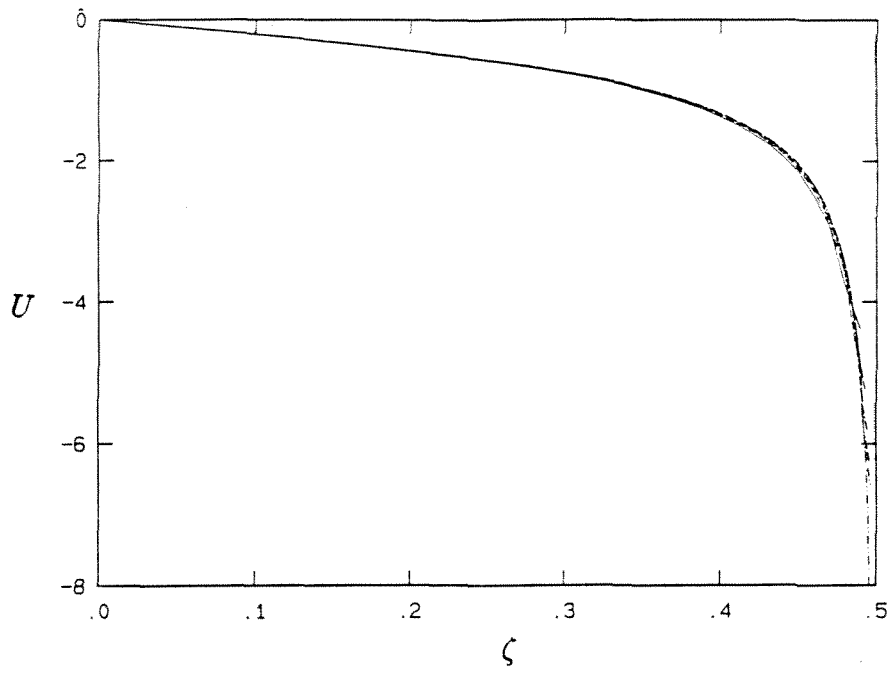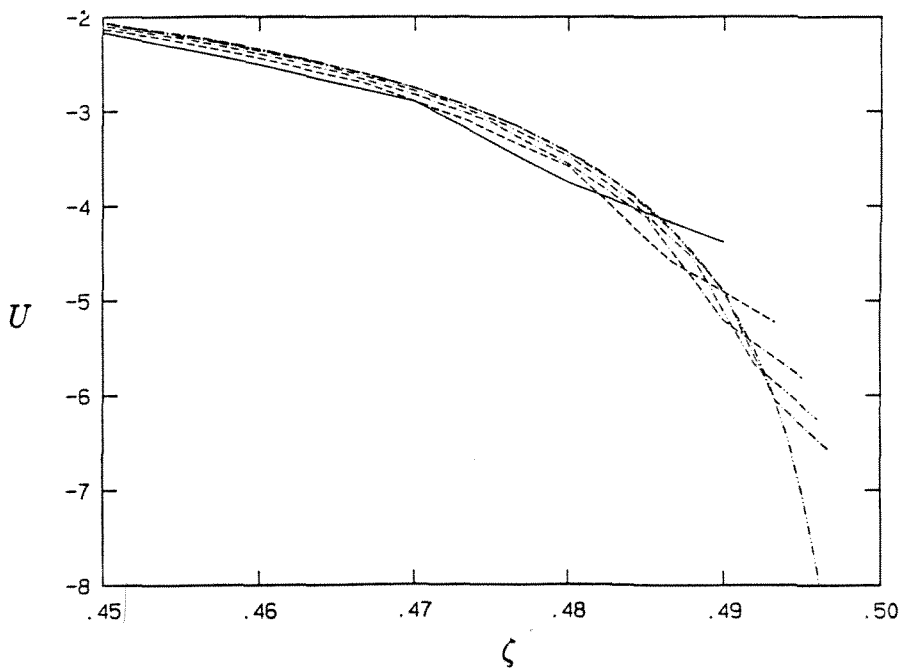
FIGURE (2.4.2) Comparison of velocity distribution on a normal flat plate to potential flow theory for (a) $0 < \zeta < 0.5$; (b) $0.45 < \zeta < 0.5$. $N_\eta = 5$; —— $N = 50$; – – – – $N = 75$; – – · – – $N = 100$; – – · · – – $N = 125$; – · – $N = 150$; – · · – pot. flow.
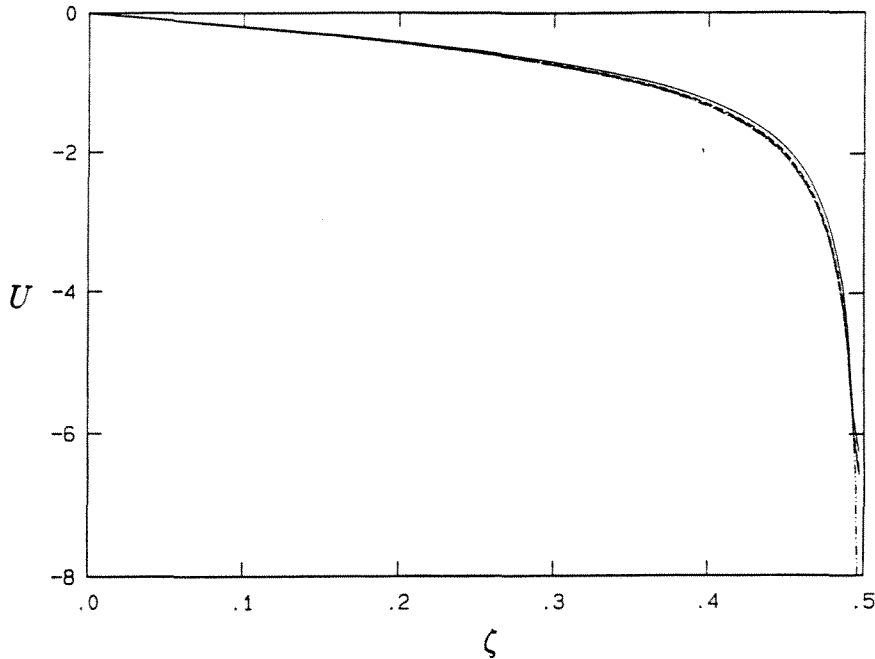
(a)
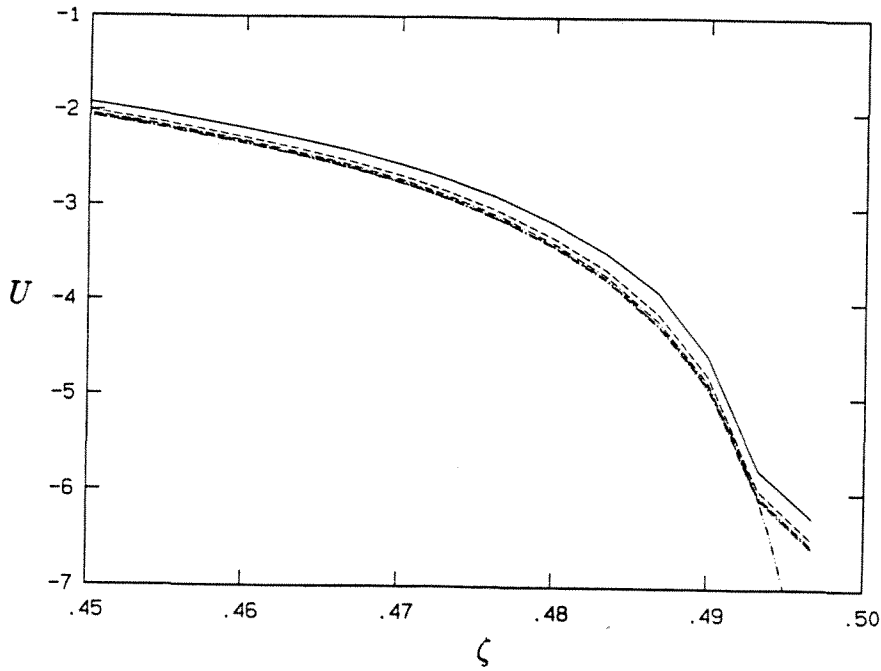
(b)

FIGURE (2.4.3) Comparison of velocity distribution on a normal flat plate to potential flow theory for (a) $0 < \zeta < 0.5$; (b) $0.45 < \zeta < 0.5$. $N = 150$; ——— $N_\eta = 1$; — — — — $N_\eta = 2$; — — · — — $N_\eta = 3$; — — · · — — $N_\eta = 4$; — · — $N_\eta = 5$; — · · — pot. flow.
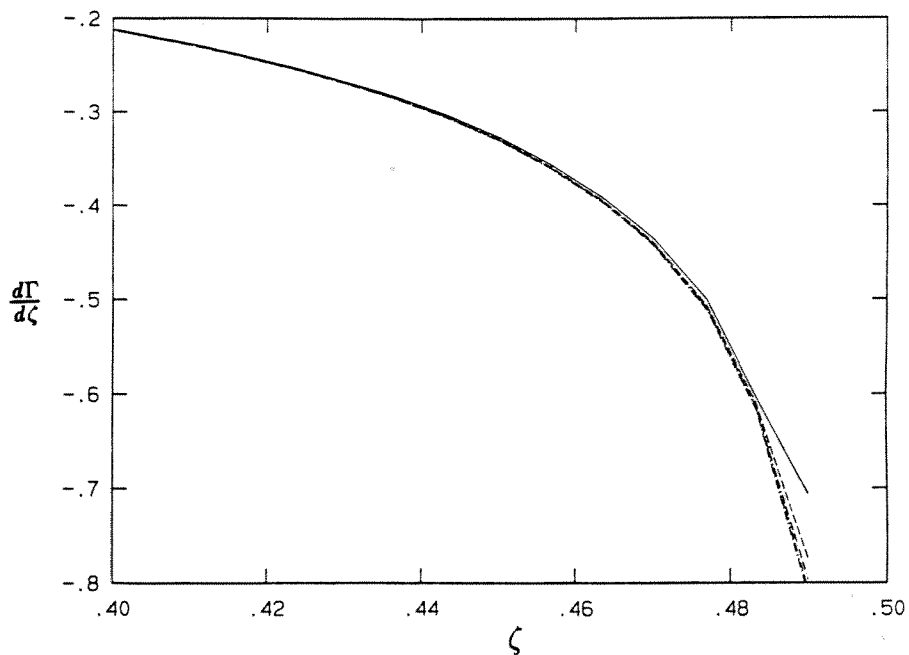
FIGURE (2.4.4) Comparison of $d\Gamma/d\zeta$ on a normal flat plate for $N = 150$; —— $N_\eta = 1$; — — — — $N_\eta = 2$; — — · — — $N_\eta = 3$; — — · · — — $N_\eta = 4$; — · — $N_\eta = 5$;
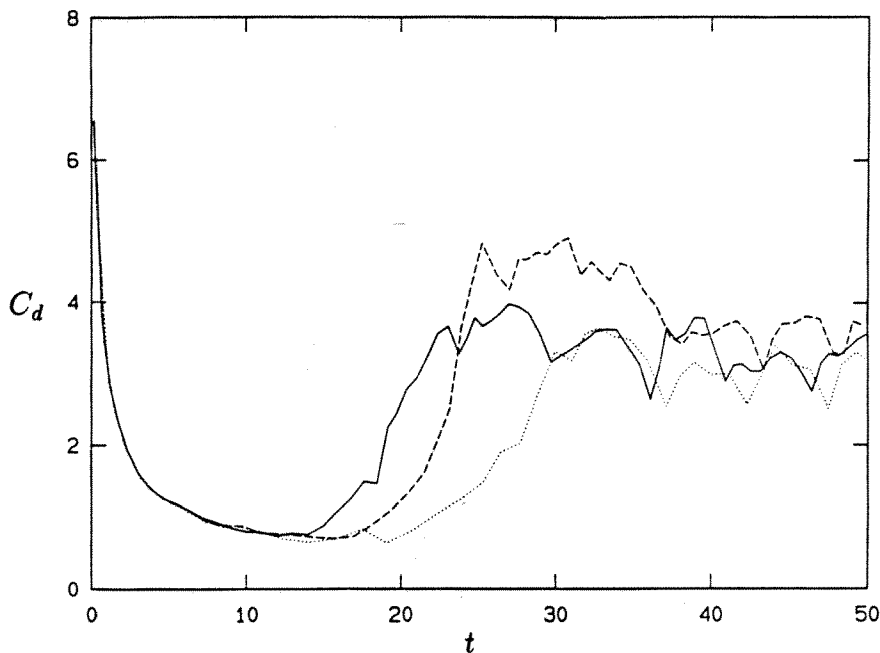
FIGURE (2.4.5) Comparison of C_d of an implusively started normal flat plate, computed using $N_\eta = 1$; · · · · $N = 90$; — — — — $N = 120$; —— $N = 150$.
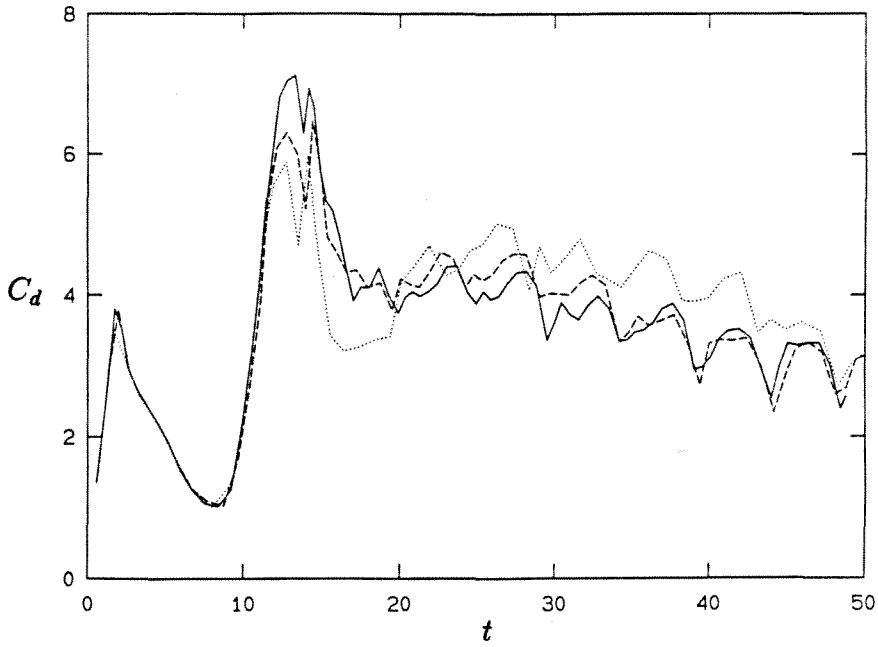
FIGURE (2.4.6) Comparison of C_d of a ramp-started, oscillating normal flat plate, computed using $N_\eta = 1$; $\cdots$ $N = 90$; $----$ $N = 120$; —— $N = 150$.
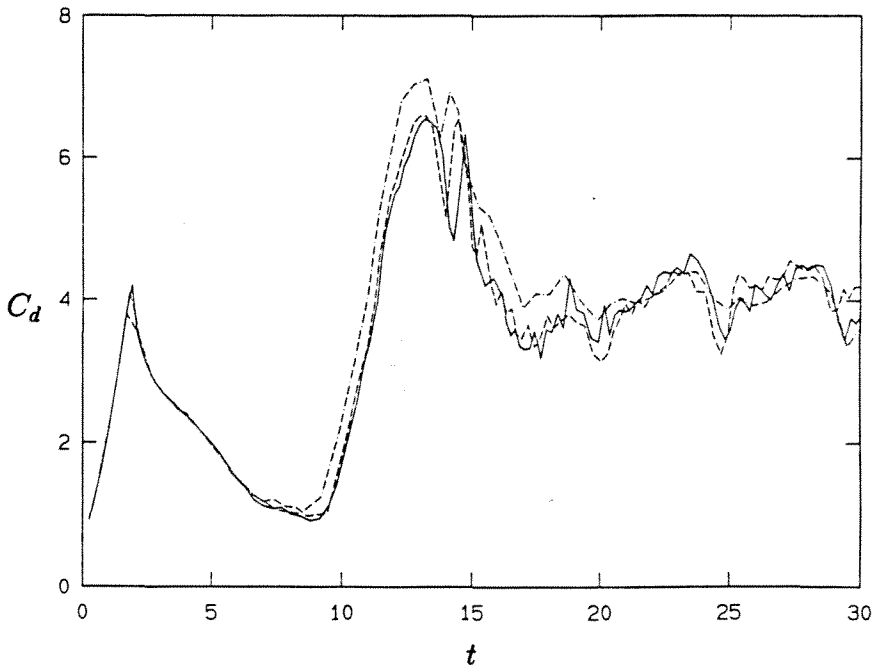
FIGURE (2.4.7) Comparison of C_d of a ramp-started, oscillating normal flat plate, computed using $N = 150$; $\cdots$ $N_\eta = 1$; $----$ $N_\eta = 2$; —— $N_\eta = 3$.
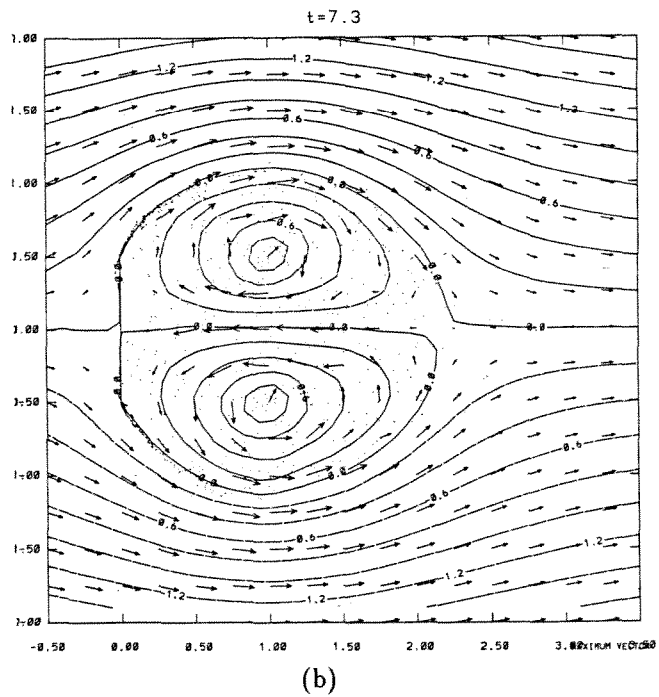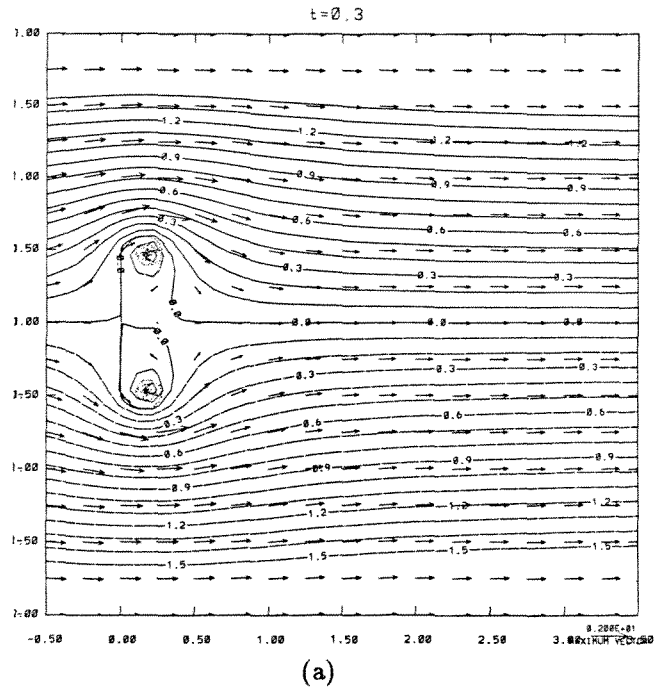
FIGURE (2.5.1) Flow-vis at different stages of an impulsively started normal flat plate. (a) $t = 0.3$; (b) $t = 7.3$; (c) $t = 50.0$.
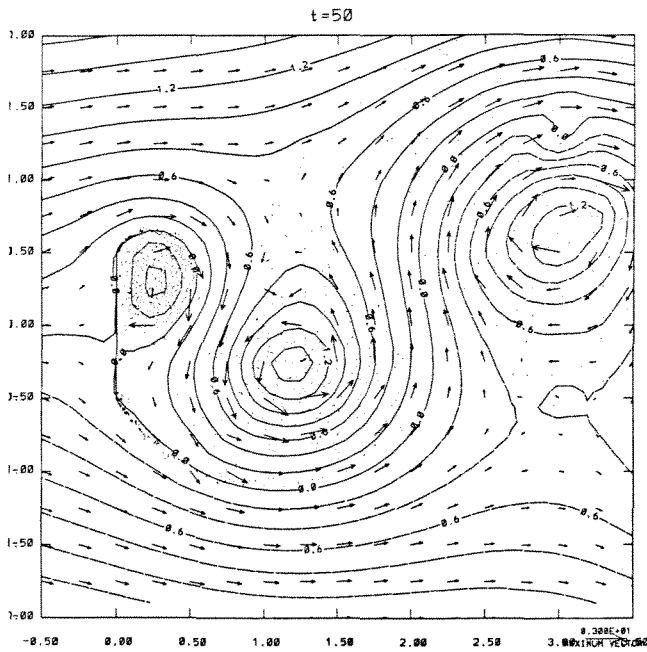
(c)

FIGURE (2.5.1) Cont.
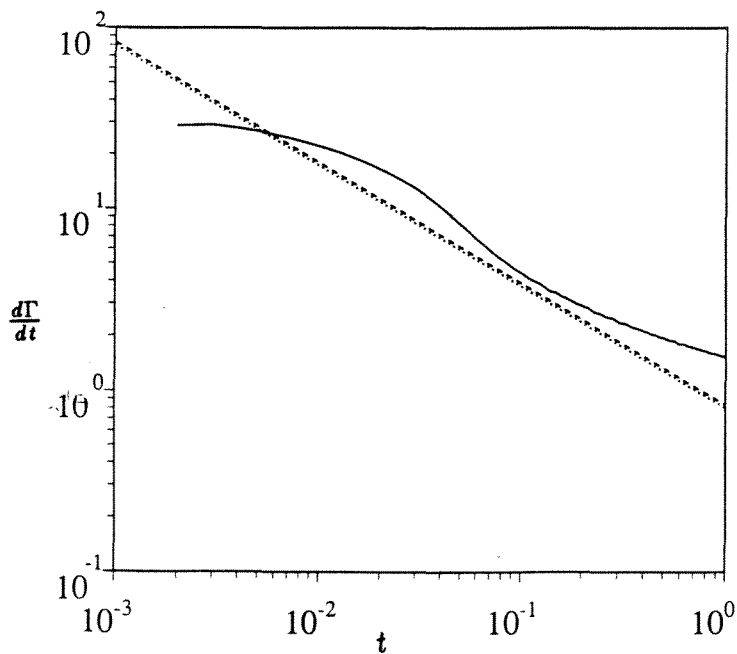
(a)

FIGURE (2.5.2) Comparison of $d\Gamma/dt$ of a normal flat plate to the similarity theory. ——— calc.;
· · · Cortelezzi and Leonard (1990); — — — — Pullin (1978). (a) impulsive-start;
(b) ramp-start with $N = 50, 75, 100, 125, 150$ and 200 in calc.
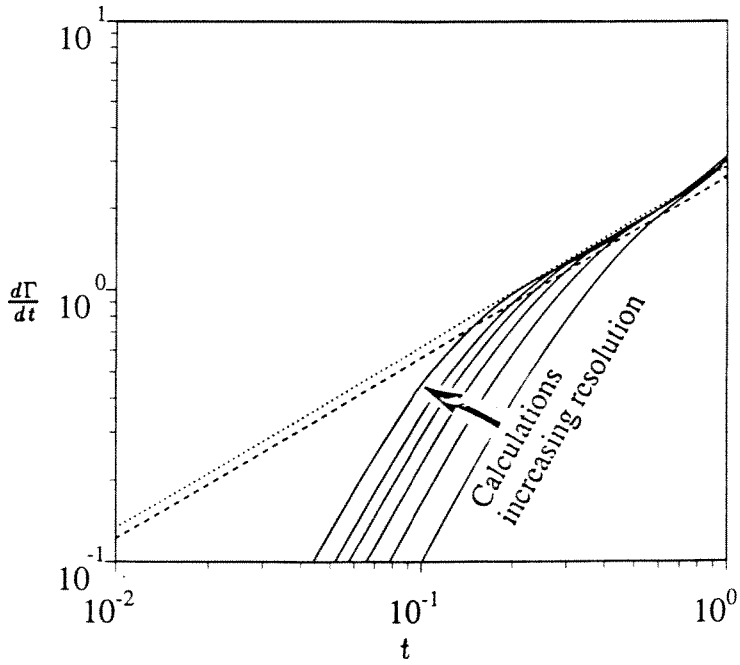
(b)

FIGURE (2.5.2) Cont.
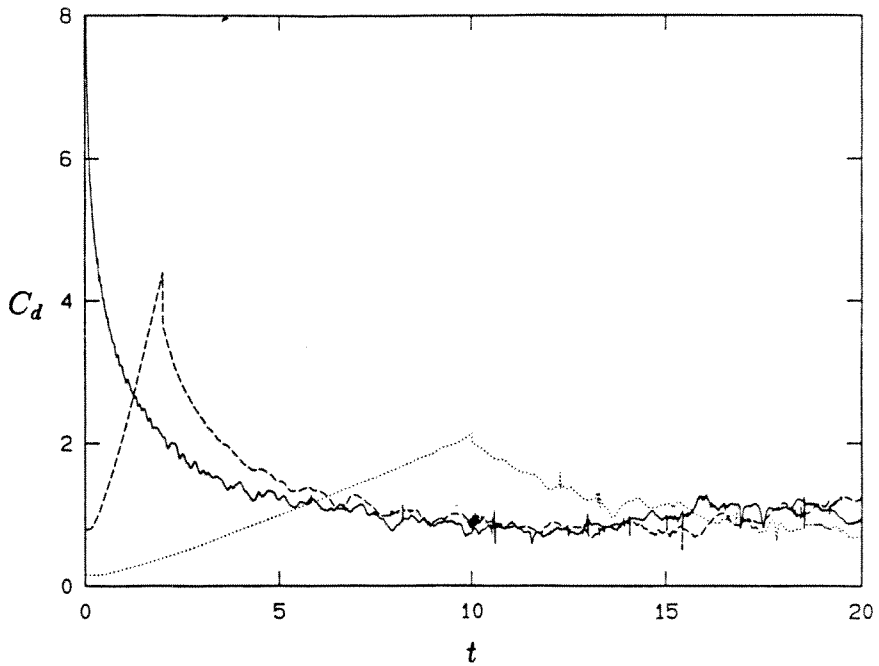
FIGURE (2.5.3) Comparison of C_d of a normal flat plate started from rest at three different accelerations. —— a=∞; — — —— a=0.5; ···· a=0.1.
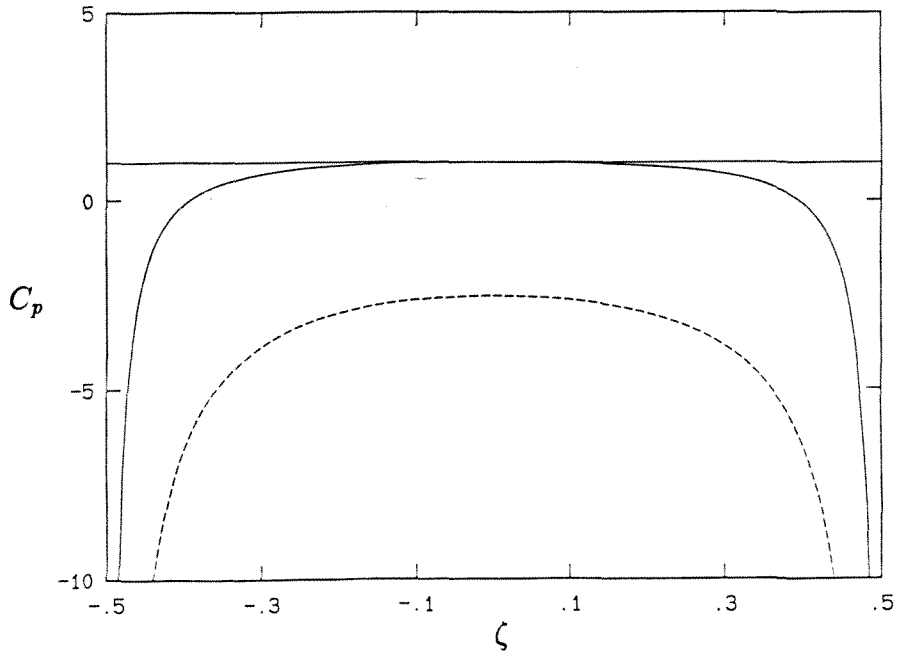
FIGURE (2.5.4) Pressure distribution on an impulsively started normal flat plate at t=0.008 ——— front face; — — — — backface.
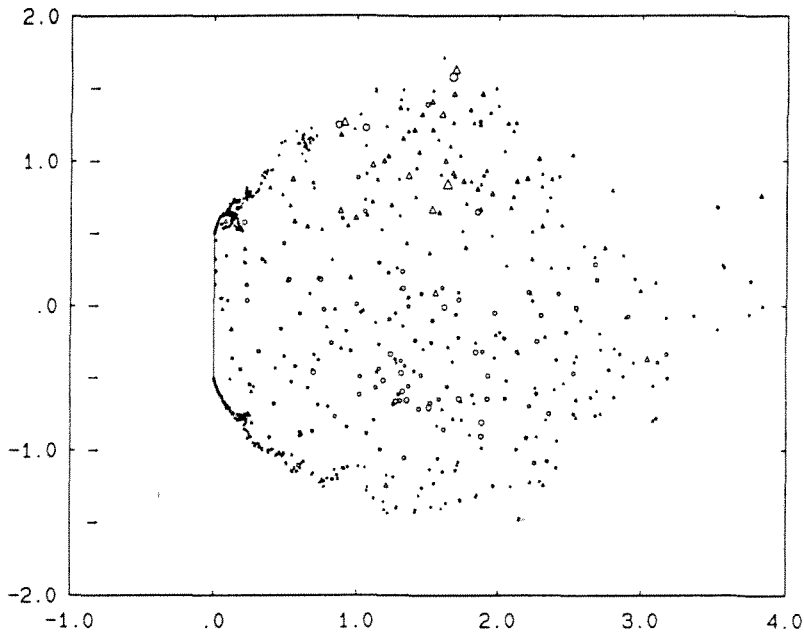
(a)

FIGURE (2.5.5) Flow-vis of a normal flat plate started from rest at three different acceleration ($t =$ 20). (a) a=∞; (b) a=0.2; (c) a=0.1.
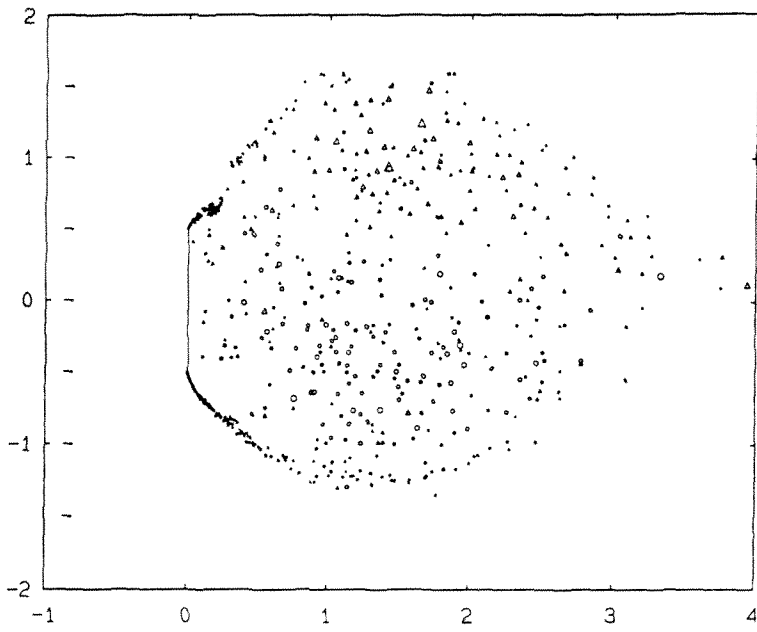
(b)
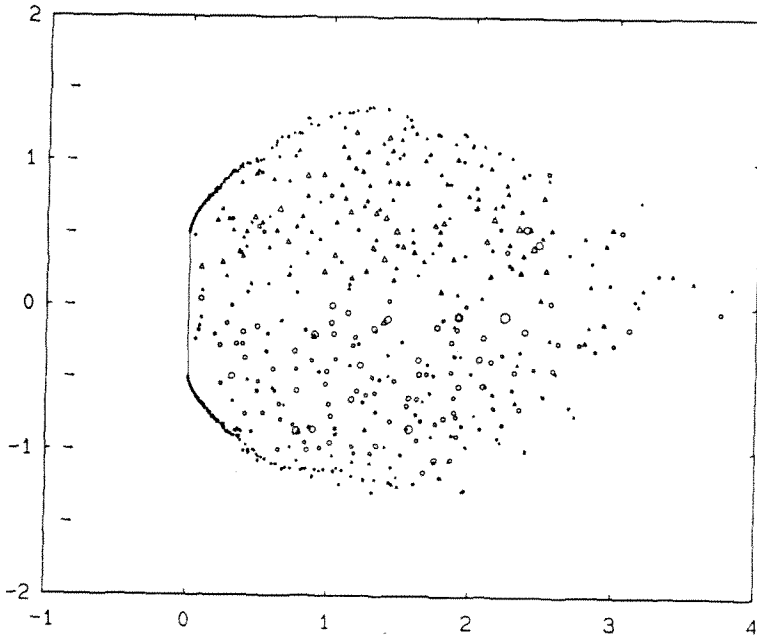
(c)

FIGURE (2.5.5) Cont.
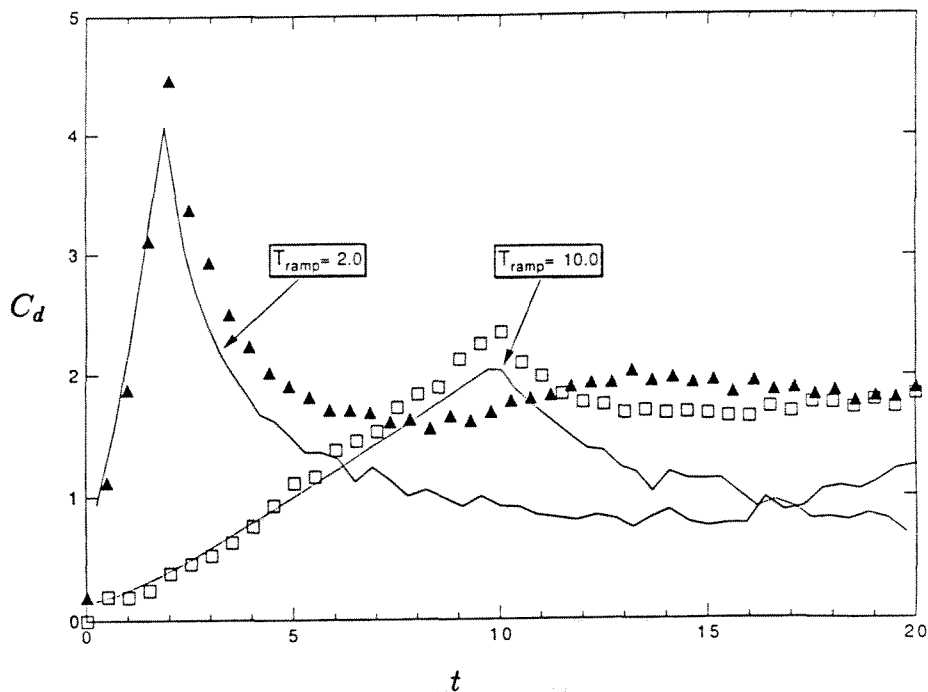
FIGURE (2.5.6) Comparison of C_d of a ramp-started normal flat plate to the expt. of Lisoski and Roshko (1989). —— calc. with a=0.5; $\cdots$ calc. with a=0.1; $\triangle$ expt. with a=0.5; $\square$ expt. with a=0.1.
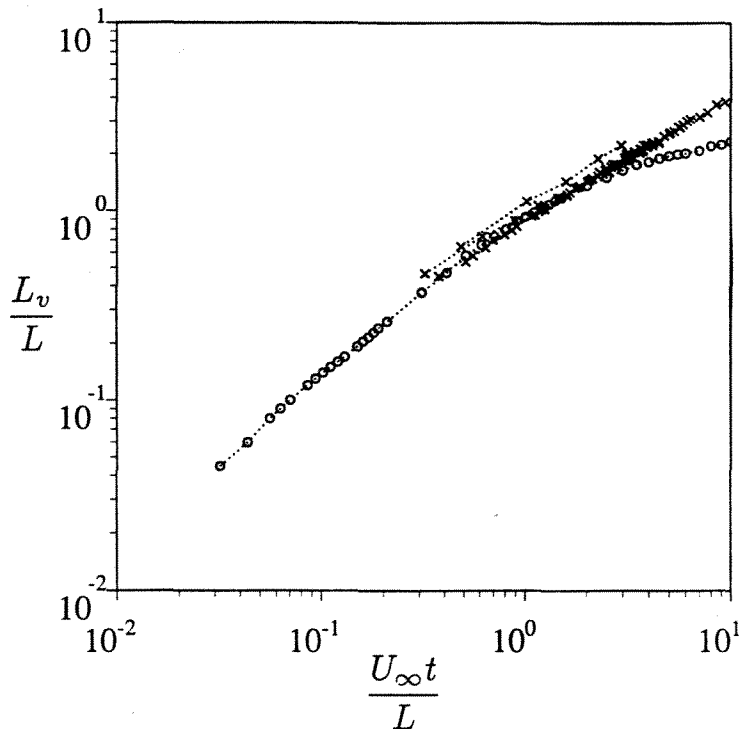
FIGURE (2.5.7) Comparison of the normalized bubble length L_v/L of an impulsively started normal flat plate to expt. o calc. ; $\times$ expt. of Taneda and Honji (1971).
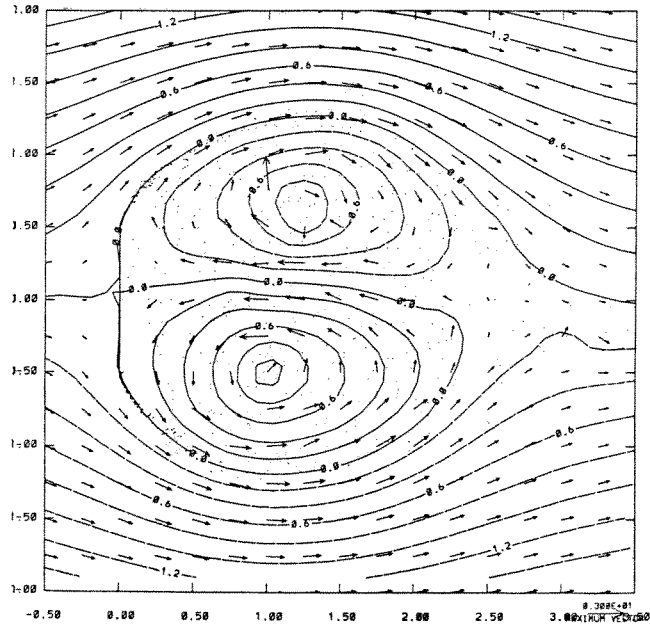
FIGURE (2.5.8) Flow-vis of an impulsively started normal flat plate at $t \simeq 10$.

(a)
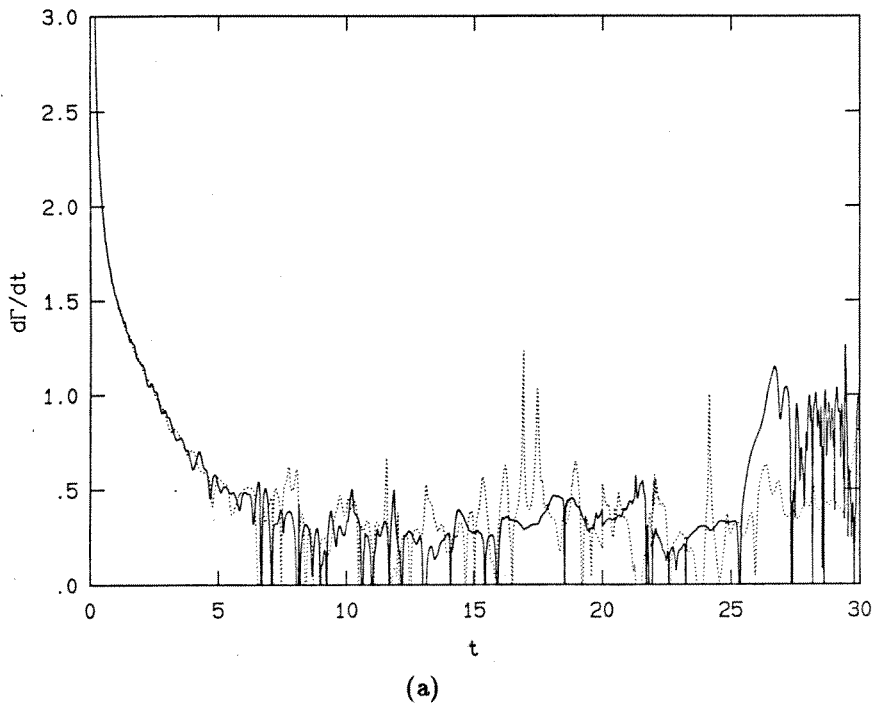
FIGURE (2.5.9) Short-time histories of (a) —— $d\Gamma/dt_{\text{upper}}$, $d\Gamma/dt_{\text{lower}}$ ⋯ ; (b) —— Γ_{upper}, Γ_{lower} ⋯ and (c)C_d of an impulsively started normal flat plate.

(b)

(c)

FIGURE (2.5.9) Cont.

t=25.0

(a)
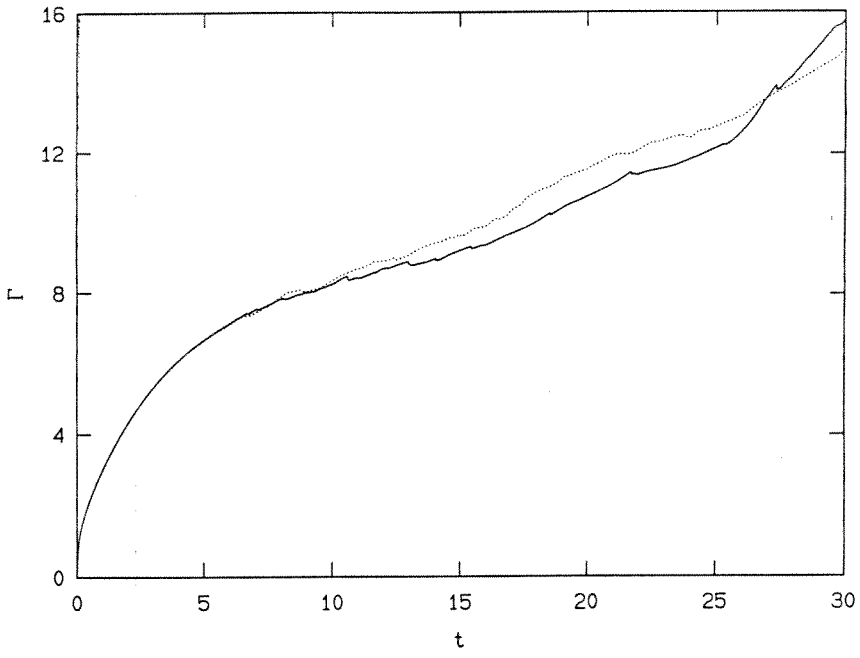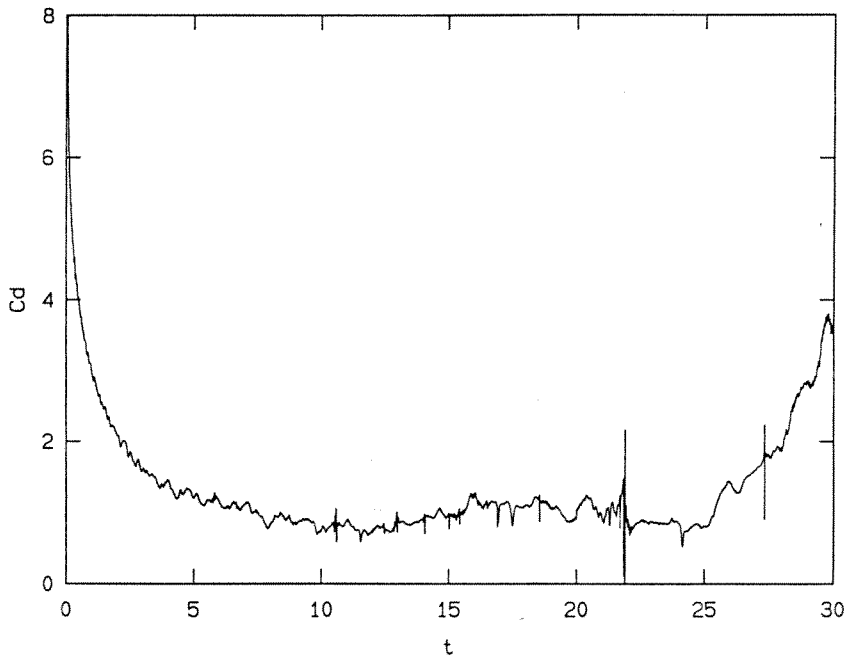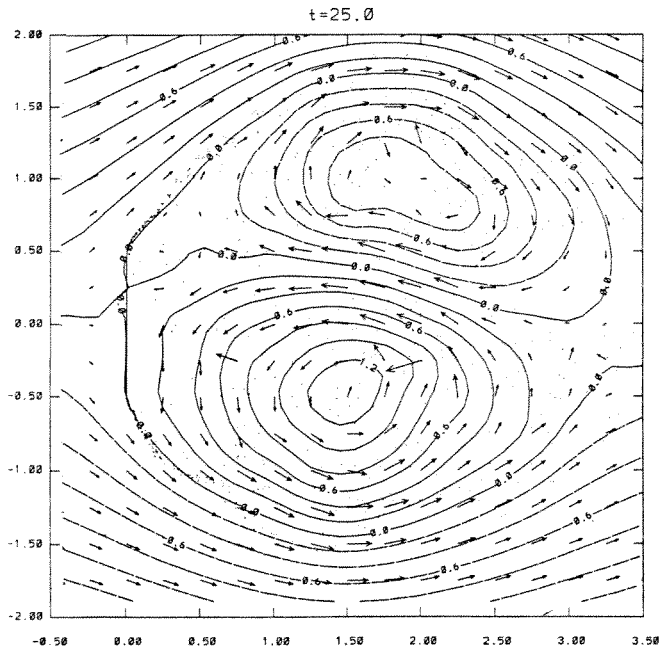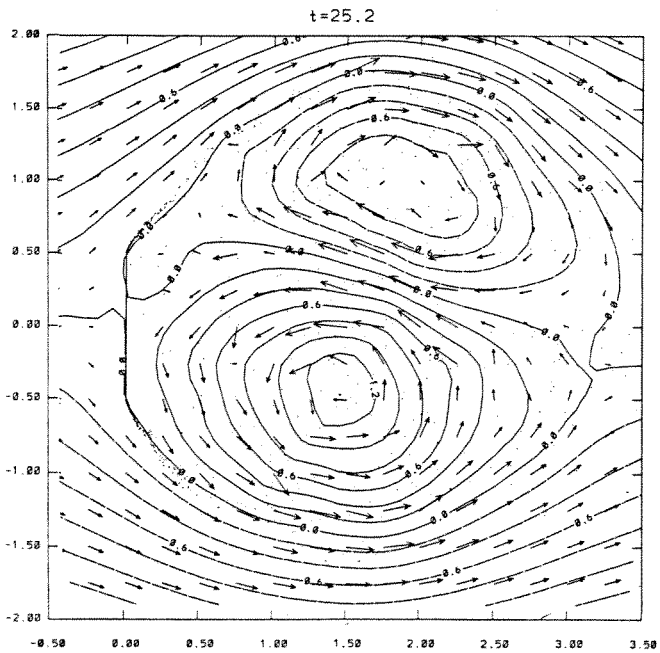
t=25.2

(b)

FIGURE (2.5.10) Flow-vis of an impulsively started normal flat plate at the onset of the asymmetric shedding mode. (a) $t = 25.0$; (b) $t = 25.2$; (c) $t = 25.4$; (d) $t = 25.6$; (e) $t = 25.8$; (f) $t = 26.0$; (g) $t = 27.0$.

t=25.4

(c)

t=25.6

(d)

FIGURE (2.5.10) Cont.

t=25.8

(e)

t=26.0

(f)

FIGURE (2.5.10)   Cont.

t=27.0

(g)

FIGURE (2.5.10)   Cont.

t=25.4

FIGURE (2.5.11) Zoom-in plot of the flow of Fig. (2.5.10c), $t = 25.4, \psi \times 10$.
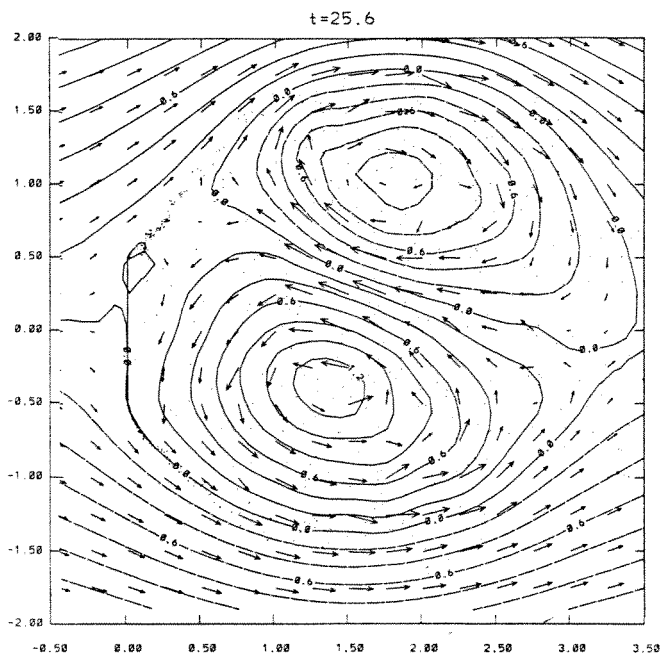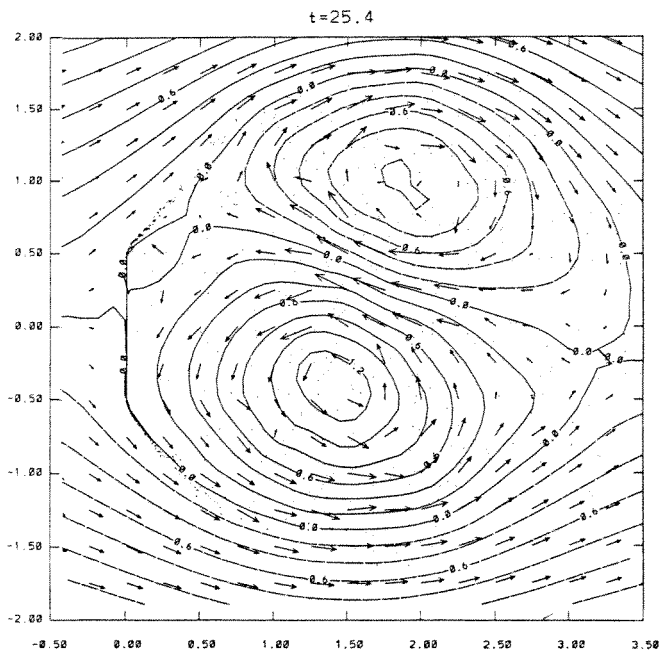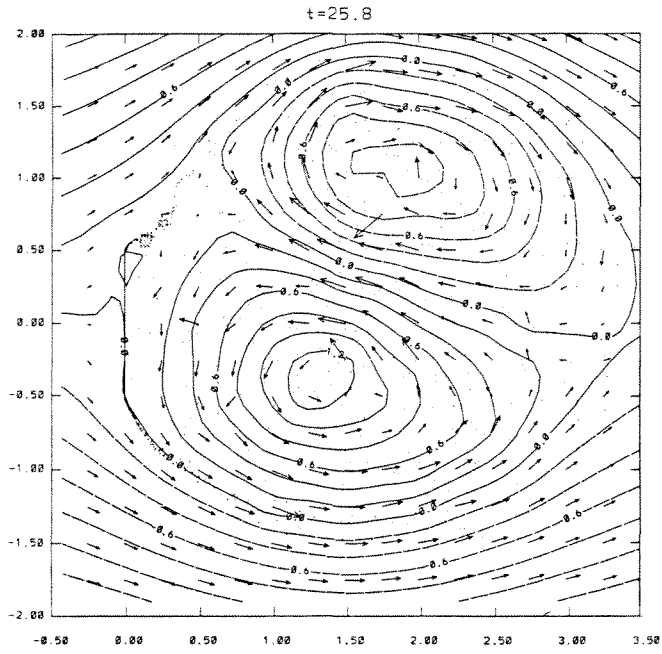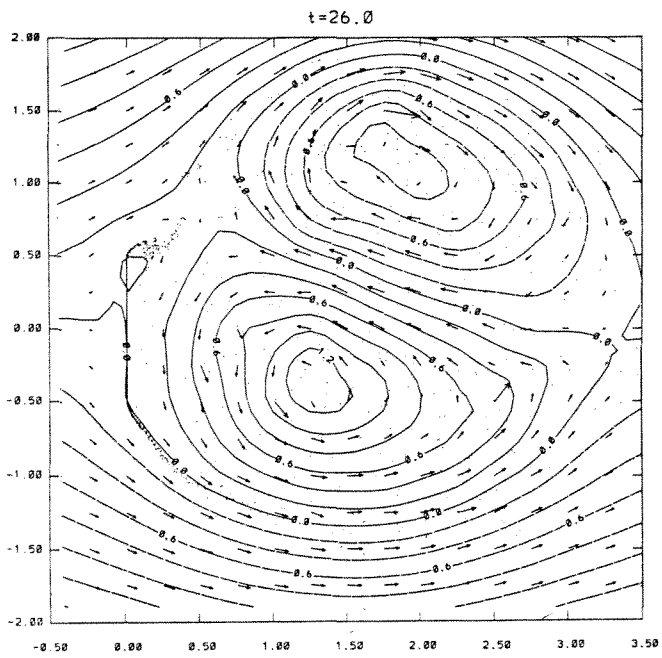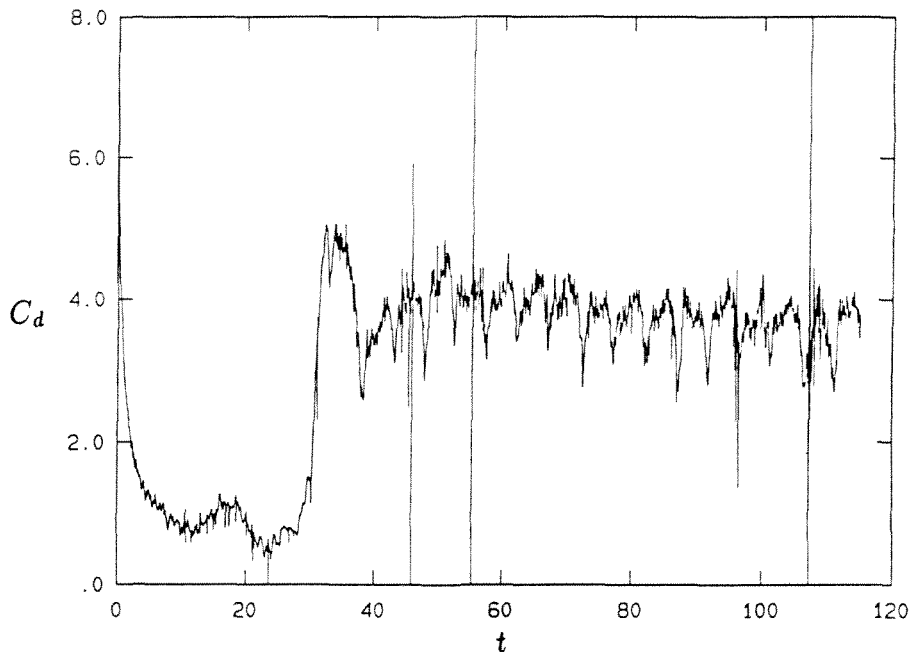
(a)
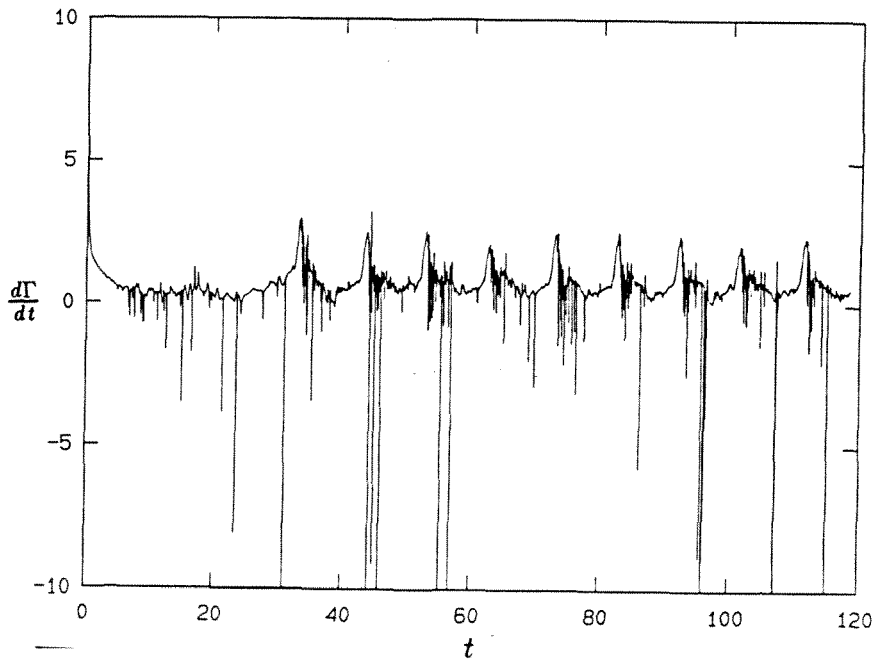
(b)

FIGURE (2.5.12) Long-time histories of (a) C_d, (b) $d\Gamma/dt_{\text{lower}}$ and (c) $d\Gamma/dt_{\text{upper}}$ of an impulsively started normal flat plate.
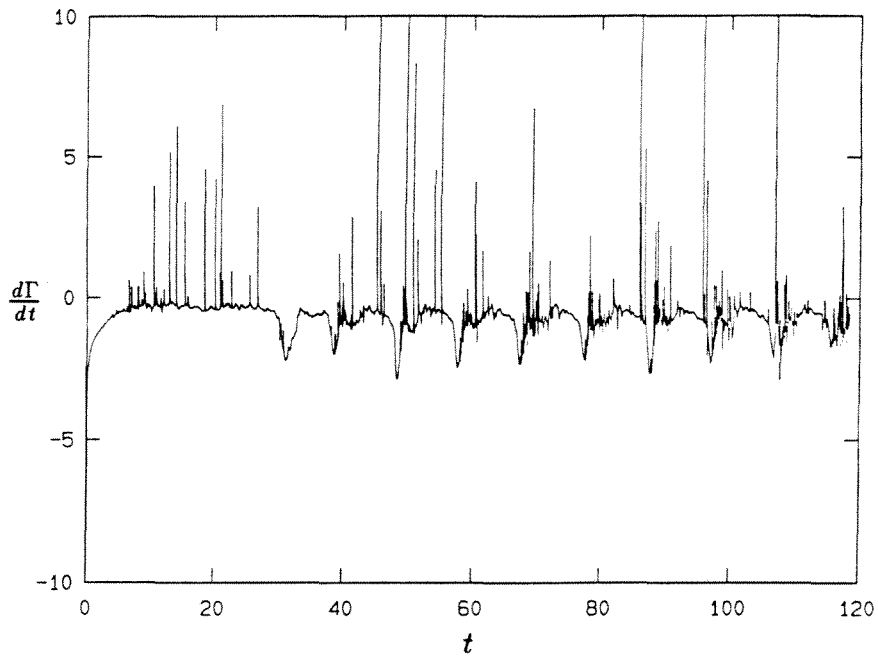
(c)

FIGURE (2.5.12) Cont.
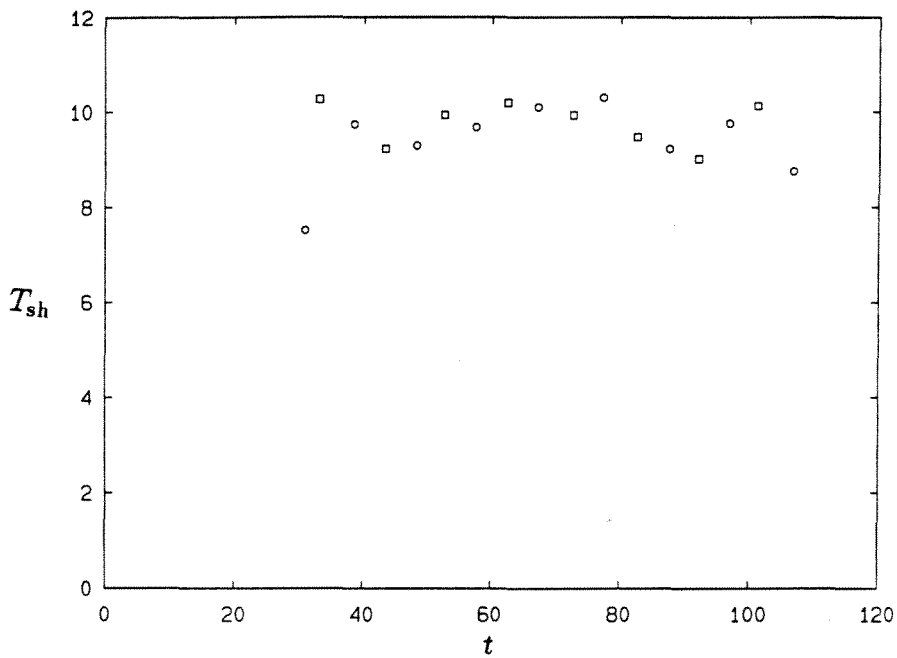
(a)

FIGURE (2.5.13) Time histories of (a) T_{sh} and (b) $|d\Gamma/dt|_{max}$ of an impulsively started normal flat plate.
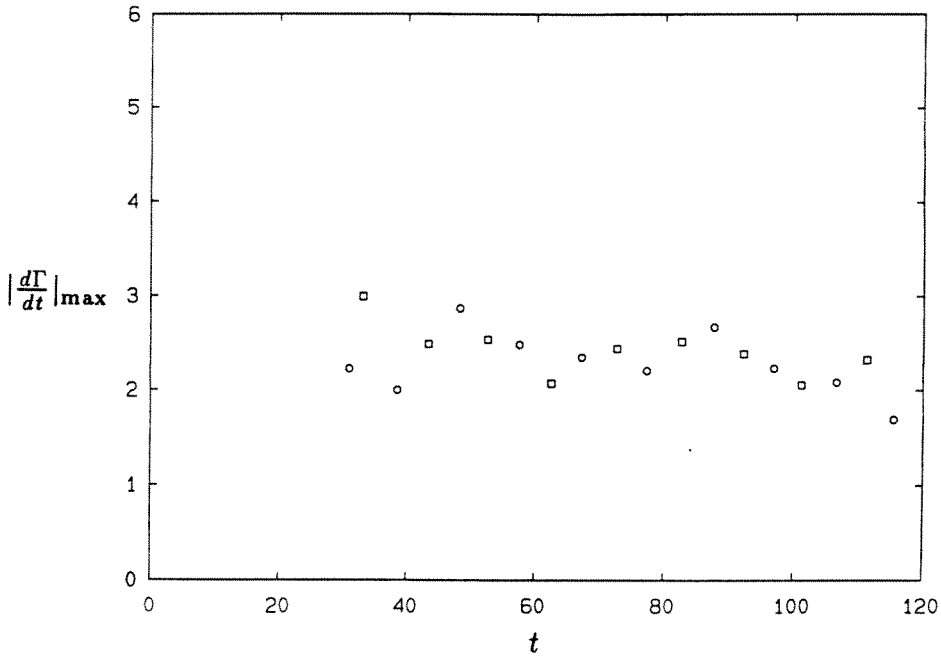
(b)

FIGURE (2.5.13) Cont.
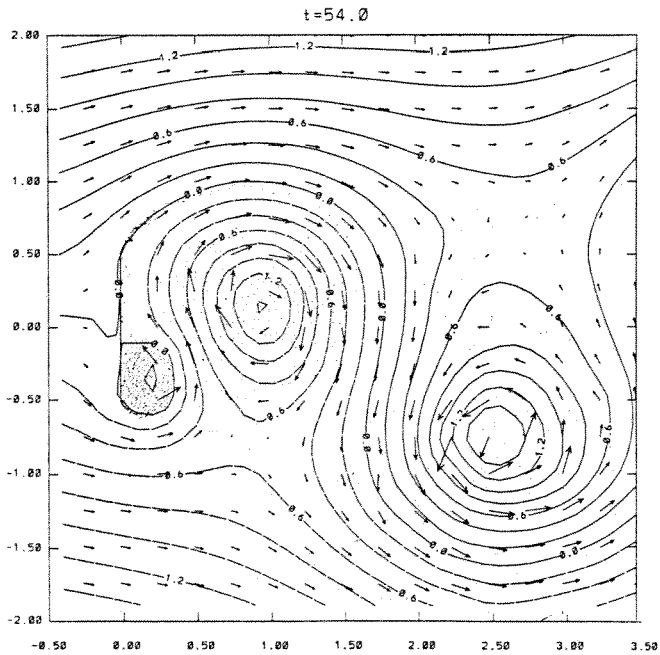
(a)

FIGURE (2.5.14) Flow-vis of an impulsively started normal flat plate in the asymmetric shedding mode, (a) $t = 54.0$; (b) $t = 55.0$; (c) $t = 56.0$; (d) $t = 57.0$; (e) $t = 58.0$.

t=55.0

(b)

t=56.0

(c)

FIGURE (2.5.14)   Cont.

t=57.0

(d)

t=58.0

(e)

FIGURE (2.5.14)   Cont.

(a)

(b)
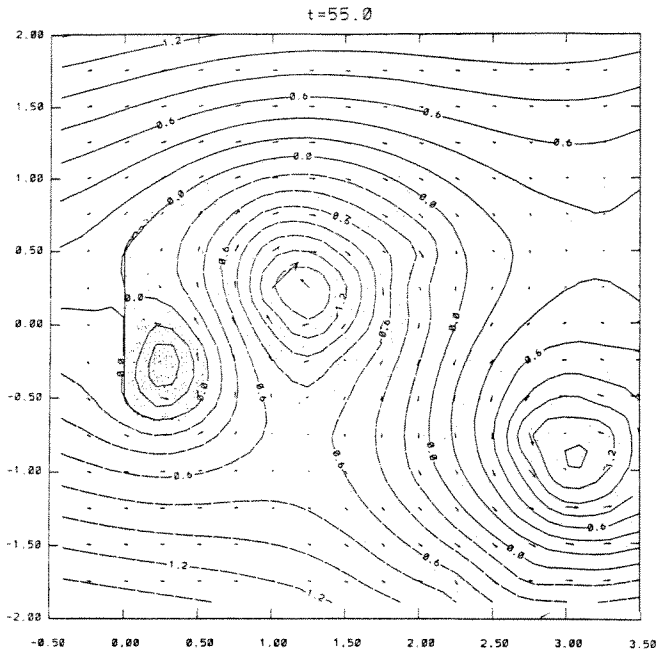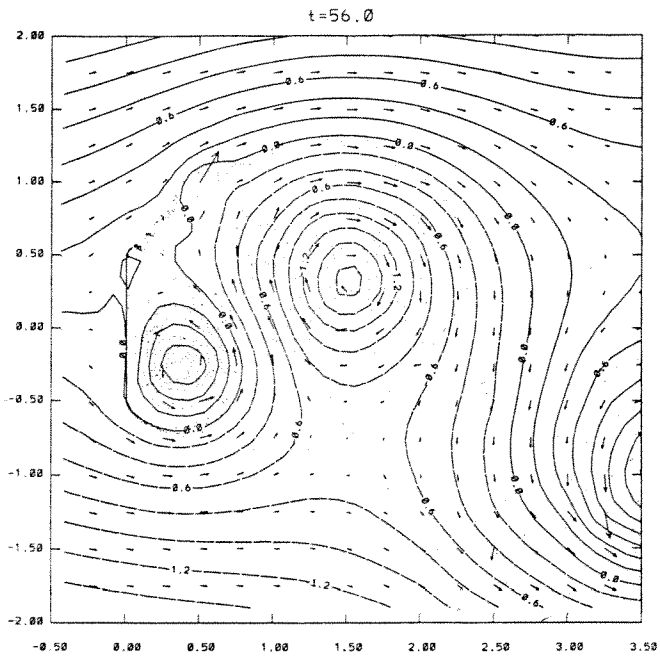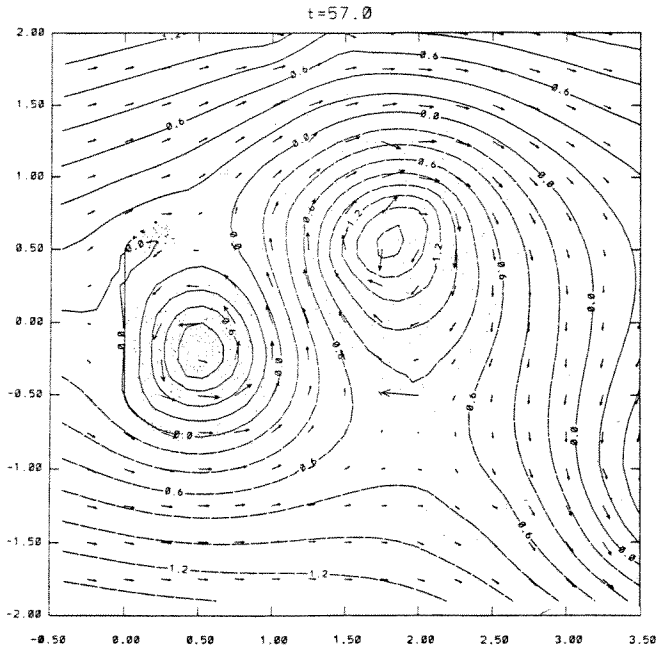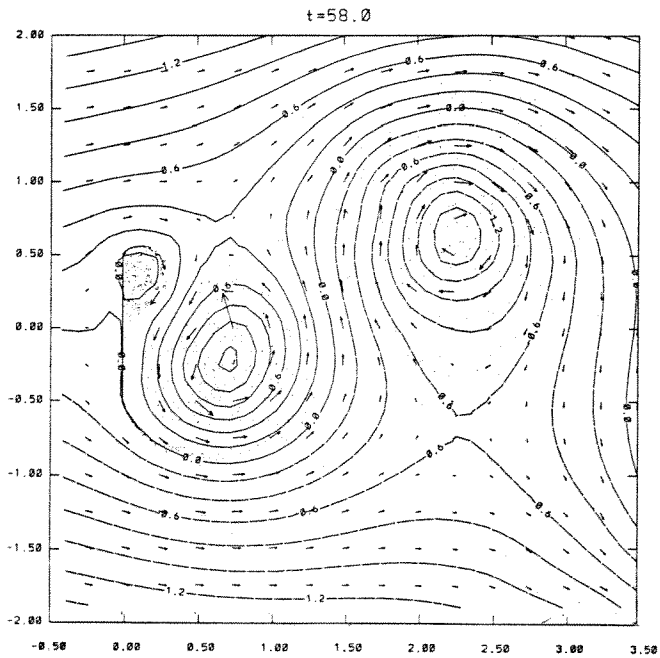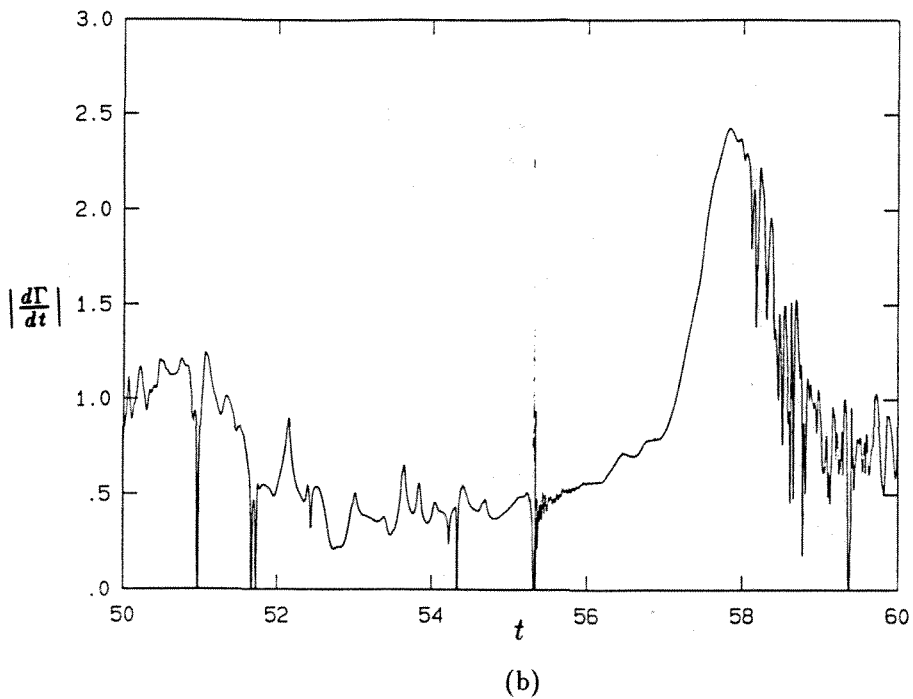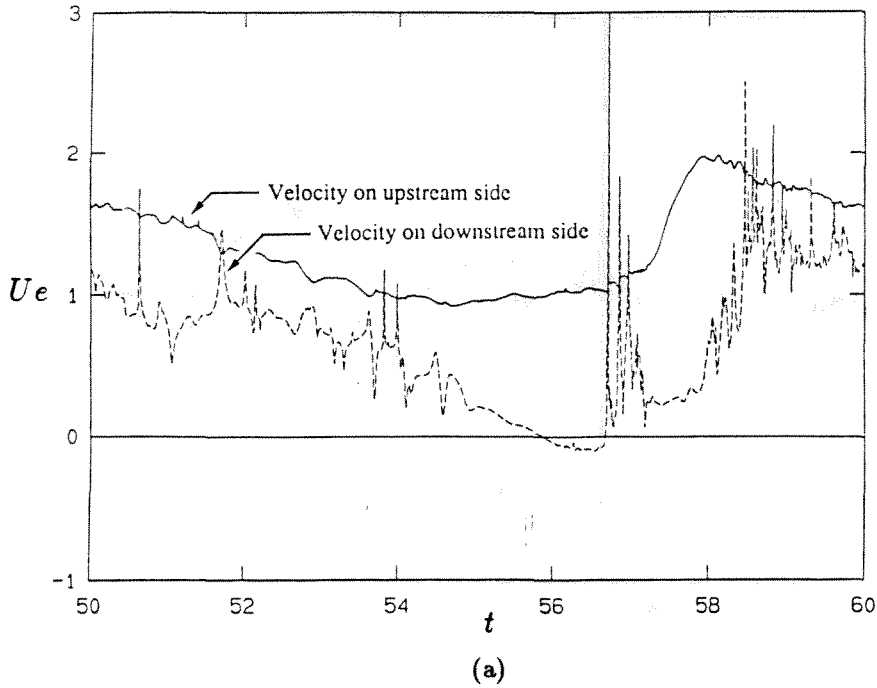
FIGURE (2.5.15) Time histories of (a) Ue_{upper}, (b) $|d\Gamma/dt|_{\text{upper}}$ and (c) C_d over approx. one St cycle of an impulsively started normal flat plate at large time.

(c)
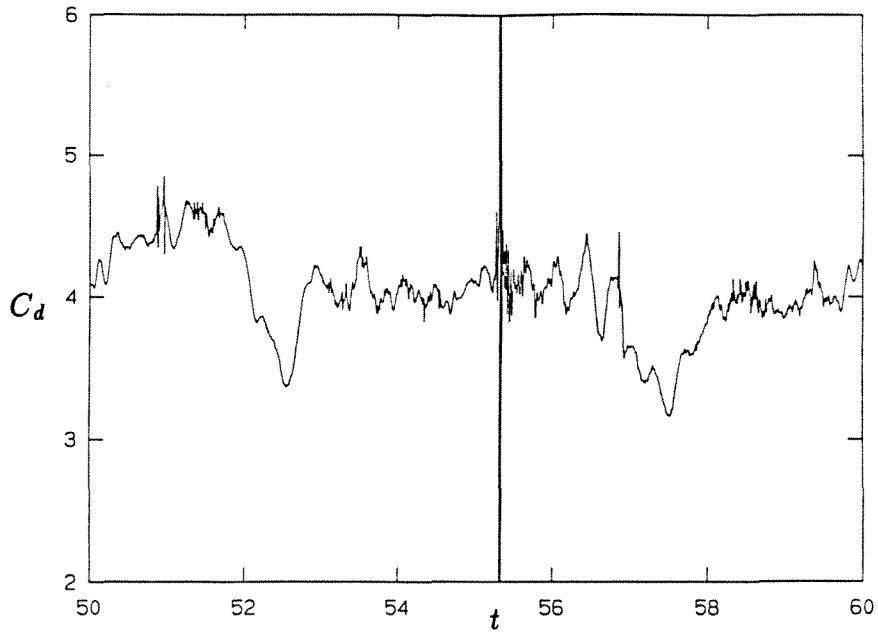
FIGURE (2.5.15) Cont.
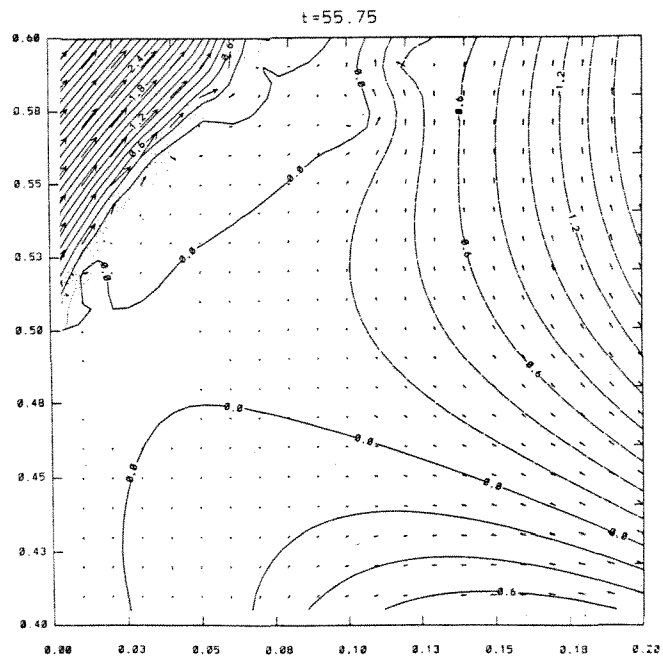
t=55.75

(a)

FIGURE (2.5.16) Zoom-in plots of the flow of Fig. (2.5.14) showing the beginning of vortex shedding, $\psi \times 100$. (a) $t = 55.75$; (b) $t = 55.80$; (c) $t = 56.00$; (d) $t = 57.10$.

t =55.8

(b)

t =56.0

(c)

FIGURE (2.5.16) Cont.

t=57.1
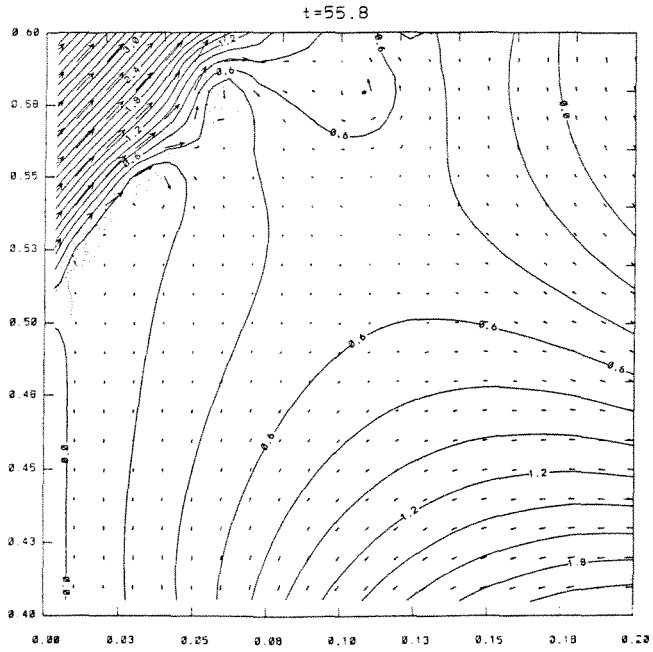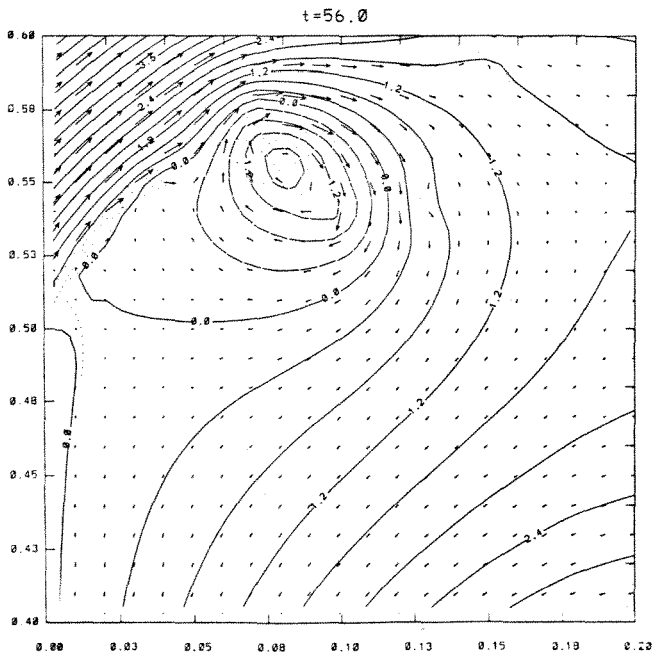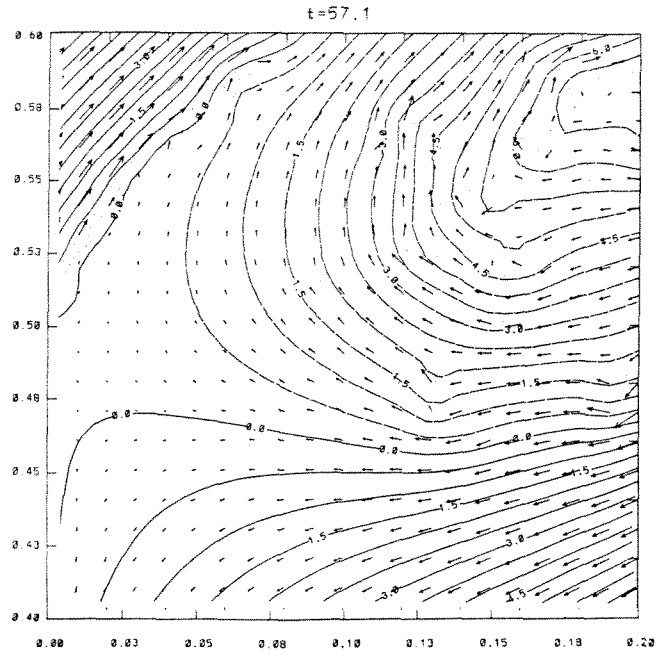
(d)

FIGURE (2.5.16) Cont.
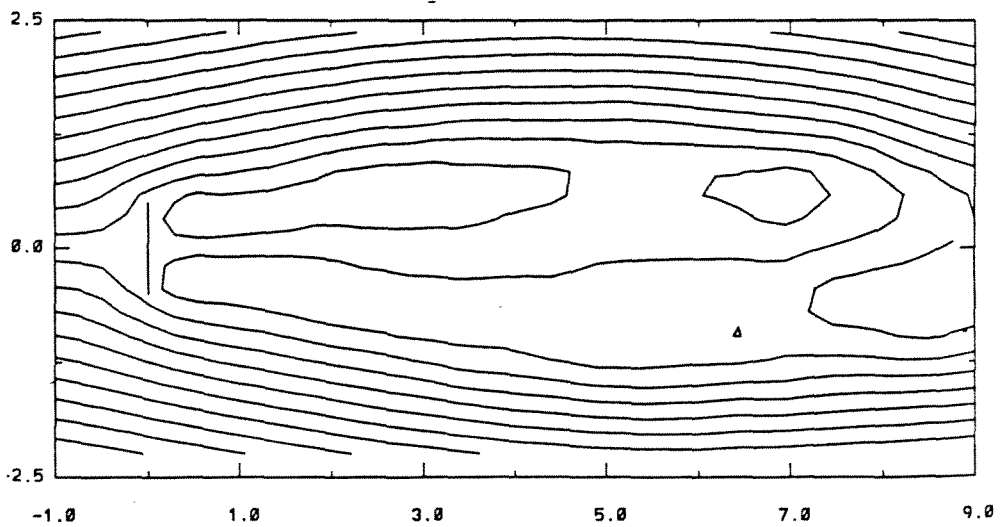
FIGURE (2.5.17) Time-averaged streamline pattern of the flow past an impulsively started normal flat plate.
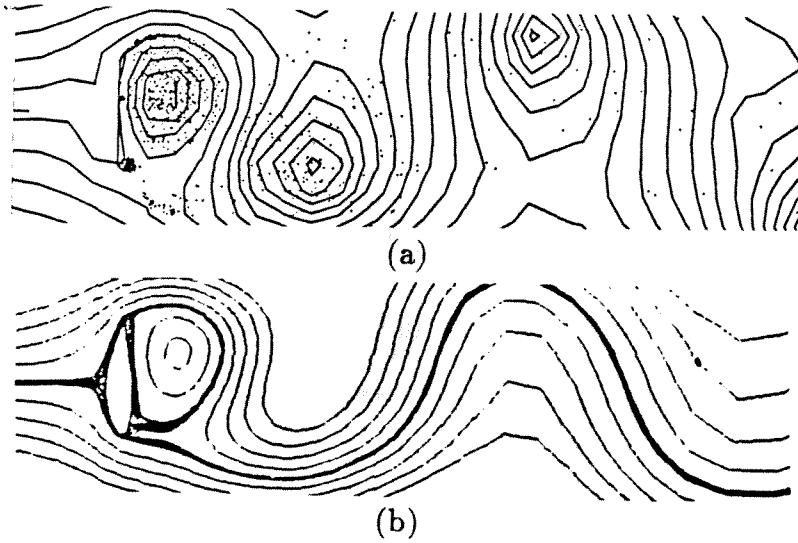
FIGURE (2.5.18) Comparison of the streamline pattern between (a) current calc. and (b) Navier-Stokes calc. of Rogers and Kwak (1988).
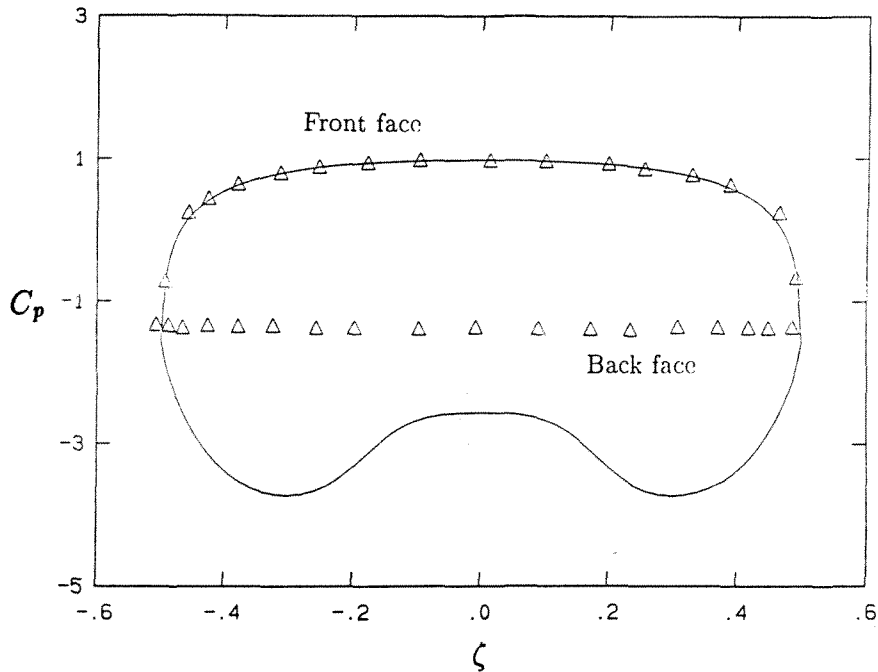
FIGURE (2.5.19) Comparison of the time-averaged pressure distributions on an impulsively started normal flat plate to expt. (a) —— calc. (b) $\triangle$ Fage and Johansen (1927).
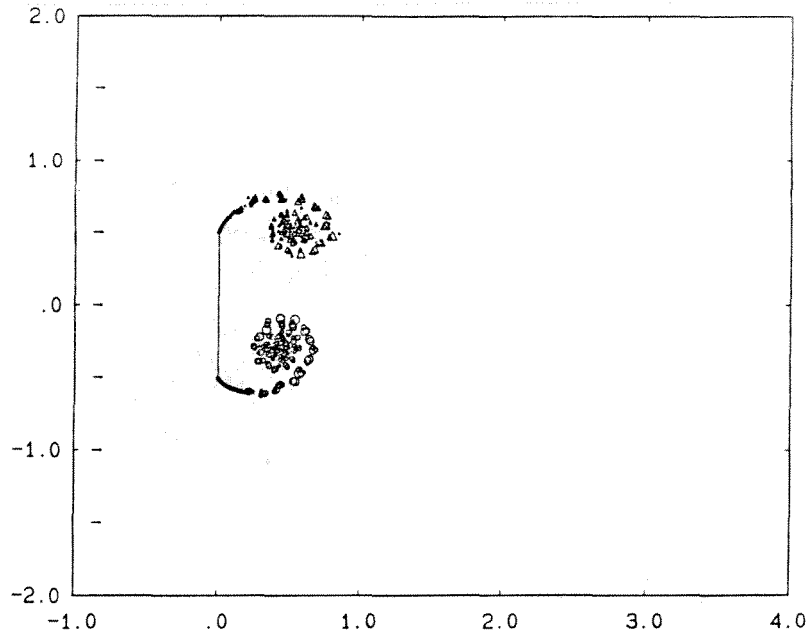
(a)
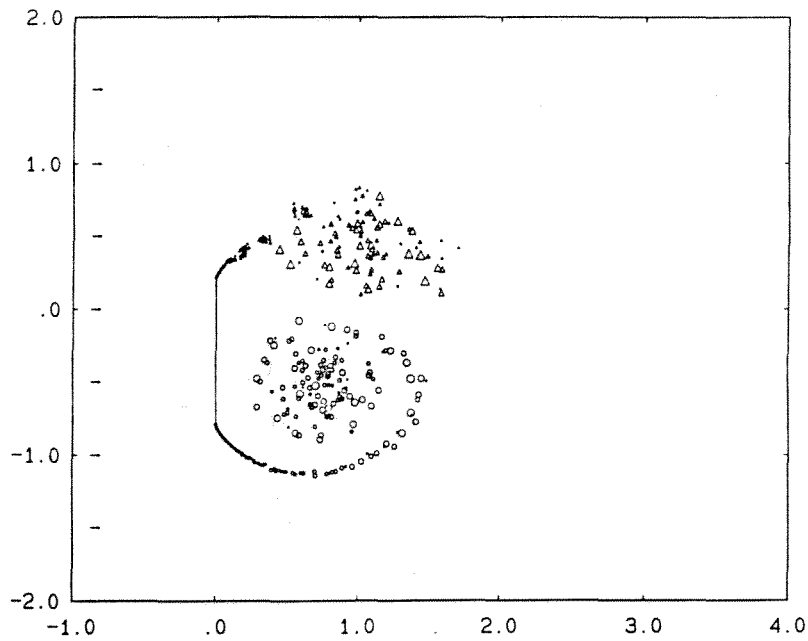
(b)

FIGURE (2.5.20) Flow-vis of a ramp-started oscillating normal flat plate, $T_r = 2.0$, $T_f = 9.0$ and $v_f = 0.2U_\infty$. (a) $t = 2.25$; (b)$t=4.50$; (c) $t = 6.75$; (d) $t = 9.00$; (e) $t = 11.25$.
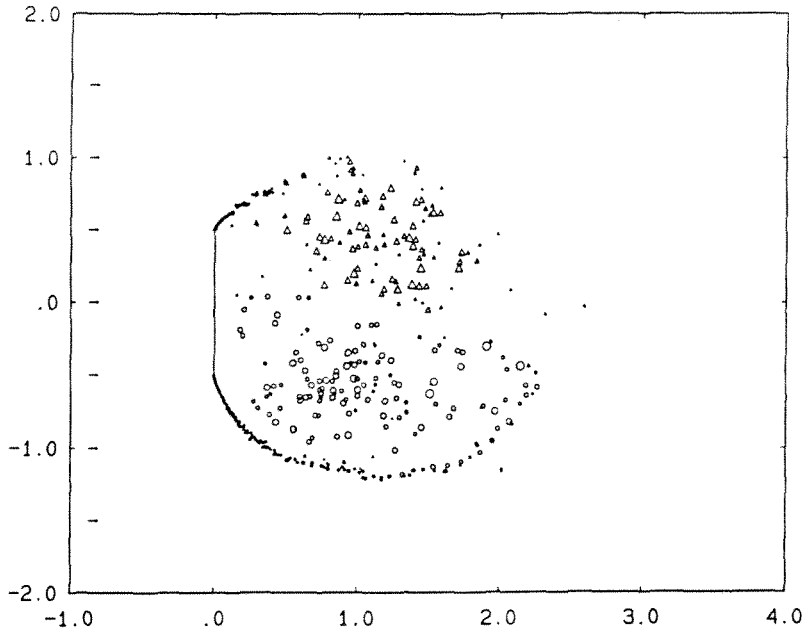
(c)
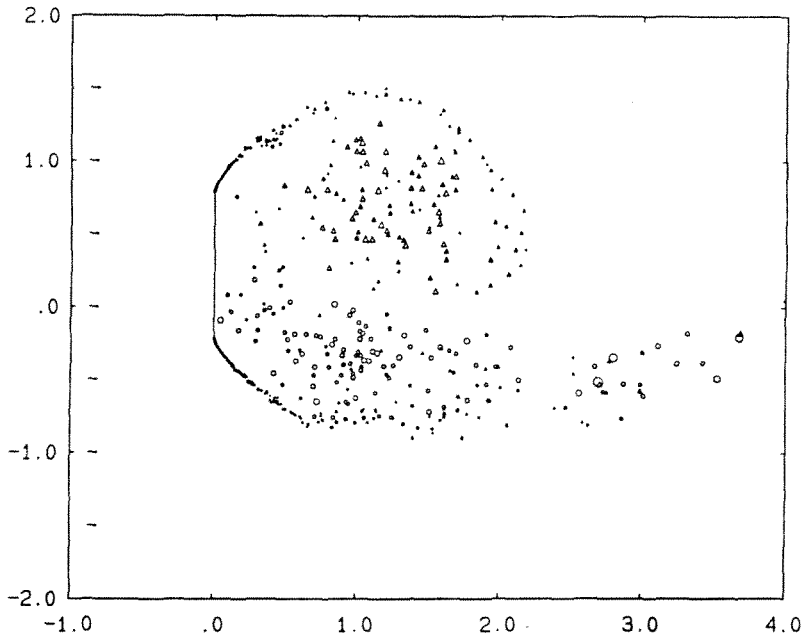
(d)

FIGURE (2.5.20) Cont.
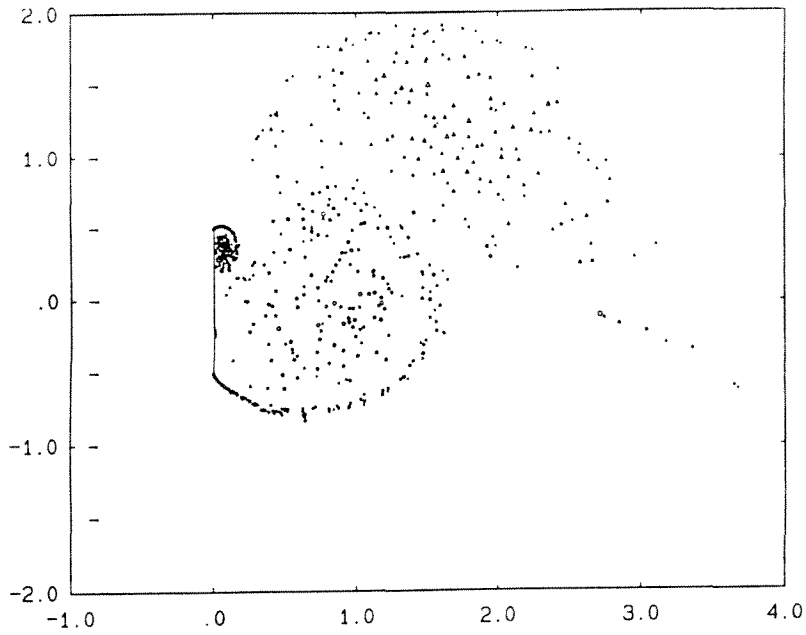
(e)

FIGURE (2.5.20) Cont.
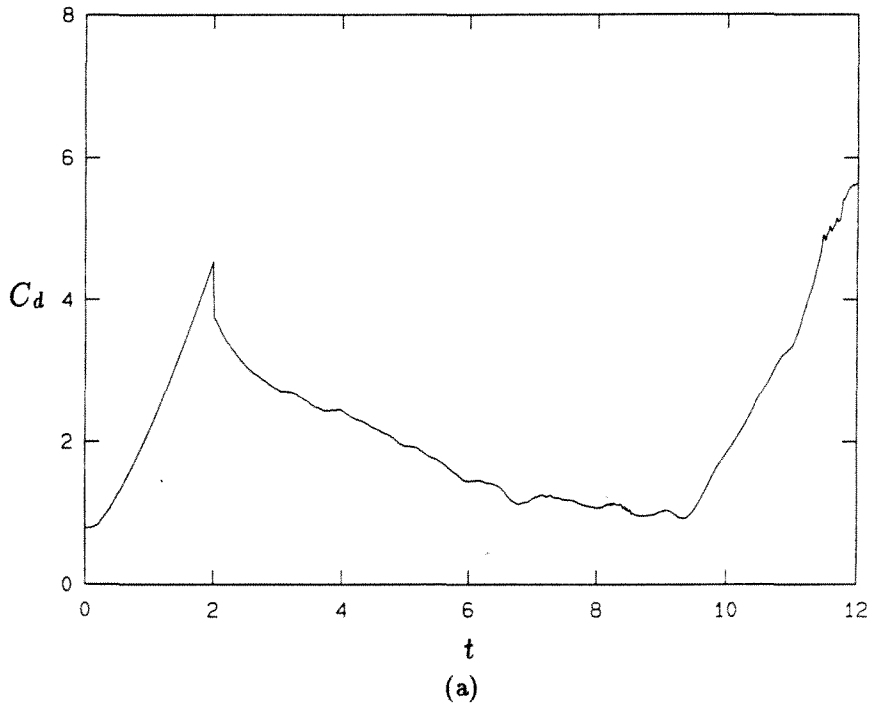
(a)

FIGURE (2.5.21) Short-time histories of (a) C_d, (b) —— $|d\Gamma/dt|_{\text{upper}}$, — — — — $|d\Gamma/dt|_{\text{lower}}$; (c) $U_{e_{\text{lower}}}$ on —— front face, — — — — backface and — — · — — , plate velocity; (d) $U_{e_{\text{upper}}}$ on —— front face, — — — — backface and — — · — — , plate velocity. Flow the same as Fig. (2.5.20).
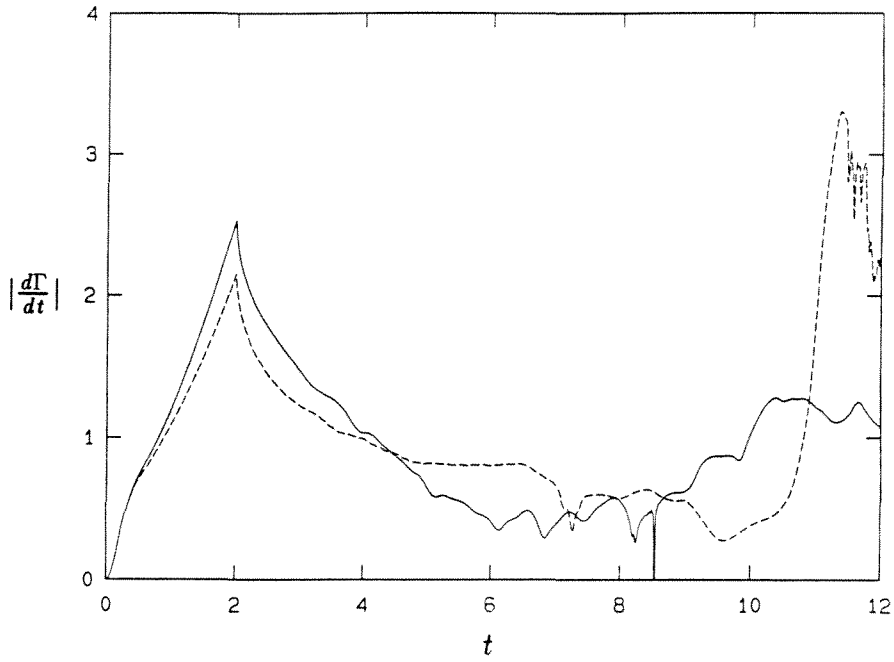
(b)
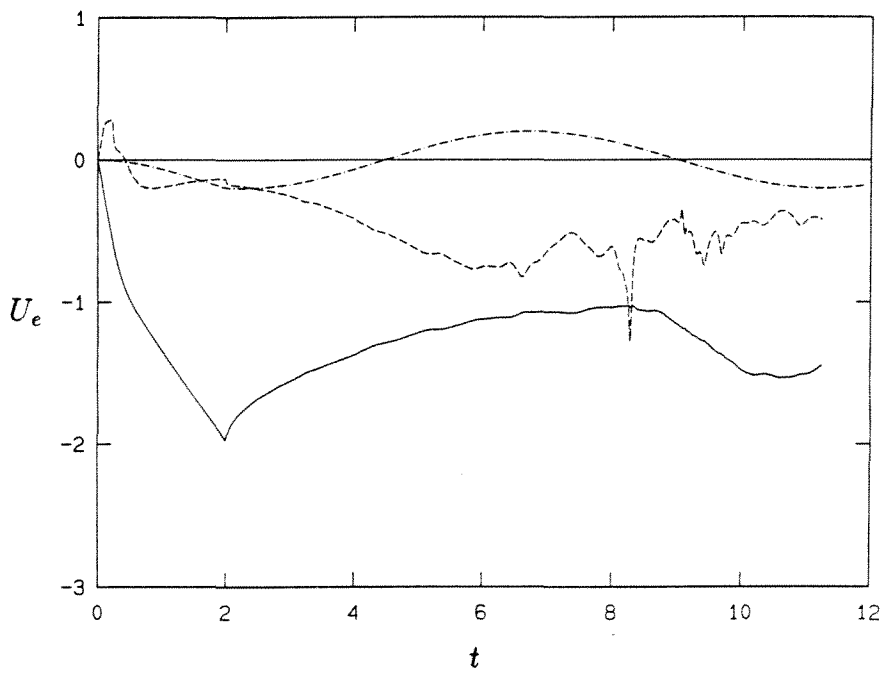
(c)

FIGURE (2.5.21) Cont.
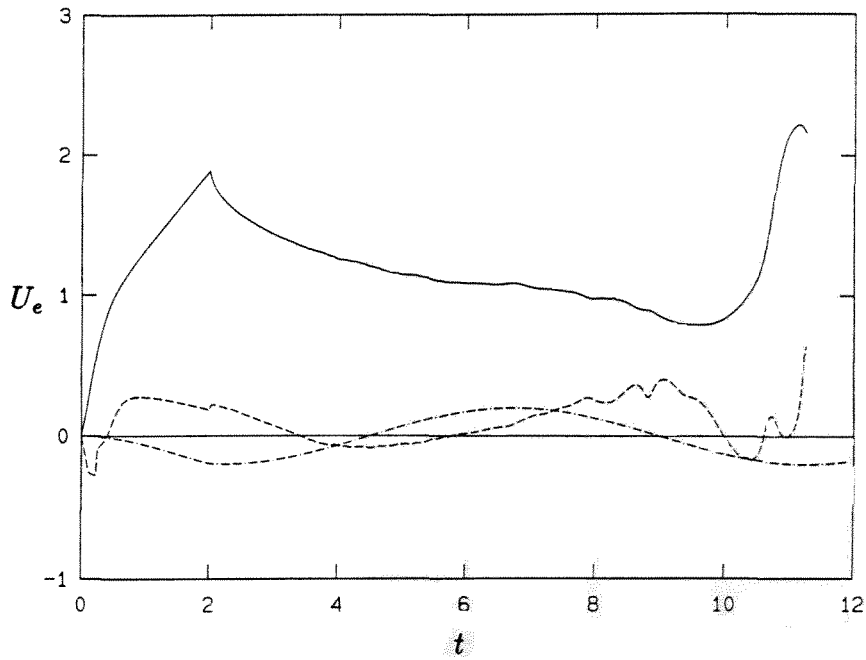
(d)

FIGURE (2.5.21) Cont.
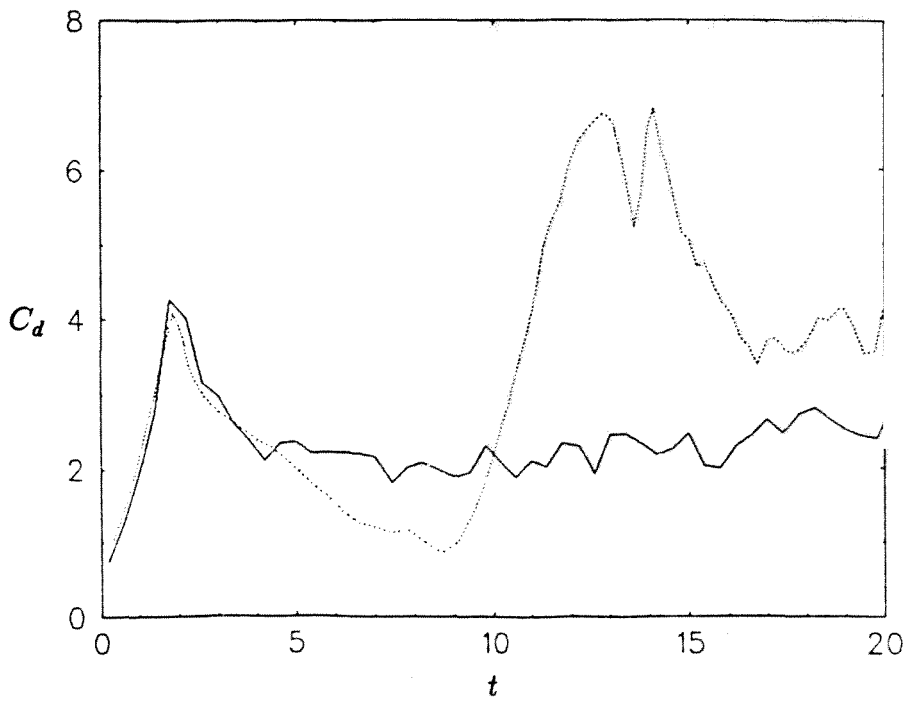
FIGURE (2.5.22) Comparison of C_d at an early time of a ramp-started oscillating normal flat plate to expt. —— calc. ···· Lisoski and Roshko (1989).
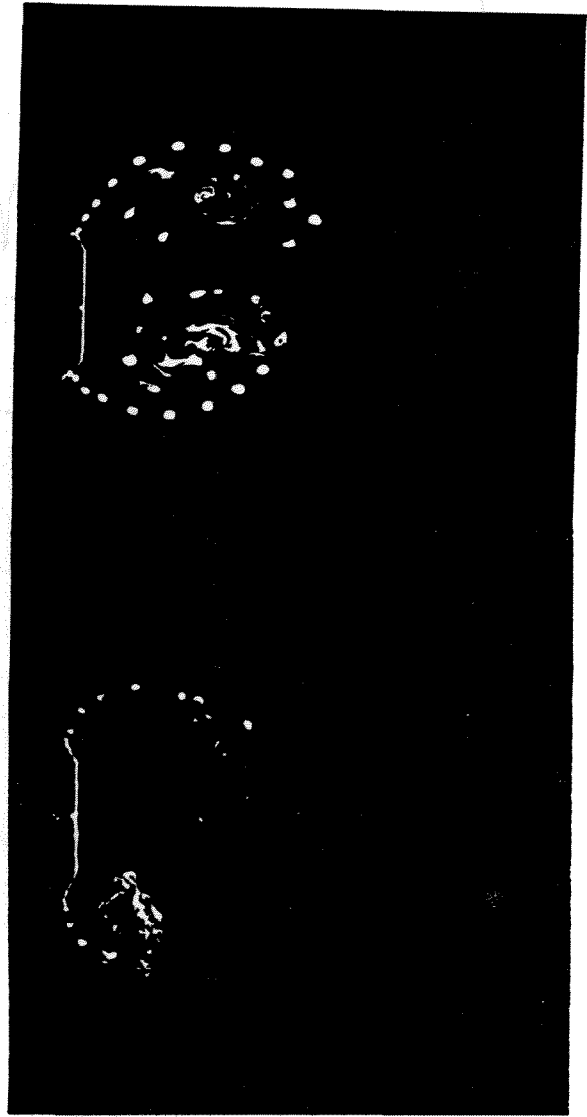
calc.   expt.

FIGURE (2.5.23) Comparison of flow-vis of a ramp-started oscillating normal flat plate to the expt.
of Lisoski and Roshko (1989). (a) $t = 5$; (b) $t = 19$.

143
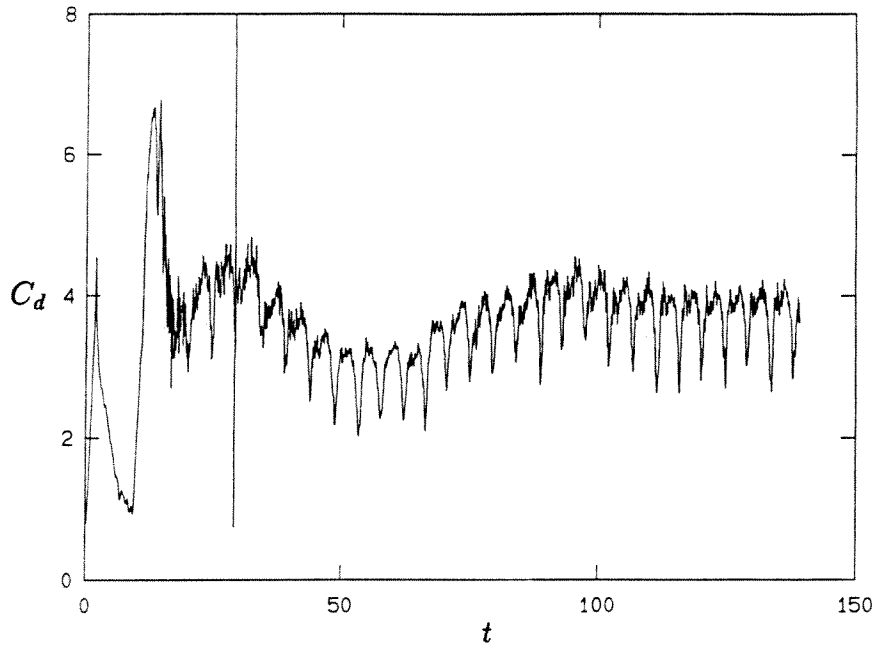
(a)
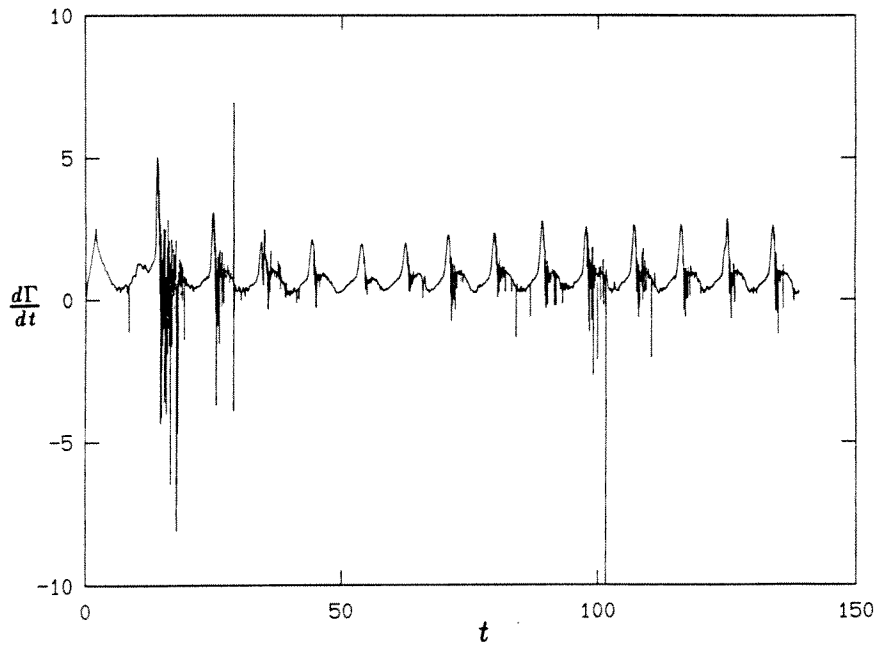
(b)

FIGURE (2.5.24) Long-time histories of (a) C_d; (b) $d\Gamma/dt|_{lower}$ and (c) $d\Gamma/dt|_{upper}$ of a ramp-started oscillating normal flat plate.
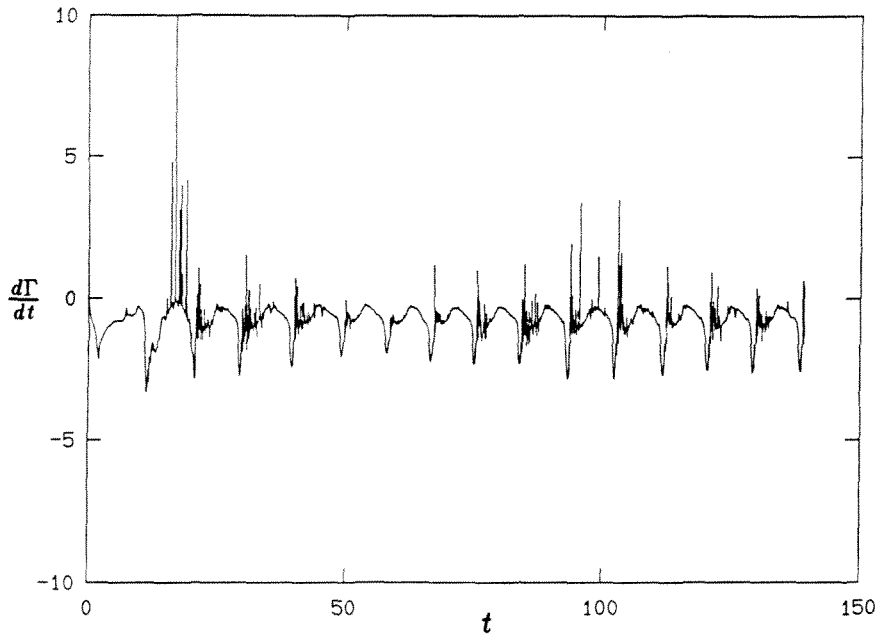
(c)

FIGURE (2.5.24) Cont.
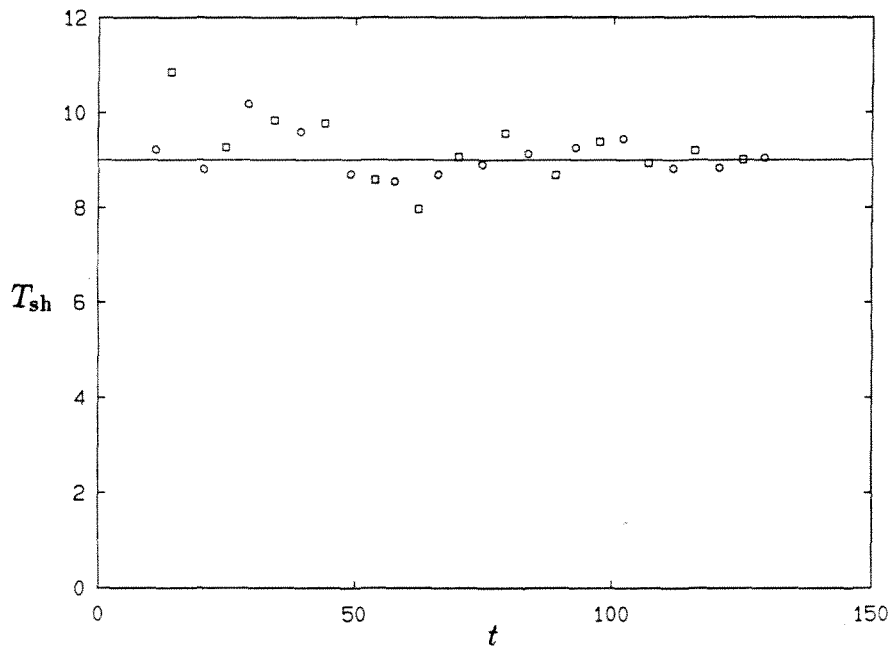
(a)

FIGURE (2.5.25) Time histories of (a) T_{sh}, (b) $|d\Gamma/dt|_{max}$ and (c) θ_{lag} of a ramp-started oscillating normal flat plate.

(b)

(c)

FIGURE (2.5.25) Cont.

(a)

(b)
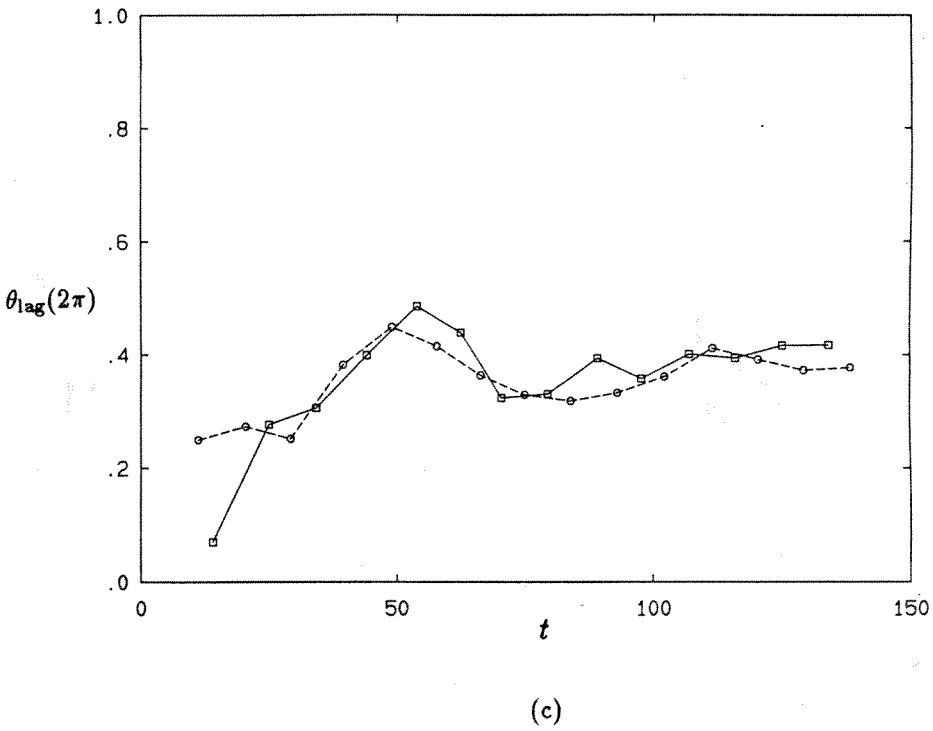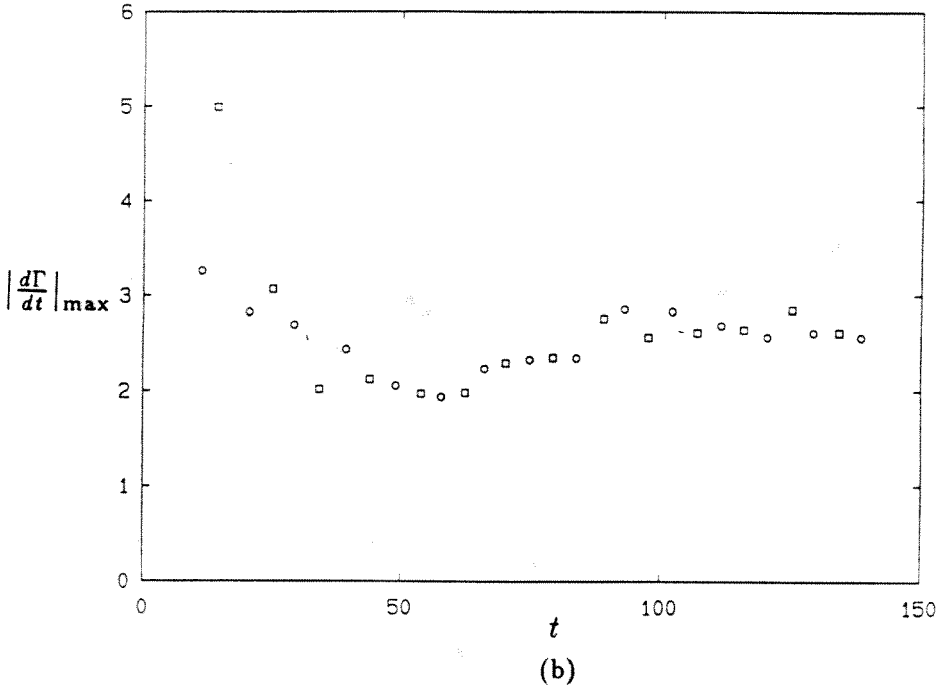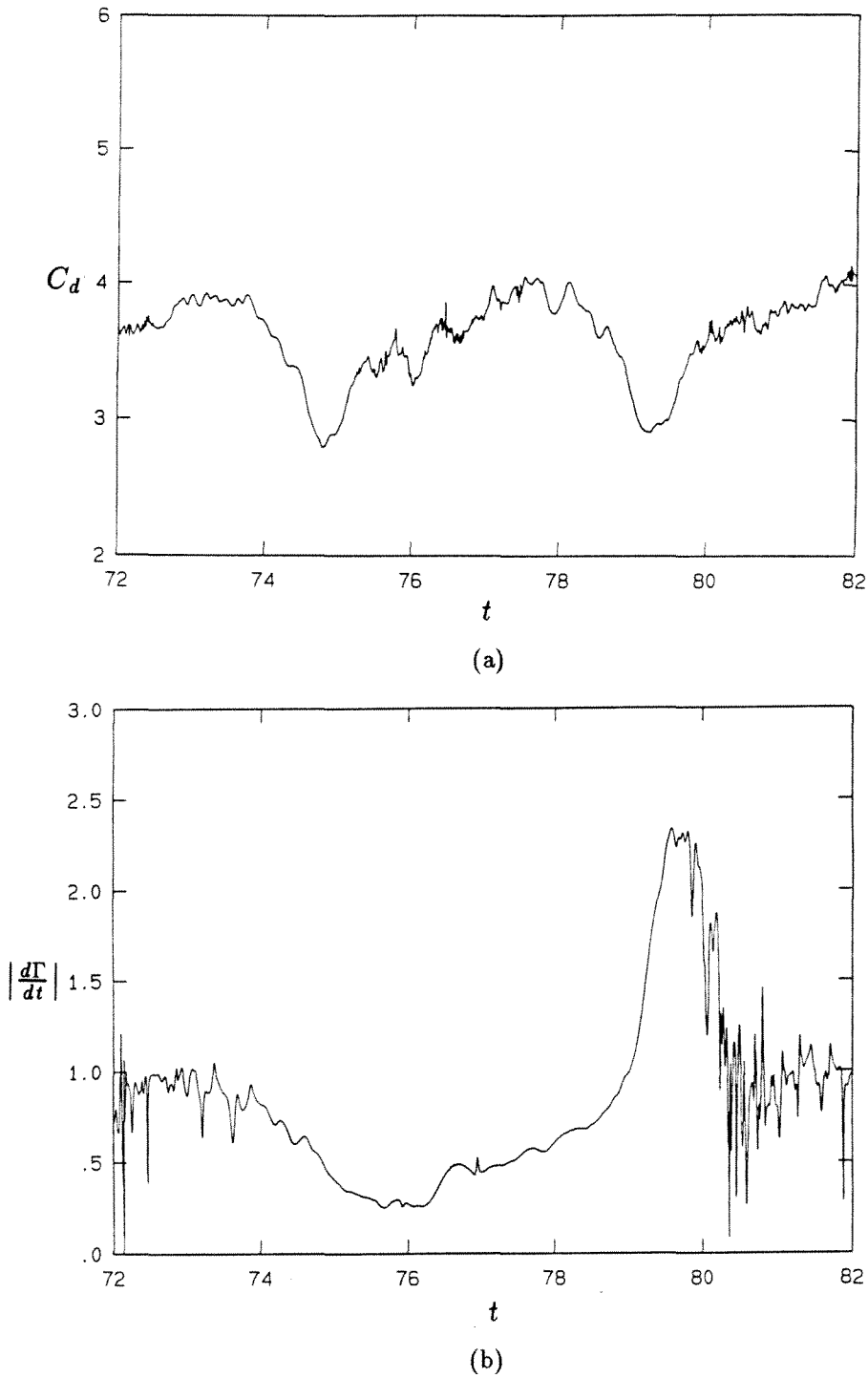
FIGURE (2.5.26) Time histories over one forcing cycle of a ramp-started oscillating normal flat plate. (a) C_d; (b) $d\Gamma/dt|_{\text{lower}}$; (c) $d\Gamma/dt|_{\text{upper}}$; (d) Ue_{upper} on —— front face; — — — — back face; — — · — — plate velocity.
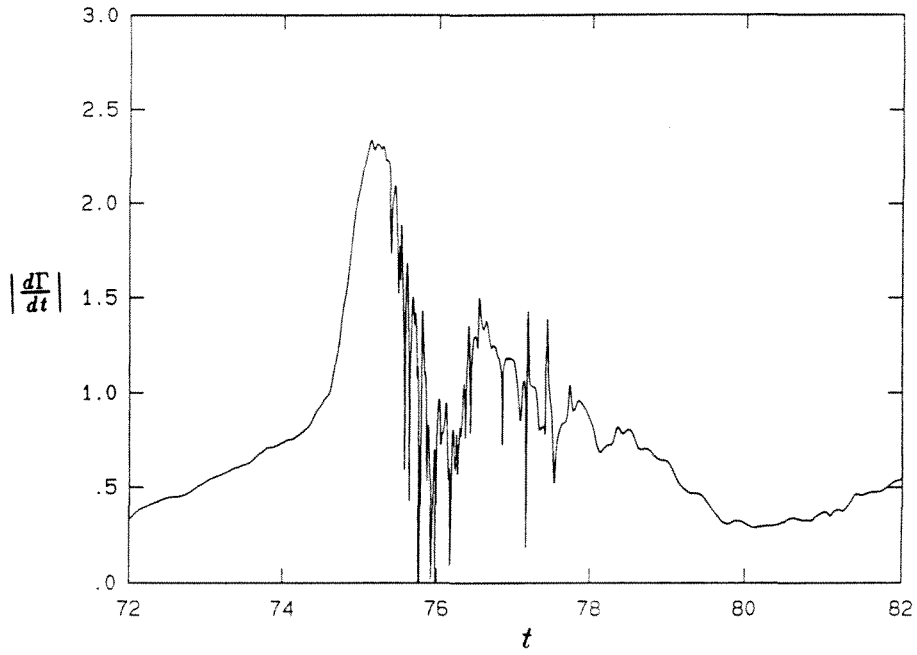
(c)
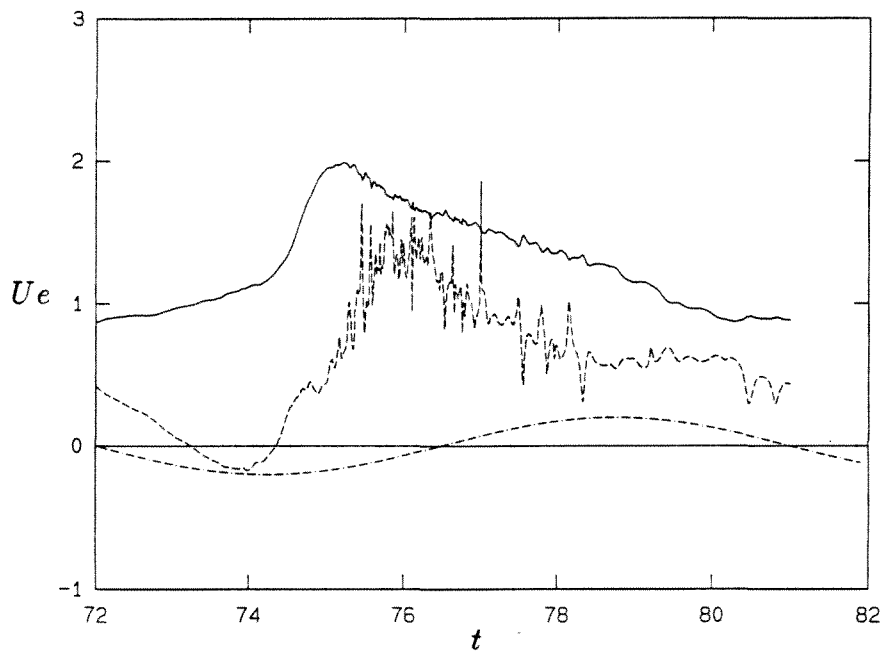
(d)

FIGURE (2.5.26)   Cont.
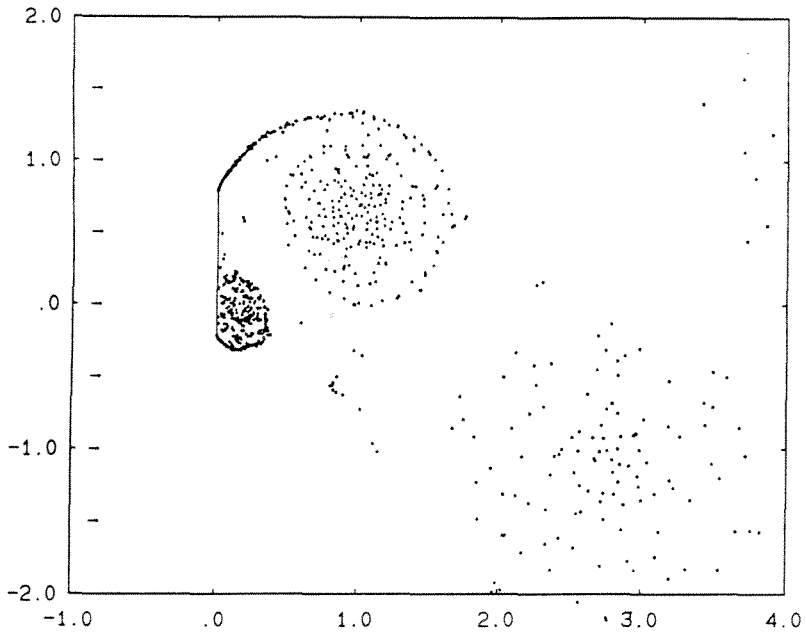
(a)
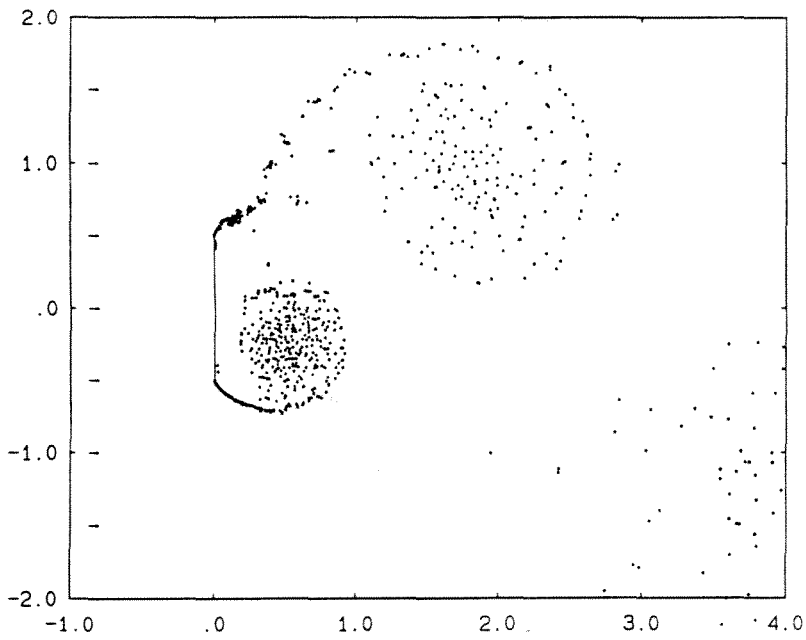
(b)

FIGURE (2.5.27) Flow-vis of a ramp-started oscillating normal flat plate at large time. (a) $t = 72$; (b) $t = 74.25$; (c) $t = 76.50$; (d) $t = 78.75$.
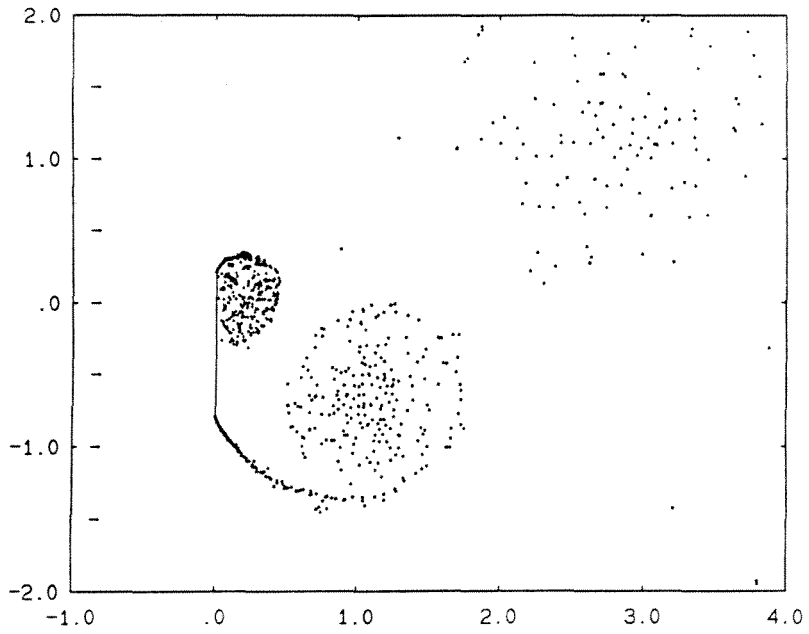
(c)
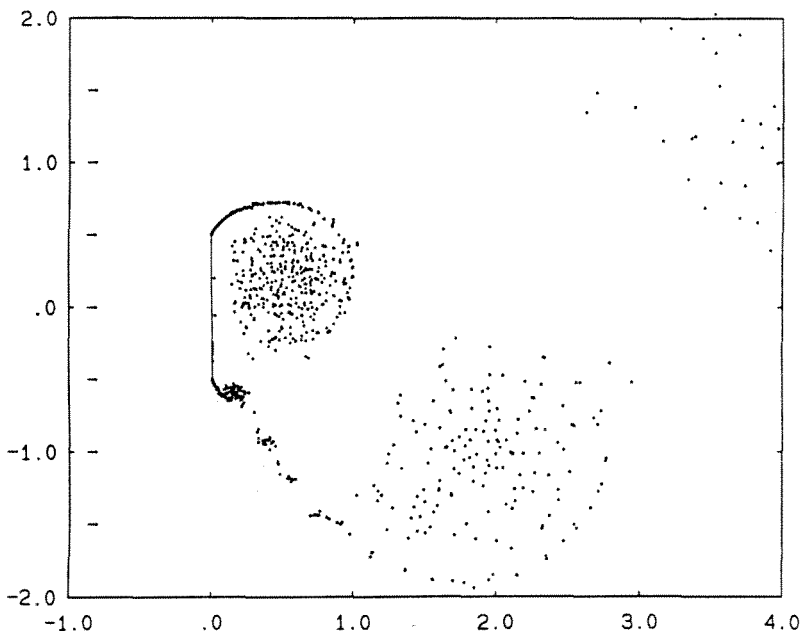
(d)

FIGURE (2.5.27) Cont.
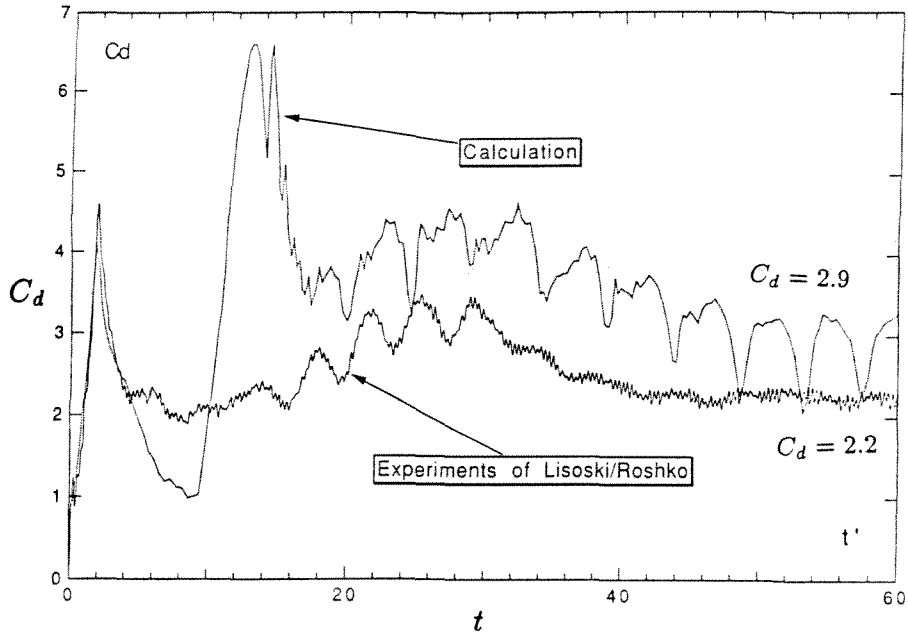
FIGURE (2.5.28) Comparison of C_d of a ramp-started oscillating normal flat plate to the expt. of Lisoski and Roshko (1989).

(a)
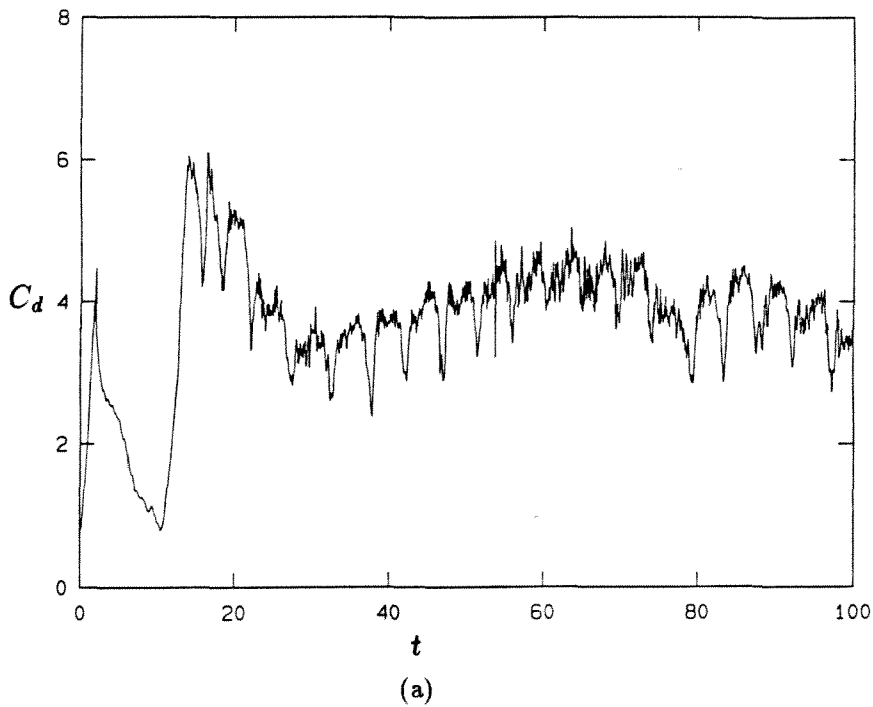
FIGURE (2.5.29) Time histories of (a) C_d; (b) $d\Gamma/dt|_{lower}$ and (c) $d\Gamma/dt|_{upper}$ of a ramp-started oscillating normal flat plate, $T_r = 2$, $T_f = 11$ and $v_f = 0.2U_\infty$.
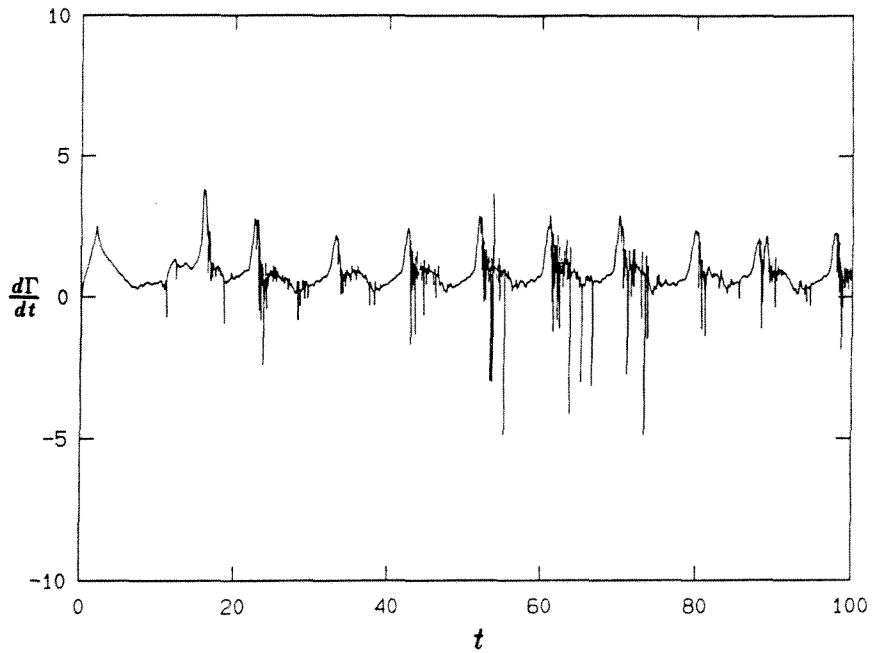
(b)

(c)
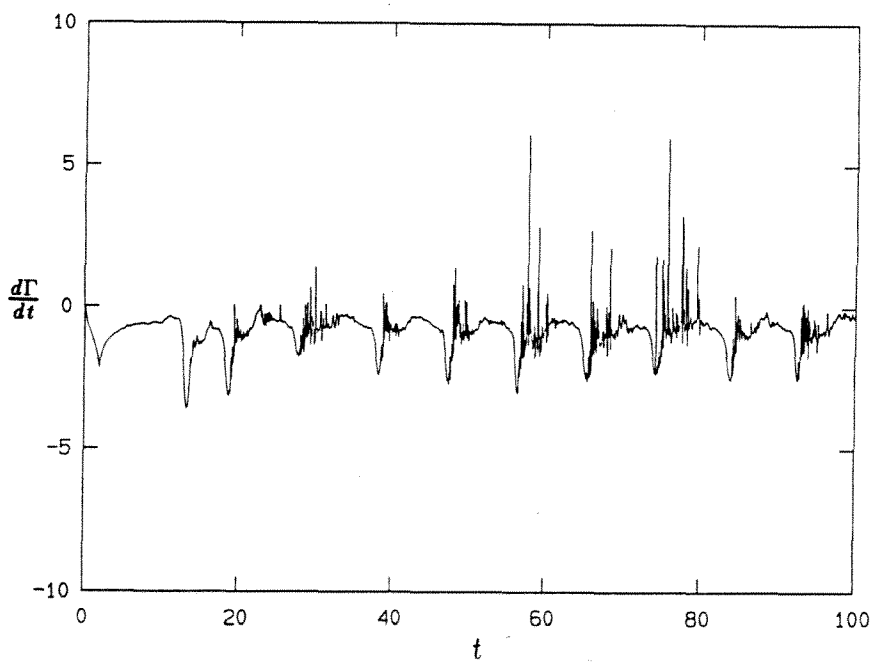
FIGURE (2.5.29) Cont.
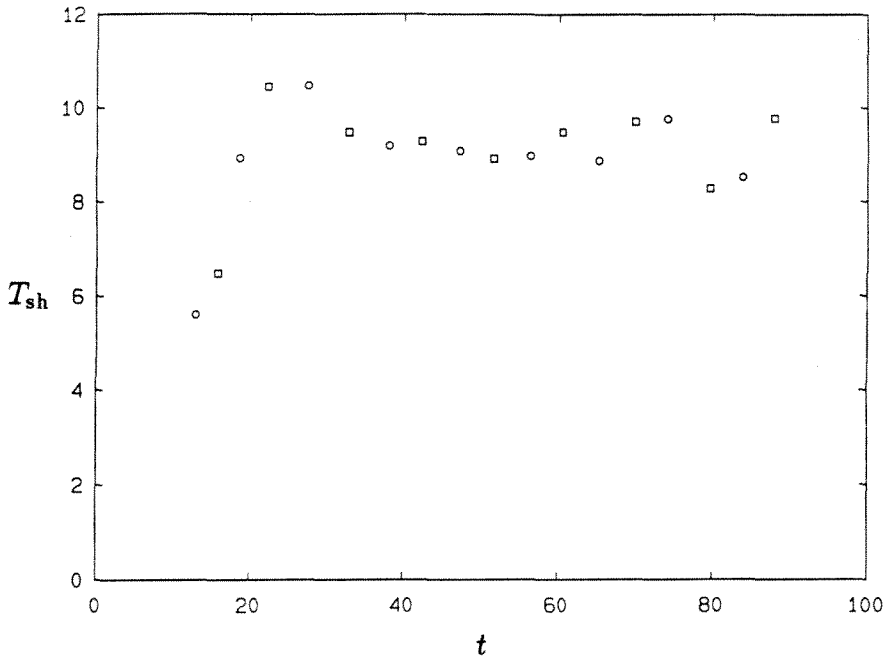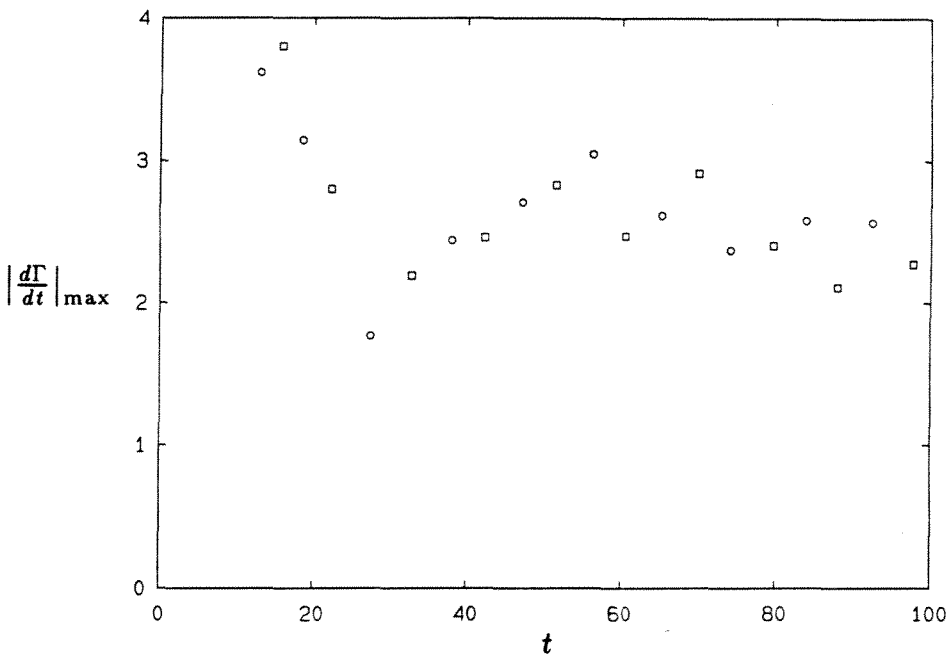
FIGURE (2.5.30) Time histories of (a) T_{sh}; (b) $|d\Gamma/dt|_{\text{max}}$; (c) θ_{lag} of a ramp-started oscillating normal flat plate. Parameters the same as Fig. (2.5.29).
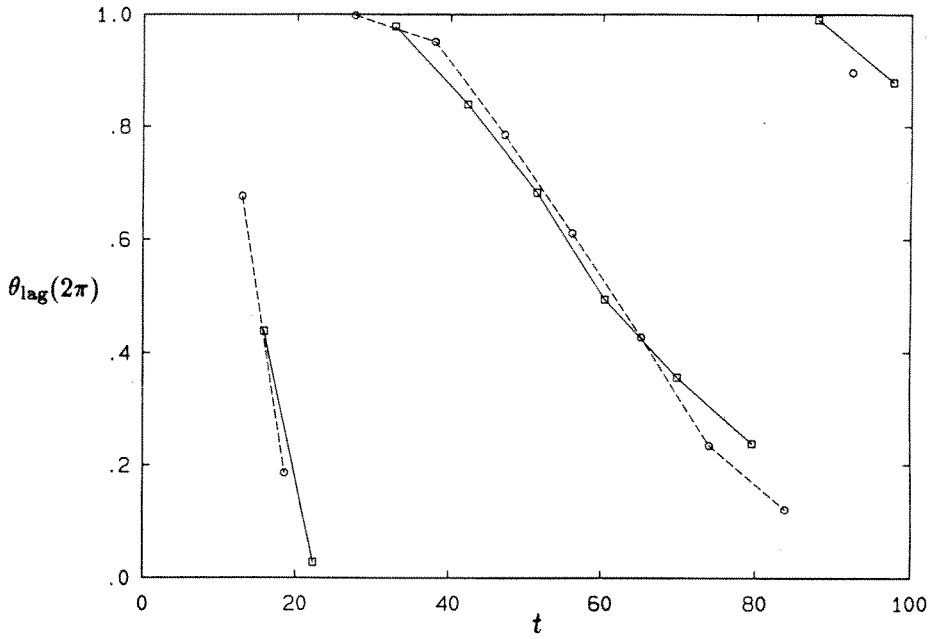
(c)

FIGURE (2.5.30) Cont.
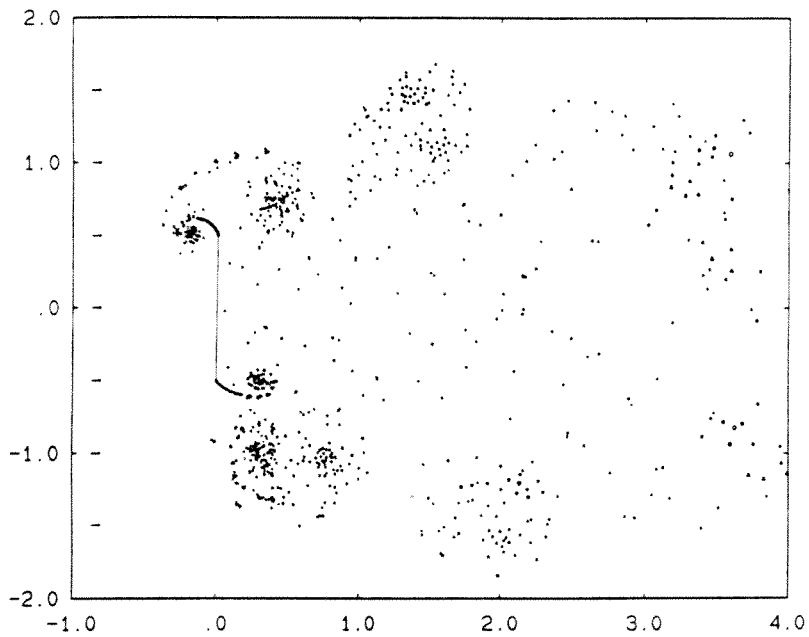
(a)

FIGURE (2.5.31) Flow-vis of a pitching normal flat plate, $T_f = 1$, $\alpha_{f_{max}} = 36.5°$. (a) $t = 15.00$; (b) $t = 15.25$; (c) $t = 15.50$; (d) $t = 15.75$; (e) $t = 16.00$.
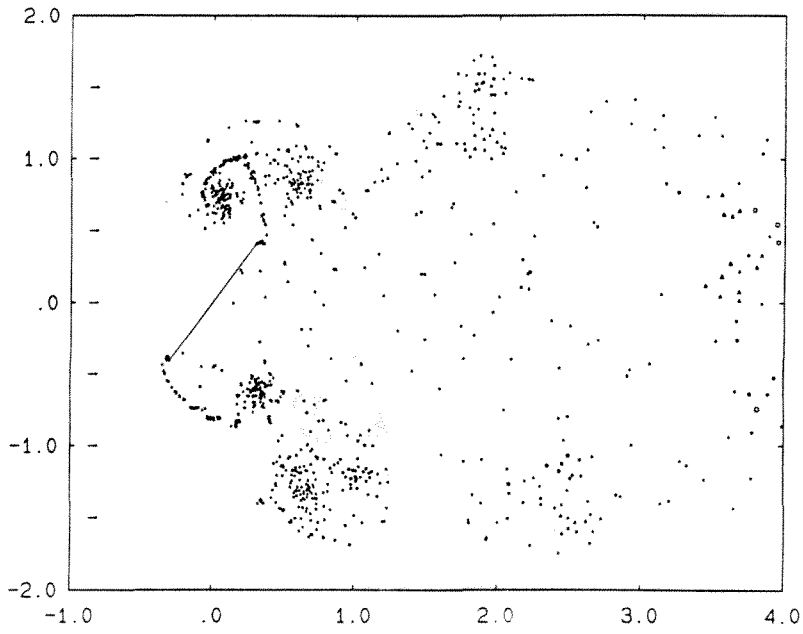
(b)
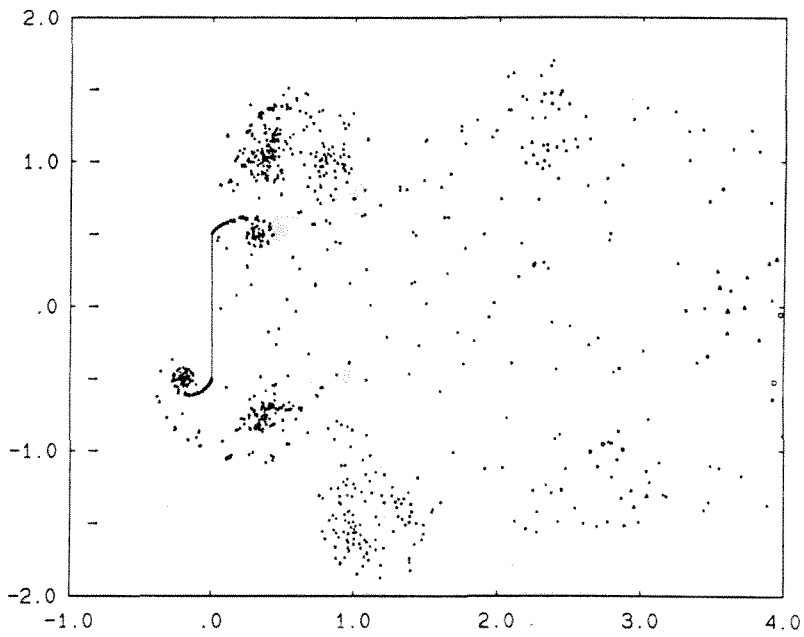
(c)

FIGURE (2.5.31) Cont.
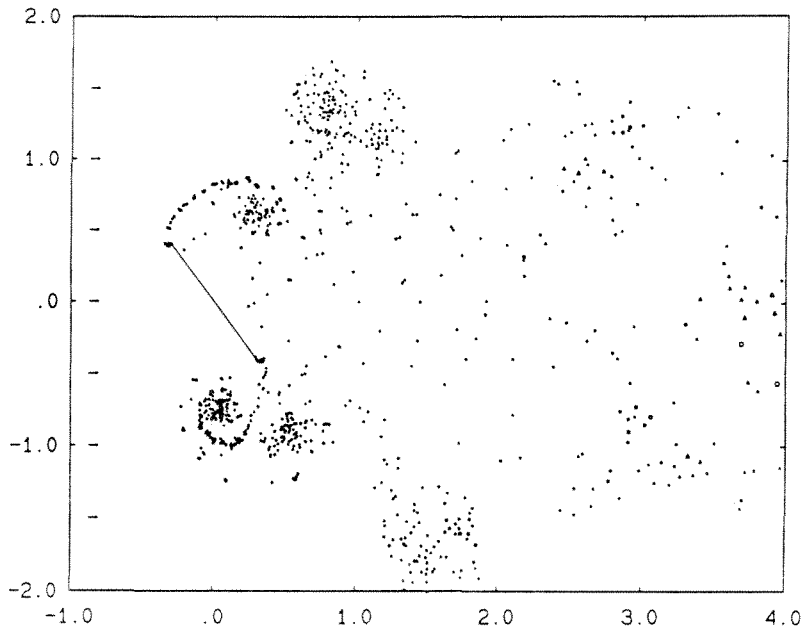
(d)
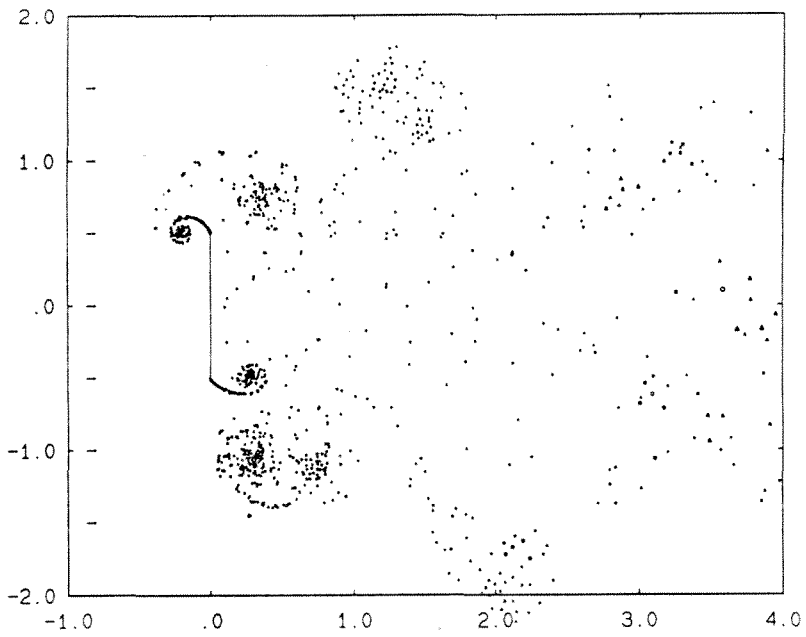
(e)

FIGURE (2.5.31) Cont.
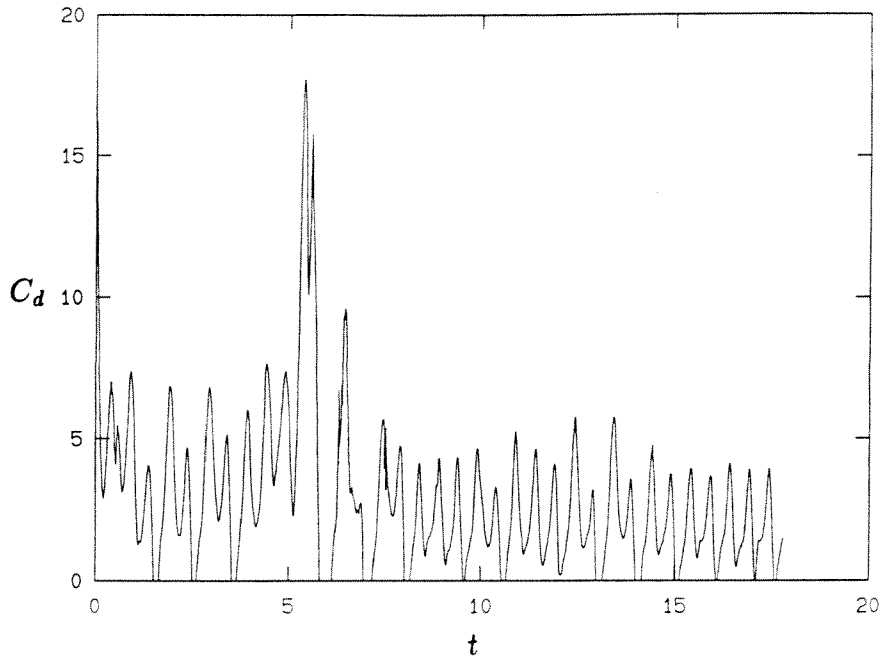
(a)
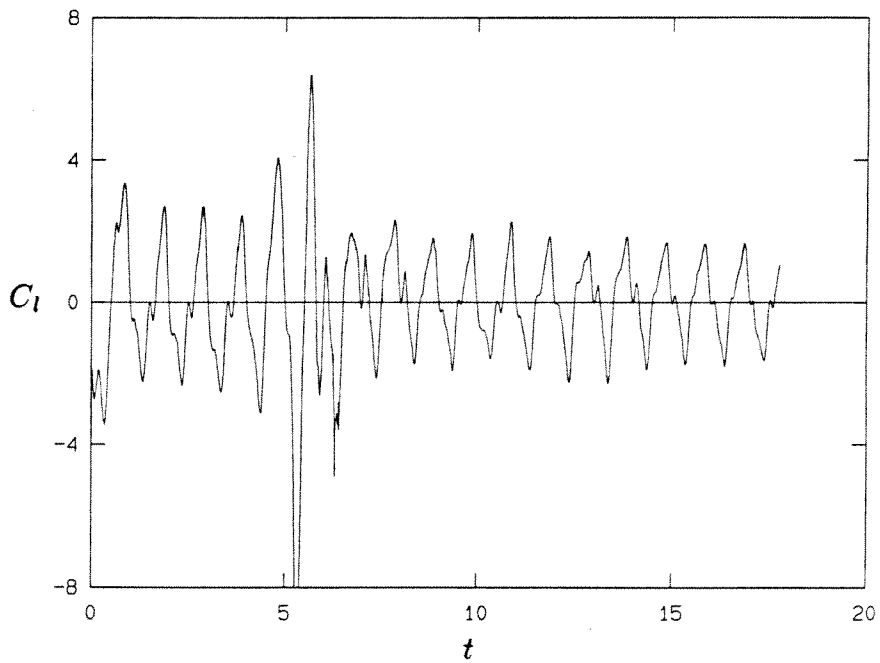
(b)

FIGURE (2.5.32) Time histories of (a) C_d, (b) C_l, (c) $d\Gamma/dt|_{\text{lower}}$ and (d) $d\Gamma/dt|_{\text{upper}}$ of a pitching normal flat plate. Parameters the same as Fig. (2.5.31).

$\dfrac{d\Gamma}{dt}$

t

(c)

$\dfrac{d\Gamma}{dt}$

t

(d)
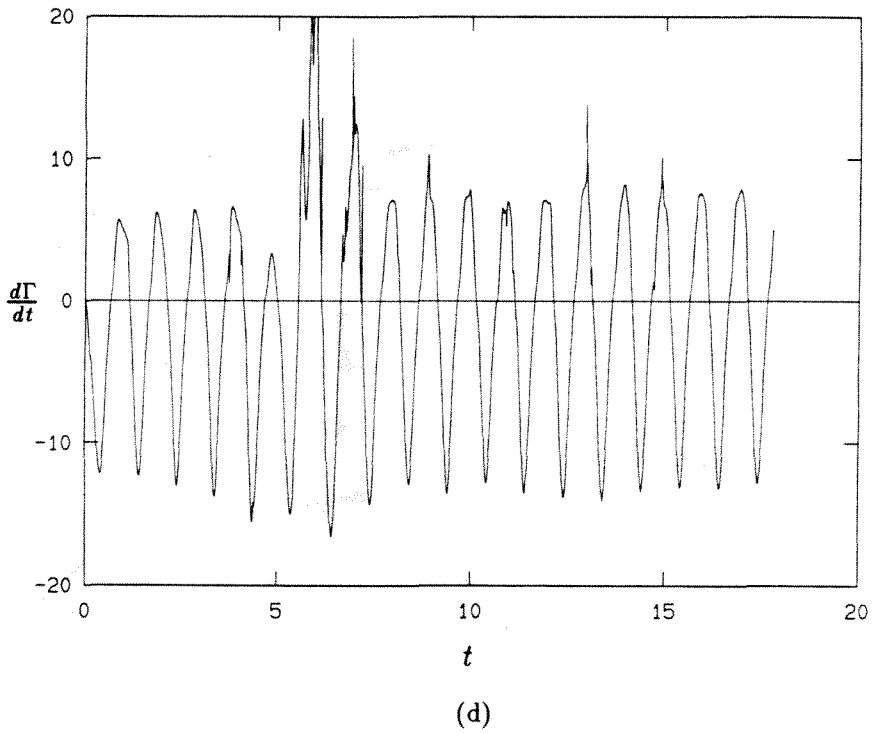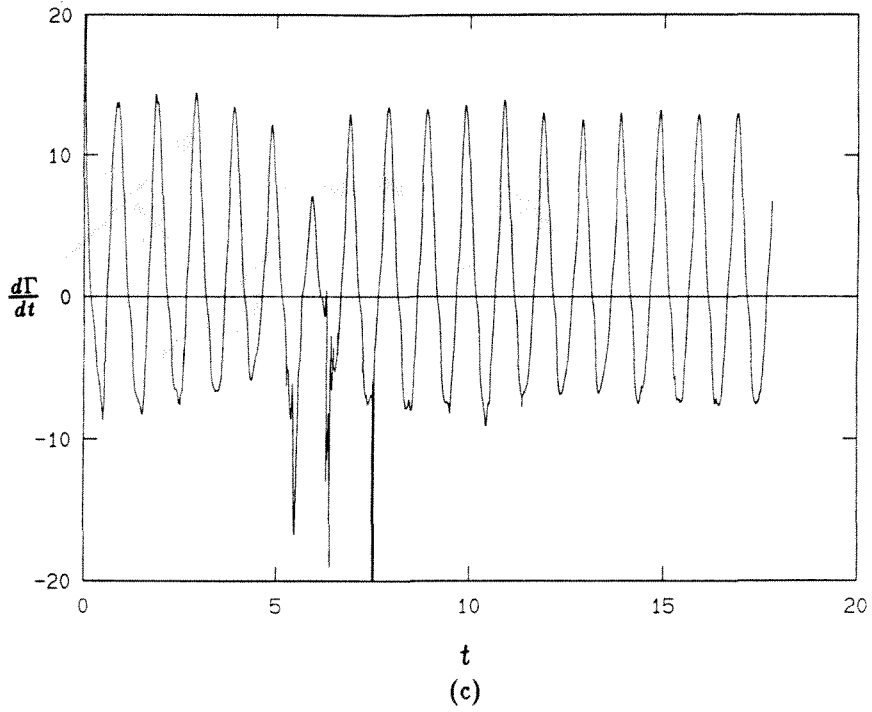
FIGURE (2.5.32) Cont.
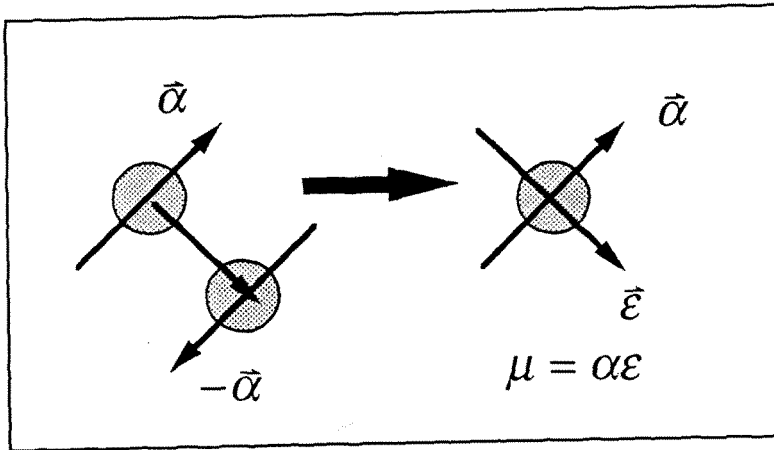
FIGURE (3.3.1) Schematic showing the merging of a pair of opposite sign vortex vectors into a vortex dipole.
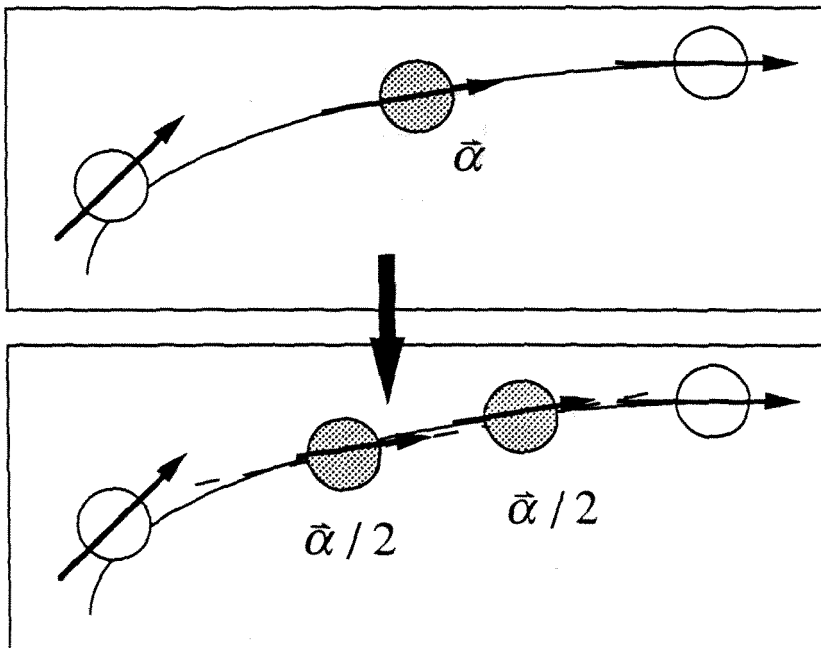
FIGURE (3.3.2) Schematic showing the remeshing of a vortex vector.
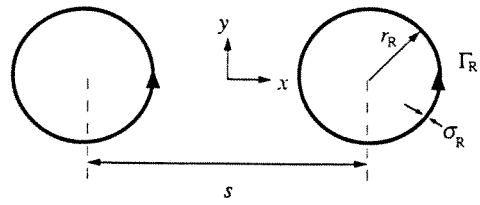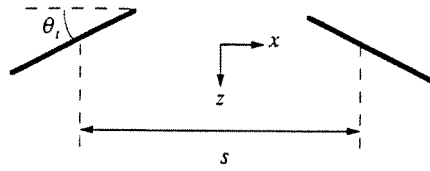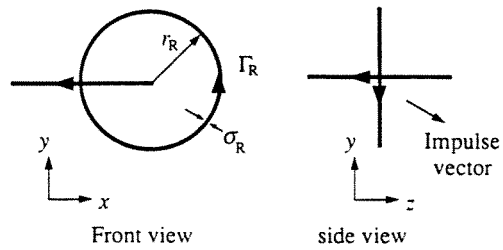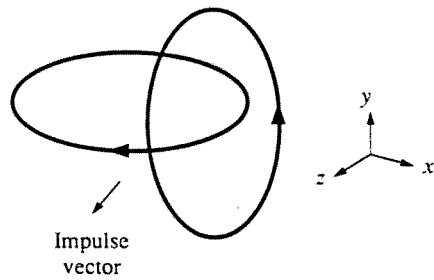
FIGURE (3.4.1) Schematic showing the problem definition of (a) vortex rings collision ; (b) vortex knots.
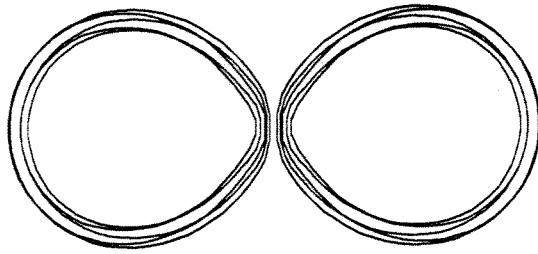
(a)
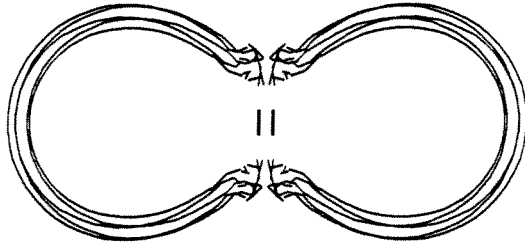
(b)
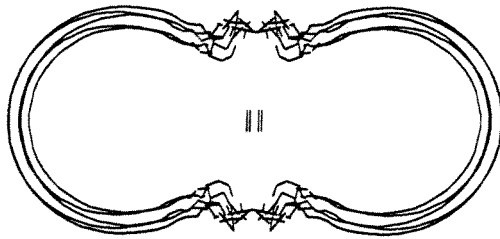
(c)

FIGURE (3.4.2) Front view of a time sequence of vortex rings collision computed using the linear viscosity model. $\nu = 4.5 \times 10^{-4}$, $n_l = 54$, $n_s = 5$, $\varepsilon_m = 0.05$. (a) $t = 6.0$; (b) $t = 7.25$; (c) $t = 8.50$; (d) $t = 9.75$; (e) $t = 11.0$.

(d)

(e)
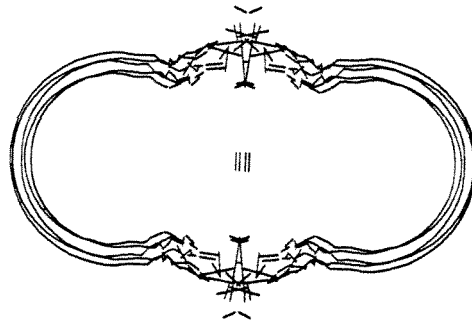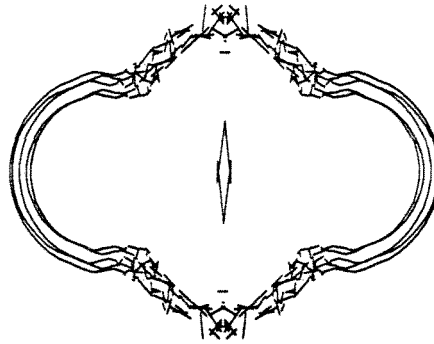
FIGURE (3.4.2) Cont.
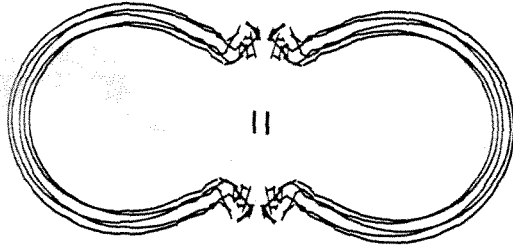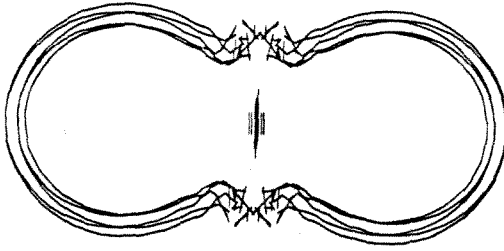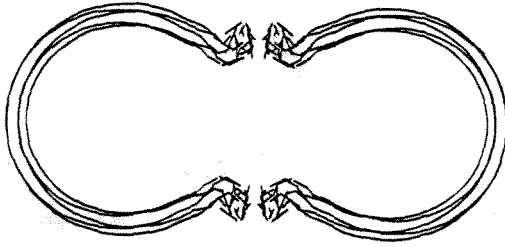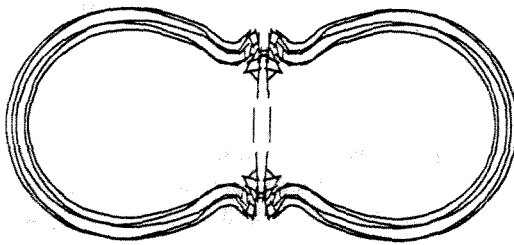
FIGURE (3.4.3) Front view of a reconnected vortex ring at $t = 8.0$. $n_l = 54$, $n_s = 5$, $\varepsilon_m = 0.05$. (a) $\nu = 4.5 \times 10^{-4}$; (b) $\nu = 5.0 \times 10^{-4}$; (c) $\nu = 6.25 \times 10^{-4}$; (d) $\nu = 12.5 \times 10^{-4}$.
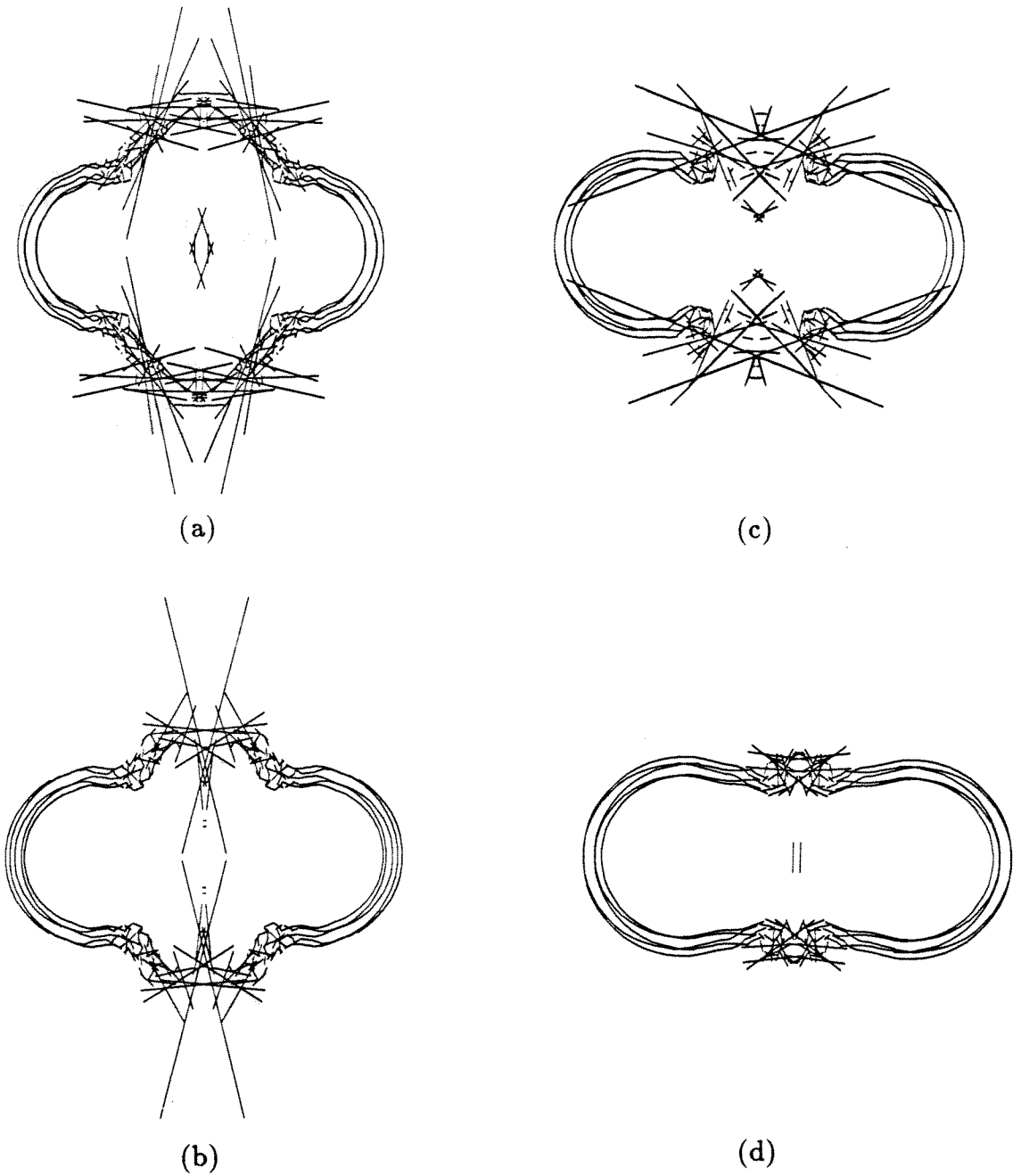
FIGURE (3.4.4) Front view of a reconnected vortex ring at the time of numerical blowup t_b. Parameters the same as Fig. (3.3.6). (a) $\nu = 4.5 \times 10^{-4}$, $t_b = 11.75$; (b) $\nu = 5.0 \times 10^{-4}$, $t_b = 10.65$; (c) $\nu = 6.25 \times 10^{-4}$, $t_b = 9.95$ and (d) $\nu = 12.5 \times 10^{-4}$, $t_b = 9.50$.

(a)   (b)
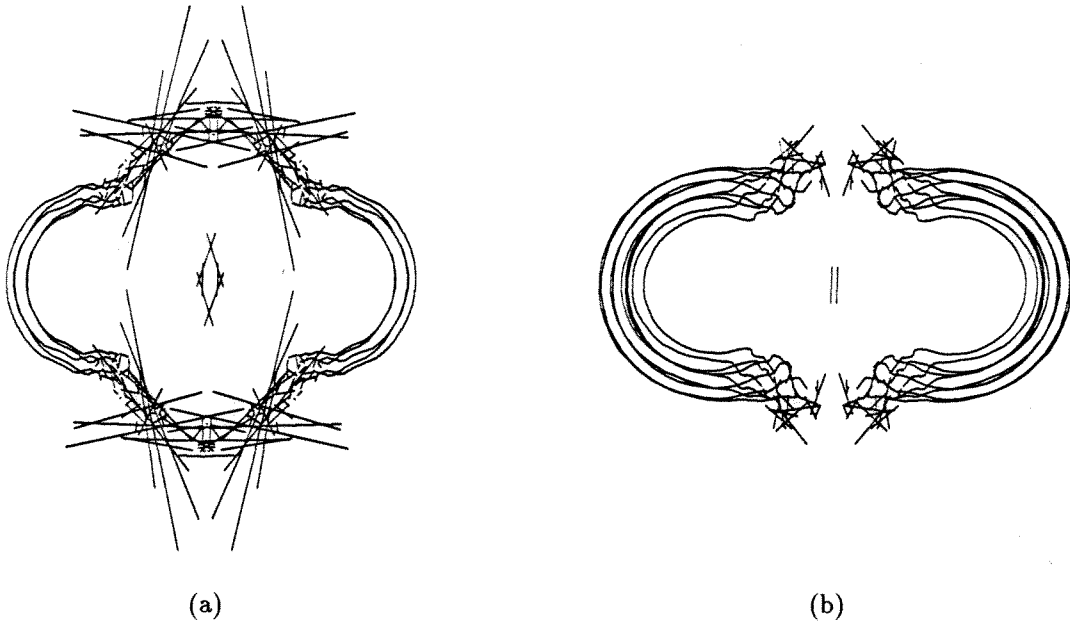
FIGURE (3.4.5) Front view of a reconnected vortex ring at $t = 11.75$, $\nu = 4.5 \times 10^{-4}$, $n_1 = 54$, $\varepsilon_m = 0.05$. (a) $n_s = 5$; (b) $n_s = 9$.

(a)   (b)
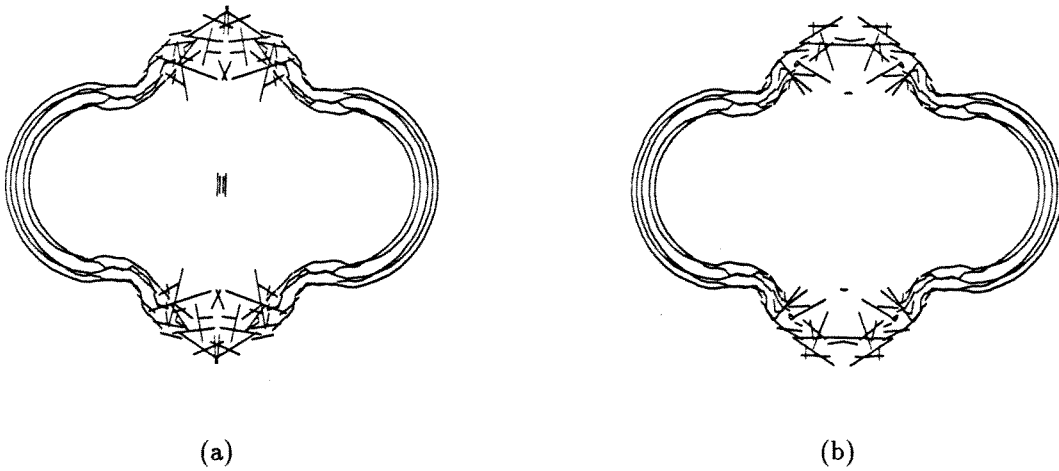
FIGURE (3.4.6) Front view of a reconnected vortex ring at $t = 10.75$. $\nu = 4.5 \times 10^{-4}$, $n_1 = 54$, $n_s = 5$. (a) $\varepsilon_m = 0.01$; (b) $\varepsilon_m = 0.05$.

(a)   (b)
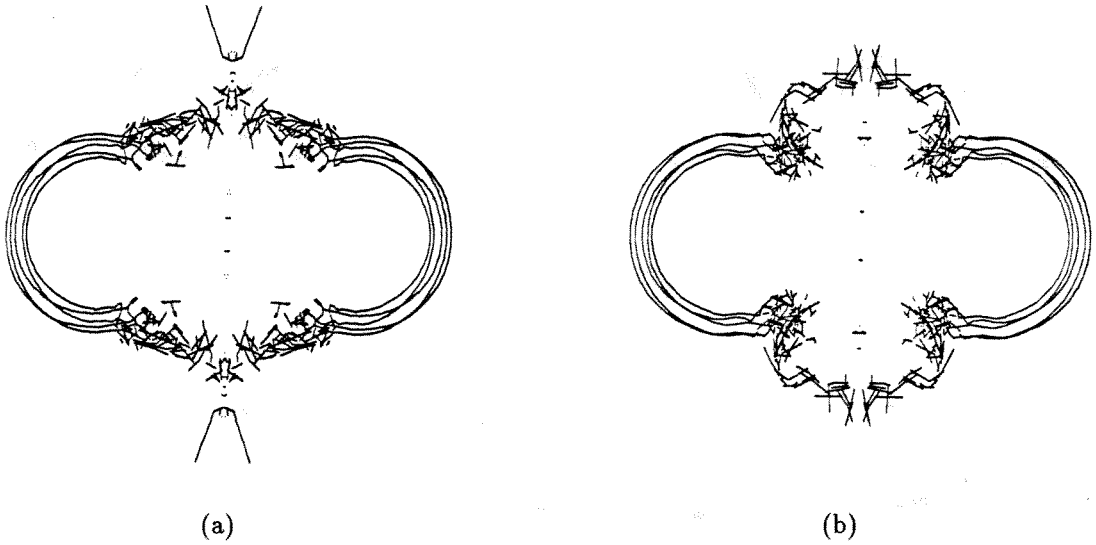
FIGURE (3.4.7) Front view of a reconnected vortex rings at the time of numerical blowup. No change in σ because of inviscid stretching. $n_l = 54$, $n_s = 5$, $\varepsilon_m = 0.05$. (a) $\nu = 0$, $t_b = 10.50$; (b) $\nu = 4.5 \times 10^{-4}$, $t_b = 10.45$.

t : 1.50   t : 7.50   t : 1.50   t : 7.50

t : 3.00   t : 9.00   t : 3.00   t : 9.00

t : 4.50   t : 10.50   t : 4.50   t : 10.50

t : 6.00   t : 12.00   t : 6.00   t : 12.00

(a)   (b)
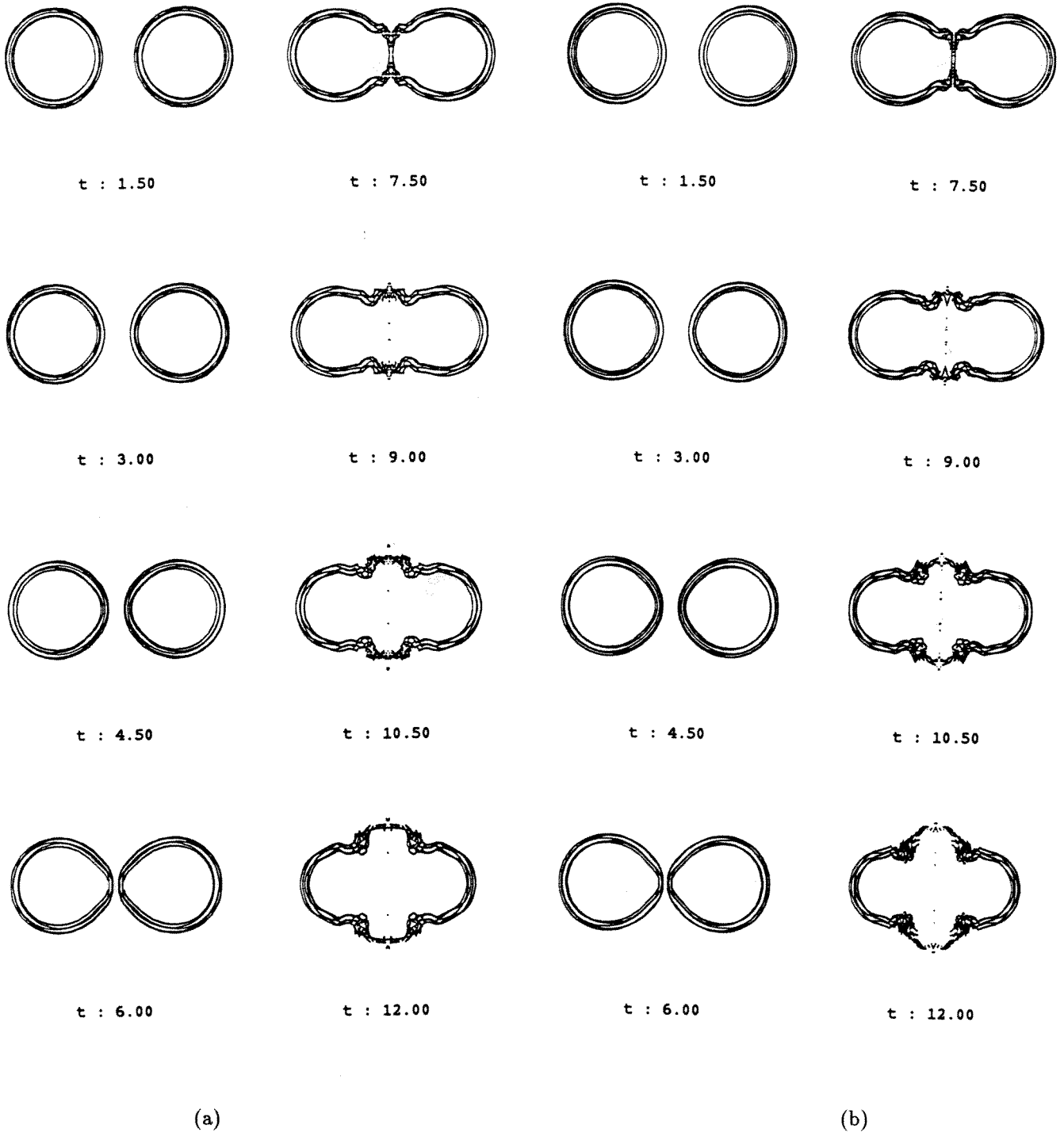
FIGURE (3.4.8) Front view of vortex-rings collision computed using the non-linear viscosity model. $n_l = 54$, $n_s = 5$, $\varepsilon_m = 0.05$. (a) $\nu_e = 1.25$; (b) $\nu_e = 1.05$.

t : 1.50   t : 7.50   t : 1.50   t : 7.50

t : 3.00   t : 9.00   t : 3.00   t : 9.00

t : 4.50   t : 10.50   t : 4.50   t : 10.50

t : 6.00   t : 12.00   t : 6.00   t : 12.00
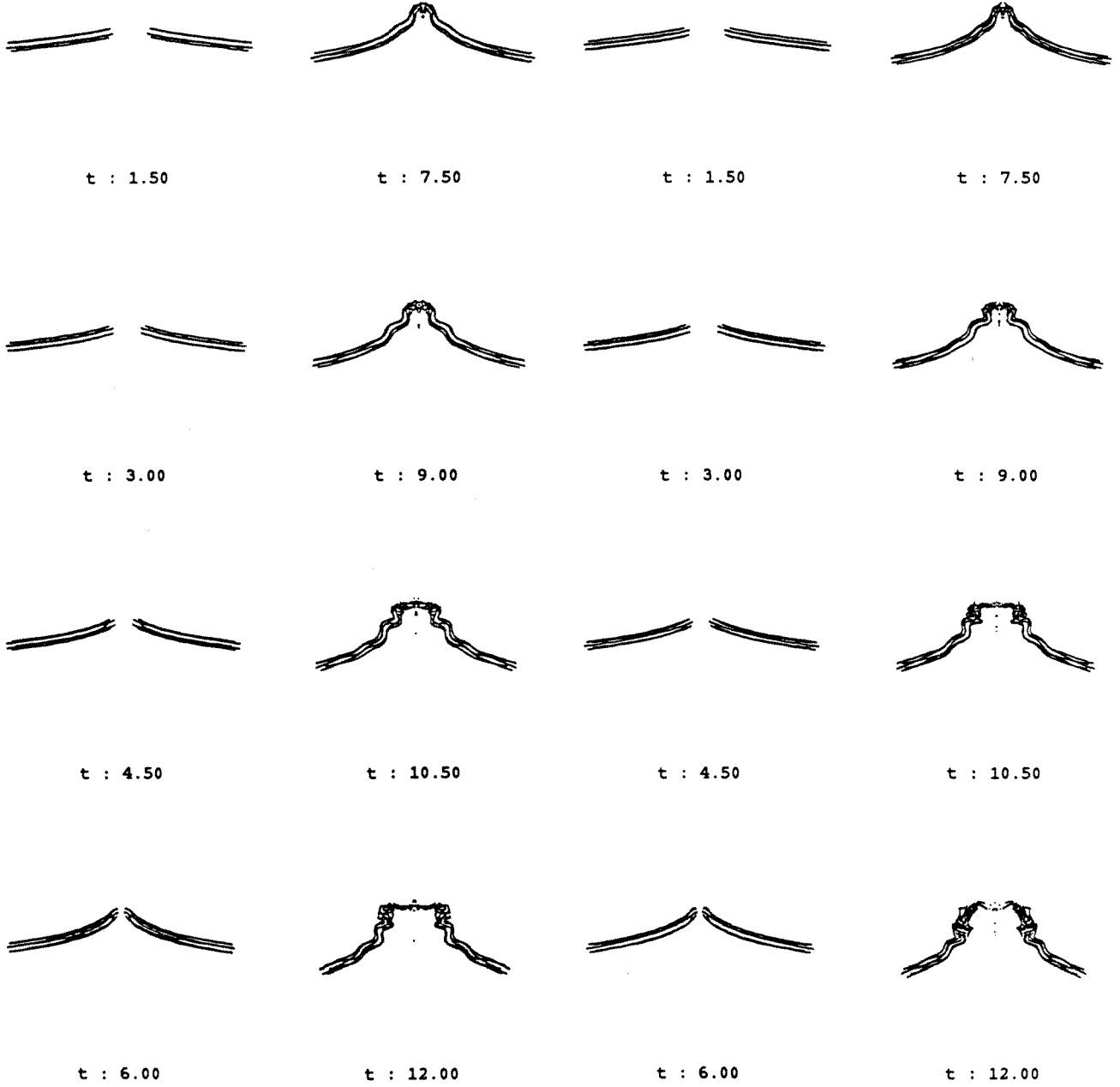
(a)   (b)

FIGURE (3.4.9) Same as Fig. (3.4.8). Top view.

t : 1.50

t : 7.50

t : 1.50

t : 7.50

t : 3.00

t : 9.00

t : 3.00

t : 9.00

t : 4.50

t : 10.50

t : 4.50

t : 10.50

t : 6.00

t : 12.00

t : 6.00

t : 12.00
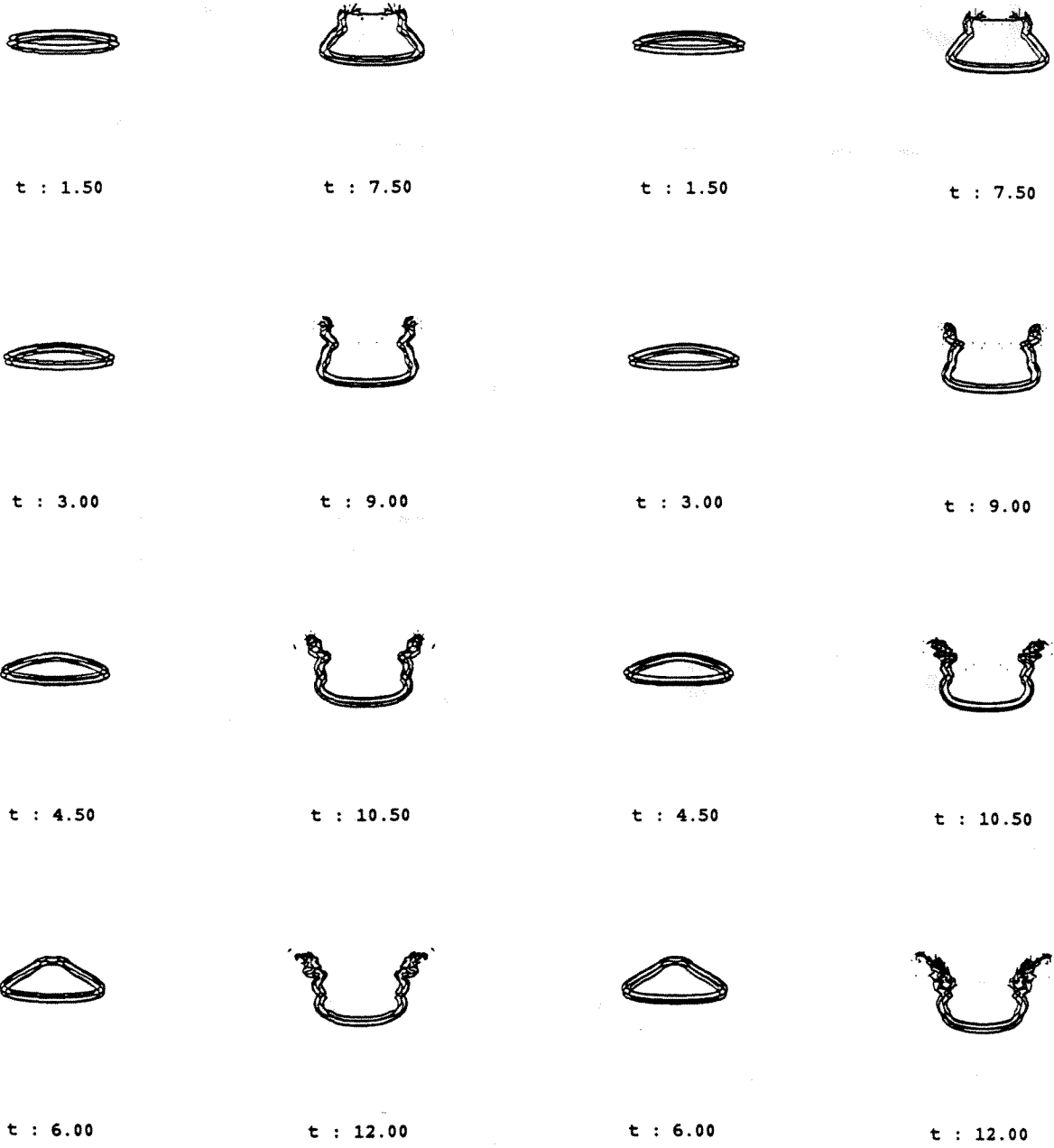
(a)

(b)

FIGURE (3.4.10) Same as Fig. (3.4.8). Side view.
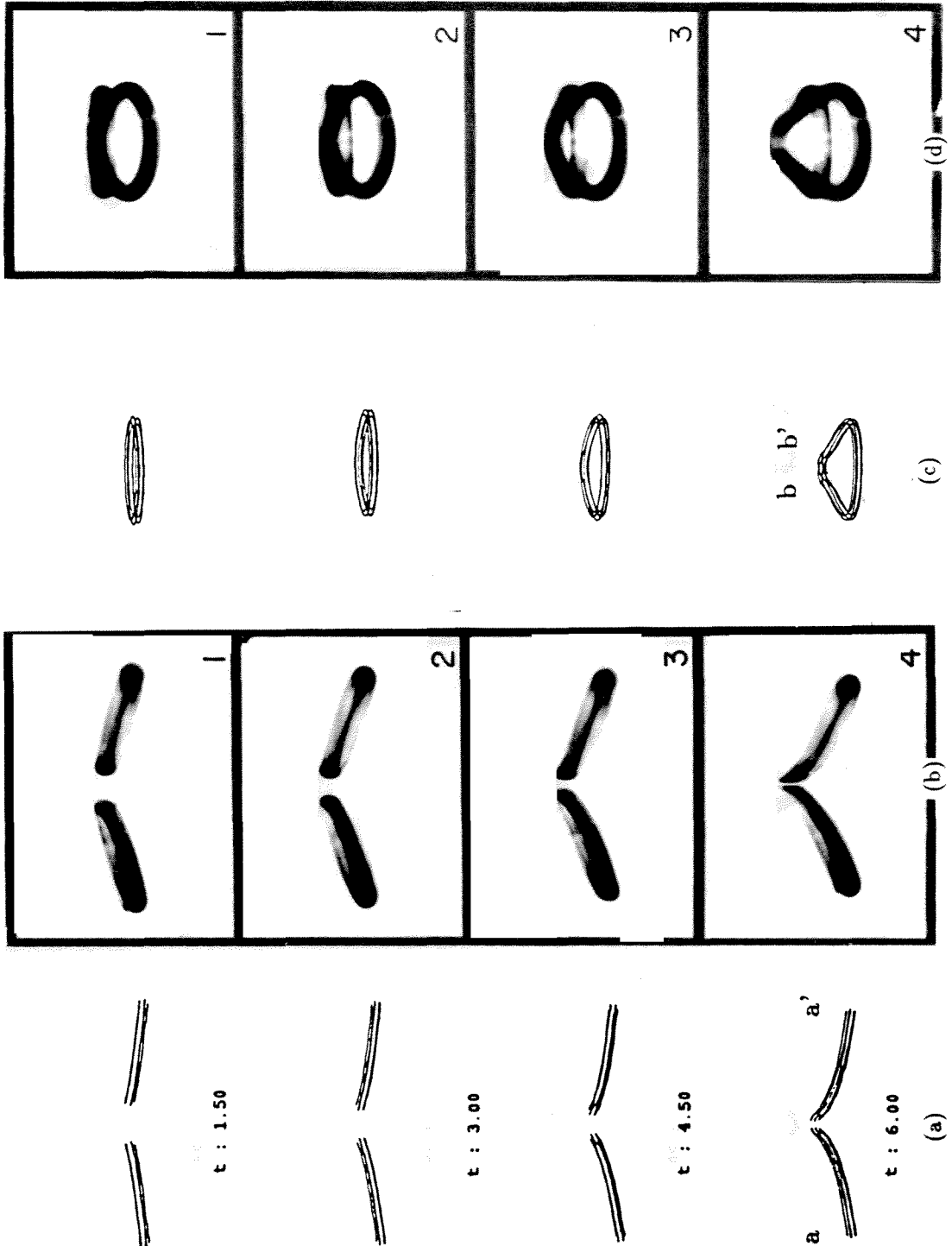
FIGURE (3.4.11) Comparison of calculation to experiments of Schatzle (1987). Parameters the same as Fig. (3.3.10a). (a) Calc., top view; (b) expt., top view; (c) Calc., side view; (d) expt., side view.

FIGURE (3.4.11) Cont.

FIGURE (3.4.11) Cont.

172
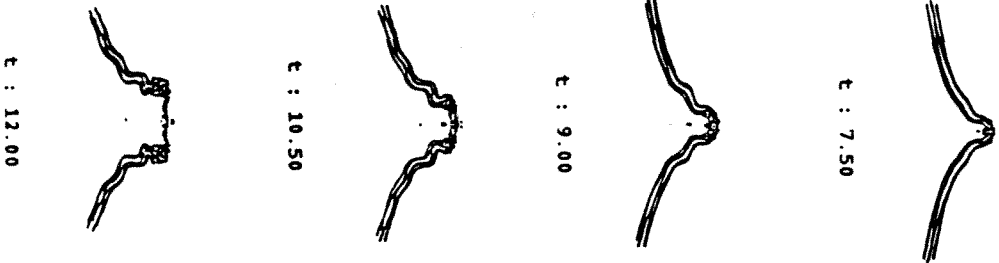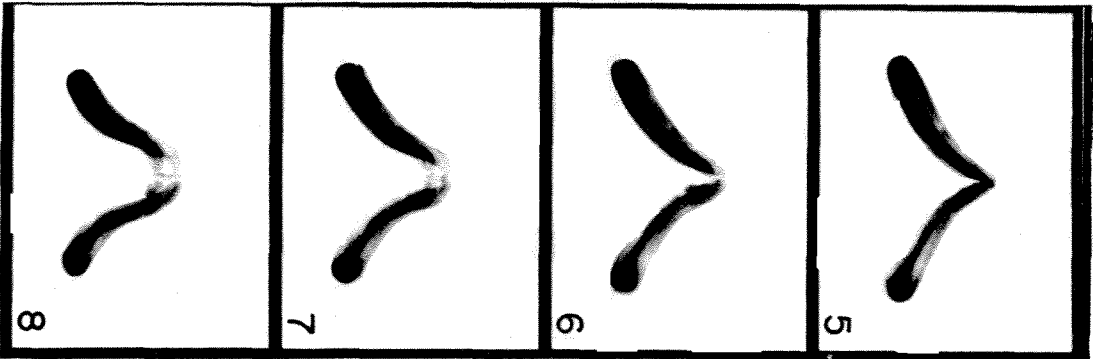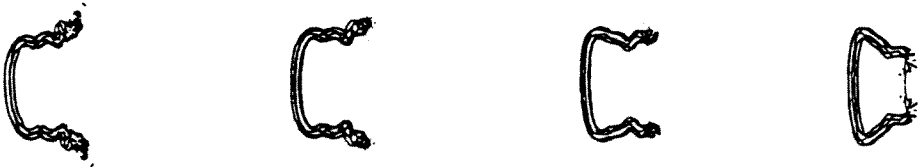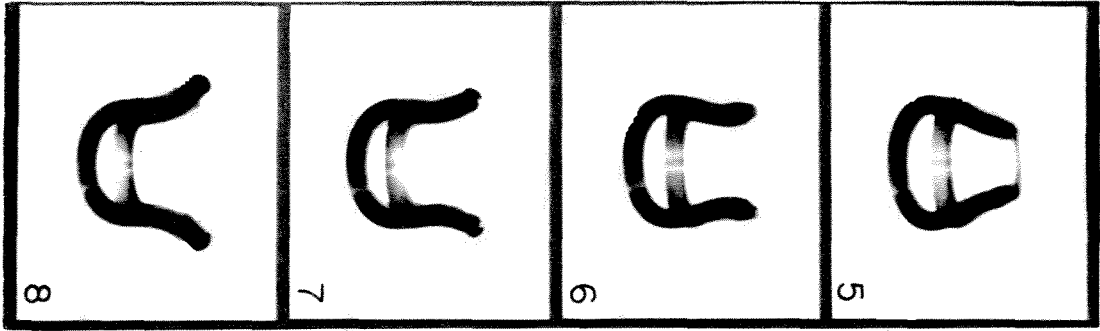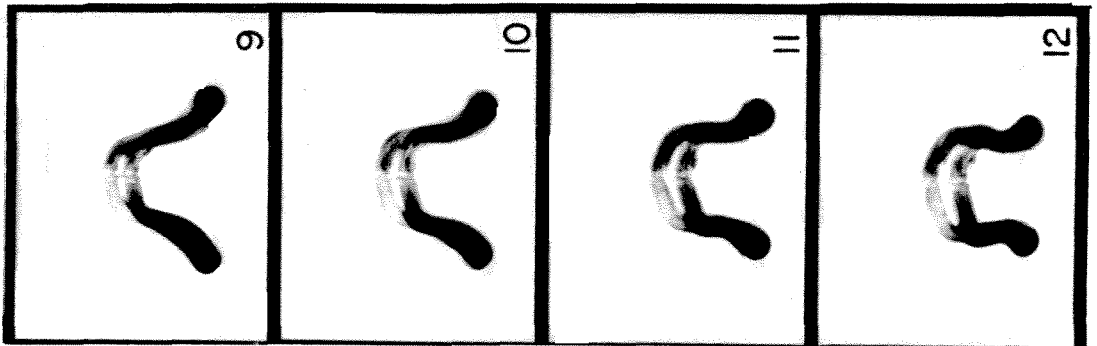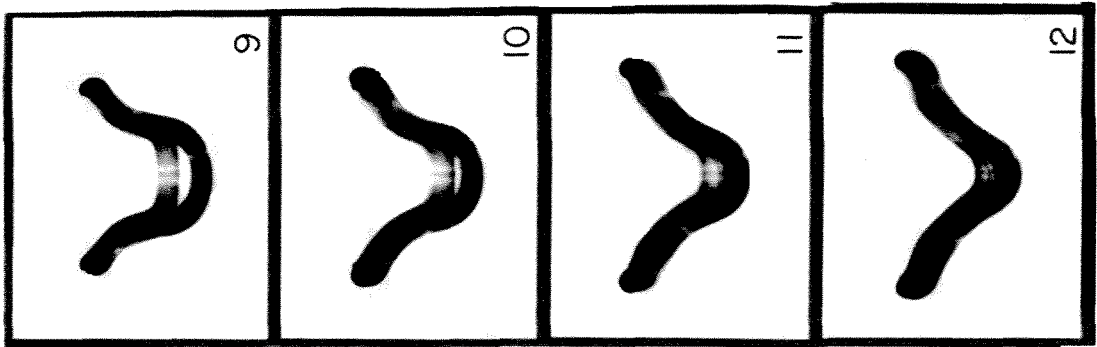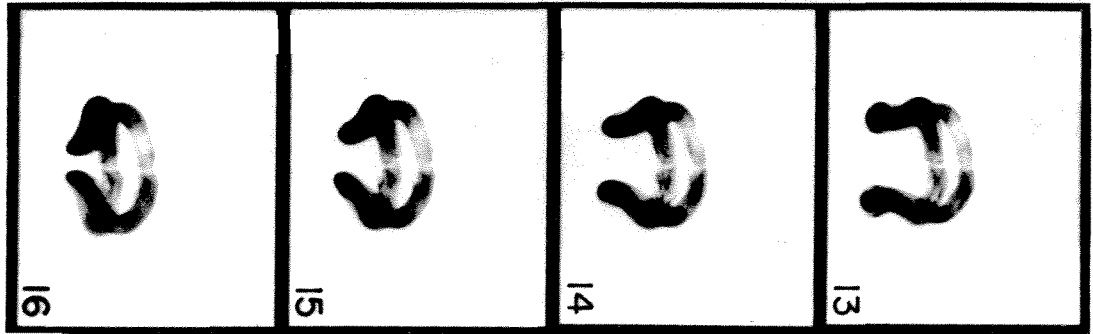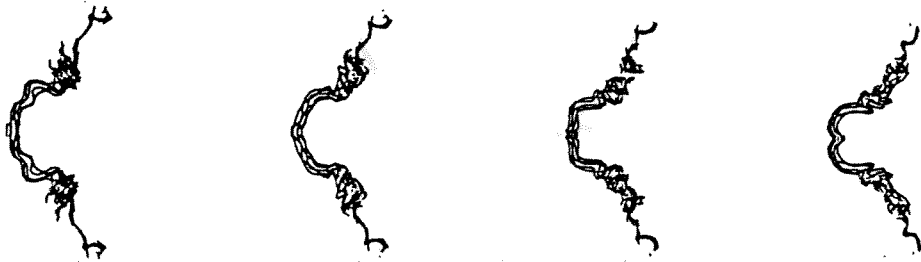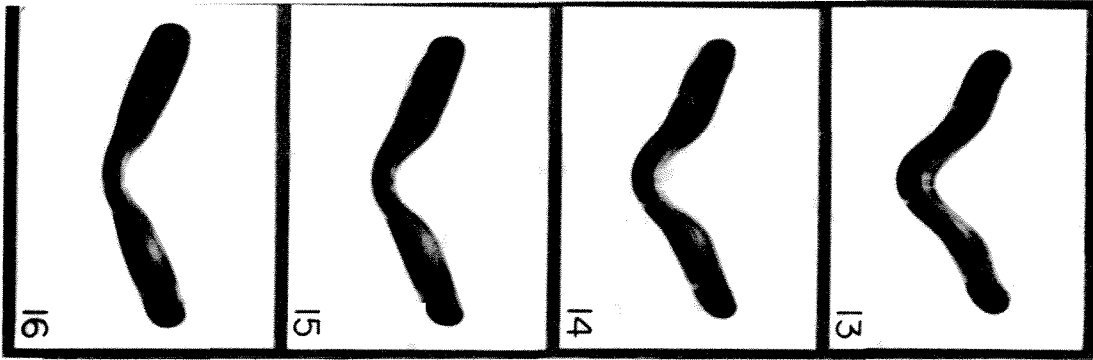
FIGURE (3.4.11) Cont.
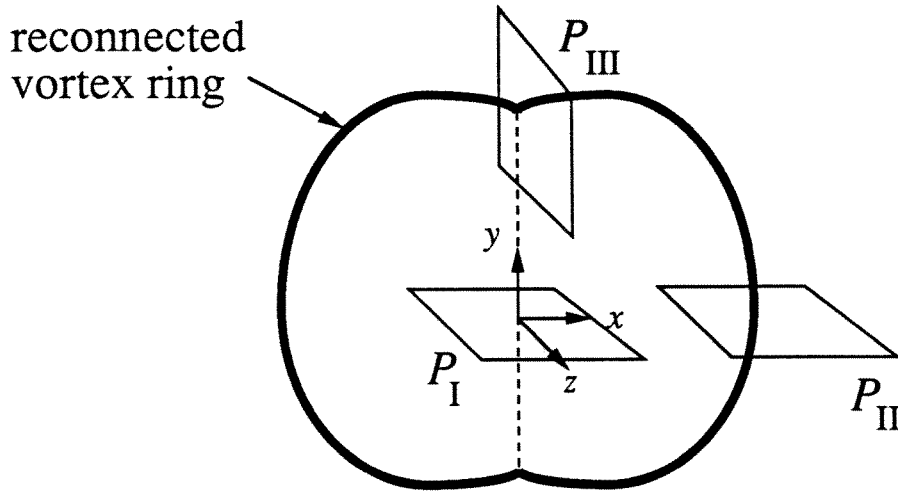
FIGURE (3.4.12) Schematic showing the cutting planes P_I, P_{II} and P_{III} where contour plots of Figs. (3.4.13) and (3.4.14) are computed.
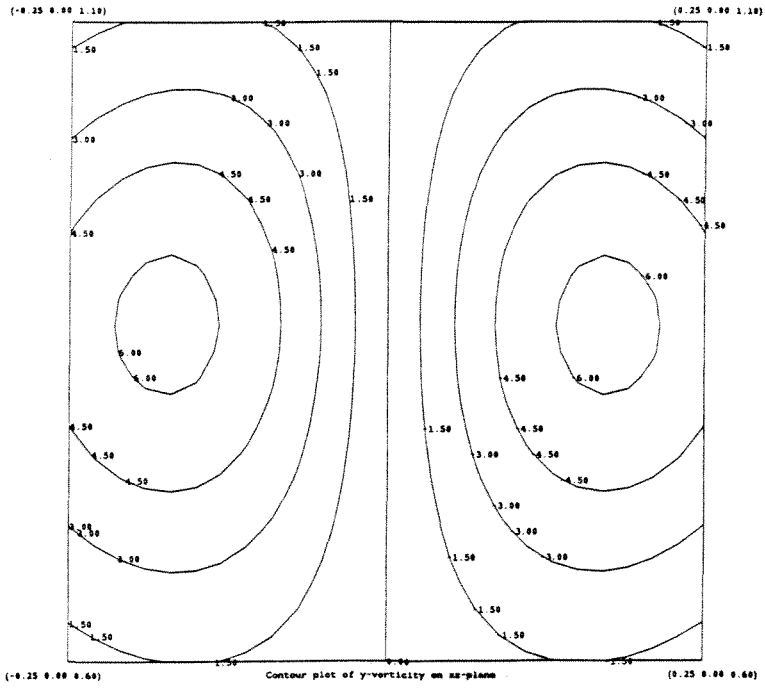
(a)
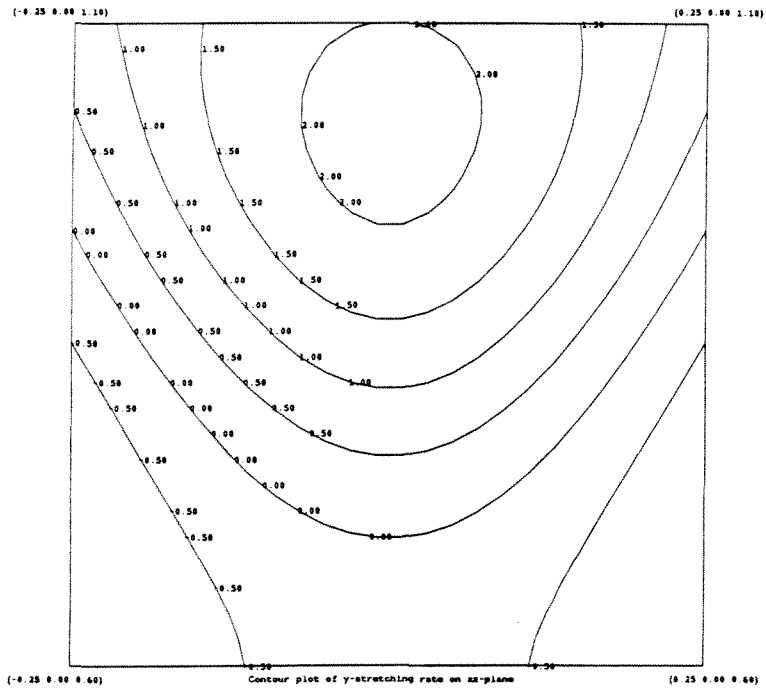
(b)

FIGURE (3.4.13) Contour plots of quantity of interest at $t = 6.0$. (a) ω_y in P_{I}; (b) $\partial v/\partial y$ in P_{I}; (c) $\partial v/\partial y$ in P_{II}; (d) ω_x in P_{III}.

(2.01 0.00 1.93) (2.51 0.00 1.93)

(2.01 0.00 1.43) Contour plot of y-stretching rate on xz-plane (2.51 0.00 1.43)

(c)

(0.00 0.05 1.08) (0.00 0.55 1.08)

(0.00 0.05 0.58) Contour plot of x-vorticity (0.00 0.55 0.58)
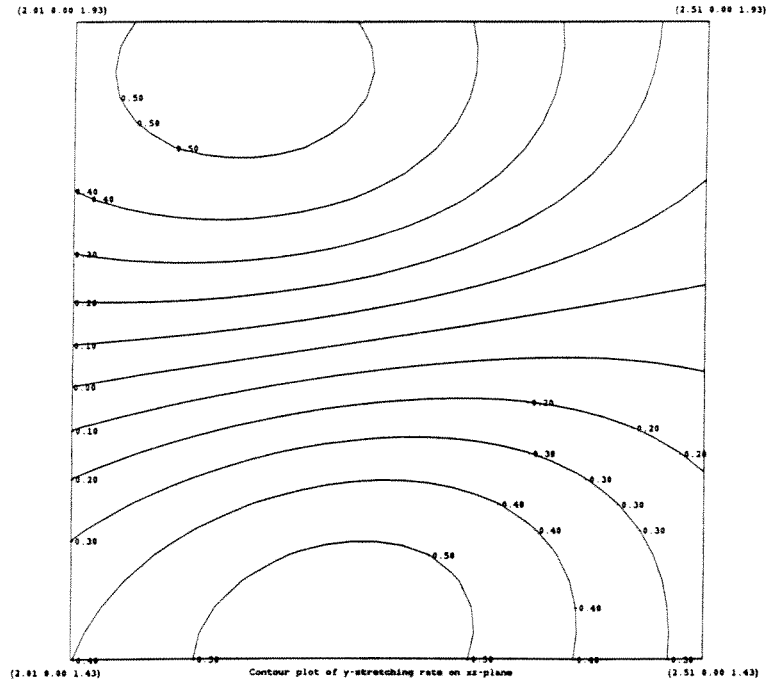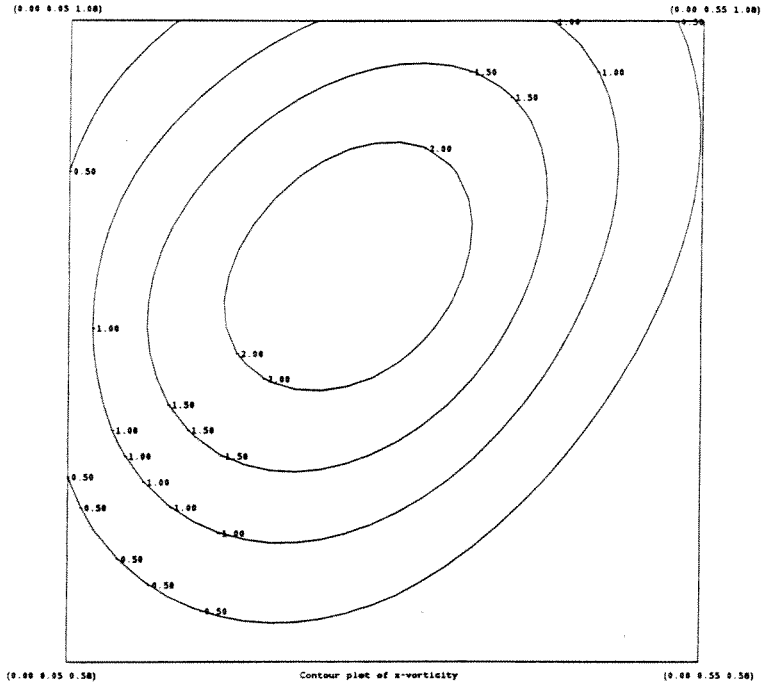
(d)
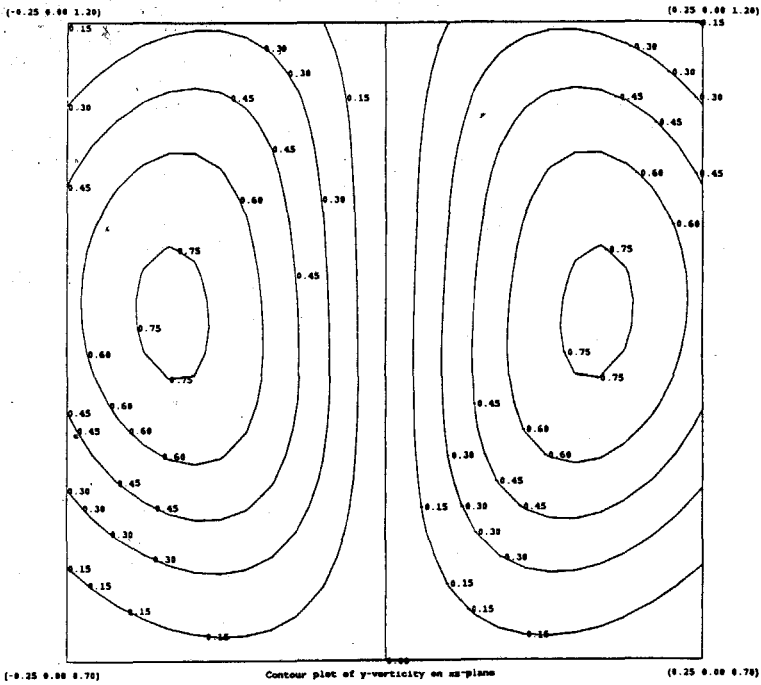
FIGURE (3.4.13) Cont.

(a)
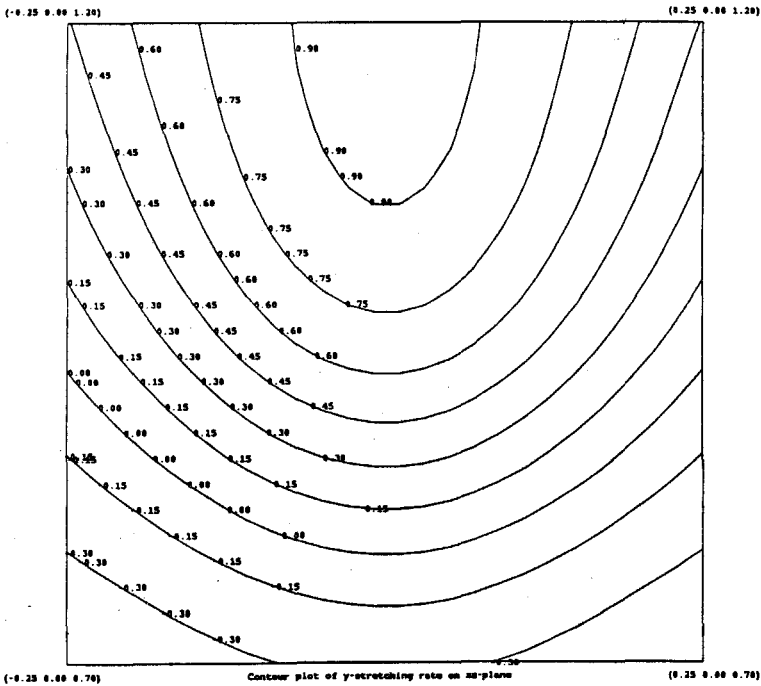
(b)

FIGURE (3.4.14) Same as Fig. (3.4.13), $t = 7.5$.
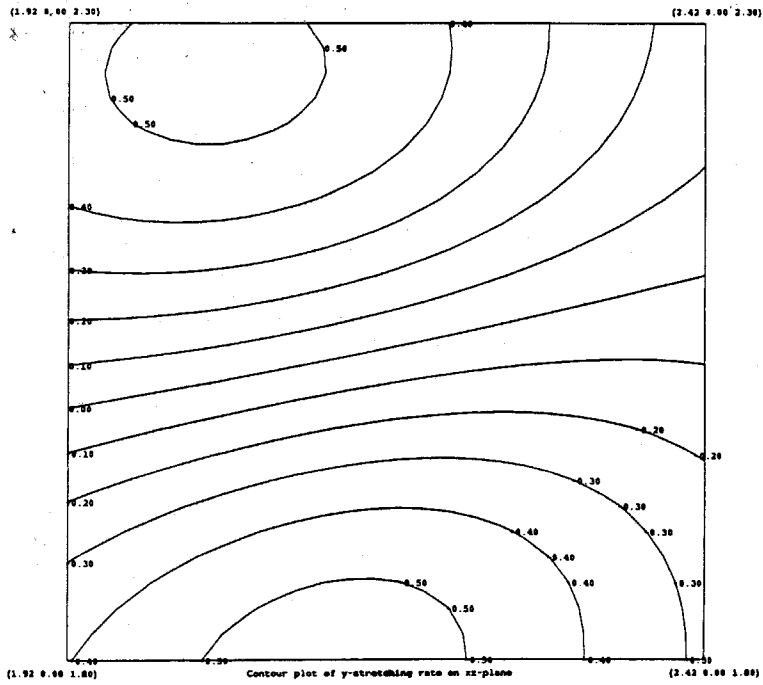
(c)
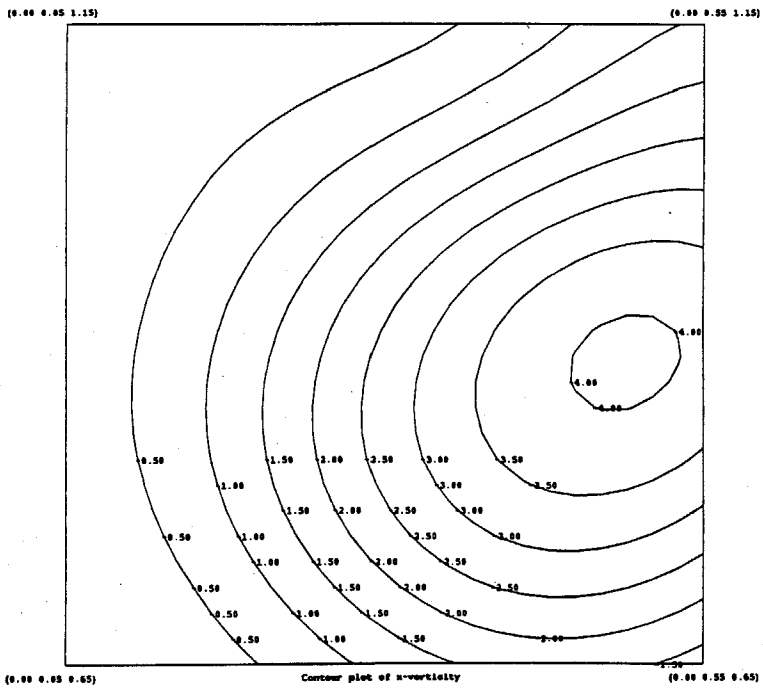
(d)

FIGURE (3.4.14) Cont.

(a)

(b)

FIGURE (3.4.15) (a) Front view of a contorted ring at $t = 10.5$. Box indicates the location of the plotting plane. Contour plots for modulus of (b) swirling velocity, (c) axial velocity, (d) out-of-plane vorticity and (e) in-plane vorticity on a plane normal to the vortex tube. (f) vector plot of in-plane vorticity.

In coordinate system centered at core and normal to mean vorticity vector (0.20 0.20)

-0.05
-0.05

-0.15

-0.10

-0.05

-0.10

-0.05

-0.05

0.00

0.00

(-0.20 -0.20)   Contour plot of axial velocity at station 4   (0.20 -0.20)

(c)
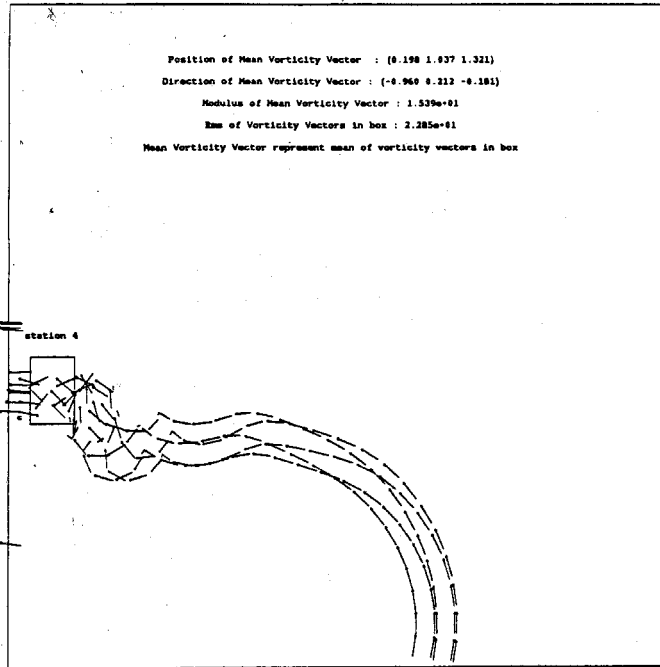
(-0.20 0.20)   In coordinate system centered at core and normal to mean vorticity vector   (0.20 0.20)

2.00   1.50

1.50

2.50

2.00

2.50

2.00

3.00

2.00

3.00

2.00   2.50   3.00

1.50

2.00   2.50

1.50   2.00

1.50

(-0.20 -0.20)   Contour plot of normal vorticity at station 4   (0.20 -0.20)

(d)

FIGURE (3.4.15) Cont.

(e)

(f)

FIGURE (3.4.15) Cont.
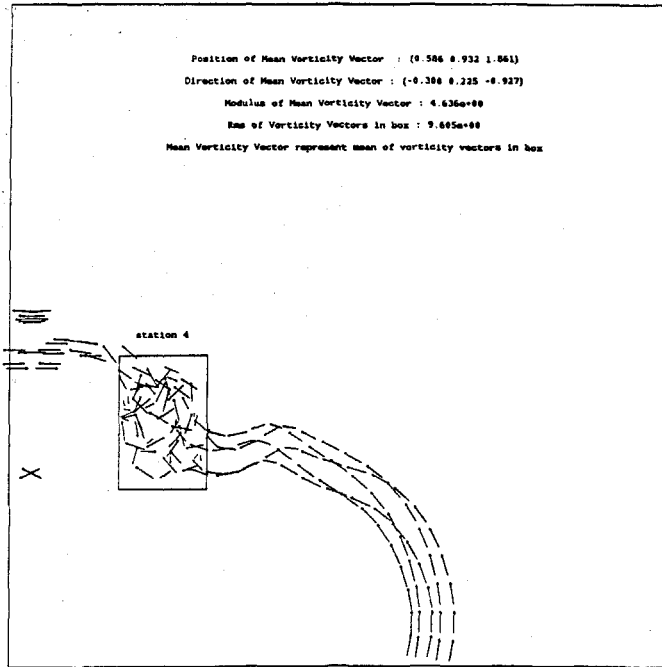
(a)
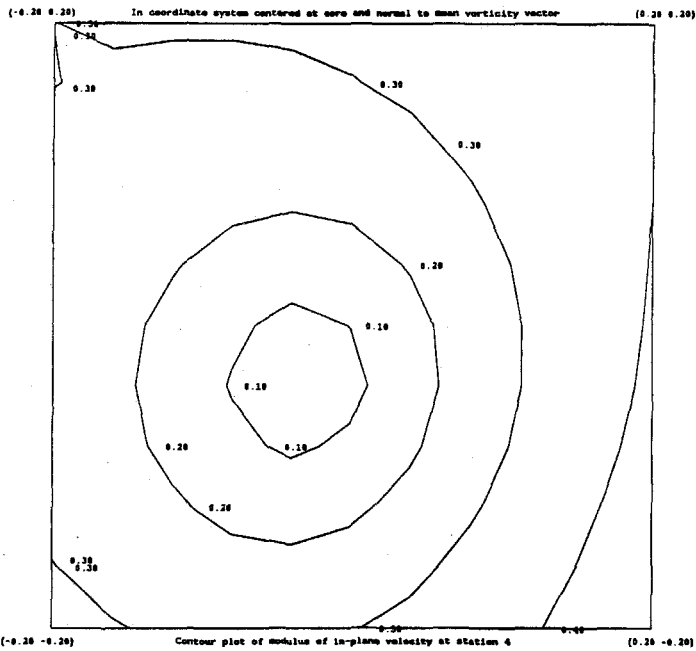
(b)

FIGURE (3.4.16) Same as Fig. (3.4.15), $t = 12.0$.
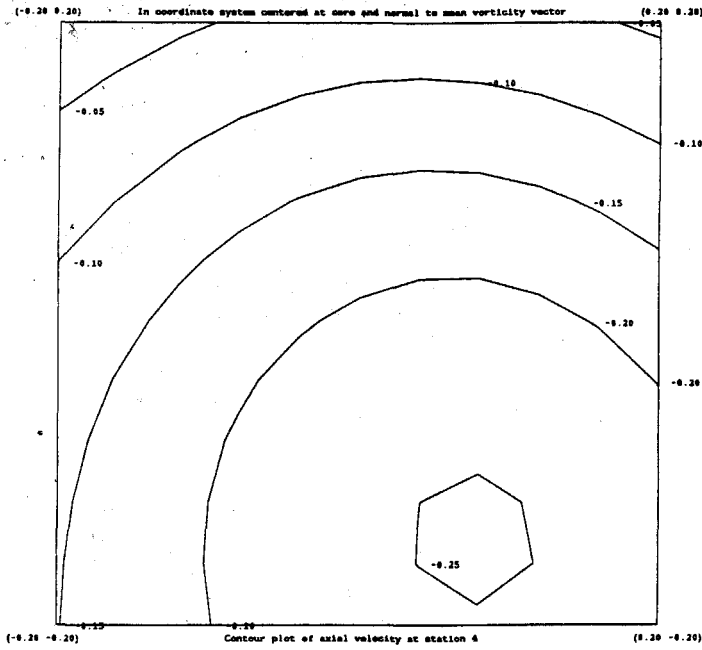
(c)
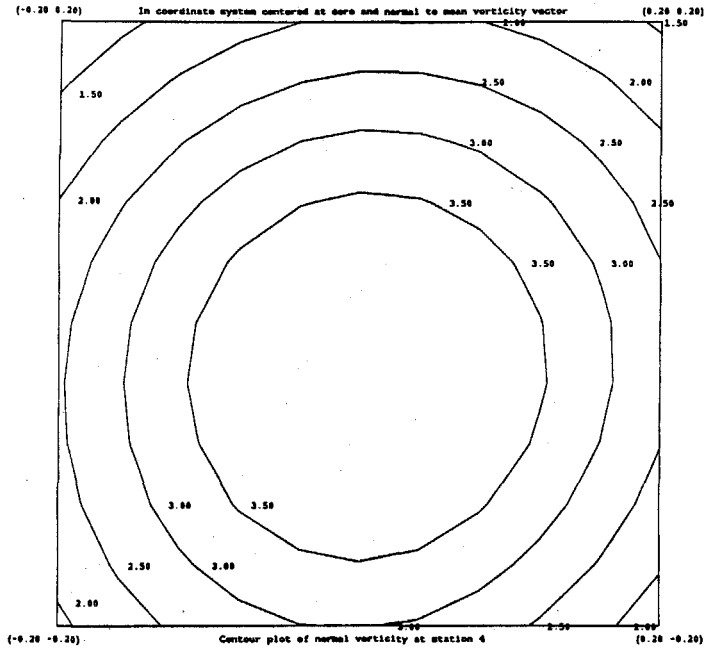
(d)

FIGURE (3.4.16) Cont.

(e)

(f)

FIGURE (3.4.16) Cont.

t : 0.50   t : 2.50   t : 4.50   t : 6.50

t : 1.00   t : 3.00   t : 5.00   t : 7.00
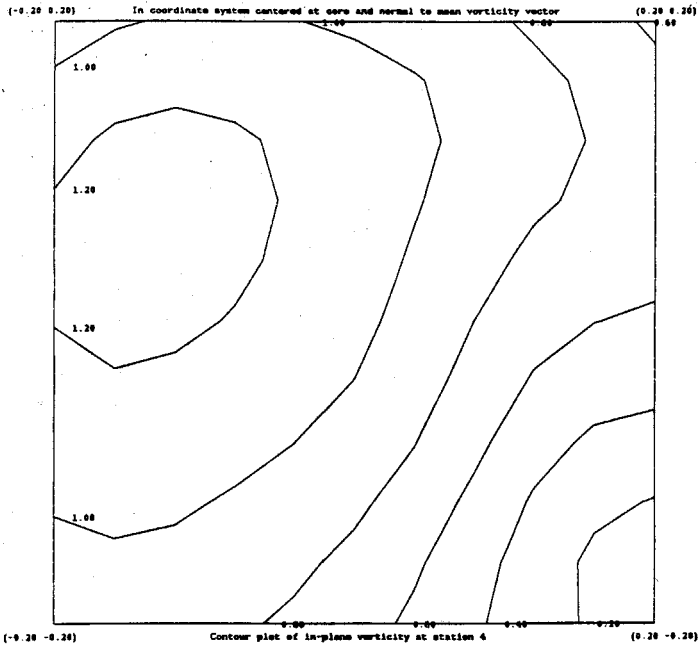
t : 1.50   t : 3.50   t : 5.50   t : 7.50
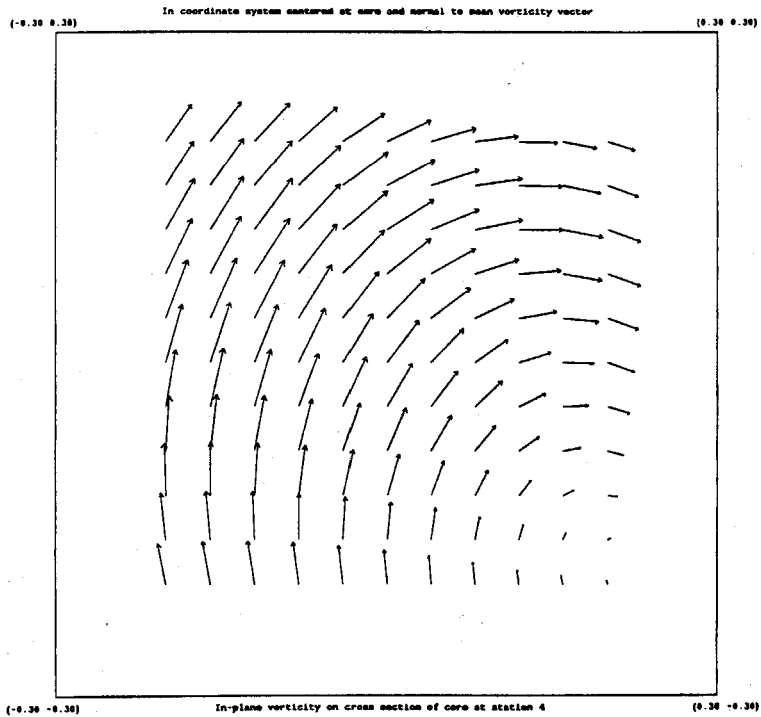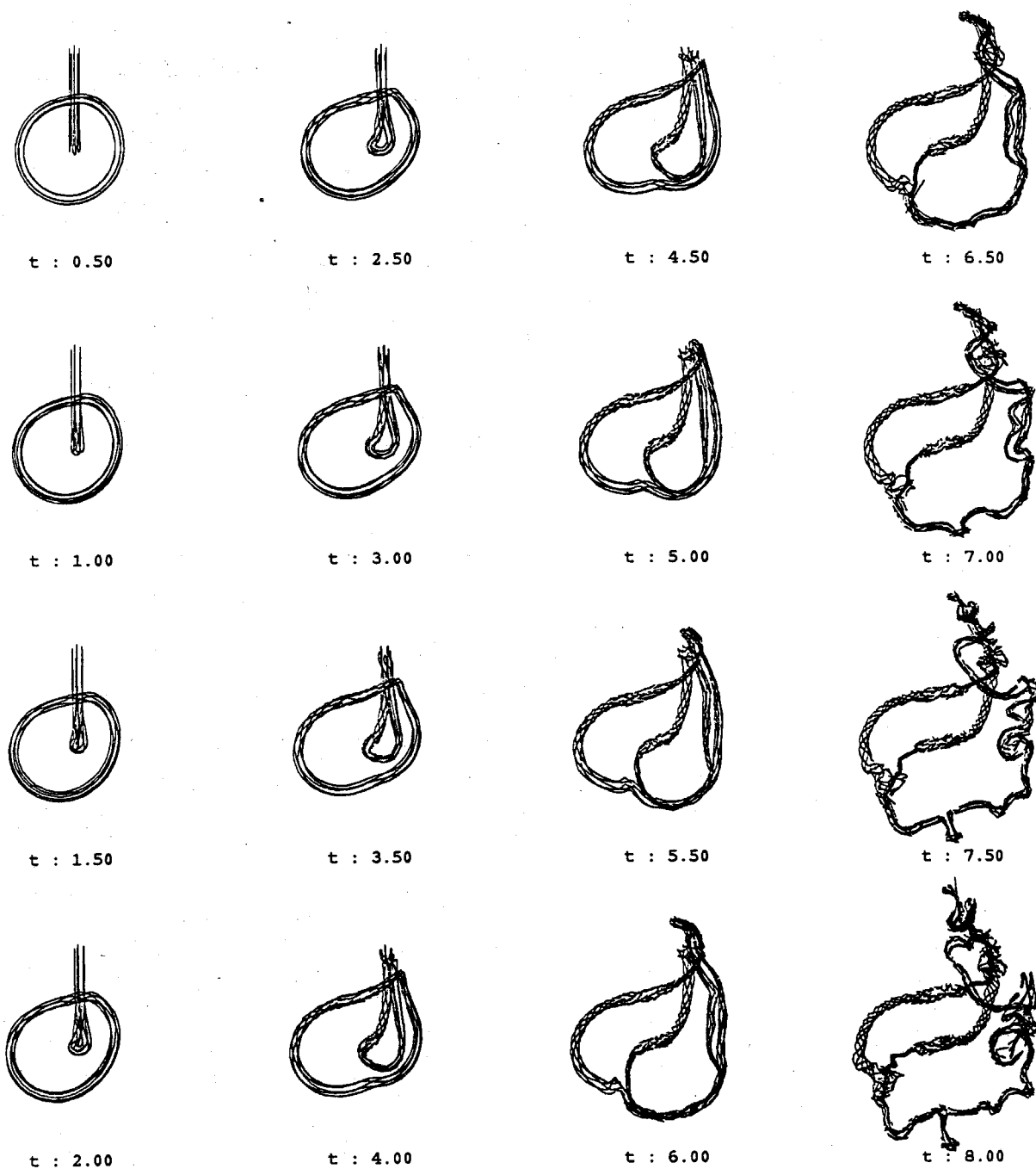
t : 2.00   t : 4.00   t : 6.00   t : 8.00

(a)

FIGURE (3.4.17) Time sequence of vortex knots interaction. (a) Front view; (b) side view.

t : 0.50

t : 2.50
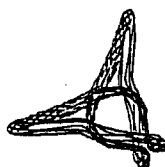
t : 4.50

t : 6.50

t : 1.00
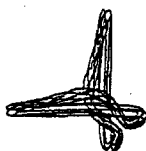
t : 3.00
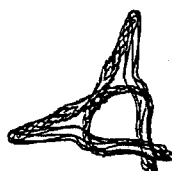
t : 5.00

t : 7.00
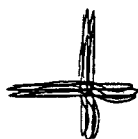
t : 1.50
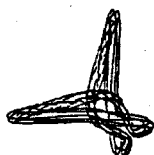
t : 3.50
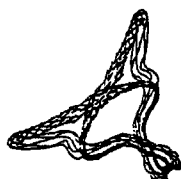
t : 5.50
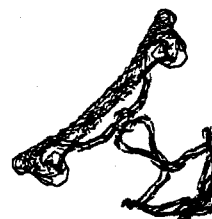
t : 7.50

t : 2.00
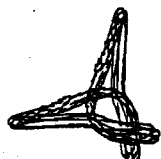
t : 4.00
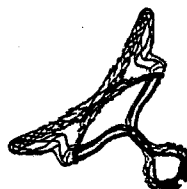
t : 6.00

t : 8.00

(b)

FIGURE (3.4.17) Cont.
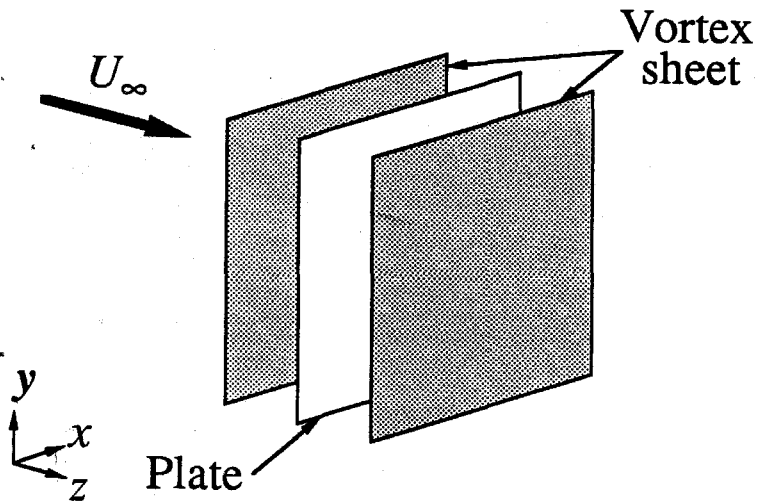
FIGURE (4.1.1) Schematic showing a flat plate with vortex sheets on both sides.
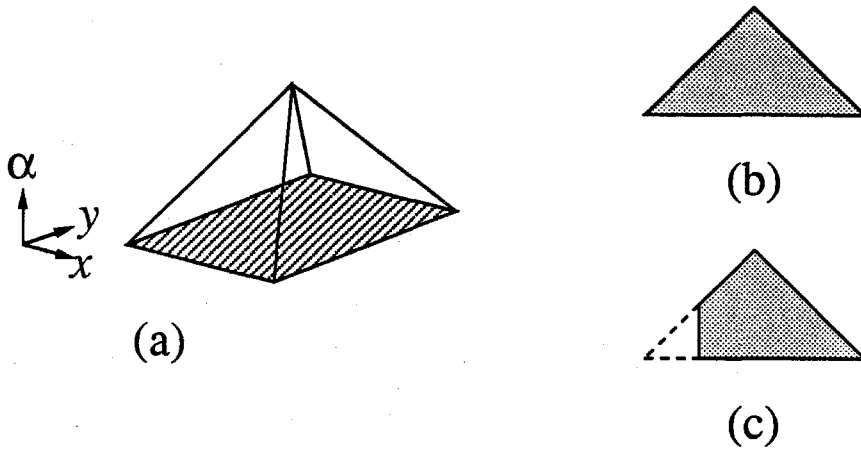
FIGURE (4.1.2) Schematic showing (a) pyramidal distribution given by $f_x \times f_y$ for representing a vortex element; (b) triangular distribution of f_x and f_y; (c) distribution of f_x and f_y near edge.
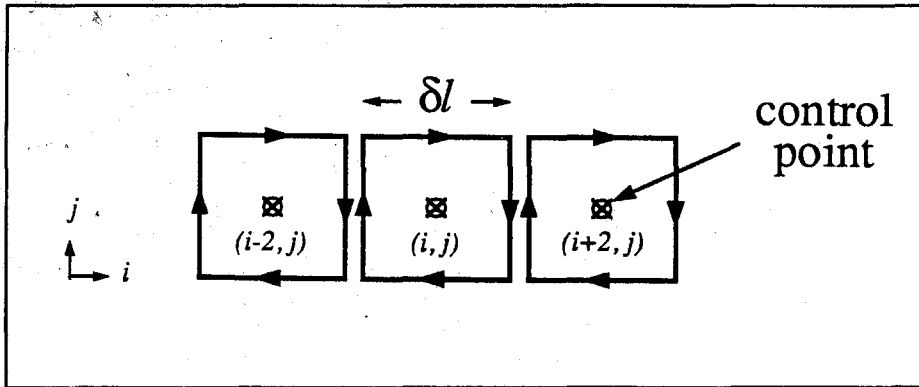
FIGURE (4.1.3) Schematic showing a vortex loop for enforcing no-through flow boundary conditions.

(a)
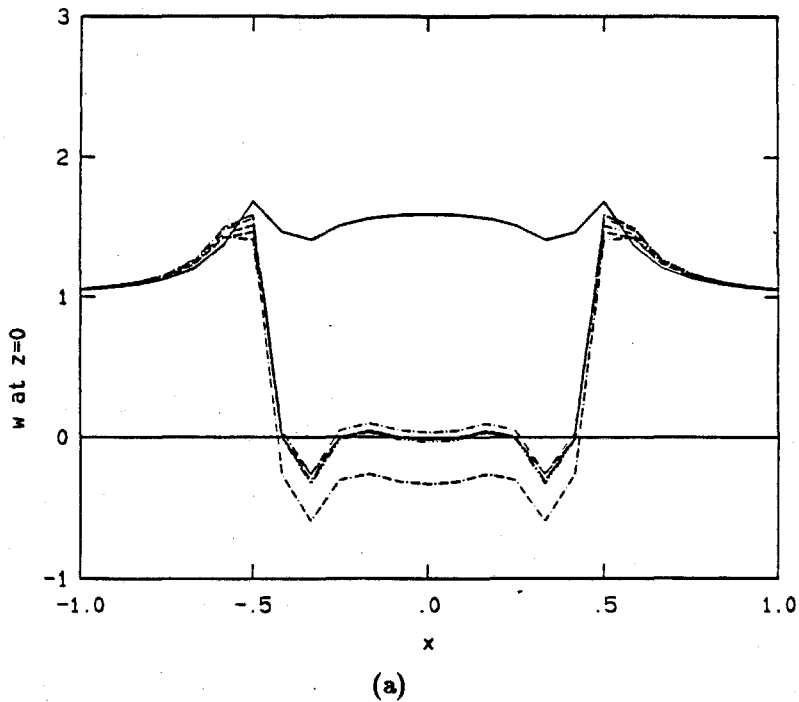
FIGURE (4.1.4) Plots of the x-distribution of w on a plate normal to flow $\underline{u} = U_\infty \hat{e}_z$, $t = 0$. —— along the edge; $- - \cdot - -$ section between edge and first control point; others, inner sections. (a) $N_p = 15$; (b) $N_p = 19$; (c) $N_p = 23$; (d) $N_p = 27$.
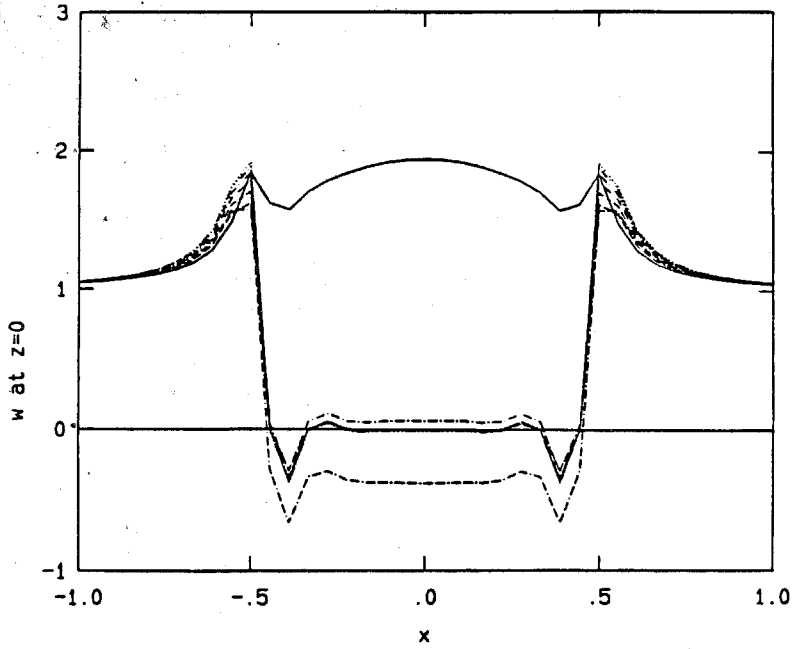
(b)
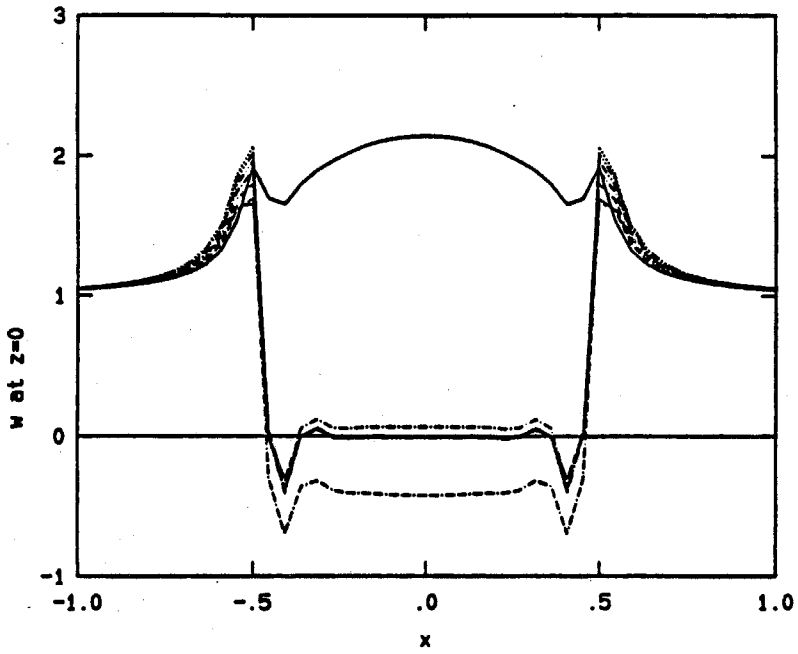
(c)

FIGURE (4.1.4) Cont.
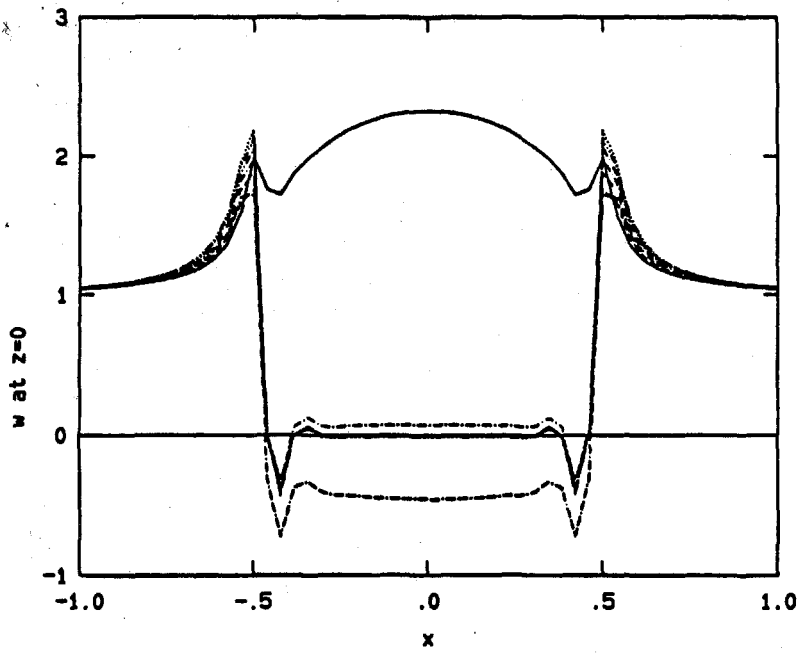
(d)

FIGURE (4.1.4) Cont.
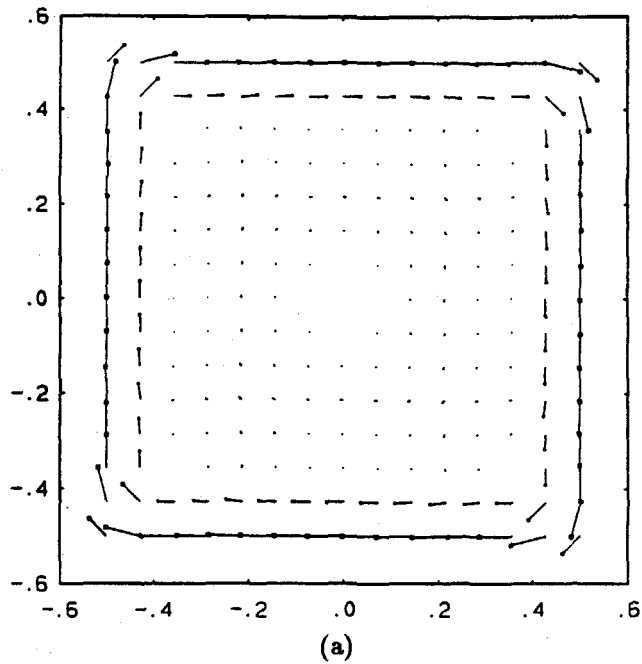
(a)

FIGURE (4.1.5) Plots of $\underline{\alpha}$ field on the boundary layer. Same as Fig. 4.1.4.

(b)

(c)

FIGURE (4.1.5) Cont.

(d)
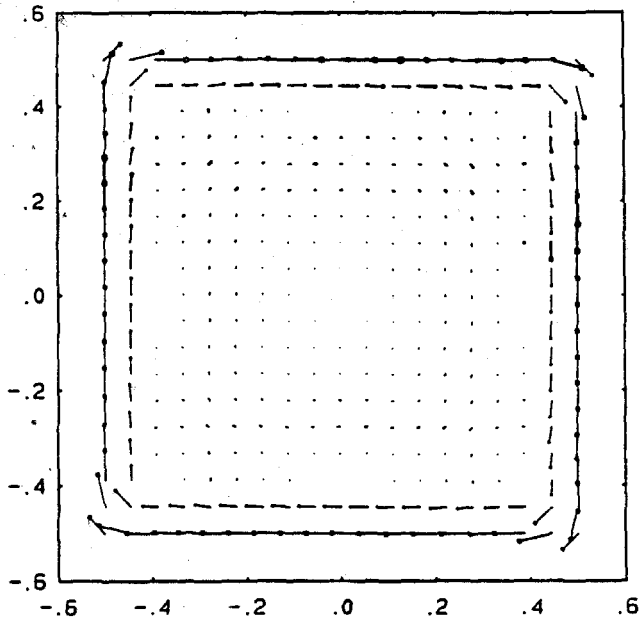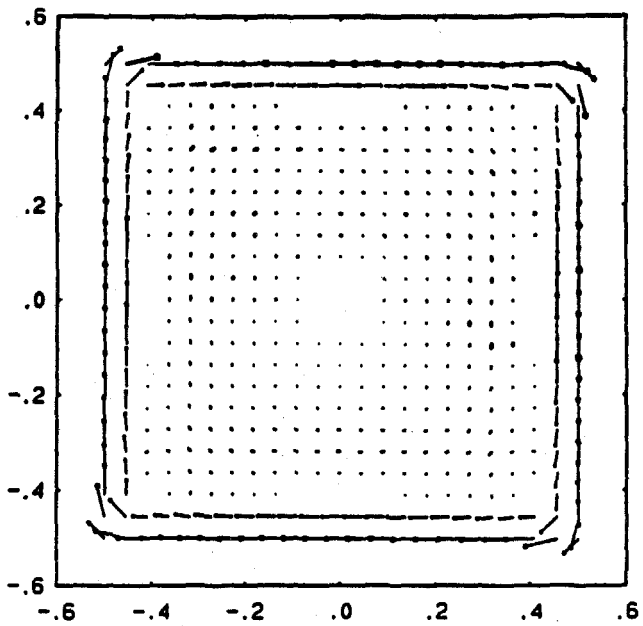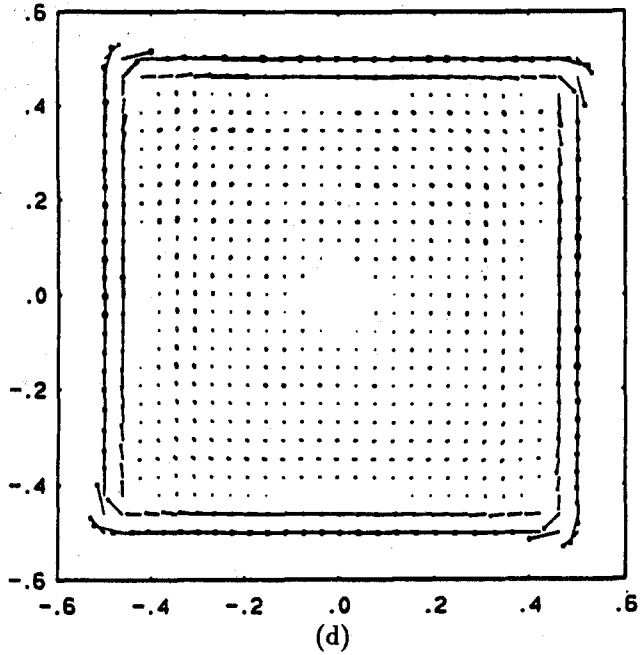
FIGURE (4.1.5) Cont.
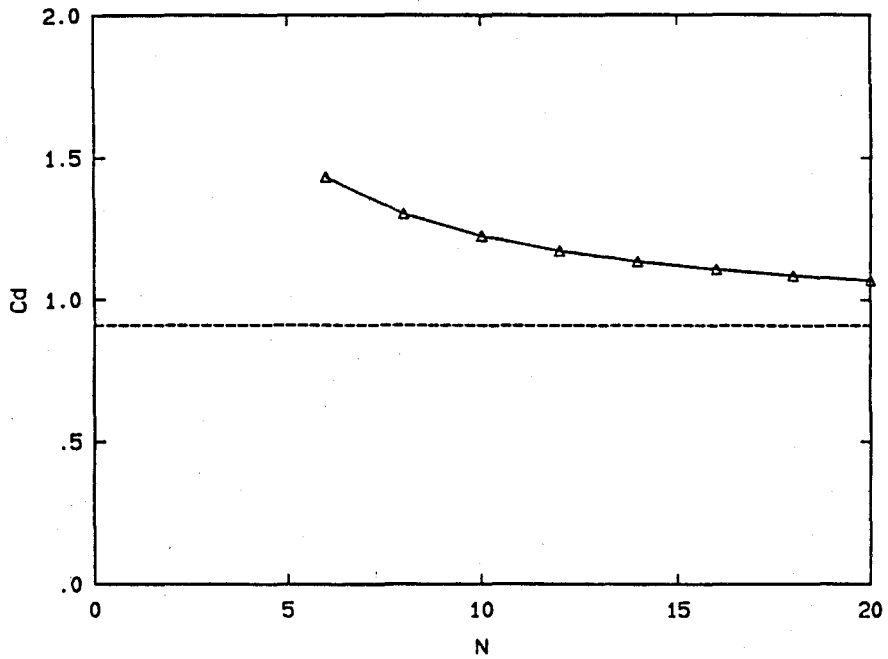
FIGURE (4.1.6) Plots of C_d that are due to the apparent mass effect of an unit acceleration versus grid resolution N_{c_n}; $-\triangle-$ current calculation; $----$ theory (Meyerhoff 1970).
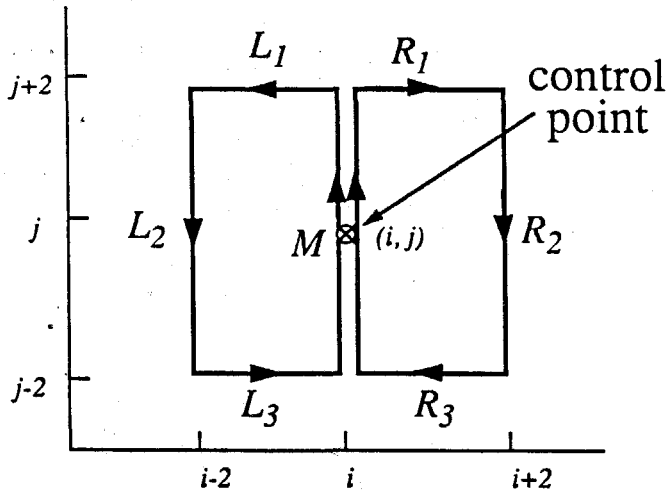
FIGURE (4.1.7) Schematic showing vortex loops for enforcing no-slip boundary conditions.
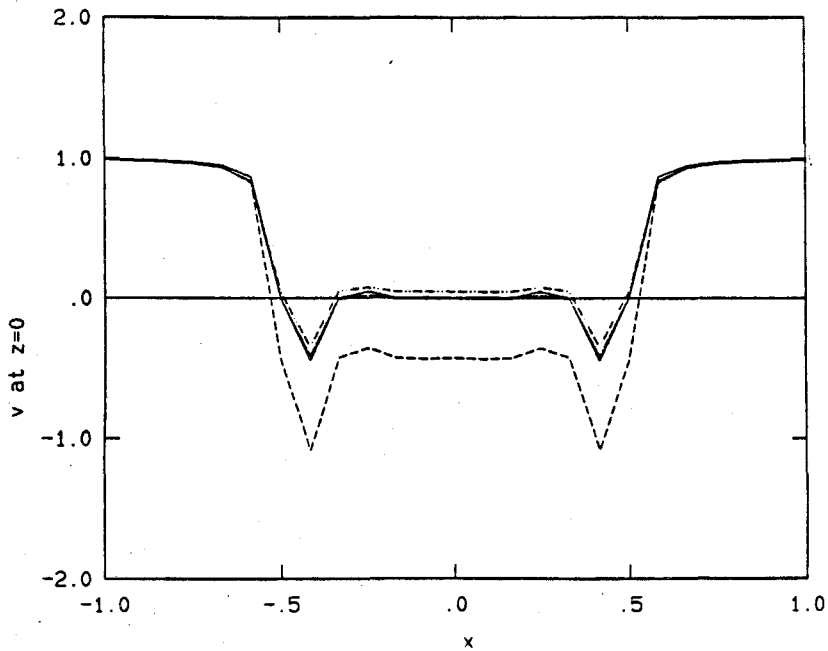
(a)

FIGURE (4.1.8) Plots of the x-distribution of v on a plate tangential to the flow $\underline{u} = U_\infty \hat{e}_y$, $t = 0$.
——— along the edge; — — — — section between the edge and the first control point;
others, inner sections. (a) $N_p = 15$; (b) $N_p = 19$; (c) $N_p = 23$; (d) $N_p = 27$.
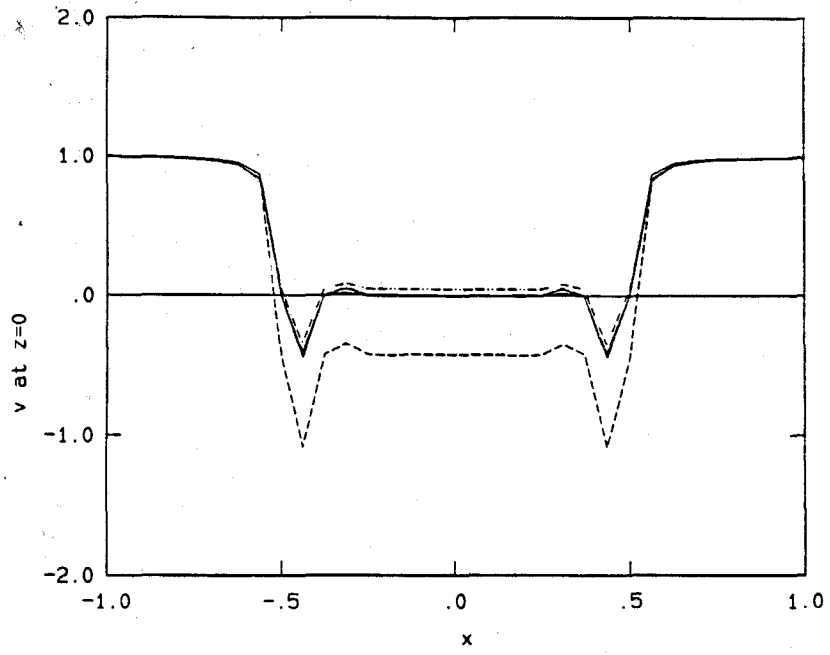
(b)
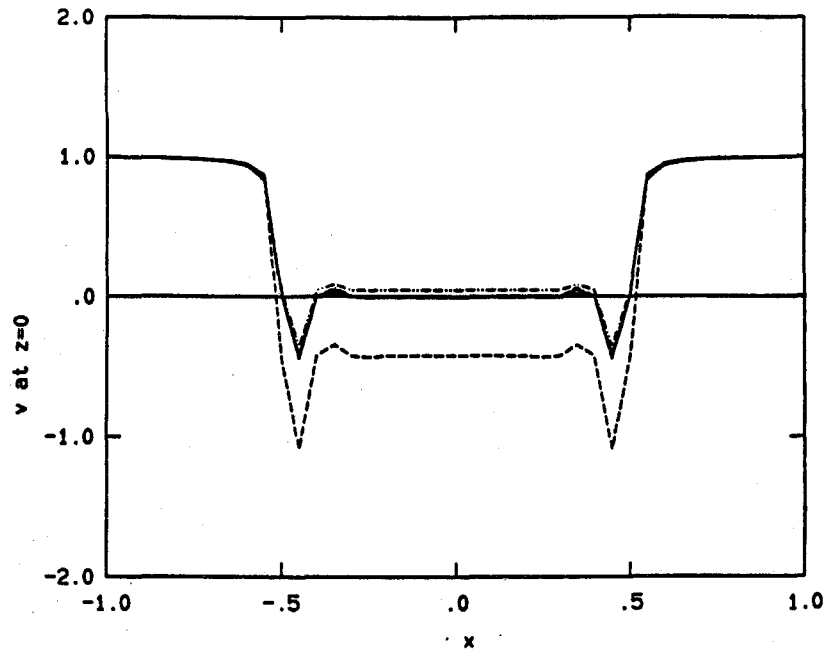
(c)

FIGURE (4.1.8) Cont.
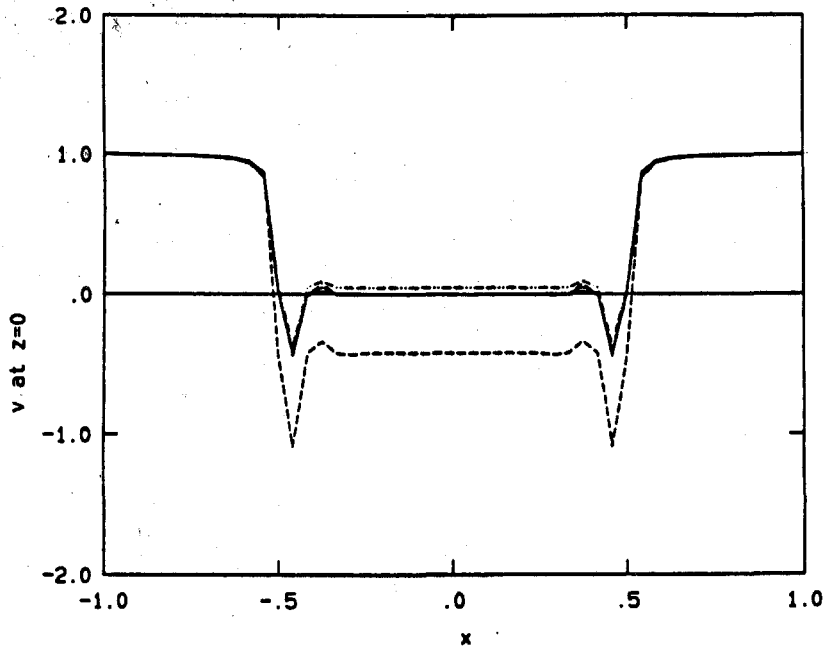
(d)

FIGURE (4.1.8) Cont.
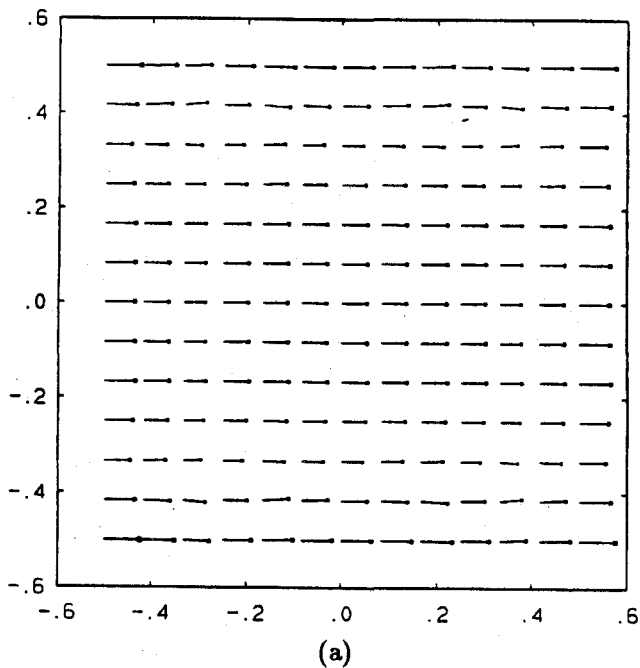
(a)

FIGURE (4.1.9) Plots of $\underline{\alpha}$ field on the boundary layer. Same as Fig. (4.1.8).

(b)

(c)

FIGURE (4.1.9) Cont.

(d)

FIGURE (4.1.9) Cont.

(a)   (b)

FIGURE (4.2.1) Schematic showing shedding points P_{shv} and shedding area A_{shv} (a) away from the corner; (b) next to corner.
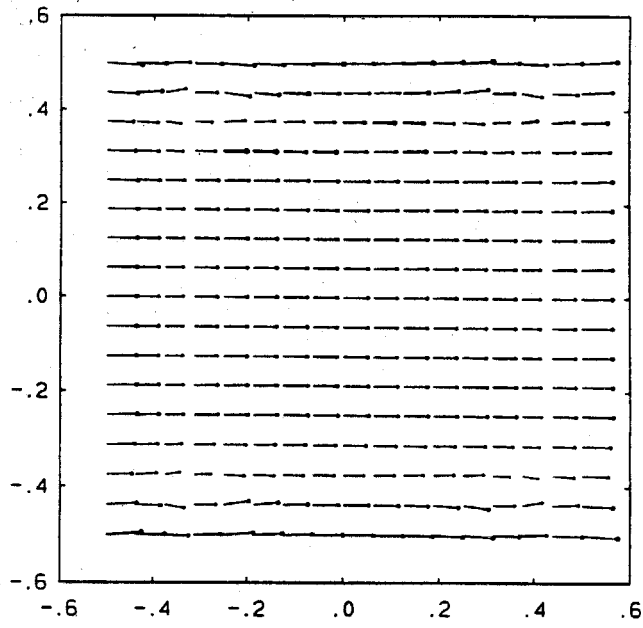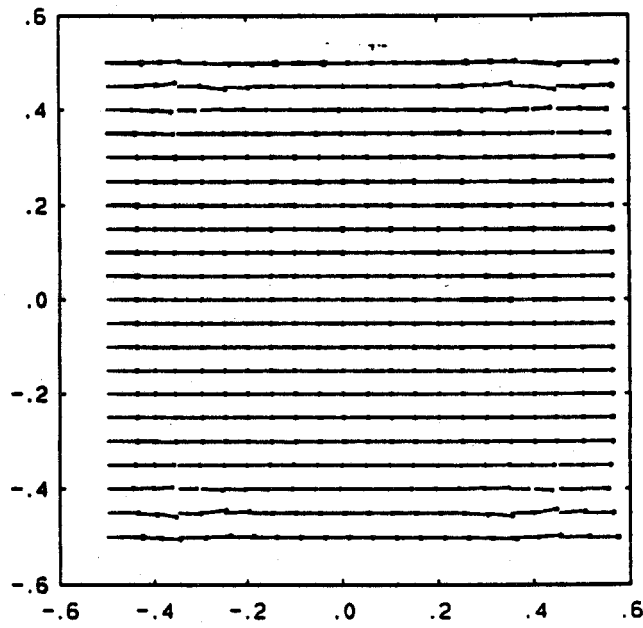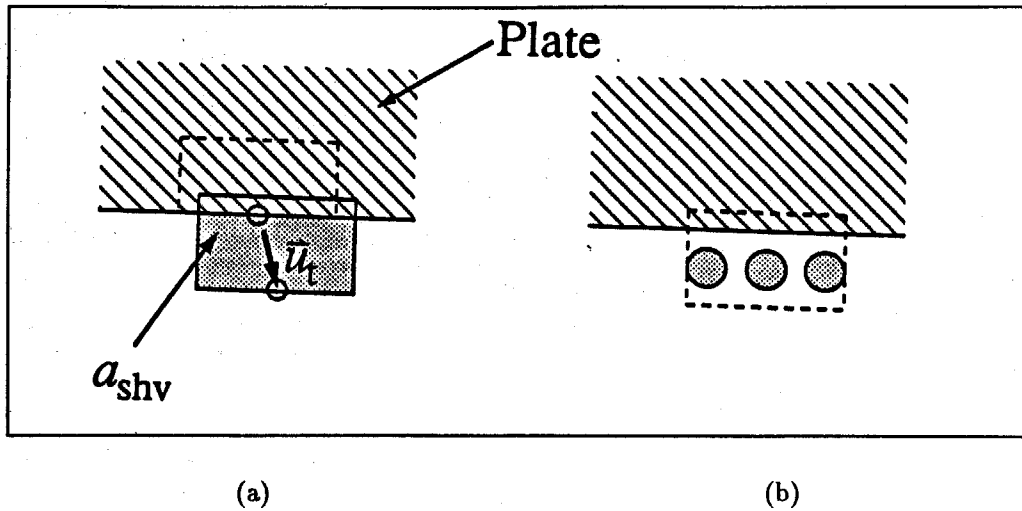
FIGURE (4.2.2) Schematic showing the shedding process. (a) portion of A_{shv} in fluid, called a_{shv}, is considered shed; (b) replaces a_{shv} by particles.

(a)
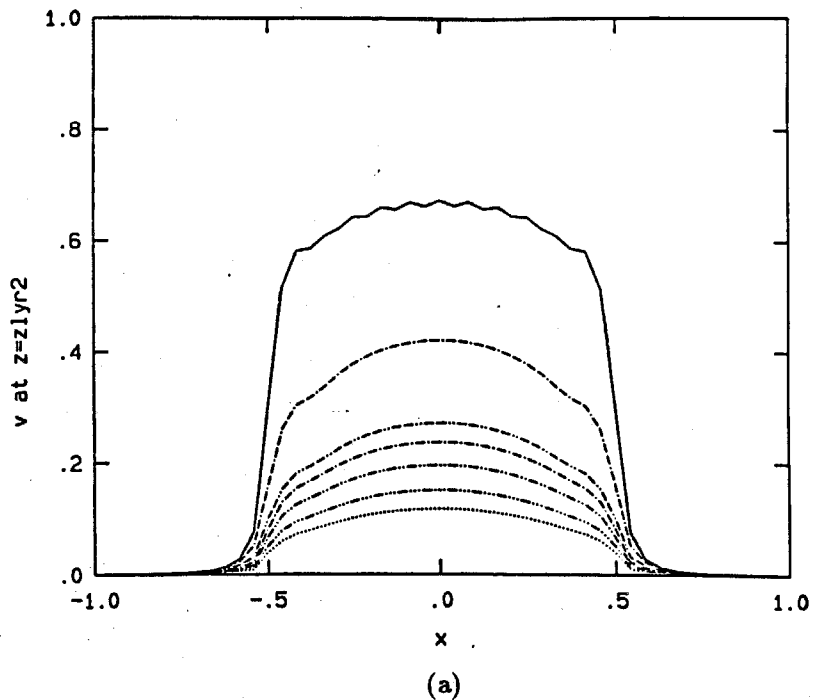
FIGURE (4.2.3) Plots of v at an edge (——) parallel to the x-axis for an impulsively started normal plate; $t = 0.02$, $\sigma = \delta l_p/3$. (a) $N_{par} = 3$; (b) $N_{par} = 5$.
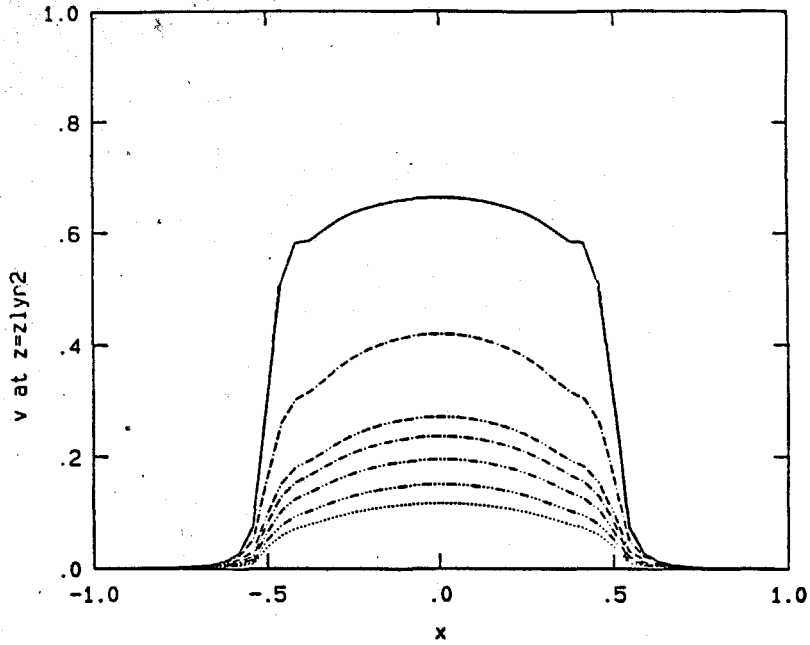
(b)

FIGURE (4.2.3) Cont.
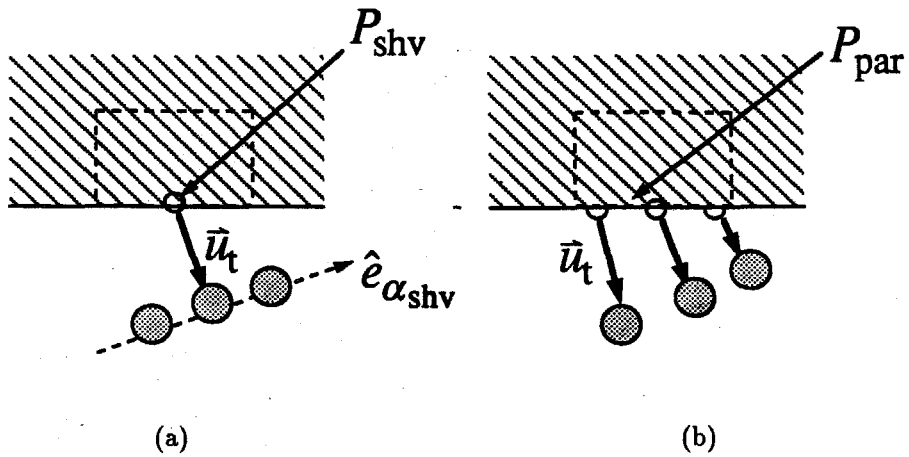
(a)   (b)

FIGURE (4.2.4) Schematic showing (a) shedding scheme a; (b) shedding scheme b.
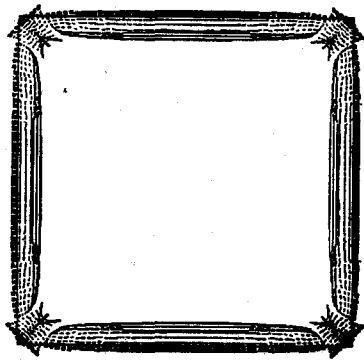
(a)
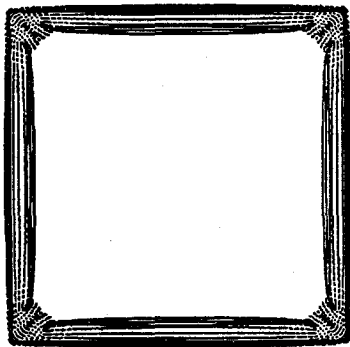
(b)

front view   oblique view

FIGURE (4.2.5) Plots of vortex particles behind a normal plate at $t = 0.15$ computed with (a) shedding scheme a; (b) shedding scheme b.
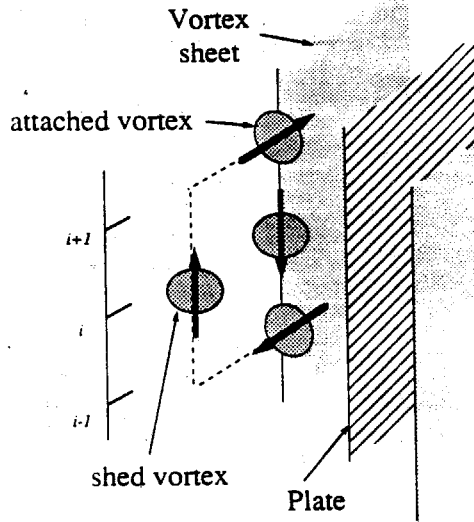
FIGURE (4.2.6) Schematic showing the use of attached vortex elements in satisfying the solenoidal condition of a shed particle.

<table>
| front view | (a) side view | oblique view |
</table>
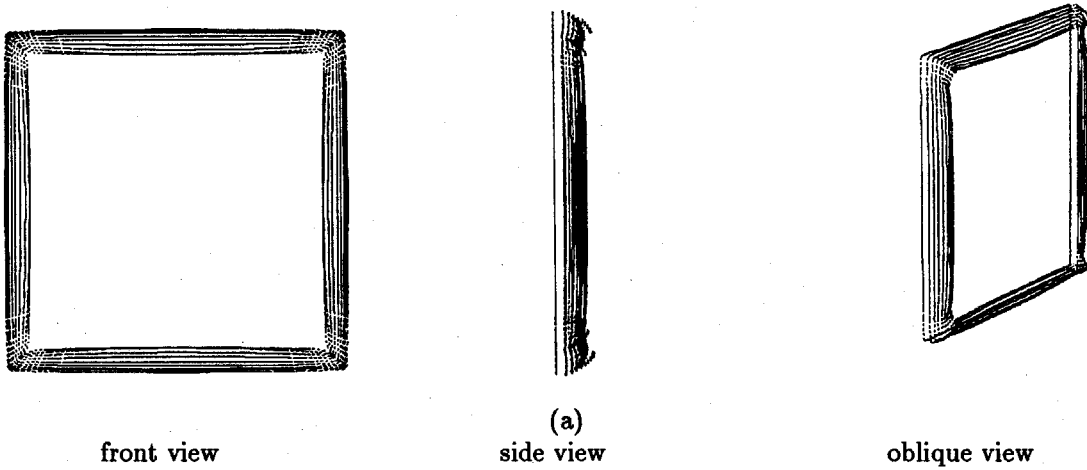
FIGURE (4.3.1) Time sequence of the flow past a normal square plate. (a) $t = 0.1$; (b) $t = 0.2$; (c) $t = 0.3$; (d) $t = 0.4$.
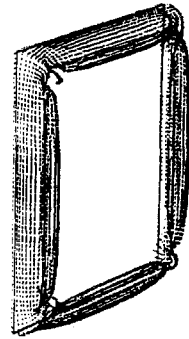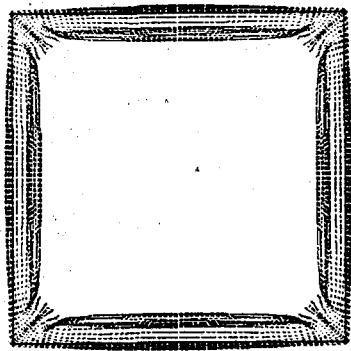
(b)
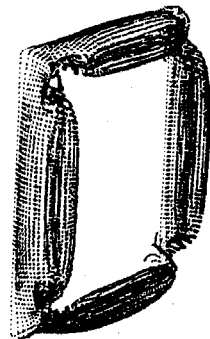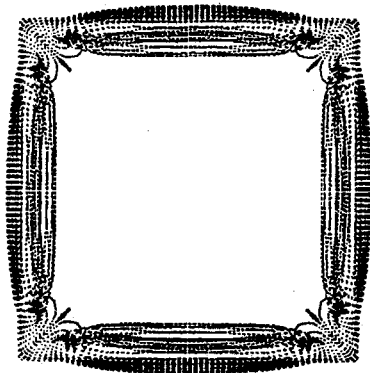
(c)
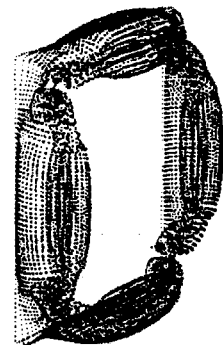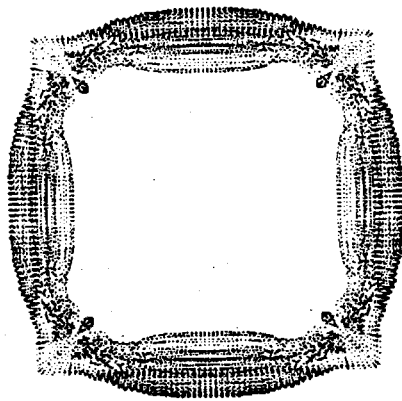
(d)

front view   side view   oblique view

FIGURE (4.3.1) Cont.

(a)

(b)

(c)
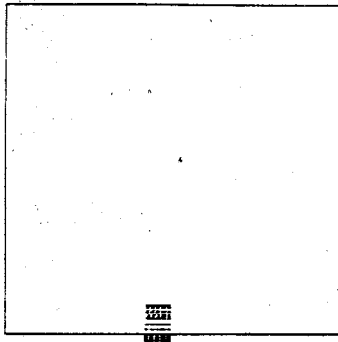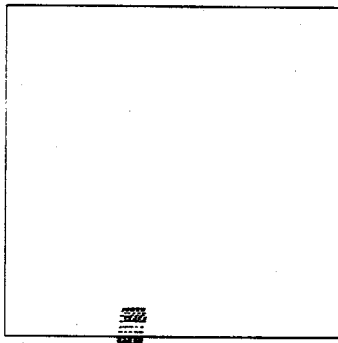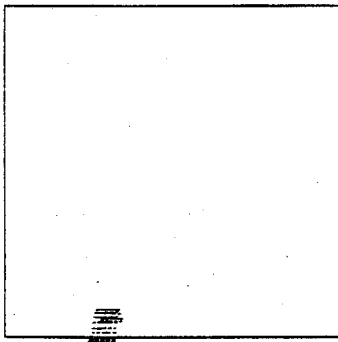
front view   side view

FIGURE (4.3.2) Streakline plots of the flow past a normal square plate at $t = 0.2$. (a) $-0.083 < x <$ 0.0; (b) $-0.167 < x < -0.083$; (c) $-0.250 < x < -0.167$; (d) $-0.333 < x < -0.250$; (e) $-0.417 < x < -0.333$; (f) $-0.5 < x < -0.417$.

(d)

(e)

(f)
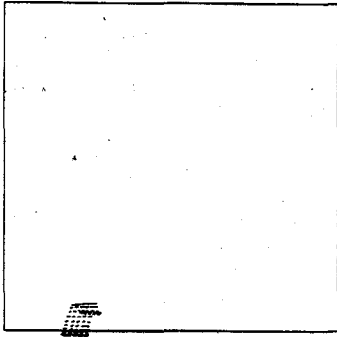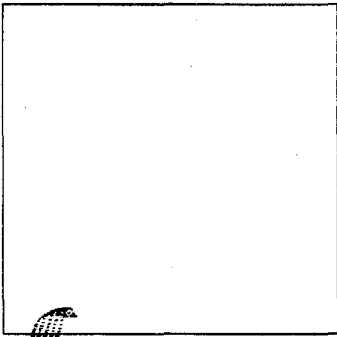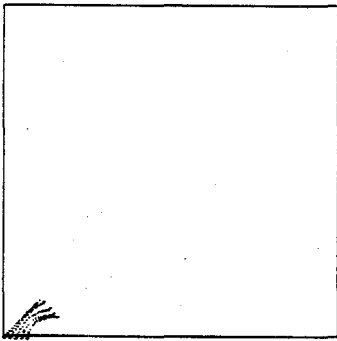
front view   side view

FIGURE (4.3.2) Cont.

(a)

(b)

(c)
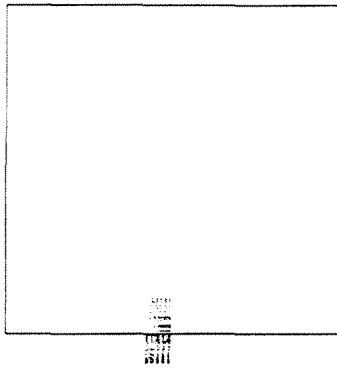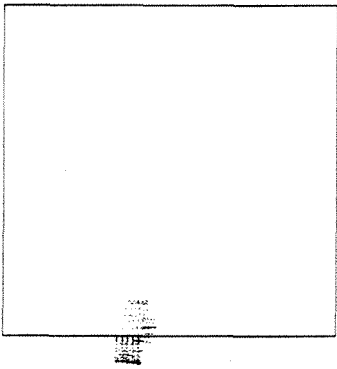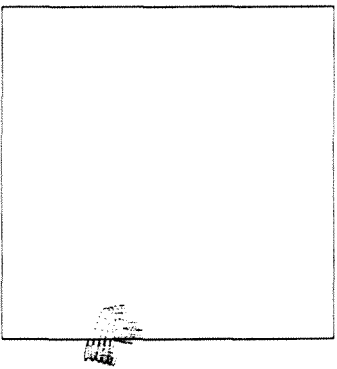
front view   side view

FIGURE (4.3.3) Streakline plots of the flow past a normal square plate at $t = 0.4$. (a) - (f) Same as Fig. (4.3.2).

(d)

(e)

(f)
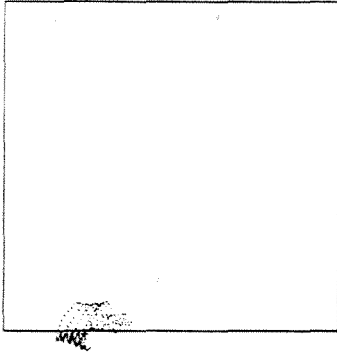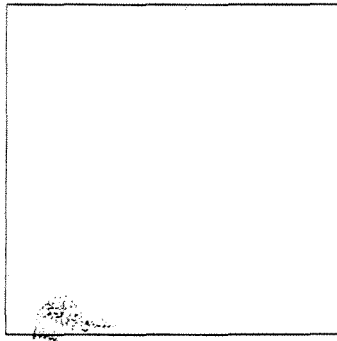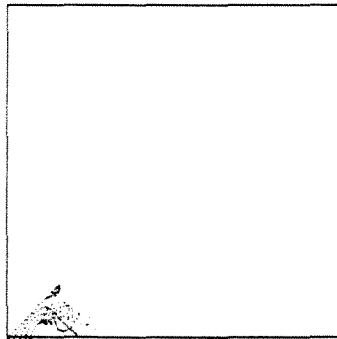
front view   side view

FIGURE (4.3.3) Cont.
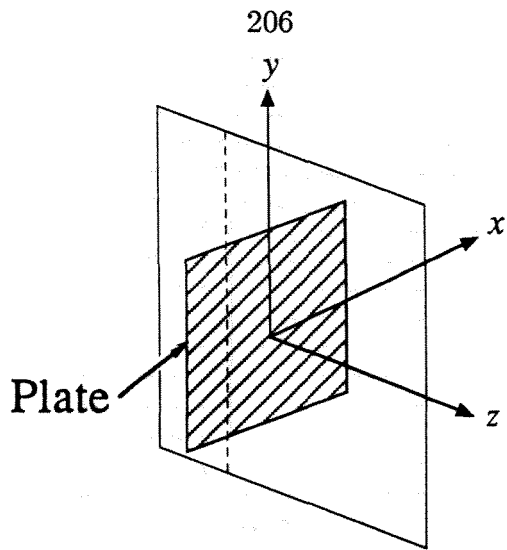
FIGURE (4.3.4) Schematic showing the cutting plane where the velocity vector field is computed.

(a)
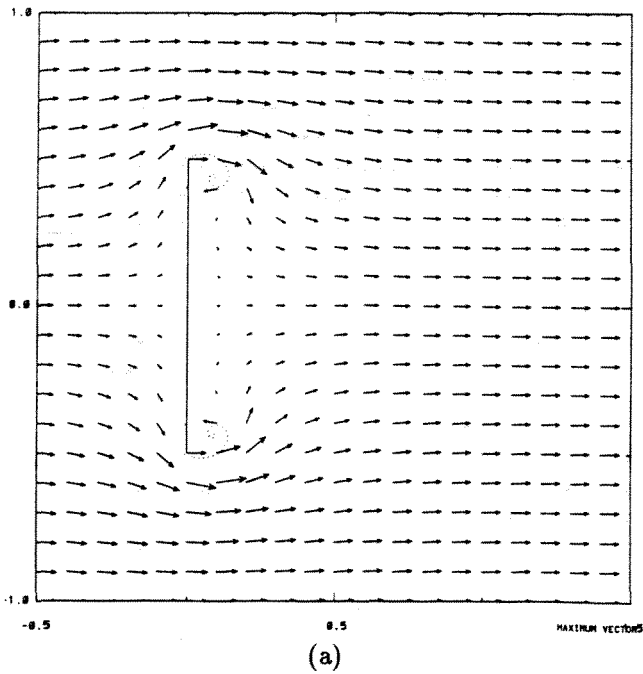
FIGURE (4.3.5) Plots of the velocity vector field at $t = 0.2$. (a) $x = 0.0$; (b) $x = 0.1$; (c) $x = 0.2$; (d) $x = 0.3$; (e) $x = 0.4$; (f) $x = 0.45$.
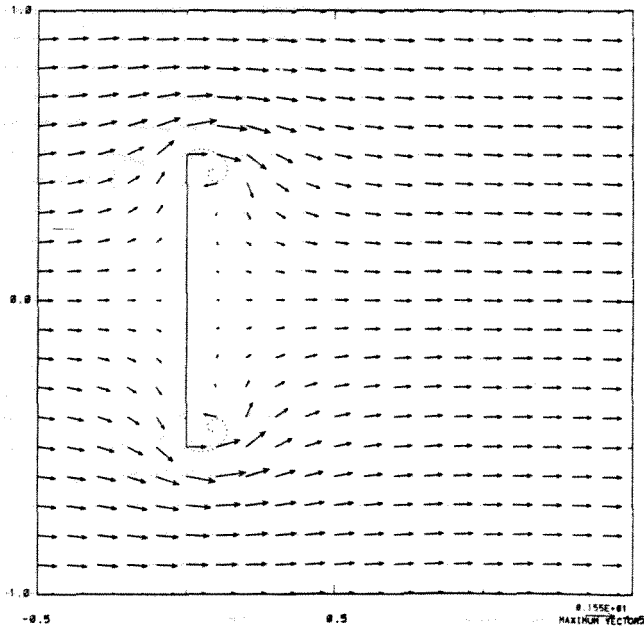
(b)
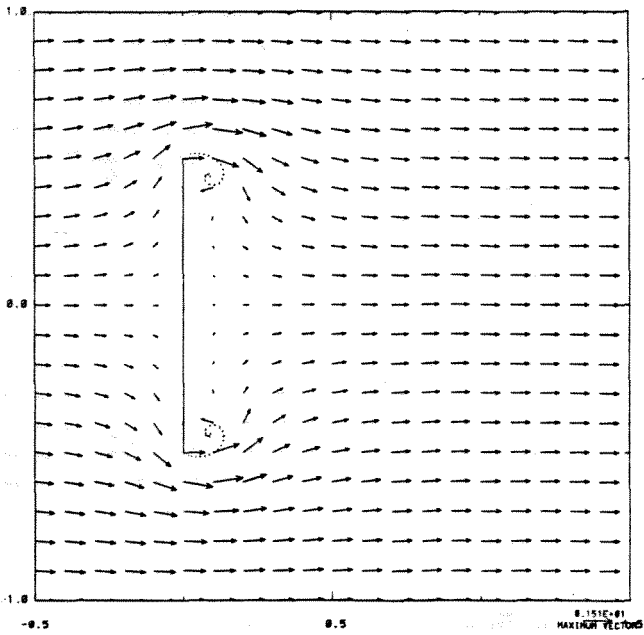
(c)

FIGURE (4.3.5) Cont.
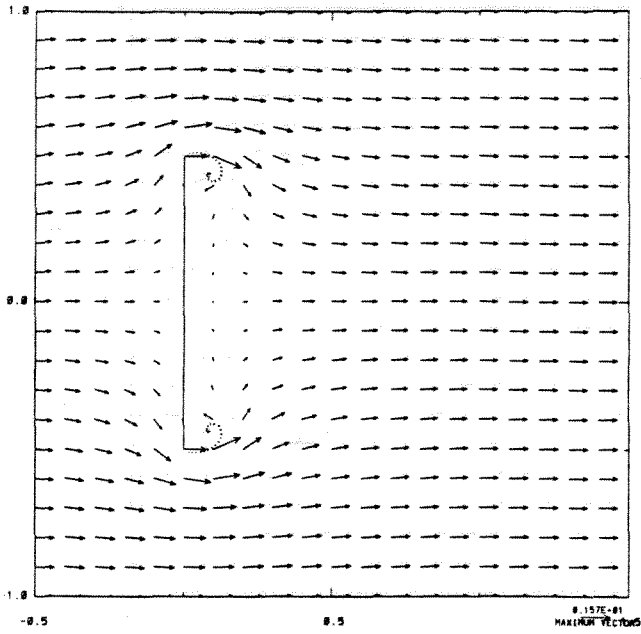
(d)
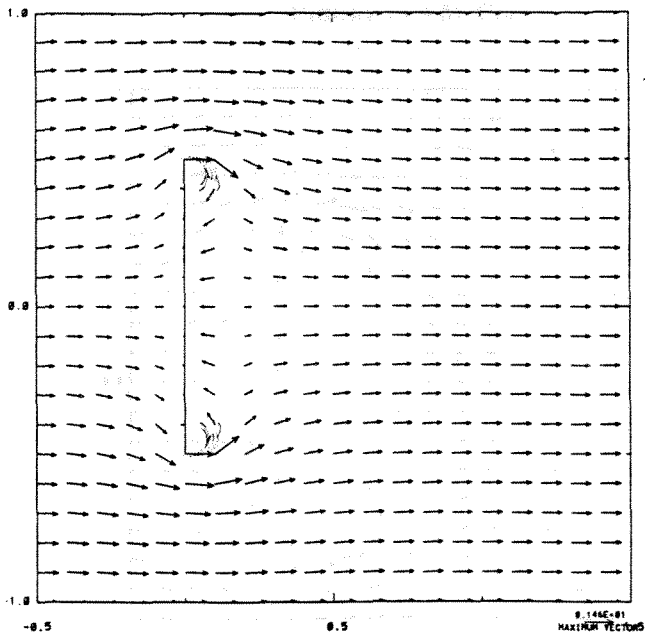
(e)

FIGURE (4.3.5) Cont.
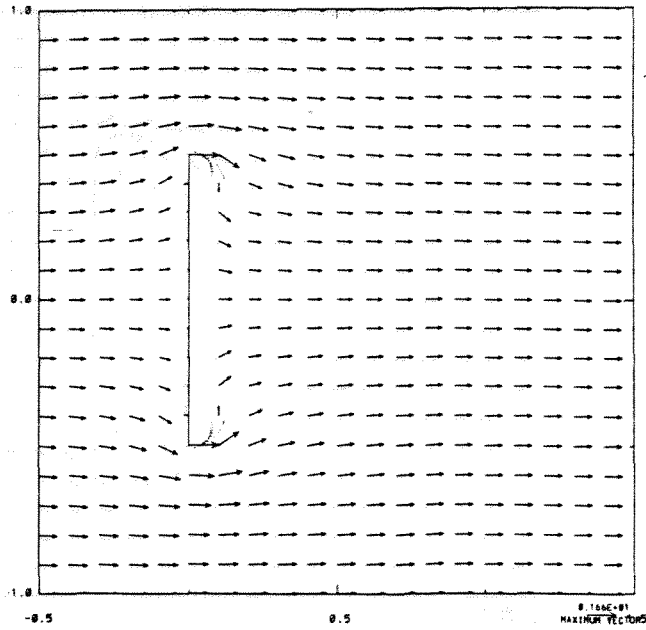
(f)

FIGURE (4.3.5) Cont.
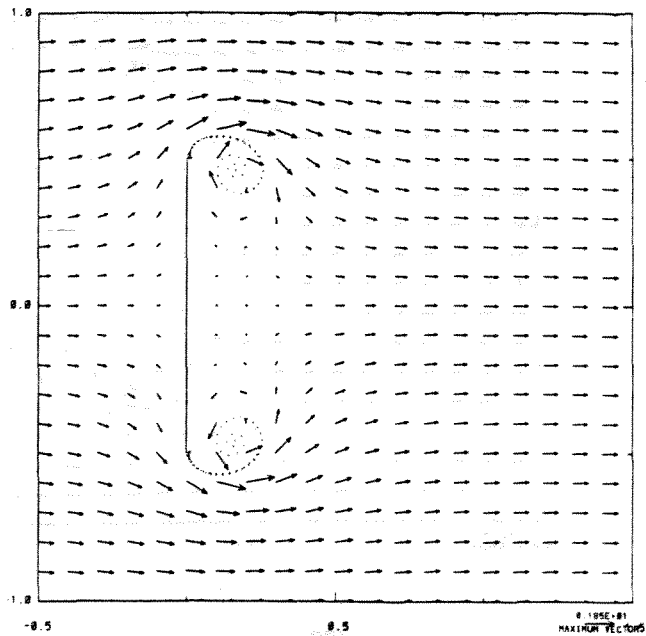
(a)

FIGURE (4.3.6) Plots of the velocity vector field at $t = 0.4$. (a) - (f) Same as Fig. (4.3.5).
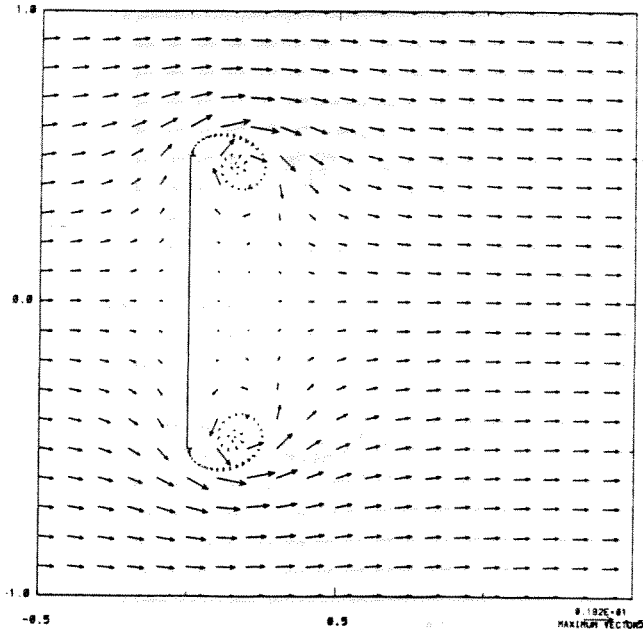
(b)
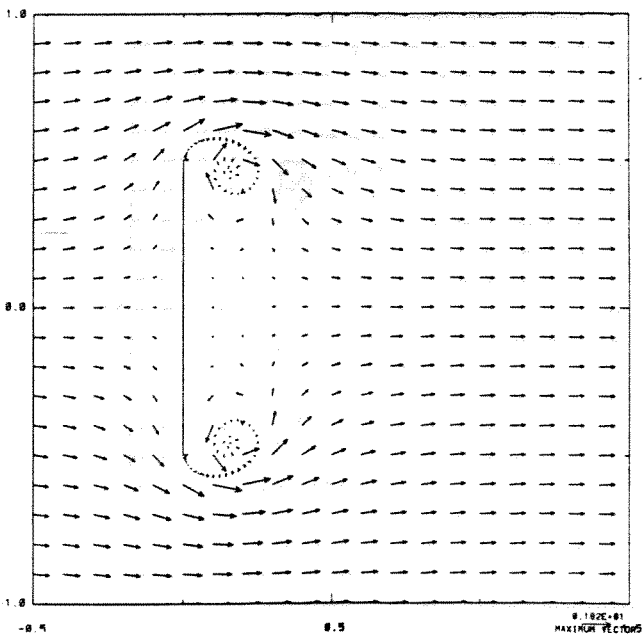
(c)

FIGURE (4.3.6) Cont.
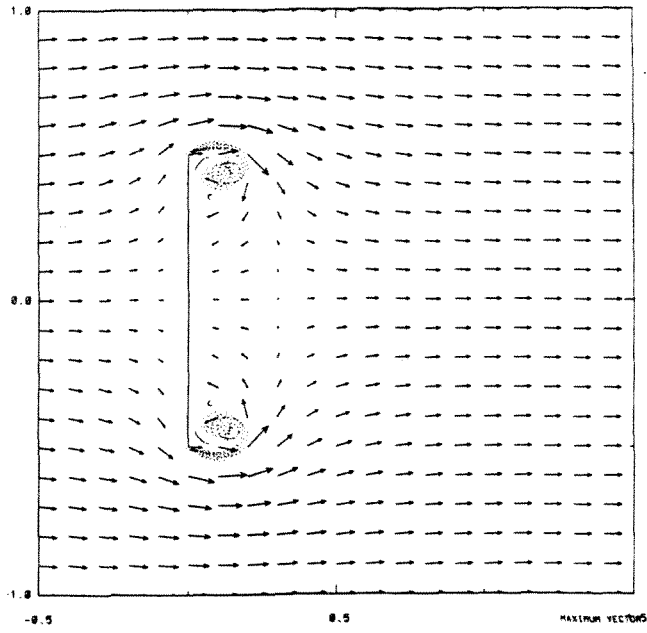
(d)
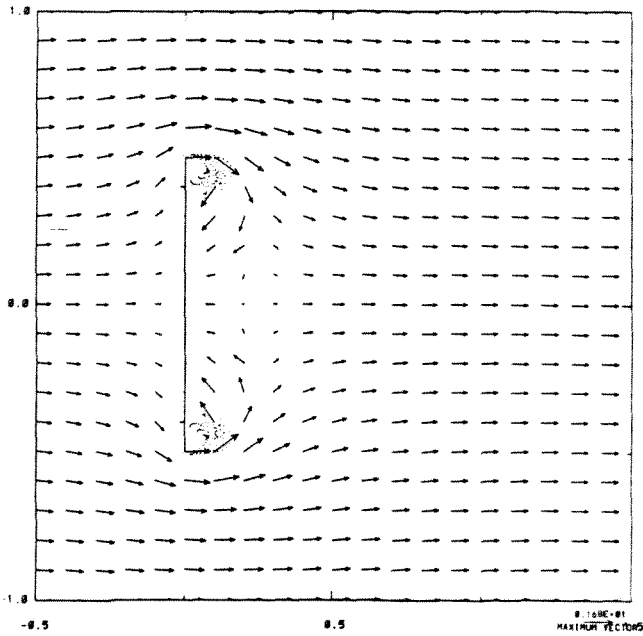
(e)

FIGURE (4.3.6) Cont.
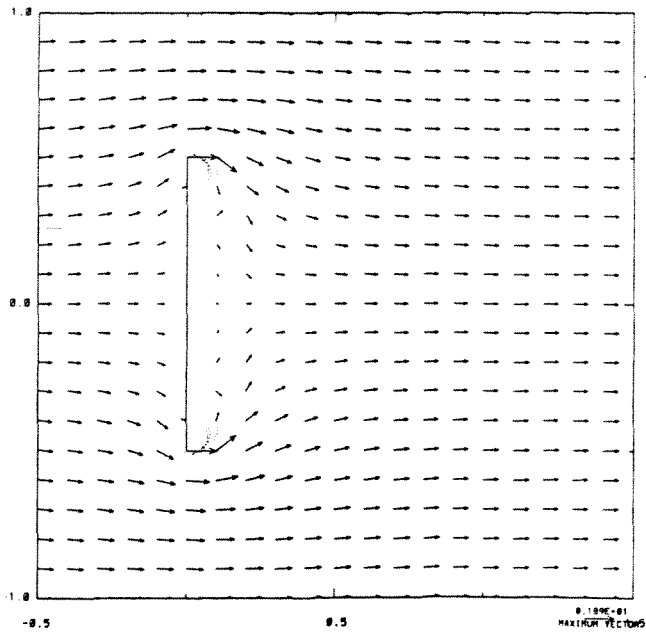
(f)

FIGURE (4.3.6) Cont.
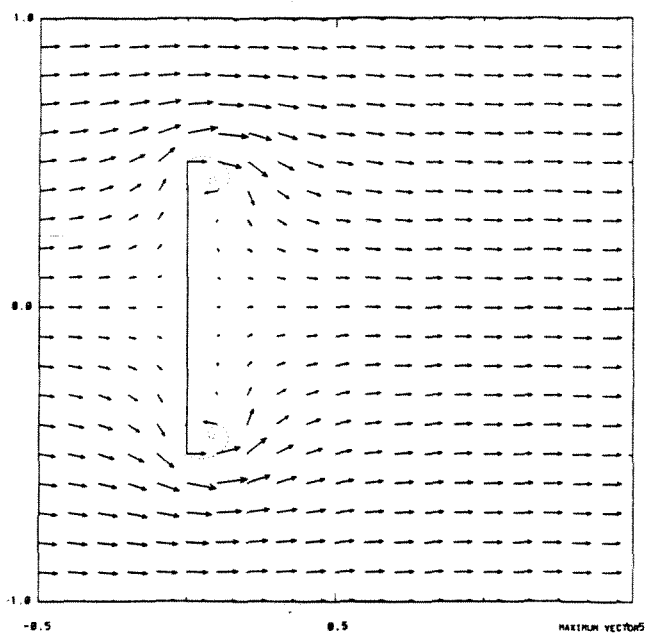
x = 0 (symmetry plane)
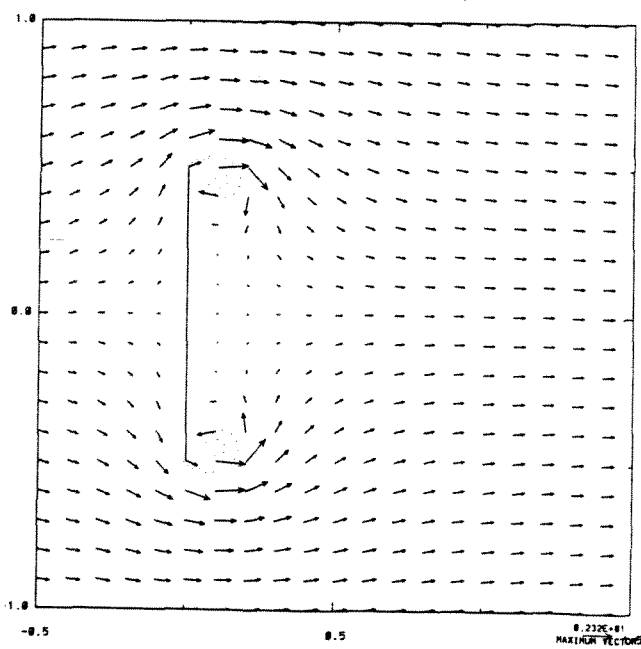
2D

(a)

FIGURE (4.3.7) Comparison of the velocity plots at $x = 0$ (symmetry plane) to a 2D solution at (a) $t = 0.2$; (b) $t = 0.4$.

x = 0 (symmetry plane)

2D

(b)

FIGURE (4.3.7) Cont.